REPORT DOCUMENTATION PAGE

Form Approved
OMB NO. 0704-0188

1. AGENCY USE ONLY (Leave Blank)	2. REPORT DATE	3. REPORT TYPE AND DATES COVERED
	9/22/00	Final, 9/1/96 - 8/31/00

4. TITLE AND SUBTITLE
Durability and Intelligent Nondestructive Evaluation of Adhesive Composite Joints

5. FUNDING NUMBERS
F49620-96-1-0458

6. AUTHOR(S)
Y. A. Dzenis

7. PERFORMING ORGANIZATION NAME(S) AND ADDRESS(ES)
University of Nebraska-Lincoln, Research Grants & Contracts Office, Lincoln, NE 68588-0430

8. PERFORMING ORGANIZATION REPORT NUMBER

9. SPONSORING / MONITORING AGENCY NAME(S) AND ADDRESS(ES)
AFOSR
801 North Randolph Street
Arlington, VA 22203-1977

10. SPONSORING / MONITORING AGENCY REPORT NUMBER

11. SUPPLEMENTARY NOTES

12 a. DISTRIBUTION / AVAILABILITY STATEMENT
Approved for public release; distribution unlimited.

12 b. DISTRIBUTION CODE

13. ABSTRACT (Maximum 200 words)

This project addressed durability and damage and fracture development and monitoring in adhesive composite joints for aerospace structural applications. Experimental and theoretical studies of static and fatigue behavior of single lap adhesive joints were performed on joints with unidirectional (UD) and cross-ply (CP) adherends made from a graphite-epoxy composite and an adhesive used in the Air Force. Joints with and without deliberately introduced cracks and delaminations were analyzed. Instrumented testing was performed by a digitally controlled servohydraulic testing machine. Damage and fracture evolution and mechanisms were analyzed by acoustic emission (AE), video microscopy, and off-line optical, scanning electron, and atomic force microscopies. A new method of acoustic emission analysis of histories of damage and fracture mechanisms was developed (patent pending). The method was shown to be especially effective for fatigue damage and fracture evolution studies. Nonlinear finite element analysis was used to compute mixed mode energy release rates for the bond cracks and delaminations as functions of crack lengths. The results showed that both UD and CP joints subjected to fatigue exhibited gradual crack propagation over a substantial portion of fatigue life. Static fracture mechanics characterization of joints under pure Mode I, II, and mixed mode loadings was also performed and exploratory results on fatigue fracture under pure mode loads are also discussed. Overall, the project provides better understanding of static and fatigue behavior of adhesive composite joints. The results can be used in the development of intelligent nondestructive evaluation approaches with predictive capabilities.

14. SUBJECT TERMS	15. NUMBER OF PAGES
	240
	16. PRICE CODE

17. SECURITY CLASSIFICATION OR REPORT	18. SECURITY CLASSIFICATION ON THIS PAGE	19. SECURITY CLASSIFICATION OF ABSTRACT	20. LIMITATION OF ABSTRACT
UNCLASSIFIED	UNCLASSIFIED	UNCLASSIFIED	UL

NSN 7540-01-280-5500

Standard Form 298 (Rev.2-89)
Prescribed by ANSI Std. 239-18
298-102

AIR FORCE OFFICE OF SCIENTIFIC RESEARCH

Grant F49620-96-1-0458

Final Progress Report

Durability and Intelligent Nondestructive Evaluation of Adhesive Composite Joints

Principal Investigator: Y. Dzenis

Department of Engineering Mechanics
University of Nebraska

September 2000

UNIVERSITY OF NEBRASKA-LINCOLN

Table of Contents

1.	Statement of the Problem Studied	2
2.	Summary of the Most Significant Results	2
3.	List of Publications and Other Outcomes	17
	Graduated Students	17
	Patent Applications	18
	Journal Papers	18
	Conference Papers	19
	Technical Reports	20
	Awards, Honors	22
	Laboratory Development	23
4.	List of Participating Scientific Personnel	23
5.	Report of Inventions	24
	Appendices	25
	1. Experimental analysis of single lap joints with unidirectional and cross-ply adherends	26
	2. Modeling of single lap joints with unidirectional and cross-ply adherends	61
	3. Analysis of single lap joints with delaminated adherends	86
	4. Acoustic emission analysis of damage and fracture micromechanisms	111
	5. Fracture mechanics characterization of joints with unidirectional and cross-ply adherends	192

1. Statement of the Problem Studied

This project addressed durability and damage and fracture development in adhesive composite joints for aerospace structural applications. Defense applications of advanced polymer matrix composites span aerospace structures, weapons systems, ammunition, ground vehicles, transportation infrastructure, electronics, and many other systems. An interest in the use of adhesive joints in these structures has increased significantly over the last several years for several reasons. The key advantage of adhesive joint technology is that it enables the development of large, low-cost, highly integrated structures. This manufacturing technique significantly reduces the high-cost hand-assembly labor steps in fabricating composite structures. Adhesive joints are ideal for joining parts in highly contoured, low observable composite structures. This technology is also critical to the repair of damaged metallic and composite structures. However, there are several problems associated with adhesive joints that impede their wider use in military and civilian applications. The first problem concerns a general lack of understanding of the fatigue behavior and durability performance of joints. The second problem concerns the inspectability and in-service monitoring of joints. These two interrelated problems were addressed in this project. The objectives of this research were comprehensive experimental and theoretical analysis of behavior of adhesive composite joints of several configurations under static and fatigue loadings and development of methods of their nondestructive monitoring.

2. Summary of the Most Significant Results

The research was organized in several technical tasks described below. The progress was documented in a series of technical reports (see next section). The research was performed in close col-

laboration with AFRL/MLBC (Dr. Steven Donaldson, Dr. Ajit Roy, Dr. Mark Forte, and Dr. Nick Pagano). Ian Saunders from Dzenis' group visited AFRL/MLBC and conducted part of his research there in the Spring of 1999. The total of 19 technical reports were delivered and discussed at AFRL/ MLBC. The most significant research results are summarized in this section.

Experimental Analysis of Mechanical Behavior of Single-Lap Adhesive Composite Joints Under Quasistatic and Fatigue Loading

Adhesive bonding has a high potential for aerospace, automotive, and other military structural applications. Adhesively bonded composite patches can be used to repair aerospace parts with minimum deterioration of aerodynamic contours. Although adhesive joints have been extensively studied during the past decades, the mechanisms of fatigue failure and life of the joints are not yet sufficiently understood. As a result, there is no reliable methods of prediction of their long-term durability. The objective of this part of the project was to study mechanical behavior and mechanisms of damage and failure in single-lap composite joints under quasistatic and fatigue loading.

Single-lap joint specimens were manufactured from high curing temperature Boeing-certified Hexcell T2G-190-12F263 graphite-epoxy composite and Cytec FM 300-2M adhesive film used in the Air Force. Six ply unidirectional $[0]_6$ and eight ply cross-ply $[0/90]_{2S}$ adherends were utilized. The specimens were 170 mm long and 25.4 mm wide with the 50.8 mm overlap. Spacer tabs were glued on both ends of the specimens. The specimens were manufactured by the secondary curing. Manufacturer recommended curing cycles were applied for both adherend and bond curing. Material surface preparation prior bonding was varied. It was found that the highest joint static strength was achieved

when the adhesive film surface was treated by a solvent. The adhesive solvent wipe was consistently applied on all specimens in this study. The filets of epoxy resin formed at the ends of the overlap during manufacturing were removed before testing.

Instrumented quasistatic tensile tests were performed by a digitally controlled servohydraulic testing machine at two displacement rates, 0.2 mm/min and 0.5 mm/min. A ball-bearing alignment coupling and wedge action grips were utilized. Overall deformation of the specimen was measured by stroke. More accurate measurements of the displacement between the points in the adherend and in the overlap were performed by an electromechanical extensometer. Damage and fracture evolution was simultaneously studied on-line by acoustic emission, acousto-ultrasonics, and video microscopy. Micromechanisms of damage were studied by fractography, scanning acoustic tomography, ultrasonic scanning, and acoustic microscopy. Over ten specimens were tested for each composite joint.

The analysis showed that quasistatic load-displacement response of joints with both unidirectional and cross-ply adherends was substantially non-linear. The slope of the diagrams first increased and then decreased. The average failure load of the joints with unidirectional adherends was 30% higher than the failure load of the joints with cross-ply adherends. Variation of the loading rate did not produce a noticeable effect on mechanical response. Substantial acoustic emission was acquired from all specimens throughout the loading range. Higher concentration of the AE events was observed near the ends of the overlap zone indicating damage development in these areas. However, final failure of joints with both unidirectional and cross-ply adherends occurred through the bond line. The bond fracture developed rather abruptly near the maximum load. Little to no composite adherend damage was observed on fracture surfaces of the failed specimens. There was a correspondence between the

overall mechanical response and cumulative acoustic emission load histories.

Instrumented fatigue testing of joints was performed on a digitally controlled servohydraulic testing machine. Sinusoidal tension-tension load function with the load ratio 0.1 was applied. The load amplitude varied from 0.4 to 0.8 of the quasistatic failure load. The resulting number of cycles to failure varied between 74 and 63,166. Damage and fracture evolution was studied on-line by acoustic emission and optical video microscopy. The total of seven specimens were tested for each of the adherend types.

Substantial damage development was detected throughout the fatigue tests by acoustic emission analysis. Damage concentrated near the ends of the overlap zone. The final failure occurred through the bond line. However, the bond fracture was not abrupt under fatigue. The bond crack usually initiated within the first 25-50% of fatigue life. Gradual crack growth in the bond line was observed throughout the remaining of the fatigue life. No indicators of crack initiation were observed on the deformation diagrams. However, a jump on the cumulative AE history curves marked bond crack initiation that was observed independently by on-line video microscopy. The S-N curves for joints with unidirectional and cross-ply adherends overlapped in the life range from 1,000 to 70,000 cycles to failure. It appeared, however, that the S-N curves for the two adherends had different slopes. The fracture surfaces of the failed specimens were fractographically examined and the final fracture areas under fatigue were identified and measured. Plotted against the fatigue load amplitude, these fracture areas exhibited a linear variation. This effect can be used in the development of a final failure criterion under fatigue. Detailed information on the experimental analysis of joints is given in Appendix 1.

Nonlinear Numerical Analysis of Single-Lap Adhesive Composite Joints with a Bond Crack

Laboratory experiments on single-lap composite joints showed that fracture of the bond line was a primary failure mechanism under both static and fatigue loading. Gradual crack growth in the bond line was observed over a substantial portion of fatigue life. The objectives of this part of the research were to develop a nonlinear finite element model for a cracked single-lap adhesive joint with laminated composite adherends and to study the effects of adherend thickness, adhesive layer, and crack length on joint response.

A two-dimensional finite element model of a single lap composite joint was developed based on the commercial FEM software ANSYS. It was assumed that the specimen was made of an orthotropic, linear elastic composite. The length of the overlap was equal to 50.8 mm. Calculated deformations of joints with unidirectional and cross-ply adherends were compared with experimental data. It was found that geometrically linear analysis could not be employed for the practical range of adherend thicknesses from 0.84 mm to 3.00 mm. Geometrically nonlinear analysis compared well with the experimental data.

The geometrically nonlinear model was used to analyze the effect of adherend thickness on the stresses in the joints without cracks. It was found that, at the same force, the relative displacements in the loading direction were smaller for the thicker adherends. However, at the same far-field stress, this effect was observed only at small stresses. The effect reversed as the far-field stress increased. The ANSYS submodeling technique was employed to study stress concentrations in the joints. It was found that, at the same far-field stress, thicker adherends produced higher stress concen-

trations in the joint. However, at the same stretching force, the results were mixed. The stress component σ_x (stretching along the specimen) was higher for the thinner adherends. However, the out-of-plane stress component, σ_z, was slightly higher for the thicker adherends. Overall, the single-lap joints made of thinner adherends had lower stress concentrations compared to the joints made of thicker adherends. This effect was due to enhanced flexibility of thinner adherends that resulted in larger nonlinear deformations and some stress relief.

Specimens with bond crack lengths 5.4, 15.4, and 35.4 mm were also analyzed by the geometrically nonlinear model. The adhesive layer was taken into account. Calculations demonstrated that stresses in the vicinity of the crack tip and stress intensity factors increased nonlinearly with the crack length. Average stresses over the uncracked overlap length also increased nonlinearly. The energy release rates for the bond crack were computed as functions of the crack length and compared with the stress intensity factors. The results were in good agreement.

The developed nonlinear model can be used for evaluation of stresses in cracked joints and formulation of relevant fatigue crack growth criteria. Fatigue crack propagation modeling can be performed in conjunction with quantitative nondestructive evaluation of the bond crack to predict life of composite joints. The analysis above showed that the mode mixity (the energy phase angle) changed as the bond crack extended. Therefore, mixed mode fracture models with variable mode mixity capability are needed for modeling the behavior of single lap joints. Detailed information on the numerical analysis of joints is given in Appendix 2.

Analysis of Joints with Delaminated Adherends

Delamination in adherends is one of the major damage modes in adhesive composite joints. Delamination may occur during the manufacturing of joints and in service due to the substantial peel and shear stresses in the adherends developed near the overlap ends. To date, little effort was devoted to the analysis of joints with delaminated adherends. The objective of this part of the research was to study the conditions of growth of delaminations in adherends in the single-lap adhesive composite joints.

Two approaches were used for the analysis of single-lap adhesive composite joint with cracks embedded between plies in the laminated adherends. The first approach was based on the modified beam theory. Resultant forces and moments in sublaminates created by delaminations were defined for arbitrary laminated adherends and multiple delaminating cracks in the adherends. These resultant forces and moments were used to evaluate the strain energy release rates for delamination propagation. The nonlinear finite element analysis of joints with delaminations was also conducted. The results were qualitatively similar to the beam theory model predictions. However, the strain energy values computed by FEM were lower than in the beam theory calculations. The nonlinear FEM model was used for the parametric studies of joint behavior.

Variations of the strain energy release rate with delamination size in the joints with one and two cracks in unidirectional and cross-ply adherends were calculated and analyzed. It was shown that for all cases, the strain energy release rate at the crack tip inside the overlap region decreased as the crack length increased. The maximum strain energy release rate was observed for the crack tip near

the end of the overlap. The strain energy release rate for the crack tip outside the overlap zone was substantially smaller than the strain energy release for the tip inside the overlap zone. The maximum strain energy release rate in joints with cross-ply adherends was greater than the energy release rate in joints with unidirectional adherends. The maximum strain energy release rate at the crack tip inside the overlap zone decreased as the depth of the crack (the distance from the adhesive bond) increased. Presence of a second delaminating crack reduced the maximum strain energy release rate for the first crack. In this case, as for the single crack, the strain energy release rate dissipated with increasing crack length. Results of experimental analysis of joints with deliberately introduced delamination cracks of different initial length and depth that was performed for the first time qualitatively corroborated all theoretical predictions. From the quantitative comparison of the experimental and theoretical data, the critical energy release rate for delamination propagation in joints was computed for the first time.

Overall, the analysis showed that single-lap composite joints are delamination tolerant. Delaminations in adherends may, however, grow when the major bond crack in the adhesive initiates and extends under fatigue. Experimental analysis of joints with delaminations in the adherends in presence of the bond cracks is in progress. The developed model can be used in conjunction with experimental nondestructive evaluation to analyze the behavior of adhesive composite joints with partially damaged adherends. Detailed information on the analysis of joints with delaminated adherends is given in Appendix 3.

Extraction of Histories of Damage Micromechanisms under Quasistatic and Fatigue Loading by Acoustic Emission Analysis

Advanced composites and joints subjected to long-term loading exhibit gradual accumulation of micro- and macro-damage of several types. These include matrix cracks, fiber breaks, fiber-matrix debonding, delaminations, and bond cracks. Substantial acoustic emission generated during quasistatic and fatigue tests of single-lap adhesive composite joints performed in this project indicated early damage development. Classification of the overall cumulative acoustic emission into the histories for different micro- and macro-mechanisms would be invaluable for better understanding the mechanisms of failure and life of joints. Acoustic emission was used to analyze overall damage evolution in composites by several authors. Different damage mechanisms were reported to produce AE signals with different parameters. However, attempts to apply single parameter discrimination to separate damage mechanisms were largely unsuccessful due to the overlap of parametric ranges for different mechanisms. Recently, transient AE analysis was applied for the AE source recognition. The approach was shown to be more reliable compared to parametric filtering. However, the transient AE analysis is not feasible for long-term fatigue testing of composites and joints. An extremely large number of AE signals under fatigue cannot be evaluated in the transient (digital waveform) format. The objective of this part of the research was to develop a new method to analyze histories of different damage mechanisms that would be suitable for fatigue analysis.

Acoustic emission from a large number of graphite-epoxy composite specimens with gradually increasing complexity of microstructure was acquired and analyzed. Based on the analysis, a new hybrid method of extraction of histories of damage micromechanisms was formulated. The method is

based on the combination of the AE transient waveform classification and multicluster filtering. It was proposed for the first time to use multiparametric regions in a suitable AE parametric space to distinguish AE signals from different damage mechanisms. The following approach for the AE analysis of damage evolution histories was formulated. AE transient waveforms are acquired along with parametric AE data. The waveforms are screened and the characteristic waveforms for different damage mechanisms are identified. AE parametric spaces are then analyzed and multiparametric regions occupied by signals of different types are identified. Finally, evolution histories for different damage micromechanisms are extracted by multicluster parametric filtering. The method described above is the subject of a patent application (see Section 5 of this report).

Capabilities of the proposed method were illustrated by examples of damage evolution in unidirectional, cross-ply, and quasi-isotropic composites subjected to quasistatic and fatigue loading. Composite panels with the lay-ups of gradually increasing complexity, $[0]_8$, $[90]_{16}$, $[0/90]_{3S}$, $[+45/-45]_{4S}$, $[90/+30/-30]_{3S}$, and $[0/+45/-45/90]_{2S}$, were manufactured from Hexcel T2G190/F263 graphite/epoxy prepreg following manufacturer-recommended curing cycle. The panels were tabbed and rectangular, 250mm x 10 mm ($[0]_8$) and 250mm x 25 mm (other lay-ups), specimens were machined by a high-speed diamond saw. Tensile testing was performed by a MTS testing machine retrofitted by a digital Instron test control and data acquisition system. AE data were acquired and analyzed by a two-channel Vallen AMS3 acoustic emission system equipped with a transient recorder. Two wideband, high fidelity B1025 Digital Wave AE sensors were used.

Qualitatively different overall, unfiltered AE count histories were observed for the $[0]_8$ and $[90]_{16}$ composites. Loading in the fiber direction produced very little emission at the load levels

below 50% of the ultimate load. At higher levels, the accumulation rate was nonuniform with considerable jumps observed at 65% and 90% of the ultimate load. Loading in the transverse direction produced the highest accumulation rate at the low load levels, from 10-20% of the ultimate load. At the load increased, the AE accumulation rate decreased and stayed almost constant to the final failure. Analysis of the transient AE data for both composites revealed three characteristic waveforms with different amplitudes, durations, and frequency spectra. The A-type signals had peak frequency in the range from 100-220 kHz. The B-type signals had higher amplitude and peak frequency between 300-700 kHz. The C-type signals had high amplitude, long duration (>1000 us), and a wide frequency spectrum. The C-type signals were extracted from the overall parametric AE data by the duration filtering. Several parametric spaces were then analyzed. Distinct parametric regions for the A-type and B-type signals were identified in the amplitude-risetime parametric space. Multicluster analysis technique was then applied to separate the accumulation histories for different AE signals. Comparisons of the classified AE histories for the two composites with the damage mechanisms identified by online video microscopy and fractographic analysis of the broken specimens allowed to correlate the damage mechanisms with the characteristic AE signals. The A-type signals were associated with matrix damage, the B-type signals with fiber breaks, and the C-type signals with macroscopic longitudinal splitting. Analysis of the classified AE histories for the $[0]_8$ composite showed that the jumps on the overall AE history plots were due to longitudinal splitting. The fiber breaks and matrix cracks in this composite accumulated rather smoothly, except for the jump in the fiber damage caused by the second splitting event at 90% of the ultimate load. Damage in the $[90]_{16}$ composite consisted almost entirely of matrix cracks with small amount of fiber breaks developed near the final failure.

Capabilities of the method were further illustrated by examples of damage evolution in cross-

ply $[0/90]_{3S}$ and $[+45/-45]_{4S}$ composites. The same three characteristic AE waveforms were identified. Parametric regions in the amplitude-risetime space obtained by the analysis of unidirectional composites were used to extract microdamage evolution histories in cross-ply composites. The transferability of the parametric regions across lay-ups of the same composite system was verified by the inverse analysis of the transient waveforms of the AE signals from the different parametric regions.

Damage evolution in quasi-isotropic $[0/+45/-45/90]_{2S}$ and $[90/+30/-30]_{3S}$ composites under quasistatic and fatigue loading was further studied. The evolution histories of several damage modes were extracted and analyzed using the method described above. The histories of damage mechanisms under fatigue were studied after removal of the frictional noise created by fretting crack faces. Overall, the hybrid transient-parametric method of analysis developed in this work was found suitable for fatigue damage evolution studies when massive transient AE data acquisition is not possible. Application of the developed method to extract histories of damage and fracture mechanisms in adhesive composite joints is in progress. Detailed information on the AE analysis of composite adherends is given in Appendix 4.

Fracture Mechanics Characterization of Adhesive Composite Joints

Laboratory experiments on the single lap joints showed that fracture of the bond line was a primary failure mechanism under both static and fatigue loadings. The objective of this part of the research was experimental fracture analysis of adhesive joints with UD and CP adherends. Static fracture mechanics characterization of joints was performed under Mode I, II, and mixed mode loads by the double cantilever beam (DCB), end notch flexure (ENF), and Arcan tests, respectively. Fracture

mechanisms in the joints were evaluated by acoustic emission analysis, on-line video microscopy, optical, SEM, and AFM fractographies, and acoustic microscopy. Several methods of data reduction were applied and compared. Results showed that the classical beam method of data reduction for the DCB and ENF tests overestimated fracture energies for both joints studied. The data reduction was therefore performed by a more accurate numerical LRAM model developed at Materials Laboratory, WPAFB. Dr. M. Forte of AFRL/MLBC performed the calculations. Analysis showed that the joints with UD adherends had higher Mode I and comparable Mode II quasi-static fracture toughness as compared to the joints with CP adherends. Exploratory fatigue experiments showed, however, that the joints with UD adherends had higher fatigue crack growth rates in both Modes I and II, for similar strain energy release rates, as compared to the joints with CP adherends. Differences between the Mode I and II fracture micromechanisms were observed by the on-line and off-line nondestructive and fractographic observations. Static fracture toughness values for Mode I and II loadings were evaluated for both joints. Fatigue experiments are in progress. The mixed mode results by the Arcan test were found incompatible with the results from the Mode I and II tests. It was concluded that a mixed mode propagation test, such as CLS, should be applied for the purpose of mixed mode fracture characterization of joints. The results of this part of the research can be used in the development of predictive models of static and fatigue behavior of single lap joints. Detailed information on the fracture analysis of joints is given in Appendix 5.

Nondestructive Evaluation of a Bond Crack in an Adhesive Composite Joint

Experiments on single-lap adhesive composite joints showed that fracture of the bond line was a primary failure mechanism in joints under both static and fatigue loadings. Gradual crack growth in

the bond line was observed under fatigue. A nonlinear model suitable for fatigue crack propagation analysis was developed. Application of this model for life prediction requires the knowledge of the crack length and crack front positions in the joint. Conventional methods of ultrasonic nondestructive evaluation are based on through-thickness wave propagation. Scanning over the joint is required to locate the crack using this approach. Ultrasonic scanning can be accomplished by a C-SCAN device in a laboratory. However, it is not always possible to apply it in the field. Portable ultrasonic inspection equipment, such as laser generated ultrasonic systems, is expensive. In addition, parts of complicated composite structures, such as the aircraft, may not be accessible by this bulky equipment. Acoustic emission and acousto-ultrasonics are promising techniques for the crack front evaluation in joints. These techniques are based on the analysis of acoustic wave propagation through-length of a joint and can be applied on-line during fatigue loading. Both methods involve standard acoustic emission sensors attached on different sides of a joint. The data can be acquired and analyzed by a portable AE system in field. The objective of this part of the research was to explore the applicability of acoustic emission to detect bond cracks in the single-lap adhesive composite joints and to develop a theoretical basis for acousto-ultrasonics nondestructive evaluation of joints.

Acoustic emission signal location analysis was performed on the AE data acquired during fatigue tests after removal of the frictional noise created by fretting crack faces. The AE system was carefully calibrated by a pencil lead break test. The results were compared with on-line microscopic observations and off-line fractographic analysis of the bond crack progression. It was shown that the position of the moving crack front under fatigue could be detected by the AE analysis with 5 mm accuracy. Fractographic and nondestructive acoustic microscopy evaluation of the crack fronts showed that the fronts were randomly curved. This crack front curvature contributed to the uncer-

tainty of the linear acoustic emission location analysis.

Exploratory pattern recognition analysis of transient acoustic emission waveforms was applied to classify AE sources in the bond crack propagation tests under fatigue. VisualClass software by Vallen Systeme, GmbH was used. The method was applied to classify the AE signals from the pure mode tests (DCB and ENF) and the mixed mode test (single lap tension). Preliminary results showed that the majority of the fracture events in the mixed mode single lap tests were similar to the fracture events in the pure Mode II tests. Relatively few Mode I events were observed in the single lap joint tests. These results shed new light on the failure mechanisms in the lap joints. The results can be used in the development of predictive models for the mixed mode loads in the lap joints.

An alternative method of crack length detection by acousto-ultrasonics analysis was also explored. Preliminary experimental study showed that the frequency transfer function of a joint with a bond crack depended on the crack length. A theoretical analysis of flexural wave propagation was needed to extract quantitative information from these data. A model of flexural wave propagation through a single-lap adhesive composite joint was developed for this purpose for the first time.

The model was based on the analysis of a two-dimensional transient wave propagation process in the adherends and the adhesive layer. Wave propagation in the adherends was modeled as acoustic wave process in semi-infinite laminated plates. Classical lamination theory was used in the derivation of the governing equations. Rotatory inertia terms were retained in the analysis. Mutual influence of the plates via adhesive layer was modeled as dynamic distributed loading over the overlap zone. General solutions describing longitudinal and flexural waves in the plates were obtained. A

leaky acoustic wave through the adhesive layer was modeled using transfer matrix approach. Unknown coefficients of the general transient solutions for the two plates and the adhesive layer were obtained from the boundary conditions on displacements and stress at interfaces. The resulting solution allowed calculation of transmitted and reflected signals for an arbitrary input acoustic signal in a single-lap joint of an arbitrary geometry and composition.

Capabilities of the model were illustrated by examples of flexural wave propagation analysis in a single-lap adhesive composite joint with unidirectional graphite-epoxy adherends. The length of the bond line was varied from 50 mm down to 5 mm. The material properties of anisotropic composite and isotropic adhesive were taken from experiments. Variations of the amplitude of the transmitted signal with frequency (the frequency transfer function) were computed for different bond lengths. The results showed that the transfer function depended heavily on the bond length. All calculated transfer functions exhibited multiple transmission maxima and minima. The width of the average transmission band (the distance along the frequency axis between the frequencies of the two adjacent transmission minima) increased as the bond length decreased. The changes in the transfer function are expected to be robust and can be used in nondestructive evaluation of the length of the bond crack by acousto-ultrasonic analysis. Experimental verification of the theoretical predictions is in progress.

3. List of Publications and Other Outcomes

Graduated Students

[1] J. Qian, M.S., "Acoustic Emission Analysis of Damage Mechanisms in Advanced Composites", Department of Engineering Mechanics, University of Nebraska-Lincoln, 1998 (Advisor: Y.A. Dzenis)

[2] I. Saunders, M.S., "Experimental Analysis of Single Lap Adhesive Composite Joints", Department of Engineering Mechanics, University of Nebraska-Lincoln, 1999, (Advisor: Y.A. Dzenis)

[3] D. Wu, M.S., "Studies of Damage Evolution in Advanced Polymer Matrix Composites Subjected to Thermomechanical Fatigue", Department of Engineering Mechanics, University of Nebraska-Lincoln, 2000, (Advisor: Y.A. Dzenis)

Continuing students: M. Qin (Ph.D.) and K. Myers (M.S.)

Patent Applications

[1] Y. Dzenis, "A Transient-Parametric Method to Discriminate Histories of Sources of Acoustic Emission", UNL Patent Disclosure No. 3015, University of Nebraska-Lincoln, 1999

[2] "A Transient-Parametric Method to Discriminate Histories of Sources of Acoustic Emission", U.S. Patent Application Serial No. 60/174,215, Y. Dzenis, UNL, 2000

Journal Papers

[1] Dzenis, Y.A. and Joshi, S.P., "Long-Term Strength and Damage Analysis of Laminated Composites," *AIAA Journal*, 1997, Vol. 35, No. 6, pp. 1057-1063

[2] Dzenis, Y.A., "Damage and Failure of Laminated Composites Under Cyclic Loading: 1 - Experimental Observation of Damage Development Within Loading Cycles", *International Journal of Fatigue*, accepted

[3] Dzenis, Y.A., "Damage and Failure of Laminated Composites Under Cyclic Loading: 2 - Development of a Mesomechanics Model", *International Journal of Fatigue*, accepted

[4] Dzenis, Y.A. and Qian, J., "Analysis of Microdamage Evolution Histories in Composites", *International Journal of Solids and Structures*, accepted

[5] Qin, M. and Dzenis, Y.A., "Analysis of Single Lap Adhesive Composite Joints with Delaminated Adherends", *Composites Part B: Engineering*, accepted

[6] Kayupov, M. and Dzenis, Y.A., "Nonlinear Analysis of Adhesive Composite Joints", *Composite Structures*, accepted

[7] Saunders, I. and Dzenis, Y.A., "Experimental Analysis of Single Lap Adhesive Composite Joints: I - Quasi-Static Behavior", *Composites Science and Technology*, submitted

[8] Saunders, I. and Dzenis, Y.A., "Experimental Analysis of Single Lap Adhesive Composite Joints: I - Fatigue Behavior", *Composites Science and Technology*, submitted

[9] Qian, J. and Dzenis, Y.A., "Extraction of Histories of Damage Micromechanisms in Unidirectional Composites", *Journal of Acoustic Emission*, submitted

Conference Papers

[1] Dzenis, Y.A., "Fatigue Damage Progression Analysis of Composites", IUTAM Symposium on Transformation Problems in Composite and Active Materials, Cairo, Egypt, March 1997.

[2] Qian, J. and Dzenis, Y., "Acoustic Emission Study of Damage Evolution in CFRP Based on Waveform Analysis", ICCE/5, Las Vegas, NE, July 1998, pp. 253-254

[3] Qian, J. and Dzenis, Y., "Extraction of Histories of Damage Micromechanisms in Unidirectional Composites by Acoustic Emission Technique", ICAC '98, Hurghada, Egypt, December 1998, pp. 497-502

[4] Dzenis, Y.A., "Fatigue Behavior of Single Lap Adhesive Composite Joints", AFOSR Mechanics and Materials Program Review, Dayton, OH, Sept-Oct 1999, pp. 21-26.

[5] Dzenis, Y.A. and Saunders, I., "Fatigue Analysis of Adhesive Composite Joints", DURACOSYS '99, Brussels, Belgium, July 1999, in press

[6] Qin, M. and Dzenis, Y.A., "Analysis of Single Lap Adhesive Composite Joints with Delaminated Adherends", ICCM-12, Paris, July 1999, pp. 261-262 (full paper in press)

[7] Kayupov, M. and Dzenis, Y.A., "Nonlinear Finite Element Analysis of a Single Lap Composite Joint with a Bond Crack", ASME Mechanics and Materials Conference, Blacksburg, VA, June 1999, p. 419

[8] Saunders, I. and Dzenis, Y.A., "Experimental Analysis of Single Lap Adhesive Composite Joints Subjected to Quasi-Static and Fatigue Loading", ICCE/6, Orlando, FL, June 1999, pp. 723-724

[9] Qian, J. and Dzenis, Y.A., "Analysis of Microdamage Evolution Histories in a Unidirectional Composite", Proceedings of PACAM VI, Applied Mechanics in the Americas, Vol. 7, Rio de Janeiro, Brazil, January 1999, pp. 601-604

[10] Dzenis, Y.A., "Fatigue Behavior of Single Lap Adhesive Composite Joints", AFOSR Mechanics and Materials Program Review, Dayton, OH, Sept-Oct 1999, pp. 21-26

[11] Dzenis, Y.A. and Kayupov, M., "Analysis of Adhesive Composite Joints", Third International Conference on Composite Structures and Technology ICCST/3 (invited), Durban, South Africa, January 2000, in press

[12] Dzenis, Y.A. and Wu, D., "Analysis of Damage Evolution in Composites under Thermomechanical Fatigue", ICCE/7, Boulder, Colorado, July 2000

Technical Reports

[1] Dzenis, Y.A., "Damage and Failure of Laminated Composites Under Cyclic Loading: 1 - Experimental Observation of Damage Development Within Loading Cycles", AFOSR Technical Report No. 1, 1997

[2] Dzenis, Y.A., "Damage and Failure of Laminated Composites Under Cyclic Loading: 2 - Development of a Mesomechanics Model", AFOSR Technical Report No. 2, 1997

[3] J. Qian and Y. Dzenis, "Acoustic emission analysis of damage mechanisms in unidirectional and cross-ply composites subjected to quasi-static loading", AFOSR Technical Report No. 3, 1998

[4] J. Qian and Y. Dzenis, "Acoustic emission studies of damage histories in quasi-isotropic laminates subjected to quasi-static and fatigue loading", AFOSR Technical Report No. 4, 1998

[5] M. Qin and Y. Dzenis, "Delamination tolerance of single lap adhesive composite joints with one crack", AFOSR Technical Report No. 5, 1998

[6] M. Qin and Y. Dzenis, "Delamination tolerance of single lap adhesive composite joints with two cracks", AFOSR Technical Report No. 6, 1998

[7] I. Saunders and Y. Dzenis, "Experimental quasi-static analysis of single lap adhesive composite joints", AFOSR Technical Report No. 7, 1998

[8] I. Saunders and Y. Dzenis, "Experimental fatigue analysis of single lap adhesive composite joints", AFOSR Technical Report No. 8, 1998

[9] M. Kayupov and Y. Dzenis, "Nonlinear analysis of single lap composite joints: effect of adherend thickness", AFOSR Technical Report No. 9, 1998

[10] M. Kayupov and Y. Dzenis, "Nonlinear analysis of cracked single lap composite joints: effect of crack length", AFOSR Technical Report No. 10, 1998

[11] A. Spivak and Y. Dzenis, "Model for flexural wave propagation through single lap composite joints", AFOSR Technical Report No. 11, 1998

[12] H. Kawakami, D. Wu, and Y. Dzenis, "Apparatus for thermomechanical fatigue analysis of polymer composites and joints", AFOSR Technical Report No. 12, 1998

[13] M. Qin and Y. Dzenis, "Experimental Analysis of Single Lap Adhesive Composite Joints with Delaminated Adherends", AFOSR Technical Report No. 13, 1999

[14] M. Qin and Y. Dzenis, "Nonlinear Finite Element Analysis of Single Lap Adhesive Composite Joints with Delaminated Adherends", AFOSR Technical Report No. 14, 1999

[15] M. Qin, Y. Dzenis, and N. Pagano, "Evaluation of Fracture Toughness of Composite Adherends as a Function of Crack Orientation with Respect to Fiber Direction", AFOSR Technical Report No. 15, 1999

[16] I. Saunders, Y. Dzenis, and M. Forte, "Fracture Mechanics Characterization of Adhesive Composite Joints Subjected to Quasi-Static Loading", AFOSR Technical Report No. 16, 1999

[17] I. Saunders, Y. Dzenis, and M. Forte, "Fracture Mechanics Characterization of Adhesive Composite Joints Subjected to Fatigue Loading", AFOSR Technical Report No. 17, 1999

[18] I. Saunders and Y. Dzenis, "Acoustic Emission Analysis of Fracture Mechanisms in Adhesive Composite Joints Loaded in Mode I, II, and Mixed Mode", AFOSR Technical Report No. 18, 1999

[19] M. Kayupov and Y. Dzenis, "Stress Concentrations Caused by a Bond Crack in a Single Lap Composite Joint", AFOSR Technical Report No. 19, 1999

Awards, Honors

Principal Investigator (Y. Dzenis):

Senior Erskine Fellowship and Visiting ME Professorship at University of Canterbury (2000)

UNL College of Engineering and Technology Faculty Research Award (2000)

UNL Department of Engineering Mechanics Faculty Award for Outstanding Teaching, Research, and Service in 1994-1998 (1999)

UNL Department of Engineering Mechanics Faculty Teaching Award (1998)

UNL College of Engineering and Technology Faculty Research Award (1997)

UNL Department of Engineering Mechanics Faculty Research Award (1997)

Graduate Students Involved in this Project:

A. Spivak	1999 UNL Best Graduate Research Assistant Award (two for the University)
M. Qin	UNL Department of Engineering Mechanics W. Brooks Fellowship Award (1999)
A. Spivak	UNL College of Engineering and Technology Milton E. Mohr Fellowship Award (1999)

J. Qian	UNL College of Engineering and Technology Milton E. Mohr Fellowship Award (1998)
A. Spivak	UNL Department of Engineering Mechanics Graduate Research Award

Laboratory Development

With partial support from this grant, a comprehensive experimental laboratory on polymer composites and NDE was developed by the PI at UNL in 1996-2000. The laboratory consists of composite manufacturing, characterization, and testing equipment and includes such unique experimental devices as a complete thermal analysis system with two dynamic mechanical thermal analyzers, a unique set of devices for thermomechanical fatigue testing of polymer composites (a novel cyclic heating device and a TMF test control and data acquisition system were designed and built at UNL with support from this grant), a state-of-the-art acoustic emission system (augmented with an advanced pulser for acousto-ultrasonic studies with support from this grant), and a unique set of four ultrasonic nondestructive evaluation devices with overlapping resolutions and fields of view in the range from centimeters to nanometers. The latter include C-SCAN, scanning acoustic tomograph, 'true' scanning acoustic microscope, and scanning probe microscope.

4. List of Participating Scientific Personnel

Principal Investigator: Y. Dzenis

Graduate Students:

Fully supported J. Qian (M.S.),

I. Saunders (M.S.)

M. Qin (Ph.D.)

Partially supported	D. Wu (M.S.)
	A. Spivak (Ph.D.)
	H. Kawakami (Ph.D.)
	K. Myers (M.S.)
Research Associate:	M. Kayupov

Advisors and Contributors at AFRL/MLBC:

M. Forte, A. Roy, S. Donaldson, N. Pagano

5. Report of Inventions

The new hybrid transient-parametric method of acoustic emission analysis of histories of damage micromechanisms described in section 2 is being patented by UNL on behalf of the PI (U.S. patent pending). Report of Inventions (DD Form 882) is being filed in parallel with this report.

APPENDICES

APPENDIX 1: EXPERIMENTAL ANALYSIS OF SINGLE LAP JOINTS WITH UNIDIRECTIONAL AND CROSS-PLY ADHERENDS

Contributors: I. Saunders, A. Roj (AFRL)

1.1 Introduction 27

1.2 Experimental 32
- 1.2.1 Materials and manufacturing 32
- 1.2.2 Surface preparation 36
- 1.2.3 Specimen geometry and nomenclature 37
- 1.2.4 Mechanical testing 38
- 1.2.5 On-line microscopy and fractography 40

1.3 Static Response 42
- 1.3.1 Mechanical behavior 42
- 1.3.2 Fractography 45

1.4 Fatigue Response 48
- 1.4.1 Fatigue life and overall fracture history 48
- 1.4.2 Deformation histories 49
- 1.4.3 Fractography 51
  - 1.4.3.1 Optical fractography 52
  - 1.4.3.2 SEM and AFM fractography 56
- 1.4.4 S-N curves 56
- 1.4.5 Correlation between load amplitude and final fracture area 30

1.5 Summary 58

1.6 References 59

Appendix 1 of this report consolidates data and information obtained during the quasi-static and fatigue investigation of single lap joints manufactured from graphite-epoxy composites and Cytec FM 300-2M industrial adhesive used in the Air Force. The joints with unidirectional $[0]_6$ and cross-ply $[0/90]_{2S}$ adherends were analyzed and compared. The effect of surface preparation on mechanical response was studied. The fracture and damage mechanisms and histories were evaluated by on-line video microscopy and optical, scanning electron, and atomic force fractographies. The final fast fracture surface area under fatigue was correlated with the fatigue load amplitude.

1.1 Introduction

Advanced polymer composite materials are steadily replacing metals in modern aerospace, motor, and other high technology industries. Their high strength-to-weight ratio and fatigue durability have ensured specific niches in modern design applications. As the importance of advanced composites is growing steadily, so must the supporting technologies such as composites lay-up, curing, machining, and joining.

Joining technologies are important for manufacture and repair of complex composite structures. This is especially true for large composite structures in aircraft, such as wing and fuselage skins, and for the repair of old or damaged structures.

Two primary bonding techniques exist: mechanical fastening and structural adhesive

bonding. The joining technique used on a particular composite structure depends on the application and the material composition. Composites used in aircraft are usually joined by a combination of mechanical fasteners and adhesives, whereas those used in automobiles are often joined only with adhesives [1].

As bonding methods continuously improve, the joining of composite parts is gradually shifting from mechanical fastening to adhesive bonding. Adhesive joints have a number of advantages to mechanical fasteners [1]. These include:

- Higher joint efficiency index (strength/weight ratio)
- Lower part count
- No strength degradation of adherend due to fastener holes
- Less expensive and simpler manufacturing techniques
- Lower maintenance cost
- Smoother aerodynamic contours
- Larger stress bearing area and more uniform stress distribution
- Vibration damping and shock absorption
- Heat and electrical conductance insulation

Repair of old or damaged aerospace structures is often performed with composite patches. This includes bonding of composites to metals and bonding of composites to other composites. Adhesively bonded composite patches have the following advantages to metal patches:

- Better conformity to aerospace structural contours
- Possibility to tailor composite lay-up to reinforce major loading directions

- Applicability to modern stealth structures

Current advances in structural adhesives technology are revolutionizing methods of manufacture and assembly in virtually every modern industry. Structural adhesives are often based on epoxy resins. These adhesives possess relatively high modulus and strength and can be used to produce load-bearing joints. Advanced epoxy adhesives show good strength retention at elevated temperatures. Major advantages of the epoxy adhesives as compared to other adhesives are:

- High-strength, particularly on rigid substrates such as composites and metals
- Better resistance to hostile environments
- Better retention of strength over long periods of sustained or alternating loading

Due to the numerous advantages of adhesive bonding described above, the adhesive joints have received considerable attention in the literature. Materials science and manufacturing issues have been studied [1-7]. Two major aspects have to be taken into account during bond manufacturing, the surface preparation and the bondline control. The type and amount of surface preparation required for a strong adhesive bond depend on the adhesive and the materials being bonded. The bondline thickness control ensures repeatability of joints and uniformity of their performance characteristics.

Much effort has been devoted to the mechanical analysis of adhesive composite joints. A body of evidence has been accumulated on static behavior of joints. Strength of materials and finite element approaches have been utilized to analyze the stress fields in the adhesive and the adherends. Methods of joint design have been developed [8-10].

Figure 1 shows some of the various types of joint configurations used in practical applica-

tions. The stress analysis methods have been applied to these joints. It was shown that the scarf and the stepped lap joints exhibit lower stress concentrations compared to the other designs. Selection of a particular joint design, however, depends not only on stresses, but on practicality too. The single lap joint is often preferred because of the simplicity of its manufacture and its applicability to thin adherends. The single lap design can also be advantageous for patching of damaged structures with single-sided access.

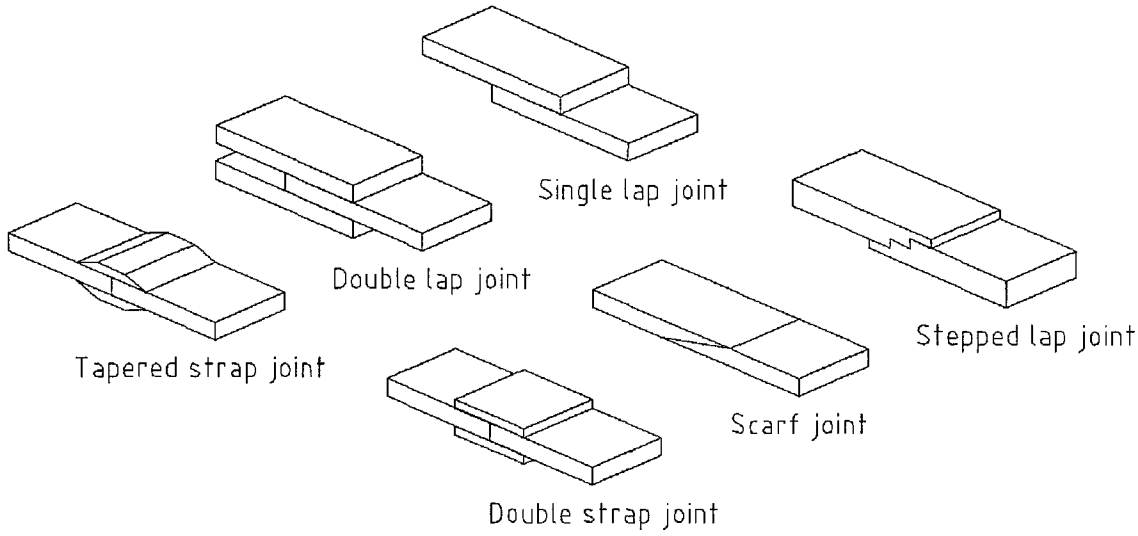

Figure 1: Adhesive joints configurations

Currently, two major factors are impeding the wider use of adhesive composite joints in industry. The first concerns their long-term durability. No reliable method exists to predict fatigue behavior of adhesive joints. The second concerns their inspectability and certification. There is no fully satisfactory NDE technique capable of evaluating joint quality after manufacturing and in service.

Despite of the relatively large volume of literature on adhesive joints, their failure, espe-

cially under fatigue, is not yet fully understood. The failure of adhesive joints with homogeneous adherends, such as metals, usually occurs either along an interface between the adhesive and adherend (interfacial or adhesive mode) or in the bulk region of the adhesive layer (cohesive mode). The cohesive failure usually indicates that the joint was manufactured properly. However, even a well manufactured joint may fail in the adhesive mode. In joints with composite adherends, the situation may be further complicated by damage and fracture in the adherends. The bond cracks have been observed to deviate into the composite adherends causing failure through composite delamination [11].

Evaluations of damage and fracture mechanisms and histories are necessary for the development of predictive models and joint failure analysis. Monitoring damage and fracture development is needed for reliable nondestructive evaluation of joints.

Advanced composite materials exhibit superior fatigue performance as compared to conventional materials [12]. Along with their high strength-to-weight and stiffness-to-weight ratios, the fatigue durability is one of the main reasons for the use of composites in advanced, fatigue-critical applications, such as aerospace structures. The exceptional fatigue characteristics of composites are due to their inherent damage tolerance. Cumulative damage in composites in the form of broken fibers, matrix cracks, fiber-matrix disbonds, and delaminations can be substantially more extensive than damage in conventional materials.

Different crack paths in joints have been observed in experiments. Possible failure modes in adhesive composite joint on an aircraft were classified in [13] as cyclic debonding, delamination, adherend fatigue, or a combination of these. Experiments on cracked lap shear specimens [14] produced fatigue failure in the form of cyclic debonding with the fracture being cohesive in

nature and with some 0° fiber pull-off from the adherends. Other experiments, such as those performed on double lap joints [11], indicated that the fracture path may deviate into composite adherend. In these experiments [11], the crack originated at one edge, propagated through one of the outer adherends, then jumped through the adhesive layer and continued within the inner adherend.

Information on fracture mechanisms and history under fatigue is important for the development of predictive models of fatigue behavior. The literature survey shows that the fatigue failure mechanisms of joints were studied to a limited extent.

The objective of this research was to perform a systematic experimental study of the mechanical behavior of single lap adhesive composite joints with two different composite adherends. The joints with unidirectional and cross-ply graphite-epoxy adherends bonded with an industrial epoxy adhesive used in the Air Force were analyzed and compared. The results of the quasi-static and fatigue analysis are presented.

1.2 Experimental

1.2.1 Materials and manufacturing

The adherends were manufactured from Hexcel T2G-190-12-F263 Boeing-certified graphite-epoxy prepreg. The 152 x 152 mm (6 x 6 inch) composite panels were manufactured in a two-chamber press-clave (Figure 2) under controlled temperature, pressure, and vacuum environments. The manufacturer recommended curing cycle was used.

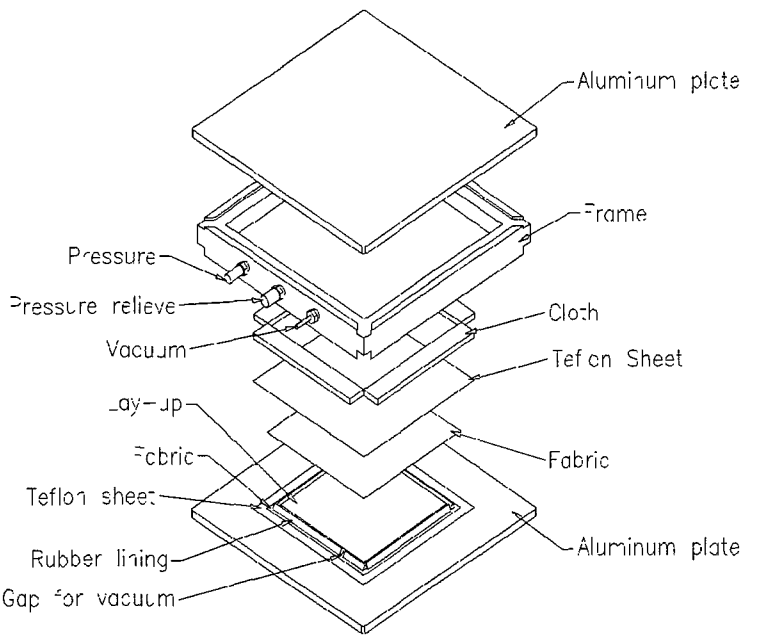

Figure 2: Manufacturing assembly

Two different composite lay-ups were manufactured: a unidirectional $[0]_6$ and a cross-ply $[0/90]_{2S}$. The material properties of the composite adherends are shown in Table 1. The axes used in Table 1 are indicated in Figure 3. The unidirectional (UD) ply properties were obtained experimentally (see Appendix 4). The cross-ply (CP) composite properties were calculated using the lamination theory.

Table 1: Elastic properties of unidirectional and cross-ply composite adherends

Property	UD composite	CP composite
E_x	132.7 GPa	71.2 GPa
E_y	8.83 GPa	71.2 GPa
E_z	8.83 GPa	8.83 GPa
ν_{xy}	0.36	0.045
ν_{yz}	0.30	0.32
ν_{xz}	0.36	0.32
G_{xy}	4.76 GPa	4.76 GPa
G_{yz}	3.40 GPa	4.00 GPa
G_{xz}	4.76 GPa	4.00 GPa

Strips of 25.4 mm (1 inch) in width were cut from the composite panels to act as tabs (spacers) at the ends of the lap joint specimens (see Figure 3). The adherends and the spacers were bonded in the same press-clave (Figure 2), following the curing cycle recommended by the adhesive manufacturer.

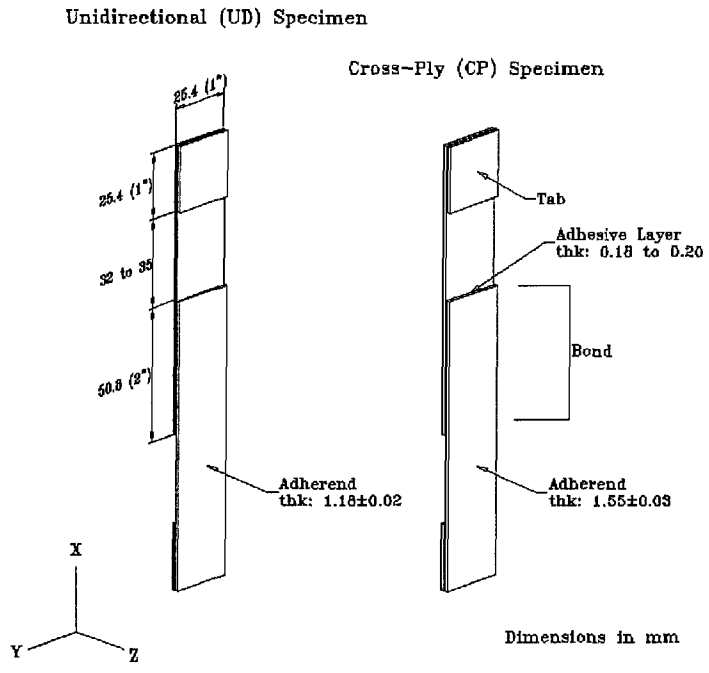

Figure 3: Specimen geometry

The adhesive used in this research was Cytec FM300-2M epoxy adhesive film. The film contained a polyester fiber mat support (about 10% by volume). The fiber mat assured improved handling of the film and more uniform bondline thickness. Table 2 presents the mechanical properties of the cured adhesive.

Table 2: Elastic properties of cured adhesive

Property	Value
E	3.75 GPa
ν	0.34
G	0.83 GPa

1.2.2 Surface preparation

As mentioned above, adequate surface preparation is important for the adhesive bond strength. Peel plies used in composite manufacturing provide reasonably rough adherend surface, that may be suitable for direct bonding. However, the peel plies leave contaminants on the composite surface that may reduce bond strength. These contaminants can be removed by an appropriate chemical treatment. In order to evaluate the need for special surface preparation prior to bonding, unidirectional composite joints with and without surface treatment of the adhesive and the adherends were prepared and tested. The treatment was accomplished by a solvent wipe of the surfaces prior to bonding. A Miller Stephenson cleaning solvent MS-944/CO2 was used. It was found that the solvent wipe treatment almost doubled the quasi-static strength of the unidirectional joints (see section on *Static Response*). An additional roughening of the surfaces of the adherends by a light grit blast did not provide further improvement. The solvent wipe treatment was then applied during manufacturing of all other specimens in this experimental program.

1.2.3 Specimen geometry and nomenclature

The specimen geometry is shown in Figure 3. The 25.4 mm (1 inch) wide specimens were cut from the bonded and tabbed panels obtained by the manufacturing procedure described above.

The single lap joint specimens had an overlap (bond) length of 50.8 mm (2 inches). This overlap was chosen based on those described in the literature [11]. The relatively large bond area aided in crack propagation studies.

All unidirectional adherends had a $[0]_6$ lay-up. All cross-ply adherends had a $[0/90]_{2S}$ lay-up. An edge view of the end of the overlap in a specimen with the cross-ply adherends is shown in Figure 4. The fillet was uniformly removed from all specimens in an effort to reduce the experimental scatter.

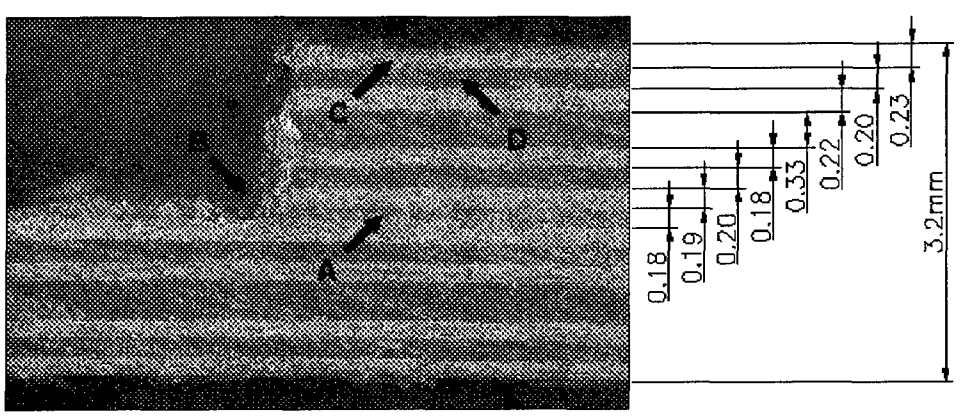

A Adhesive layer
B Fillet removed
C 0° ply
D 90° ply

Figure 4: Photo of bond edge of cross-ply specimen

The following specimen nomenclature was used to differentiate between different adherends and surface treatments in static tests:

- UDU Unidirectional adherends, untreated surfaces
- UDT Unidirectional adherends, treated surfaces (solvent wipe)
- CP Cross-ply adherends, treated surfaces (solvent wipe)

In addition, two numbers were used to identify a particular specimen. The first number referred to the composite panel. The second number referred to the number of specimen cut from that panel. For example, a specimen UDU12 had unidirectional adherends, the surfaces were untreated before bonding, and it was the 2nd specimen cut from the 1st panel.

The following fatigue specimen nomenclature was used:

- UD Unidirectional adherends, treated surfaces
- CP Cross-ply adherends, treated surfaces

Similarly, two numbers were used to identify a particular specimen. The first number referred to the composite panel. The second number referred to the specimen cut from that panel. For example, a specimen UD63 had unidirectional adherends, and it was the 3rd specimen cut from the 6th panel.

1.2.4 Mechanical testing

Figure 5 presents a schematic of the mechanical test configuration. The specimen is shown with an extensometer attached in position. The extensometer (MTS model 832.12G-2D) was

attached by means of rubber bands. The legs of the extensometer were affixed at the 35 mm and 10 mm positions above the midpoint of the adhesive joint. The gauge length was 25 mm.

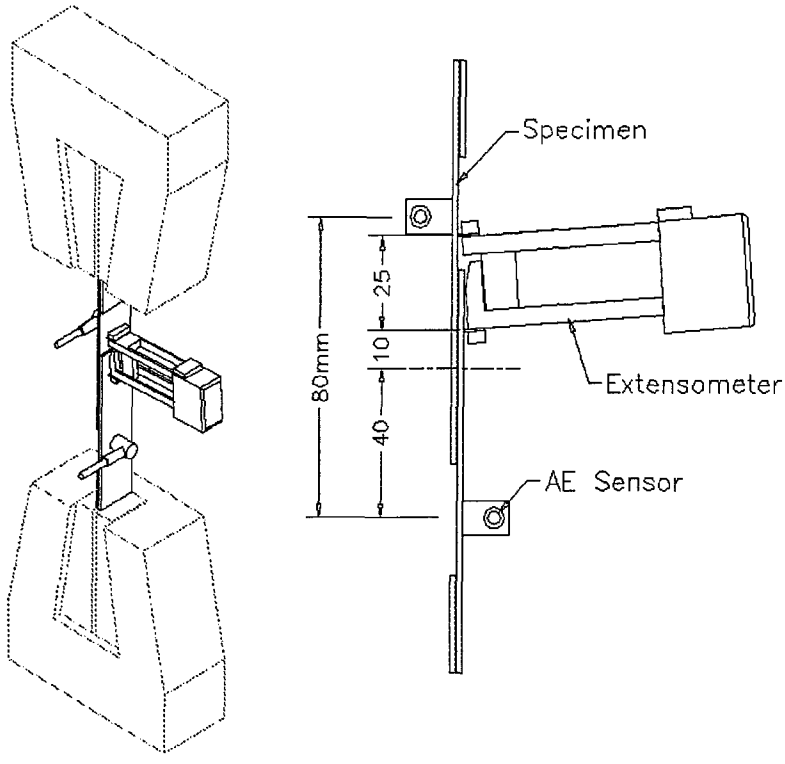

Figure 5: Specimen assembly for mechanical testing

The testing was performed on a servohydraulic MTS testing machine digitally controlled by an Instron control and data acquisition system. All quasi-static tests were stroke controlled with Instron 8500 software. Two displacement rates, 0.2 mm/min and 0.5 mm/min, were used during quasi-static testing of the unidirectional specimens. The displacement rate for the cross-ply specimens was 0.5 mm/min. All fatigue tests were load controlled with Instron Max software. A 0.1 load ratio and a 1 Hz frequency were used.

The specimens were clamped with serrated wedge action grips that left imprints on the adherend surfaces. These imprints were carefully checked after each test to ensure that uniform loading was being applied. An MTS 10 MT load cell was used to measure loads. The tests were performed with a Satec spherical alignment coupling attached to the top grip.

Acoustic emission (AE) emitted from the specimens was collected and analyzed. Figure 5 shows the specimen with acoustic emission sensors attached in position. The procedure and the results of AE analysis of joints are described in Appendix 4.

1.2.5 On-line microscopy and fractography

A Panasonic GP KR222 digital camera was used for on-line video microscopy (Figure 6). The same system was used for off-line fractographic analysis of fracture surfaces. A close focus 18-108 mm manual zoom lens was used for small magnifications. A VZM II 0.75-3′ zoom microscope head was used for larger magnifications. A fiber optic light source was used to illuminate specimens. For some images, the light source was held at an angle to make the three-dimensional features more discernible.

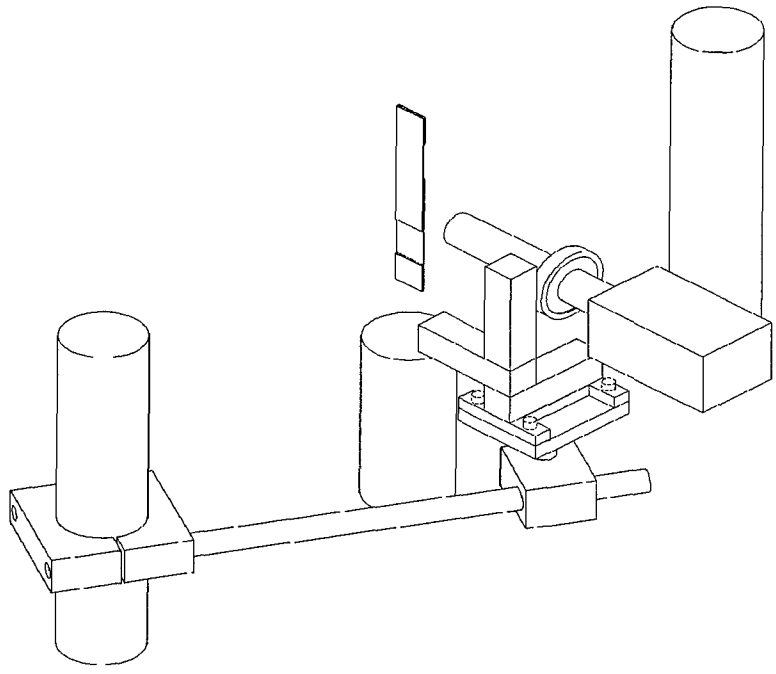

Figure 6: Assembly for on-line video microscopy

Development of fracture in the joint specimens was followed on a Sony video monitor. Digital image acquisition was done with a JVC GV-PT2 video printer that was able to capture a picture directly from the camera and then transfer it to a computer.

The crack initiation and propagation under static and fatigue loading were monitored with this system on-line. The optical fractography was performed with the same system off-line. In addition to optical observations, scanning electron microscopy (SEM) and atomic force microscopy (AFM) were used to characterize the fracture surfaces. SEM observations were performed on the gold coated specimens by a standard Jeol scanning electron microscope. AFM observations were performed by the Nanoscope (Digital Instruments) and M-5 (PSI) systems. The AFM scanning was performed in an intermittent contact (tapping) mode.

1.3 Static Response

1.3.1 Mechanical behavior

Results of the quasi-static testing of the UD and CP specimens are shown in Figures 7 and 8, respectively. Figure 7 compares the load-displacement diagrams for unidirectional specimens with treated (solid lines) and untreated (dashed lines) surfaces. The diagrams exhibit similarity at lower loads. The displacements of the untreated specimens (UDU) were slightly larger than the displacements of the treated specimens (UDT). However, the observed average strength of the UDU specimens was almost 50% lower than that of the UDT specimens (Table 3). At lower loads, the load-displacement curves of all UD specimens showed a non-linearity (stiffening). At higher loads, the UDT specimens exhibited another non-linearity (softening), that started at about 18 kN. The untreated specimens (UDU) did not exhibit this second non-linearity, probably because they failed at the lower load levels.

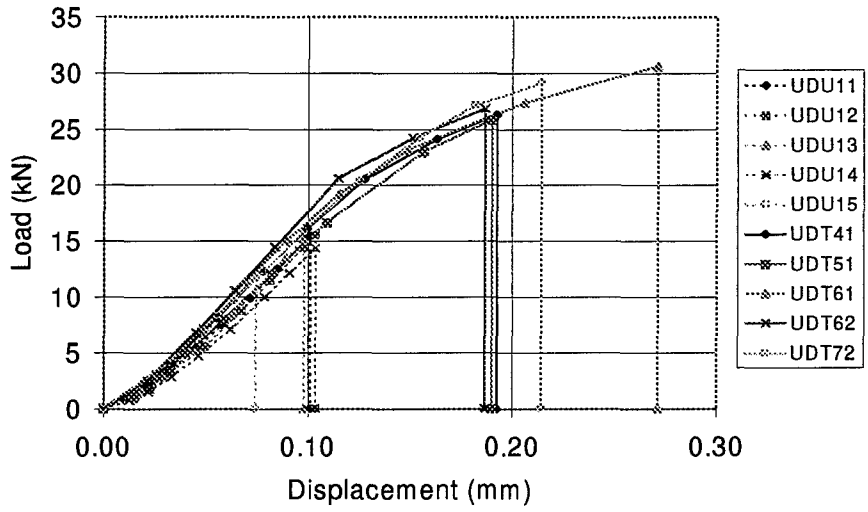

Figure 7: Static load-displacement response of UD specimens

Figure 7 contains information about the tests performed at different loading rates. The treated specimens UDT41 and UDT51 were tested at the displacement rate 0.2 mm/min while the treated specimens UDT62 and UDT72 were tested at the displacement rate 0.5 mm/min. The comparison of their mechanical response shows no remarkable difference in either the shape of the load-displacement diagram or the ultimate properties.

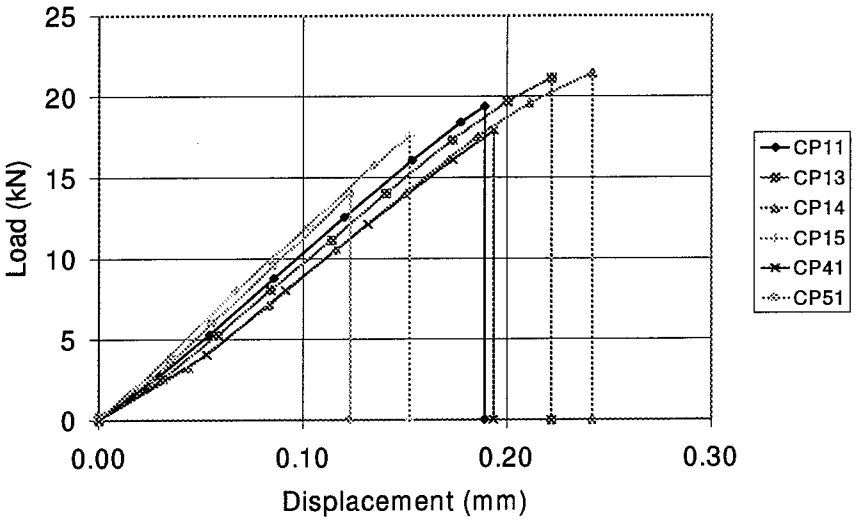

Figure 8: Static load-displacement response of CP specimens

Figure 8 presents load-displacement diagrams for the cross-ply specimens. Surface preparation was applied to all cross-ply specimens tested. Comparison shows that the average ultimate strength of the specimens with the cross-ply adherends was about 30% lower than that of the UDT specimens (Table 3). The non-linearities similar to the ones observed for the UDT specimens were observed for the CP specimens (Figure 8). The non-linearities were less pronounced in the case of the CP joints.

Table 3: Summary of quasi-static test results

Joint	No of spec. tested	Ultimate Load (kN)		Ultimate Displacement (mm)	
		Avg.	Std. Dev.	Avg.	Std. Dev.
UD untreated	5	14.4	1.7	0.10	0.01
UD treated	5	27.8	2.1	0.21	0.04
CP	6	18.6	2.7	0.14	0.03

On-line observations revealed that the quasi-static failure in all cases was abrupt, with no discernible crack growth phase prior to failure. In some instances, at high loads, a discoloration of the adhesive could be noticed near the ends of the overlap. The AE analysis showed damage development near the bond edge. The results are described in Appendix 4.

1.3.2 Fractography

Results of fractographic examination of broken joints are shown in Figures 9 and 10. Figure 9 compares the fracture surfaces of unidirectional untreated (UDU) and treated (UDT) specimens. It can be seen that the treated specimens exhibited more cohesive type of failure while the untreated specimens failed primarily in adhesive mode. The adhesive type of failure was accompanied with some fiber breakage and removal from the composite adherend. Some treated specimen exhibited longitudinal splits in the adhesive and adherends. However, the number of broken

fibers and longitudinal splits was small in all specimens.

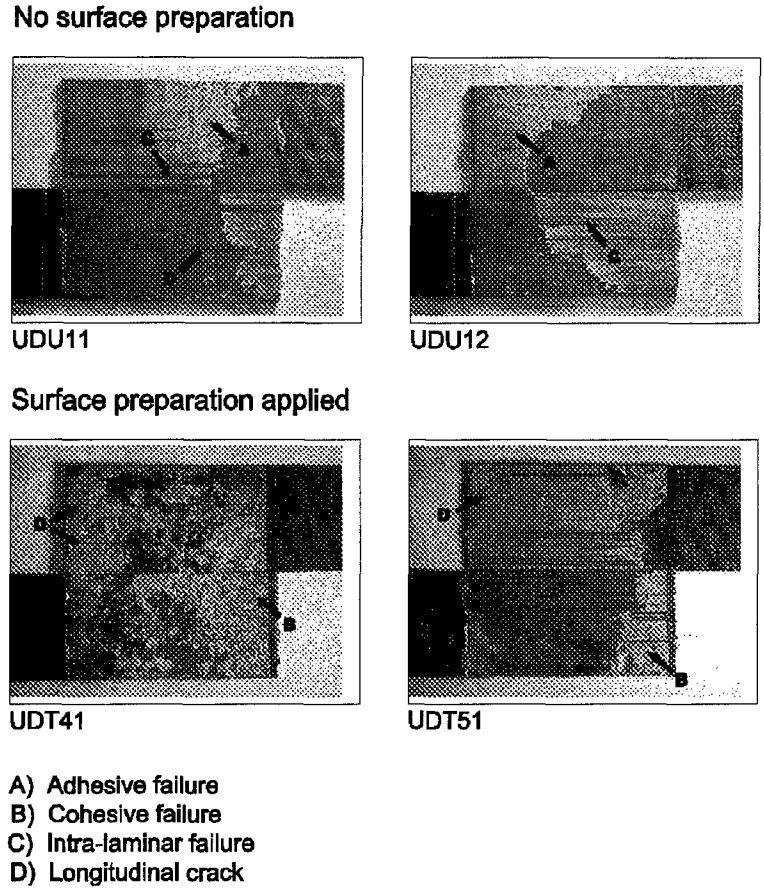

Figure 9: Fractography of joints with UD adherends

Figure 10 shows the results of fractographic examination of cross-ply specimens. The failure occurred in both adhesive and cohesive modes. The adhesive type of failure was again accompanied with some fiber breakage. Occasionally, as in the case of the specimen CP51, a part of the bond crack deviated into the composite adherend and propagated as an interlaminar crack (Figure 10). This generally resulted in lower joint strength (see Figure 8). However, this type of fracture was observed very rarely.

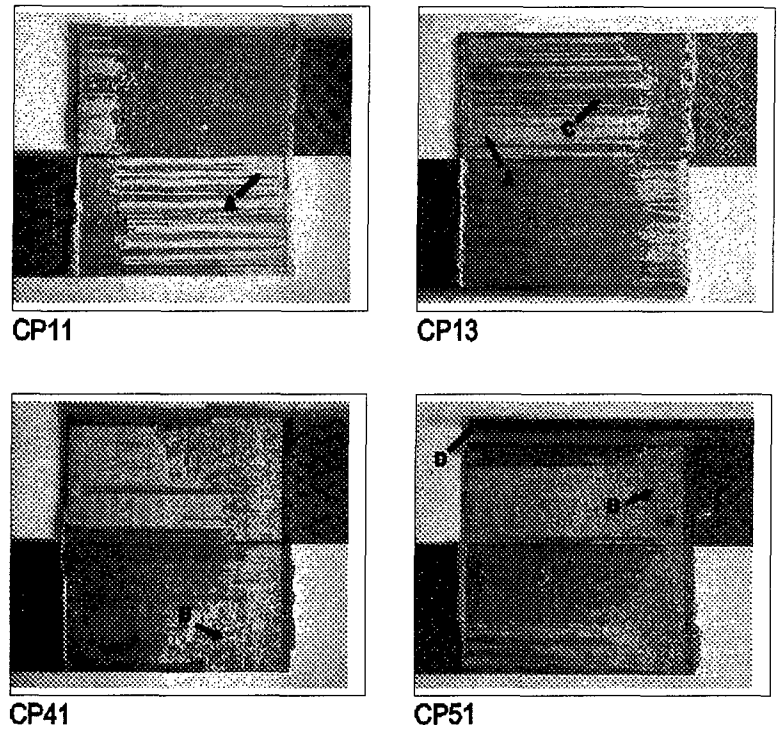

Figure 10: Fractography of joints with CP adherends

Overall, the fractographic analysis of the unidirectional and cross-ply specimens showed that the quasi-static failure of all specimens occurred mainly in the bondline, with little or no adherend fracture. The correlation of the failure modes with the mechanical response (Figures 7 and 8) showed that cohesive failure generally resulted in stronger bonds.

1.4 Fatigue Response

1.4.1 Fatigue life and overall fracture history

The low cycle fatigue load levels were chosen based on the static analysis and the trial fatigue tests. The range of load amplitudes for the UD specimens varied from 32 to 53% of the ultimate static strength. The range of load amplitudes for the CP specimens varied from 42 to 65% of the ultimate static strength. Tables 4 and 5 summarize the fatigue life data for the UD and CP joints, respectively. The number of cycles to failure ranged from 74 to 63166. The observed scatter for similar load amplitudes is common for composite materials.

Table 4: Fatigue life of UD specimens

Specimen	Load Amplitude kN	Cycles to Failure
UD44	14.6	74
UD63	12.7	3128
UD65	11.8	4186
UD64	10.8	5873
UD53	8.8	17464
UD52	8.8	17056
UD45	8.8	10009

Table 5: Fatigue life of CP specimens

Specimen	Load Amplitude kN	Cycles to Failure
CP45	11.8	2022
CP42	10.8	5598
CP52	9.8	13344
CP43	9.8	8046
CP53	8.9	19620
CP44	8.9	11814
CP55	7.9	63166

On-line observations showed that all specimens tested in fatigue failed through the bond-line. However, unlike the abrupt failure observed in the quasi-static tests, three distinct stages were observed in the fracture process under fatigue, i.e. crack initiation, gradual crack propagation (slow fracture), and final failure (fast fracture). On-line video microscopy showed that the cracks initiated at the ends of the overlap. The cracks then propagated slowly through a substantial portion of the bond length, before the final fast fracture of the joints occurred. The propagation stage lasted between 30 to 70% of the total fatigue life.

1.4.2 Deformation histories

Deformation histories for the UD and CP specimens loaded in fatigue are shown in Fig-

ures 11 and 12, respectively. The displacement was measured by the extensometer as described above. The displacement difference on the vertical axes in Figures 11 and 12 is the difference between the maximum and minimum displacements measured during a loading cycle.

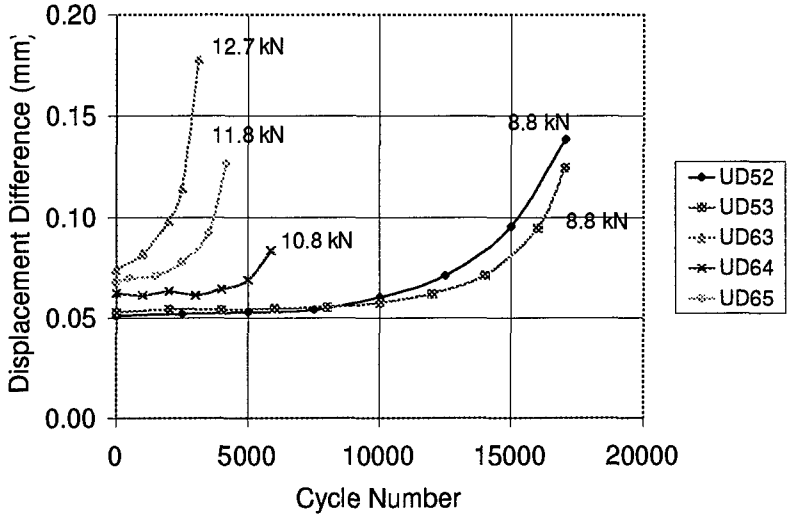

Figure 11: Deformation histories for UD specimens under fatigue

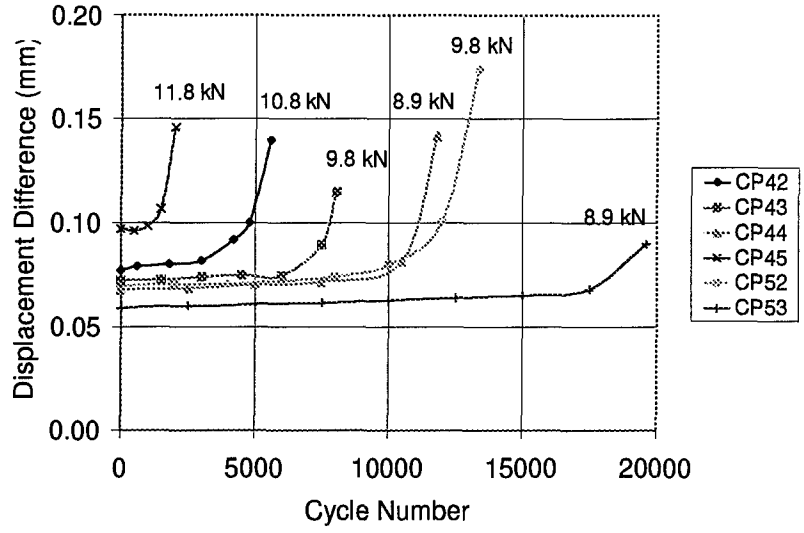

Figure 12: Deformation histories for CP specimens under fatigue

Analysis shows that the deformations were nearly constant for all specimens in the beginning of the fatigue tests. At some points during the tests, the deformations began to increase. For most specimens, the deformations grew monotonically to failure. Correlations between the deformation histories in Figures 11 and 12 and the on-line observations showed that the deformations began to increase in the crack propagation stage. Similar features were observed on the filtered AE history plots. The details are given in Appendix 4.

1.4.3 Fractography

1.4.3.1 Optical fractography

Optical microphotographs of fracture surfaces of the joints broken in fatigue revealed that, as in the case of the quasi-static loading, the final fracture was through the bondline, with little or

no visible adherend damage. The fracture occurred in both adhesive and cohesive modes. The adhesive type of fracture was accompanied with some fiber breakage and removal from the composite adherends. However, the extent of the fiber fracture was generally low. Some specimens did not exhibit this type of fracture at all.

The slow and fast fracture surface areas created during the second and third stages of the fatigue fracture process could be identified on the specimens by the naked eye. The color of the slow fracture surfaces was generally lighter than the color of the fast fracture surfaces. The slow fracture surface areas were marked on the optical fractographs. The analysis showed that, in general, the slow fracture was more adhesive as compared to the fast fracture. The slow cracks propagated through a substantial portion of the total bond area. In all cases, two cracks initiated and propagated from both ends of the overlap. Judging by the final crack fronts, the propagation of the cracks was not symmetric. Furthermore, the crack fronts were not always perpendicular to the loading direction. However, the geometry of the final crack fronts is not necessarily indicative of the geometry of the crack fronts earlier in fatigue fracture process.

A correlation between optical fractography and AE location histories is analyzed in Appendix 4.

1.4.3.2 SEM and AFM fractography

As mentioned above, the naked eye could distinguish the color differences between the slow and fast fracture areas. This contrast was somewhat reduced by the digital image acquisition procedure. It was still possible to determine the transition between the slow and fast fracture areas

in optical fractographs. However, the resolution of the optical system was not sufficient to quantify the differences in surface morphology. An attempt was therefore made to characterize these differences by scanning electron and atomic force microscopies.

The results of SEM observations are presented in Figures 13-15. First, the interface between the slow and fast fracture areas was identified. Figure 13 shows the transition from the slow to fast fracture. The transition line is clearly seen in the bottom image magnified to 500x. The slow fracture area lies to the left of the transition line, and the fast fracture area is to the right. The arrow in the bottom image indicates the global direction of crack propagation. The surfaces on both sides of the transition line were studied in greater detail in Figures 14 and 15.

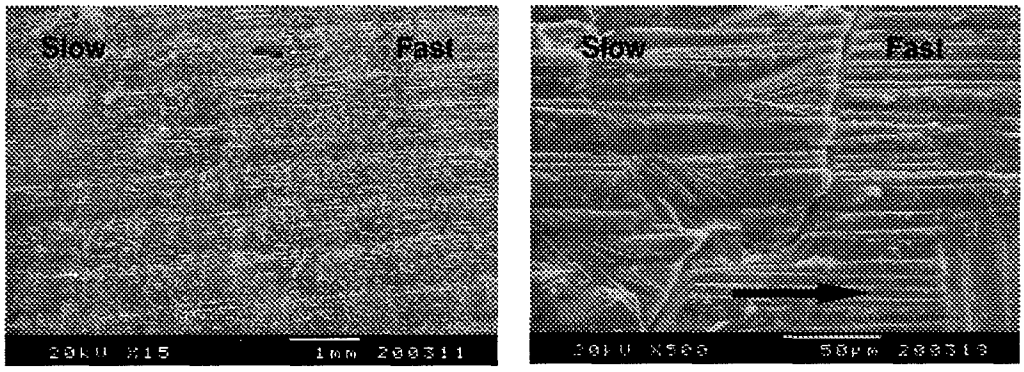

Figure 13: SEM images of the transition between slow and fast fracture

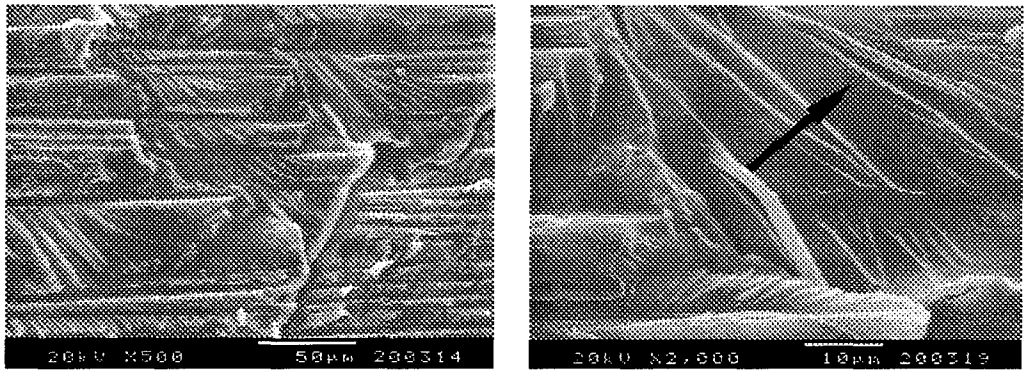

Figure 14: SEM images of the slow fracture

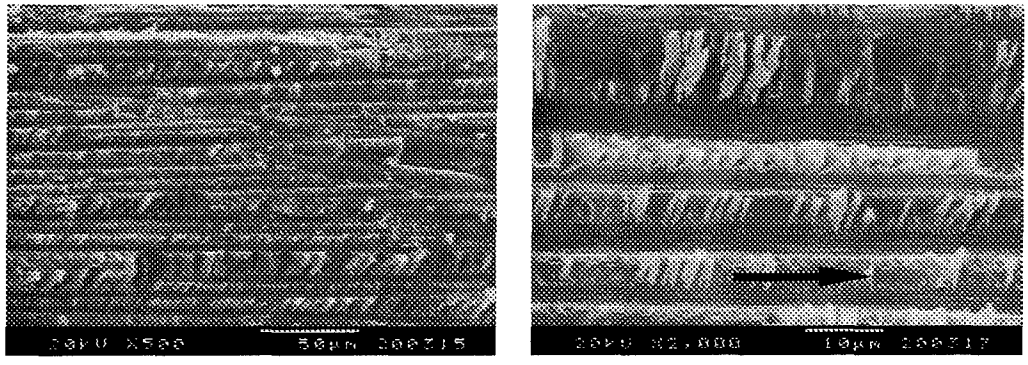

Figure 15: SEM images of the fast fracture

Figure 14 shows the slow crack growth area magnified to 500x and 2000x. The ridges on the surface of the epoxy adhesive fractured in the cohesive mode (right image) lie at approximately 45° to the specimen axis. The arrow on that image indicates the probable local direction of crack propagation at the end of the slow crack propagation stage.

The fast fracture surface was studied in Figure 15. The orientation of hackles on the fast fracture surface indicated that the fast crack propagated in the loading direction (see arrow in the

right image). The hackles in Figure 15 are spaced more closely than the ridges on the slow fracture surface (Figure 14). The analysis of the density of fiber imprints in Figures 13-15 showed that, in the localized area studied, the fast fracture was primarily in the adhesive mode (along the interface between the adhesive layer and the adherend) while the slow fracture was in the mixed adhesive/cohesive mode.

The AFM fractography of the slow and fast fracture surfaces formed during fatigue was difficult because of the high roughness of these surfaces. Figure 16 shows a three-dimensional image of the transition between the slow and fast fracture areas. The slow fracture area has an angled ridge pattern similar to that found by SEM analysis (Figures 13 and 14). The 3D nature of the AFM image allows one to observe and quantify the surface morphology. The analysis of Figure 16 showed that the height of the consecutive steps in the ridge pattern of the slow fracture area was in the range from 0.2-0.6 μm. The drop at the transition line between the slow and fast fracture areas was about 1.8 μm deep.

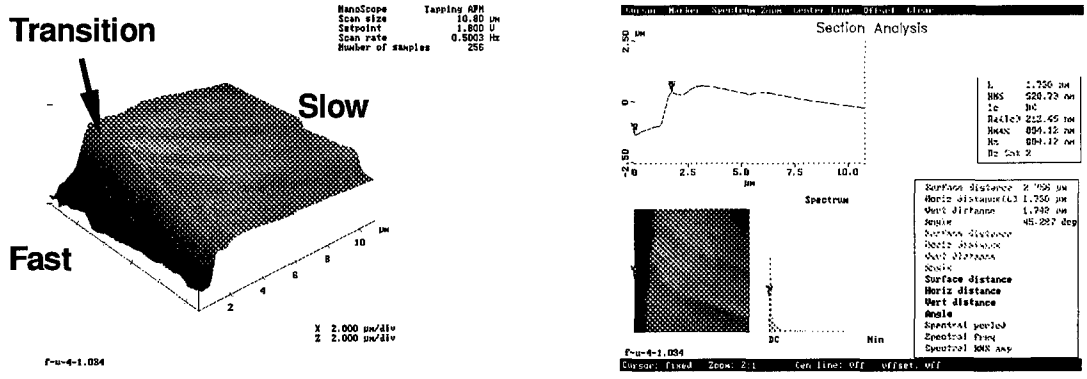

Figure 16: AFM image of the transition from slow fracture to fast fracture

1.4.4 S-N curves

S-N curves for the UD and CP specimens are plotted in Figure 17. The lines represent linear least square fit through the experimental data for joints with different adherends. The life curves for the UD and CP specimens were found to overlap for the load levels tested, but they might have different slopes.

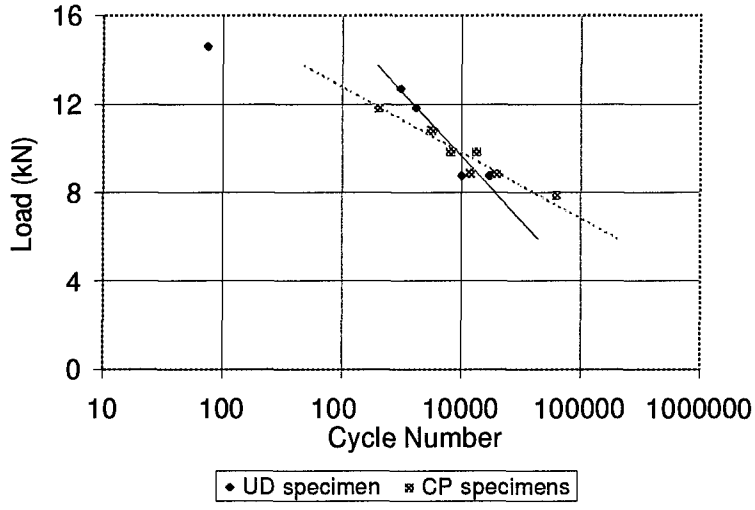

Figure 17: S-N curves

The similarity of the fatigue lives of the UD and CP specimens is interesting, as they had markedly different static strengths, as established in the previous section.

1.4.5 Correlation between load amplitude and final fracture area

The final fast fracture surface area for different specimens was measured on the optical fractographs by means of CAD tools. The results expressed as a percentage of the total bond area

were plotted against the fatigue load amplitude. The combined data for both UD and CP specimens are shown in Figure 18. The results for the joints with different adherends show remarkable similarity. The line in Figure 18 represents a linear least square fit through the experimental data (note: some data points overlapped; two data points were excluded from the least square approximation). The analysis shows that a correlation may exist between the fatigue load amplitude and the final fast fracture surface area. The linear least square approximation passes nearly through the origin of the coordinates in Figure 18. This information may be used for the development of final failure criteria for fatigue.

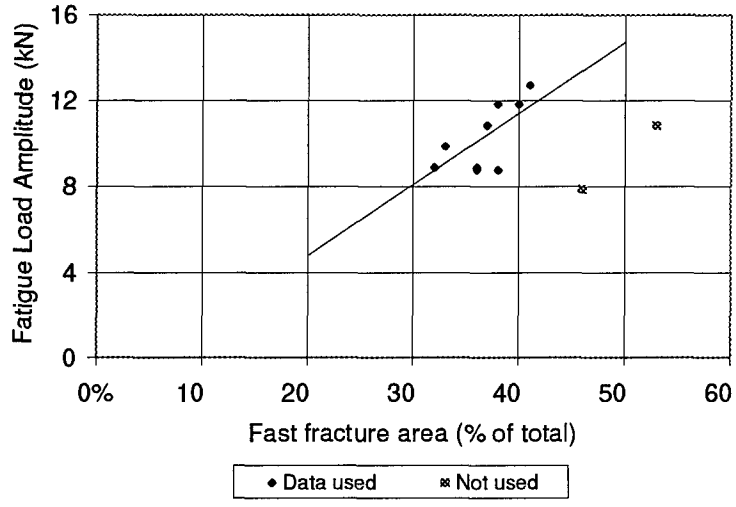

Figure 18: Correlation between fast fracture surface area and fatigue load amplitude

1.5 Summary

Quasi-static tests revealed that solvent treatment of the adhesive film and the adherends was necessary for good bond strength. Quasi-static loading resulted in a non-linear deformation and an abrupt failure for both unidirectional and cross-ply specimens. The unidirectional specimens were substantially stronger than the cross-ply specimens. The quasi-static failure occurred mainly in the adhesive layer, with little or no adherend fracture. Fractographic analyses showed that the stronger bonds usually exhibited more cohesive failure. On-line observations indicated little visible internal damage development in joints prior to bond crack initiation and failure. Most damage was produced at the ends of the overlap region. The damage development might be responsible for the second deformation non-linearity but seemed to have little effect on the final crack path that was through the bondline. The obtained results served as a base for the fatigue studies of the single lap adhesive composite joints.

Low cycle fatigue tests showed no remarkable difference in fatigue behavior of the UD and CP specimens. The S-N curves for joints with the two adherends overlapped in the load range tested, although the curves might have different slopes. As in the case of quasi-static loading, the fatigue specimens failed through the bondline with little or no visible adherend damage. Three stages of fracture were observed under fatigue: crack initiation, slow crack propagation, and fast final fracture. The slow fracture was more adhesive in nature compared to the fast fracture. Deformation histories provided indications of the onset of the bond crack initiation. A correlation between the fatigue load amplitude and the final fast fracture surface area may exist.

The results obtained in this part of the research were used for FE modeling validation (see

Appendix 2). They were also augmented by AE analysis described in Appendix 4. The results will be further used to validate predictive models of mechanical behavior of single lap adhesive composite joints. Development of such models and acquisition of necessary input data are now in progress.

1.6 References

[1] Schwartz, M. M., "Joining of Composite Matrix Materials", 1994, pp. 34-51.

[2] Baker, A.A., "Repair Techniques for Composite Structures", Composite Materials in Aircraft Structures, New York: Longman Scientific & Technical, 1990, pp. 207-227.

[3] Structural Adhesives: Development in Resins and Primers, A.J. Kinlock, Ed., Elsevier 1986.

[4] Cochran, R.C., et al., "Composite Repair Material and Design Effort", AGARD-CP-402, Paper 16, 1986.

[5] Parker, B.M., "Adhesive Bonding of Contaminated Carbon Fiber Composites", Conference on Structural Adhesives in Engineering, Bristol, July 2-4, 1986, Paper C164/86.

[6] Poncuis, A.V. and Wenz, R.P., "Mechanical Surface Preparation of Graphite-Epoxy Composite for Adhesive Bonding", SAMPE Journal, 1985, September, pp. 50-57.

[7] Parker, B.M. and Waghorne, R.M., "Surface Pretreatment of Carbon Fiber Reinforced Composites for Adhesive Bonding", Composites, 1982, Vol. 13, pp. 280-288.

[8] Vinson, J.R. and Sierakowski, R.L., "Joining of Composite Materials Structures", The Behavior of Structures Composed of Composite Materials, Martinus Nijhoff, 1986, pp. 237-283.

[9] Jones, R. M., "Mechanics of Composite Materials", 2nd edition, Taylor & Francis, Inc., 1999.

[10] Blackman, B. R. K., Dear, J. P,Kinloch, A. J., Macgillivray, H., Wang, Y., Williams, J. G., Yayla, P., "The Failure of Fiber Composites and Adhesively Bonded Fiber Composites Under High Rates of Strain", Journal of Materials Science, 30, 1995, 5885-5900.

[11] Roy, A. K., Donaldson, S. L., and Schoeppner, G. A., "Bonded Joints of Unidirectional and Cross-Ply Laminates: An Experimental Study", AAIA SDM, Orlando, 1997.

[12] Fatigue of Composite Materials, K.L. Reifsnider, Ed., Elsevier, 1991.

[13] Hart-Smith, L. J., "Analysis and Design of Advanced Composite Bonded Joints", NASA CR-2218, National Aeronautics and Space Administration, 1974.

[14] Mall, S., Johnson, W. S., and Everett, R. A., "Cyclic Debonding of Adhesively Bonded Composites", NASA Langley research center, NASA TM-84577.

APPENDIX 2: MODELING OF SINGLE LAP ADHESIVE COMPOSITE JOINTS WITH UNIDIRECTIONAL AND CROSS-PLY ADHERENDS

Contributor: M. Kayupov

2.1 Introduction 62

2.2 Computational Model 63
2.2.1 Geometry 63
2.2.2 Boundary conditions 64
2.2.3 Materials 65
2.2.4 Mesh 66

2.3 Experimental Validation 67

2.4 Analysis 72
2.4.1 Stress distributions 72
2.4.2 Stress intensity factors and energy release rates 75
2.4.3 Effect of adhesive layer 79
2.4.4 Effect of adherend lay-up 81

2.5 Summary 83

2.6 References 84

Appendix 2 of this report presents results of numerical analysis of single lap adhesive composite joints. Geometrically linear and nonlinear FE models of single lap joints with unidirectional and cross-ply adherends are developed and described. Experimental validation of the nonlinear model is presented. Stress distributions in the bondline are analyzed. Stress intensity factors computed by two different methods are compared. Effects of adhesive layer and adherend lay-up on energy release rates are evaluated.

2.1 Introduction

A number of models of adhesive joints have been recently developed and studied [1-4]. However, the mechanisms of failure and life of joints are not yet sufficiently understood. Laboratory experiments on single lap composite joints presented in Appendix 1 of this report showed that fracture of the bond line was the primary failure mechanism under both static and fatigue loadings. Gradual crack growth in the bond line was observed over a substantial portion of fatigue life.

The objective of this porion of the research was to develop an adequate finite element model for a single lap adhesive joint with arbitrary laminated adherends. Effects of crack length, adhesive layer, and adherend lay-up on joint response were analyzed.

2.2 Computational Model

2.2.1 Geometry

The geometry of the two-dimensional computational model is the cross-sectional geometry of the specimens used in the laboratory experiments in Appendix 1 of this report (Figure 1*a*). Specimen adherends are made of Boeing-certified Hexcel T2G-190-12-F263 high-temperature graphite-epoxy composite. Unidirectional and cross-ply lay-ups specified in Appendix 1 are analyzed. Cytec FM 300-2M epoxy adhesive film is the adhesive. The film thickness is 0.2*mm*. The center of symmetry of the specimen coincides with the center of the coordinate system *Oxz*. The specimen width along axis *Oy* perpendicular to plane *Oxz* is equal to 25.4*mm*. Figure 1, *b* shows a bond crack with length L_{cr}. The crack separates the adherends and grows downward staring from the upper edge of the overlap.

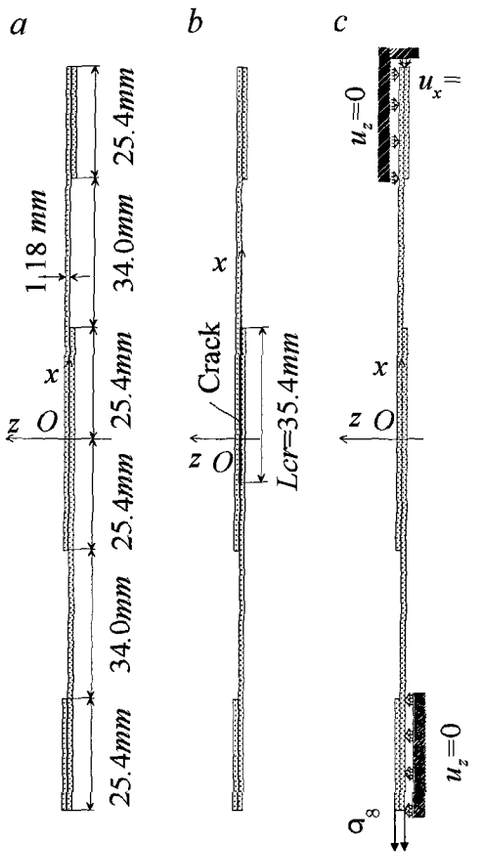

Figure 1: Specimen geometry and coordinate system (a), crack position (b), and boundary conditions (c)

2.2.2 Boundary conditions

Upper specimen part is gripped in the vertically motionless grip of the loading machine. This is modeled by assuming zero vertical displacements (u_x=0) on the top specimen surface and zero horizontal displacements (u_z=0) on the part of adherend's surface shown in, Figure 1, c. Lower specimen part is gripped in the lower machine grip which moves downward during the

experiments and stretches the specimen. The loading is simulated by applying uniformly distributed load P on the bottom of the specimen surface. Calculations are carried out for variable P and for the fixed values of P equal to 166.8, 333.6, and 463.8 MPa that correspond to the total stretching force F of 10, 20, and 27.8kN, respectively. The last value represents the average force that caused failure of UD specimens during quasistatic loading (Appendix 1). Other specimen surfaces including the crack faces are considered load free. The latter is because the loading opens up the crack and the opposing crack faces do not contact each other for all crack lengths and loads considered.

2.2.3 Materials

It is assumed that the specimen adherends are made of an orthotropic linear elastic material with deformability defined by the generalized Hooke's law:

$$\begin{pmatrix} \varepsilon_x \\ \varepsilon_y \\ \varepsilon_z \\ \gamma_{yz} \\ \gamma_{xz} \\ \gamma_{xy} \end{pmatrix} = \begin{pmatrix} a_{11} & a_{12} & a_{13} & a_{14} & a_{15} & a_{16} \\ a_{21} & a_{22} & a_{23} & a_{24} & a_{25} & a_{26} \\ a_{31} & a_{32} & a_{33} & a_{34} & a_{35} & a_{36} \\ a_{41} & a_{42} & a_{43} & a_{44} & a_{45} & a_{46} \\ a_{51} & a_{52} & a_{53} & a_{54} & a_{55} & a_{56} \\ a_{61} & a_{62} & a_{63} & a_{64} & a_{65} & a_{66} \end{pmatrix} \cdot \begin{pmatrix} \sigma_x \\ \sigma_y \\ \sigma_z \\ \tau_{yz} \\ \tau_{xz} \\ \tau_{xy} \end{pmatrix} \quad (1)$$

Nonzero entries a_{ij} of the orthotropic compliance matrix are defined as follows

$$a_{11} = \frac{1}{E_x}, \quad a_{22} = \frac{1}{E_y}, \quad a_{33} = \frac{1}{E_z}, \quad a_{44} = \frac{1}{G_{yz}}, \quad a_{55} = \frac{1}{G_{xz}}, \quad a_{66} = \frac{1}{G_{xy}},$$

$$a_{12} = a_{21} = -\frac{\nu_{xy}}{E_x} = -\frac{\nu_{yx}}{E_y}, \quad a_{13} = a_{31} = -\frac{\nu_{xz}}{E_x} = -\frac{\nu_{zx}}{E_z}, \quad a_{23} = a_{32} = -\frac{\nu_{yz}}{E_y} = -\frac{\nu_{zy}}{E_z} \quad (2)$$

For the unidirectional lay-up, effective elastic parameters are:

$$E_x = 132.70\,GPa, \quad E_y = E_z = 8.83\,GPa, \quad \nu_{xy} = \nu_{xz} = 0.36 \quad \nu_{yz} = 0.30,$$
$$G_{xy} = G_{xz} = 4.76\,GPa, \quad G_{yz} = 3.40\,GPa \tag{3}$$

Effective properties of the cross-ply adherends are given in Appendix 1 of this report. Properties of the adhesive layer are defined as follows:

$$E = 2.32GPa \quad \text{and} \quad \nu = 0.4 \tag{4}$$

2.2.4 Mesh

Commercial Finite Element Method (FEM) package, ANSYS, is used for development of two-dimensional computational model. Geometrically linear and nonlinear models are developed and compared.

In the first model, the adhesive layer is not considered. It is assumed that the whole specimen has properties of the orthotropic composite material (3). 1674 two-dimensional quadrilateral 8-node elements PLANE82 with 5479 nodes are used in the model (Figure 2, *a*). Each element is defined by eight nodes having two degrees of freedom at each node: translations in the nodal x and z directions. The mesh is refined close to the crack tip (Figure 2, *b*). In this area, minimum element side length is equal to 0.036875 *mm*.

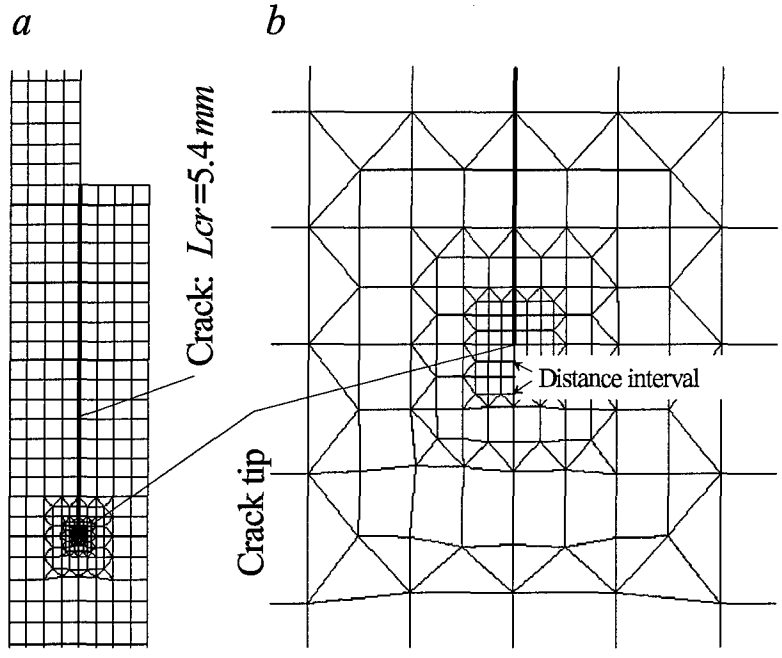

Figure 2: Mesh details around crack *(a)* and distance interval used to evaluate stress approximation *(b)*

2.3 Experimental Validation

Experimental static response of the adhesive composite joints reported in Appendix 1 is compared with finite element calculations based on the uncracked model. Geometrically linear and non-linear analyses are performed with ANSYS 2D FEM model. The displacement between the points A and B (Figure 3) of the model corresponds to the experimentally measured displacement.

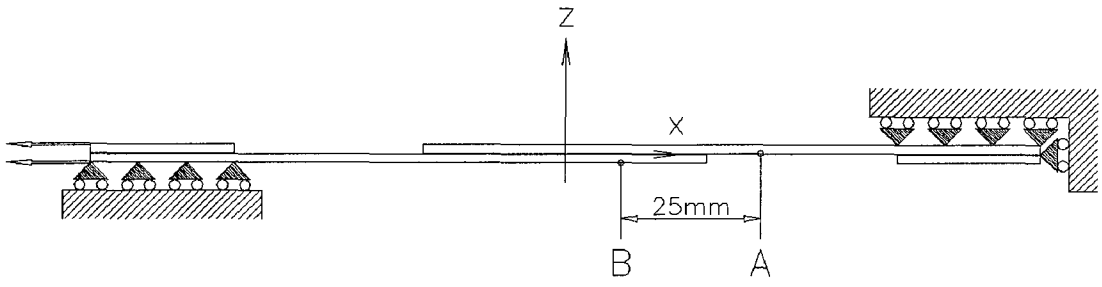

Figure 3: FEM model with reference points

The results of the calculations for the UD specimens are compared with the experimental data (Appendix 1) in Figure 4. It is seen that the geometrically linear analysis overestimates the displacements at higher loads. In addition, it does not describe the observed non-linearity at smaller loads. The geometrically non-linear analysis predicts the first non-linearity at lower loads and shows better overall correspondence with the experimental data. Neither of the analyses predicts the second non-linearity.

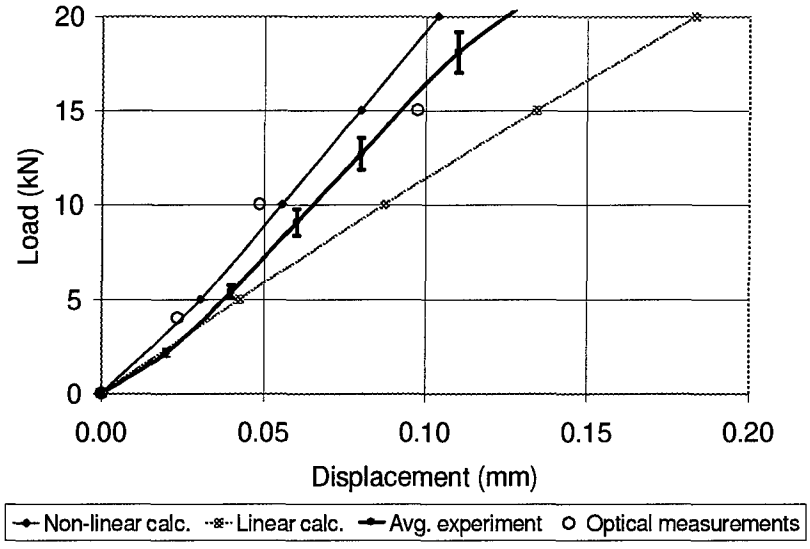

Figure 4: Comparison of UD FEM with experiment

The results of similar analysis for the CP specimens are shown in Figure 5. It is seen that the geometrically linear calculations overestimate the observed displacements severely. At the same time, the geometrically non-linear curves match the experimental results very well. As in the case of UD joints, the geometrically non-linear analysis predicts the first non-linearity at lower loads, but does not predict the second non-linearity at higher loads.

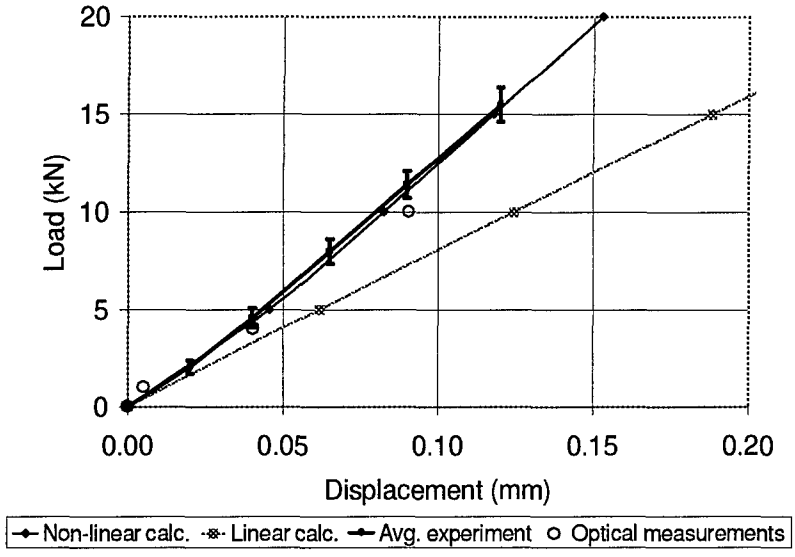

Figure 5: Comparison of CP FEM with experiment

In addition to extensometry reported in Appendix I, global specimen deformation was measured (Figure 6). The results are presented in Figure 7 and shown in Figures 4 and 5 as hollow dots. Good correspondence is observed with the geometrically nonlinear calculations.

From the analysis of both types of specimens, it can be concluded that the deformation of the joints studied in this work was geometrically nonlinear. Parametric analyses conducted in [5] showed that geometrically linear analysis could not be employed for the practical range of adherend thicknesses from 0.84 *mm* to 3.00 *mm*.

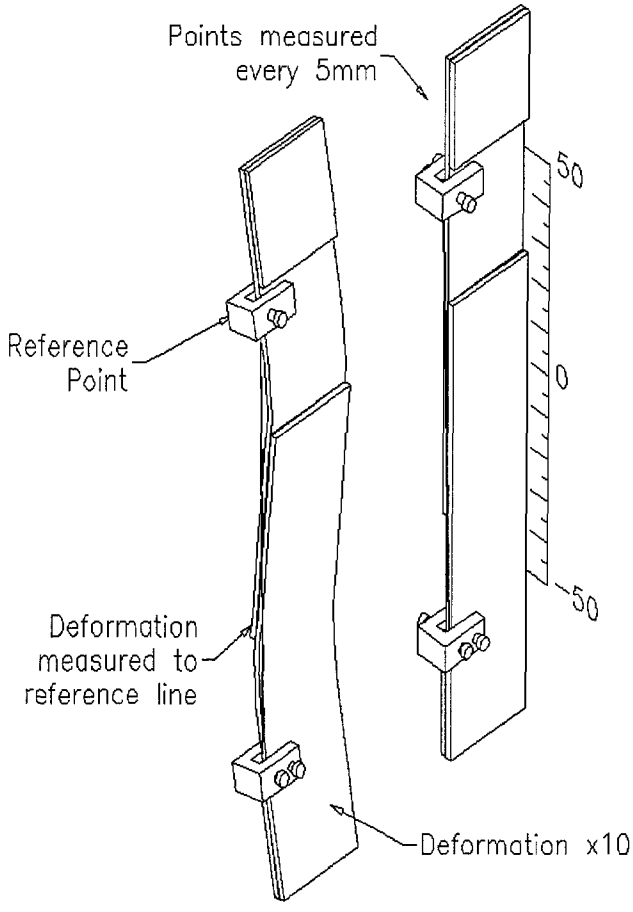

Figure 6: Global deformation measurement method

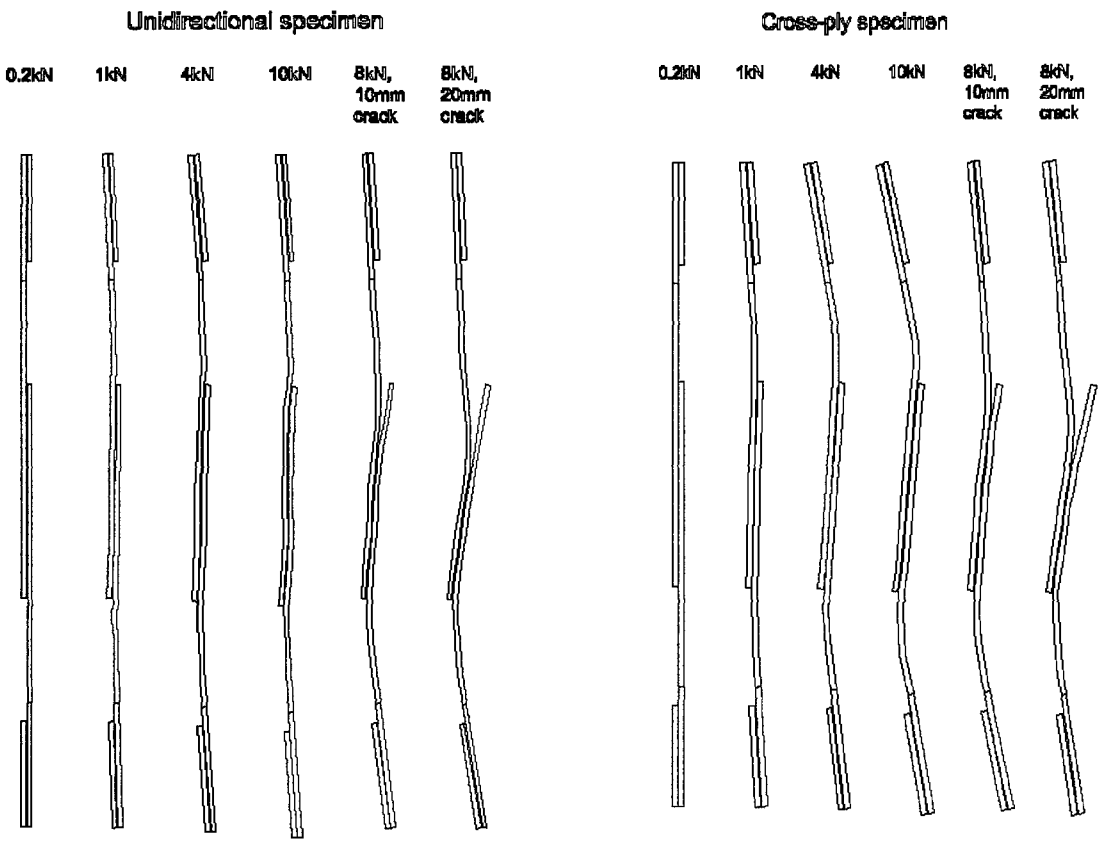

Figure 7: Global deformation of UD and CP joints (displacement magnified x10)

2.4 Analysis

2.4.1 Stress distributions

Stress tensor components in the UD specimen σ_x, τ_{xy}, and σ_z (Figure 8, *a*, *b*, and *c*, respectively) are calculated at points on axis *Ox* for three different crack lengths equal to 5.4,

15.4, and 35.4 *mm* and 27.8 *kN* loading. Close to the crack tips, stresses are calculated at geometrical points placed at 0.125, 0.250, and 0.500 *mm* from crack tips. Relevant points on the graphs are connected by dotted lines. These lines have clearly visible difference in their inclination that demonstrates nonlinear dependence of stresses against crack length: two smaller cracks have similar tip stress concentrations, while tip stress concentration for the longest one is much bigger.

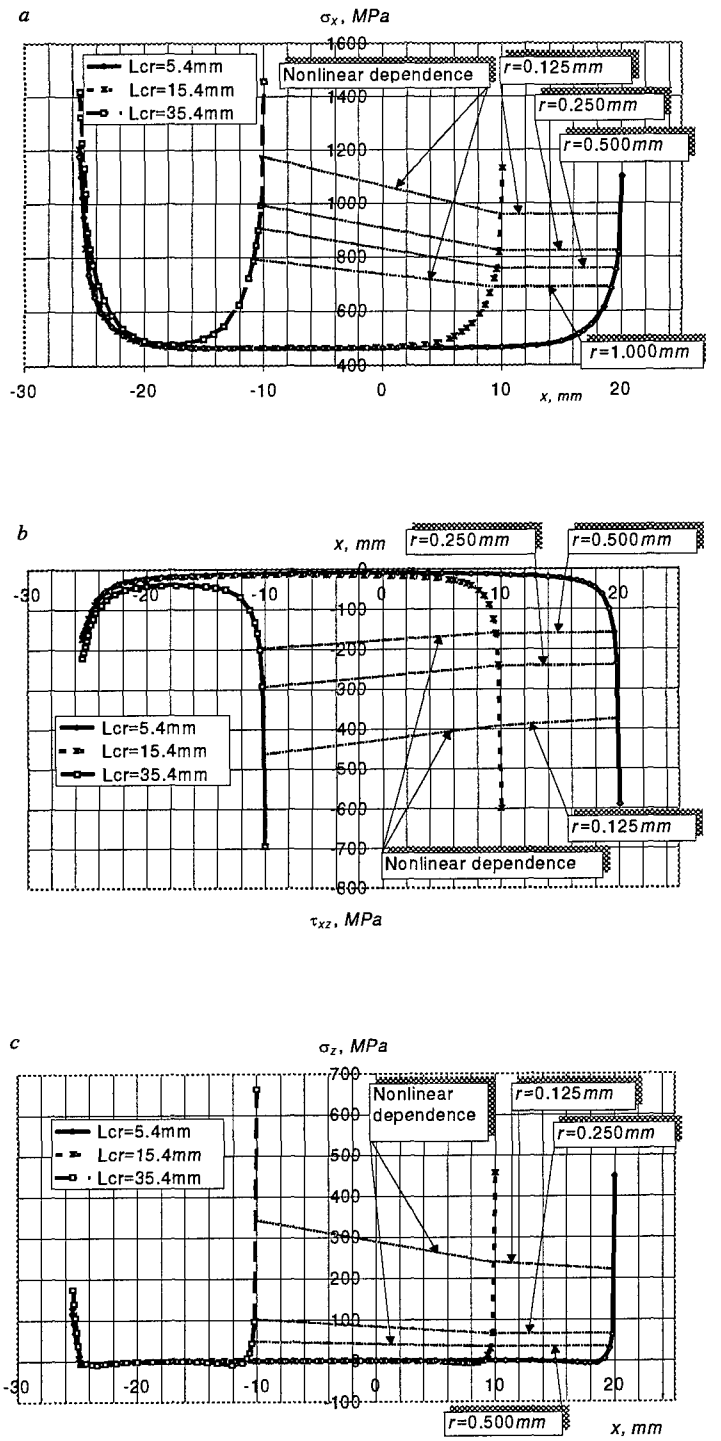

Figure 8: Stresses σ_x (a), τ_{xy} (b), and σ_z (c) in the UD joint along axis *Ox* vs crack length L_{cr}

2.4.2 Stress intensity factors and energy release rates

There are two general methods of evaluation of stress intensity factors for the model under consideration. One of them is based on independently calculated energy release rates G_I and G_{II}, [6, 7] while another developed in [8, 9] employs stress interpolation.

It is known [6, 7] that if the material is orthotropic with the crack in one plane of symmetry, the basic modes are independent and stress intensity factors for plane strain are defined as

$$K_I^2 = E_I G_I \quad \text{and} \quad K_{II}^2 = E_{II} G_{II} \tag{5}$$

where G_I and G_{II} are Mode I and Mode II energy release rates, respectively. Adopting approach proposed in paper [10], the rates can be calculated by using finite element method as follows

$$G_I = \lim_{\Delta a \to 0} \frac{1}{2\Delta a} \cdot F_z \cdot \Delta u_z \quad \text{and} \quad G_{II} = \lim_{\Delta a \to 0} \frac{1}{2\Delta a} \cdot F_x \cdot \Delta u_x \tag{6}$$

where F_x and F_z are shear and opening forces, respectively, that hold together two nearest to the crack tip nodes from different crack surfaces (Figure 9). To evaluate these forces the force values at the crack tip are used. If the forces are equal to zero, sliding and opening displacements of the nodes are defined as u_x and u_z, respectively. In case of quadrilateral 8-node elements used herein, the forces are estimated in the crack tip and the nearest node in the intact body at the direction of crack propagation. The displacements are estimated in the nearest to the crack tip two pairs of nodes, respectively.

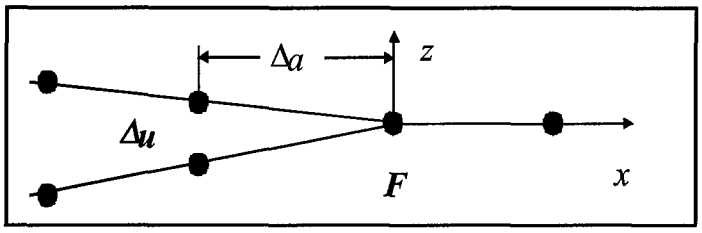

Figure 9: Energy release rate calculation

Effective moduli E_I and E_{II} are defined as

$$E_I = \sqrt{\frac{2}{b_{11}b_{22}}} \cdot \frac{1}{\sqrt{\sqrt{\frac{b_{22}}{b_{11}}} + \frac{2b_{12}+b_{66}}{2b_{11}}}}, \quad E_{II} = \frac{\sqrt{2}}{b_{11}} \cdot \frac{1}{\sqrt{\sqrt{\frac{b_{22}}{b_{11}}} + \frac{2b_{12}+b_{66}}{2b_{11}}}} \tag{7}$$

where

$$b_{ij} = a_{ij} - \frac{a_{i3}a_{j3}}{a_{33}} \qquad (i,j = 1,2,4,5,6) \tag{8}$$

Above equations (7) and (8), together with elastic parameters (3), give the following values of effective moduli

$$E_I = 12.253\,GPa \quad and \quad E_{II} = 45.508\,GPa \tag{9}$$

For the specimen model described above with crack length Lcr=10 mm, load F=27.8 kN, and Δa=0.00975 mm, finite element calculations and formulae (6) produce

$$\begin{aligned} G_I &= 0.78\,kJ/m^2 \quad \text{and} \quad G_{II} = 1.22\,kJ/m^2, \\ K_I &= 97.6\,MPa\cdot mm^{0.5} \quad \text{and} \quad K_{II} = 236.0\,MPa\cdot mm^{0.5} \end{aligned} \tag{10}$$

Stress intensity factors K_I and K_{II} are produced using expressions (5) and (9) for the effective moduli E_I and E_{II}.

Close to the crack tip, stress tensor components are

$$\tau_{xz} = \frac{K_I}{\sqrt{2\pi r}} \quad \text{and} \quad \sigma_z = \frac{K_{II}}{\sqrt{2\pi r}} \tag{11}$$

where r is the distance from the point of the observation to the crack tip. If the mesh is fine enough close to the crack tip, stress intensity factors can be calculated directly by using numerically produced values for relevant stresses in the crack tip area

$$K_I = \tau_{xz}\sqrt{2\pi r} \quad \text{and} \quad K_{II} = \sigma_z\sqrt{2\pi r} \tag{12}$$

However, because of numerical errors near the crack tip, the more reliable results can be produced if the stresses are computed at several points distant from the tip and, afterwards, the least squares method or similar one can be employed [8, 9].

During this research, stresses σ_z and τ_{xz} are calculated at points on axis Ox within distance interval from 0.0417 to 0.125*mm* which does not contain points belonging to the nearest to the crack tip elements (Figure 2, *b*). Typical graphs of numerical and approximate values of stresses σ_z and τ_{xz} are shown in Figure 10, *a*, *b*, respectively. Variation of the stress intensity factors K_I and K_{II} with crack length and loading calculated by this method are shown in Figure 11, *a*, *b*, respectively. Calculated independently, values of K_I and K_{II} (10) confirm the accuracy of the adopted approach. The latter values are presented as solid circular check points in Figure 11.

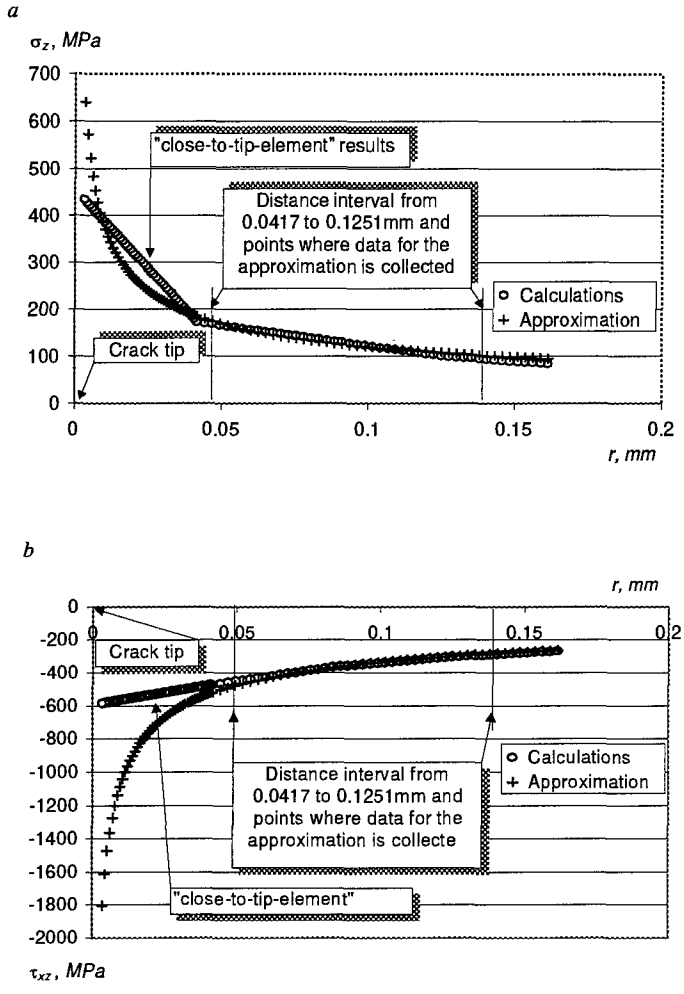

Figure 10: Numerical and approximate results: stresses σ_z *(a)* and τ_{xy} (b) close to the crack tip on axis *Ox*

As it is clearly observed in Figure 11, stress concentrations close to the tips of small cracks with lengths of 5.4 and 15.4*mm* are about the same. However, further crack growth leads to a significant increase of the stress values especially for the peel stress component (Figure 11, *a*). Along with the results described above, the stress intensity factors also vary nonlinearly with the crack length. It is interesting to mention, however, that a linear dependence is observed between the stress intensity factors and the load levels for cracks with constant lengths (Figure 11, a, b).

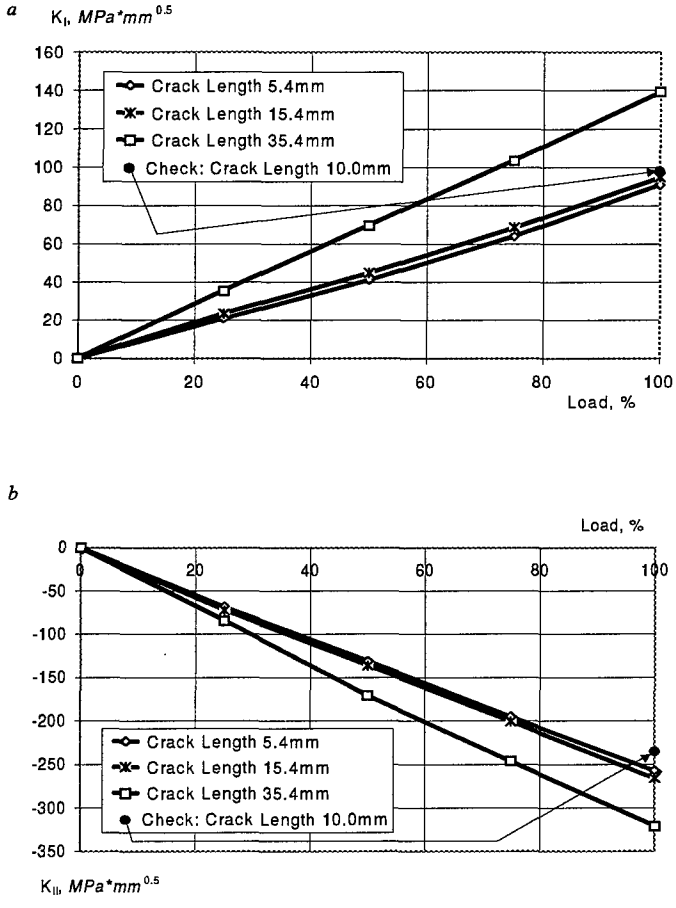

Figure 11: Stress intensity factors K_I (a) and K_{II} (b) vs crack length and loading

2.4.3 Effect of adhesive layer

A real adhesive joint is not homogeneous and contains adhesive layer with elastic properties significantly different from those of the adherends (see (3) and (4)). The experiments (Appendix 1) showed that the crack usually propagates between the adherend and adhesive (Figure 12). It is important to evaluate the effect of the adhesive layer on the analysis.

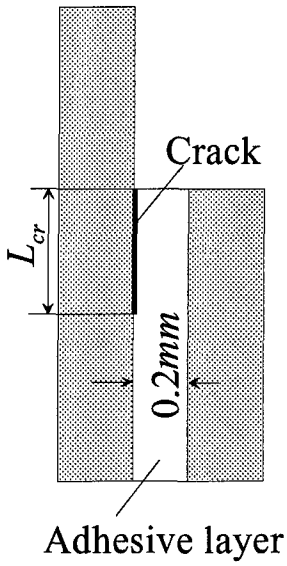

Figure 12: Crack position in the model with adhesive layer

Energy release rates for models with and without explicit adhesive layer are shown in Figure 13. Computational model contains a 10 *mm* crack. The results demonstrate that neglecting the the adhesive layer leads to underestimation of the computed energy release rate.

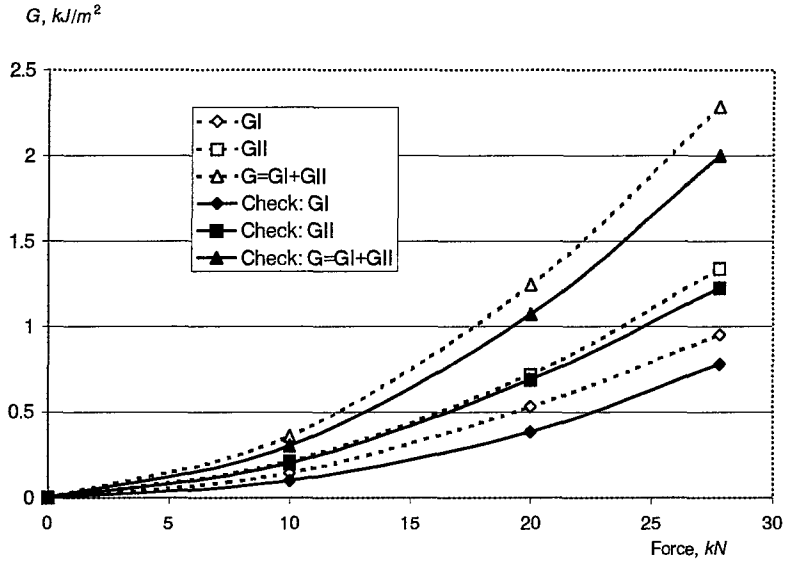

Figure 13: Energy release rates calculated using models with (dash lines) and without (solid lines) adhesive layer

2.4.4 Effect of adherend lay-up

The effect of adherend lay-up is analyzed using the model with explicit adhesive layer. Energy release rates are calculated for specimens with cracks of different lengths for the loading of 10*kN*. This case corresponds to the maximum load value during fatigue tests. As stresses, the energy release rates also vary nonlinearly with the crack length (Figure 14) when crack length becomes bigger than approximately 25 *mm*. For all crack lengths, the energy release rate of the CP joint exceeded the one of the UD joint. It is interesting to note that the fast crack that finally destroyed the UD specimens during the fatigue experiments started propagating when its lengths *Lcr* was in the interval form 30.48 to 35.56 *mm*. The corresponding total critical energy release

rate can be estimated at 0.7 kJ/m^2. (Figure 14). This value is substantially lower than the values computed for static crack initiation [5].

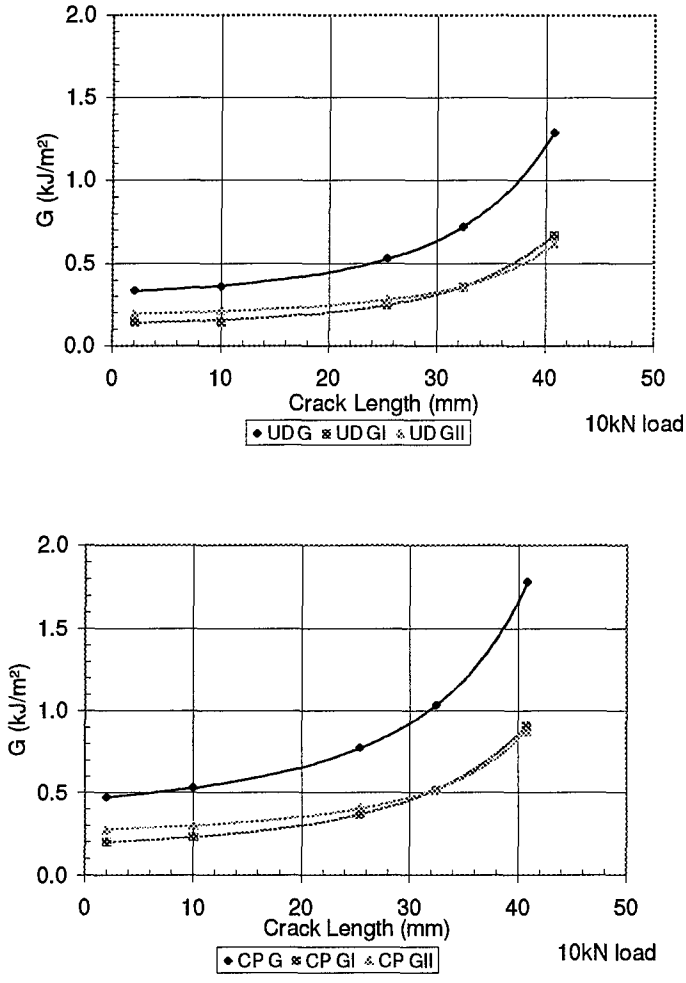

Figure 14: Energy release rates vs crack length for UD and CP joints

Variation of strain energy with load for the two adherends is shown in Figure 15. The CP joints exhibit higher energy release rates compared to the UD joints in the whole load interval studied.

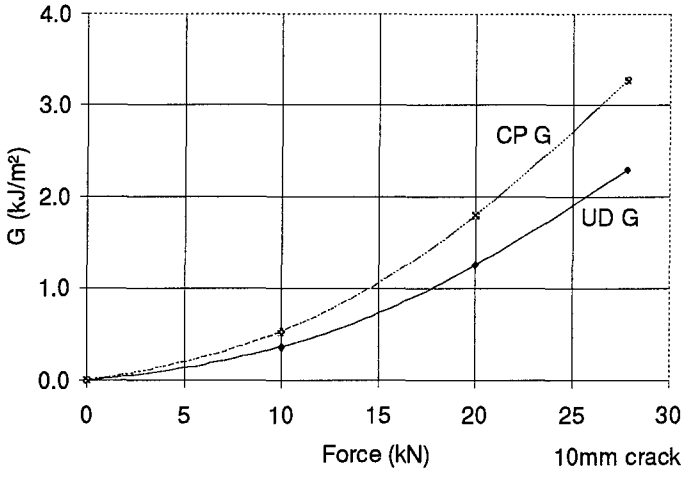

Figure 15: Energy release rates vs load for UD and CP joints

2.5 Summary

Two-dimensional FEM model of single lap adhesive composite joints with laminated adherends was developed and analyzed. Comparison with experiments (Appendix 1) showed that geometrically nonlinear analysis is required for both adherend lay-ups in the entire practical range of adherend thicknesses from 1-3 mm.

Nonlinear finite element analysis was used to study stress fields in single-lap adhesive joints containing bond cracks of different lengths. Quantitative numerical estimations of energy release rates were made for models with and without explicit consideration of adhesive layer. It was found that models that do not consider adhesive layer provide lower values of the energy release rates. It was shown that stresses, energy release rates and stress intensity factors vary non-

linearly with the crack length. However, roughly linear dependence was observed between the stress intensity factors and load. It was interesting that the calculated critical energy release rates for the fast crack initiation at the final stage of fatigue life were 2 to 3 times lower compared to the similar values calculated for crack initiation under quasistatic loading.

2.6 References

[1] Goland, M. and Reissner, E., The stresses in cemented joints, Applied Mechanics, 1, 1944, A17-A27.

[2] Roy, S., *A finite element analysis of adhesively bonded composite joints including geometric nonlinearity, nonlinear viscoelasticity, moisture diffusion and delayed failure*, Ph.D. Thesis, Blacksburg, Va., Virginia Tech Center for Adhesion Science, 1987.

[3] Tsai, M.Y., Morton, J., and Matthews, F.L., Experimental and numerical studies of a laminated composite single-lap adhesive joint. *J. of Composite Materials*, Vol. 29, No. 9, 1995, p. 1254-1275.

[4] Valentin, R.V., Finite element analysis of adhesively bonded joints, Thesis (M.S. in M.E.) School of Mechanical Engineering, Georgia Institute of Technology, 1997.

[5] Kayupov, M. and Dzenis, Y., Nonlinear finite element analysis of a single lap composite joint with a bond crack, *1999 ASME Mechanics & Materials Conference* (Blacksburg, Virginia, USA, June 27-30, 1999), p. 419.

[6] Sih, G.C., Paris, P.C., and Irwin, G.R., On cracks in rectilinearly anisotropic bodies, *International Journal of Fracture Mechanics*, Vol. 1, 1965, pp. 189-203.

[7] Trakas, K. and Kortschot, M.T., The relationship between critical strain energy release rate and fracture mode in multidirectional carbon-fiber/epoxy laminates, *American Society for*

Testing and Materials, 1997, pp. 283-304.

[8] Parton, VZ. and Perlin, P.I, *Methods of mathematical theory of elasticit* , Moscow, Nauka, 1981.

[9] Aitaliev, Sh.M., Banichuk, N.V., and Kayupov, M ., *Optimal design of extended underground structures*, Alma-Ata, Nauka, 1986.

[10] Rybicki, E.F. and Kanninen, M.F., A finite element method calculation of stress intensity factors by a modified crack closure integral, Engineering Fracture Mechanics, Vol. 9, 1977, pp. 931-938.

APPENDIX 3: ANALYSIS OF SINGLE LAP ADHESIVE COMPOSITE JOINTS WITH DELAMINATED ADHERENDS

Contributor: M. Qin

3.1 Introduction 87

3.2 Beam Theory Analysis 88
3.2.1 Model formulation 88
3.2.2 Parametric studies 92

3.3 FEM Analysis 96
3.3.1 Model formulation 96
3.3.2 Parametric studies 99

3.4 Experimental Analysis 101
3.4.1 Specimens and testing 101
3.4.2 Experimental observations of delamination propagation 103
3.4.3 Evaluation of critical energy release rate 108

3.5 Summary 109

3.6 References 110

Delamination in adherends is important damage mode in adhesive composite joints. In Appendix 3 of this report, modified beam theory and nonlinear FEM analysis were used to analyze single lap adhesive composite joints with delaminated adherends. Joints with unidirectional and cross-ply adherends were evaluated and compared. Variations of the strain energy release rate with delamination size and depth were calculated. Growth of delaminations of different initial size and depth was studied experimentally and compared with the results of calculations. Critical strain energy release rate for delamination propagation in the adherends was obtained for the first time by comparison of the experimental and FEM data.

3.1 Introduction

Polymer matrix composites find increasing use in repair of aerospace structures. Adhesively bonded composite patches are capable of minimizing balance and clearance problems on control surfaces and can be readily formed to complex aircraft contours. Reinforcement in the patch can be tailored to suit the loading configuration and to minimize undesirable stiffness increase. Delamination in adherends is one of the important damage modes in adhesive composite joints. Delamination may occur during manufacturing of joints or in service due to substantial interlaminar peel and shear stresses developed in the adherends near the overlap edges. Growth of delaminations in the adherends of a single lap adhesive composite joint is addressed in this work.

Substantial effort was devoted over the years to elastic analysis of adhesive joints. Goland and Reissner [1] analyzed stress distributions in the adhesive layer of a single lap joint. It was

shown that both peel and shear stresses in the adhesive layer can be large. The peel stress is induced by the overall load eccentricity and is especially significant near the edges of the overlap. Large out-of-plane stresses can result in delamination of composite adherends. Williams [2] used the beam theory approach to calculate the strain energy release rates for cracked laminates. The strain energy release rates were defined in terms of membrane forces, transverse shear forces, and bending moments at the crack tip. Recently, Tong et al. [3] used the approach [2] to calculate the strain energy release rates for a single lap adhesive joint with unidirectional adherends. It was shown that the strain energy release rate decreased as the crack length increased.

In this research, the approach [2, 3] is modified and generalized for joints with delaminated adherends of arbitrary lay-up. Variation of the strain energy release rate with delamination size and depth in the joints with unidirectional and cross-ply adherends is calculated and analyzed. The results are compared with geometrically linear and non-linear FEM analyses and experimental observations. The critical energy release rate for delamination propagation in the adherends is obtained for the first time.

3.2 Beam Theory Analysis

3.2.1 Model formulation

Consider a model of a single lap joint with delamination crack [3] (Figure 1). Assume that the two composite adherends have the same lay-up, thickness t, and the same free length l. The overlap length of the joint is $2c$. The delamination crack between the plies of the adherend has tip

A inside the joint overlap and tip B outside the joint overlap. Figures 2 and 3 show the stress resultants acting in the cross sections at crack tips A and B, respectively. These stress resultants were calculated by the modified solution [3] using expressions for the stress functions in the bondline obtained by the modified method [1].

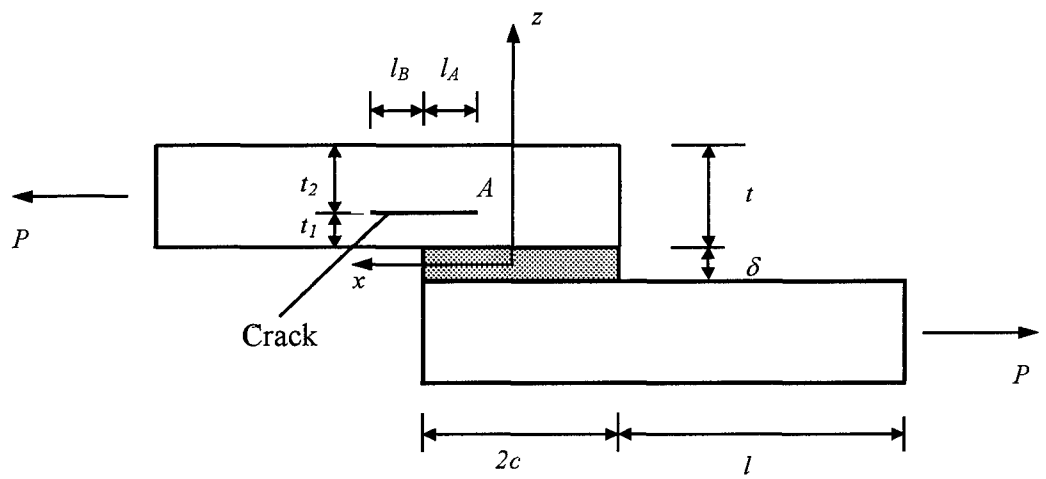

Figure 1: Single lap joint with delaminated adherend

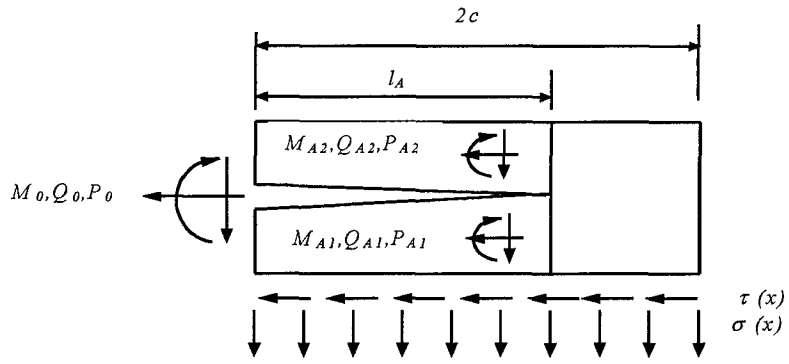

Figure 2: Stress resultants in the cross-section at the crack tip A

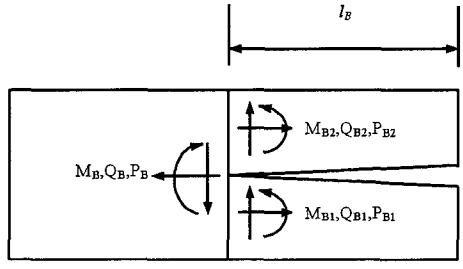

Figure 3: Stress resultants in the cross-section at the crack tip B

The total strain energy release rate at the delamination tips can be calculated as a sum of the energy release rates caused by the bending moments, shear forces, and membrane forces:

$$G = G_M + G_Q + G_P \tag{1}$$

Equations for the partial energy release rates (1) in joints with unidirectional composite

adherends are given in [3]. In this work, a general case of a single lap adhesive composite joint with arbitrary laminated adherends is considered. The partial energy release rates for the orthotropic adherends with an arbitrary lay-up can be defined as follows:

$$G_M = \frac{1}{2}d_{11}^{(1)}M_1^2 + \frac{1}{2}d_{11}^{(2)}M_2^2 - \frac{1}{2}d_{11}(M_1+M_2)^2 \tag{2}$$

$$G_Q = \sum_{i=1}^{n_1}\frac{1}{G'_{xy}}\int_{z_{i-1}}^{z_i}\left[\frac{3Q_1}{4t_1}\left(1-\frac{z^2}{t_1}\right)\right]^2 dz + \sum_{i=1}^{n_2}\frac{1}{G'_{xy}}\int_{z_{i-1}}^{z_i}\left[\frac{3Q_2}{4t_2}\left(1-\frac{z^2}{t_2}\right)\right]^2 dz - \sum_{i=1}^{n}\frac{1}{G'_{xy}}\int_{z_{i-1}}^{z_i}\left[\frac{3(Q_1+Q_2)}{4t}\left(1-\frac{z^2}{t}\right)\right]^2 dz \tag{3}$$

$$G_P = \sum_{i=1}^{n_1}\frac{1-\nu_{xy}^i\nu_{yx}^i}{2}\frac{(P_1/n_1)^2}{E_x^i t_1} + \sum_{i=1}^{n_2}\frac{1-\nu_{xy}^i\nu_{yx}^i}{2}\frac{(P_2/n_2)^2}{E_x^i t_2} - \sum_{i=1}^{n}\frac{1-\nu_{xy}^i\nu_{yx}^i}{2}\frac{((P_1+P_2)/n)^2}{E_x^i t} \tag{4}$$

where i is the ply index; the ply constants in the laminate axes are defined by the following equations:

$$\frac{1}{E_x} = \frac{1}{E_1}\cos^4\theta + \left(\frac{1}{G_{12}} - \frac{2\nu_{12}}{E_1}\right)\sin^2\theta\cos^2\theta + \frac{1}{E_1}\sin^4\theta$$

$$\nu_{xy} = E_x\left[\frac{\nu_{12}}{E_1}(\sin^4\theta + \cos^4\theta) - \left(\frac{1}{E_1}+\frac{1}{E_2}-\frac{1}{G_{12}}\right)\sin^2\theta\cos^2\theta\right]$$

$$\frac{1}{G_{xy}} = 2\left(\frac{2}{E_1} + \frac{2}{E_2} + \frac{4\nu_{12}}{E_1} - \frac{1}{G_{12}}\right)\sin^2\theta\cos^2\theta + \frac{1}{G_{12}}(\sin^4\theta + \cos^4\theta)$$

The coefficients $d_{11}^{(1)}, d_{11}^{(2)}$, and d_{11} are the bending stiffnesses for the lower and upper sublaminates and the total laminate, respectively. The numbers n_1, n_2 and n represent the ply numbers for the lower and upper sublaminates and the total laminate, respectively. The crack tip index (A or B) is omitted in the Eqs (2-4), for simplicity.

Note that the mode partitioning of the total energy performed in [2, 3] appears to be incorrect, according to [4]. Therefore, only the total energy was analyzed in this work.

3.2.2 Parametric studies

The model described above was used to calculate the strain energy release rates in single lap joints with adherends made of Hexcel T2G190-12-F263 graphite-epoxy composite. Joints with six-ply unidirectional and cross-ply adherends were analyzed. The mechanical properties of the graphite-epoxy ply were E_{11} = 132.7 GPa, $E_{22} = E_{33}$ = 8.83 GPa, $\nu_{12} = \nu_{13}$ = 0.36, G_{12} = 4.76 GPa. The ply thickness was 0.17 mm. The joint had a free length of 150 mm and an overlap length of 60 mm.

Figure 4 compares the total strain energy release rate at the crack tip A inside the overlap for the joints with the unidirectional and cross-ply adherends. The delamination was located between the first and second plies nearest to the adhesive layer. The applied far-field tensile stress in the adherends was 400 MPa in both cases. It is seen that in both cases, the strain energy release

rate decreased as the crack length increased. The strain energy release rate for the cross-ply joint (Figure 4b) was higher than the strain energy release rate for the unidirectional joint (Figure 4a) for all crack lengths, l_A, studied.

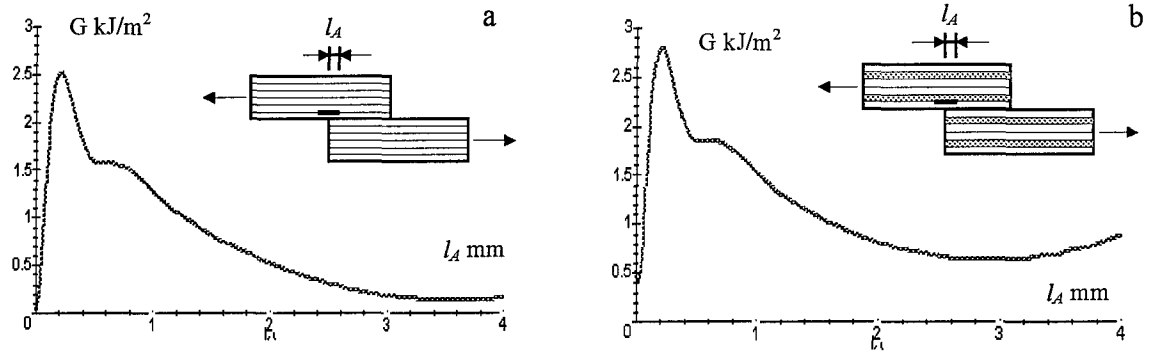

Figure 4: Variation of strain energy release rate at the crack tip A with crack length: joints with UD (a) and CP (b) adherends

Figure 5 shows the total strain energy release rate at crack tip B outside the overlap for the joints with the unidirectional and cross-ply adherends. Both joints were loaded by the far-field stress 400 MPa. It is seen that for both joints, the strain energy release rate at crack tip B was substantially smaller compared to the strain energy release rate at crack tip A (Figure 4). The strain energy release rate in the joint with the cross-ply adherends (Figure 5b) was higher than the energy release rate in the joint with the unidirectional adherends (Figure 5a).

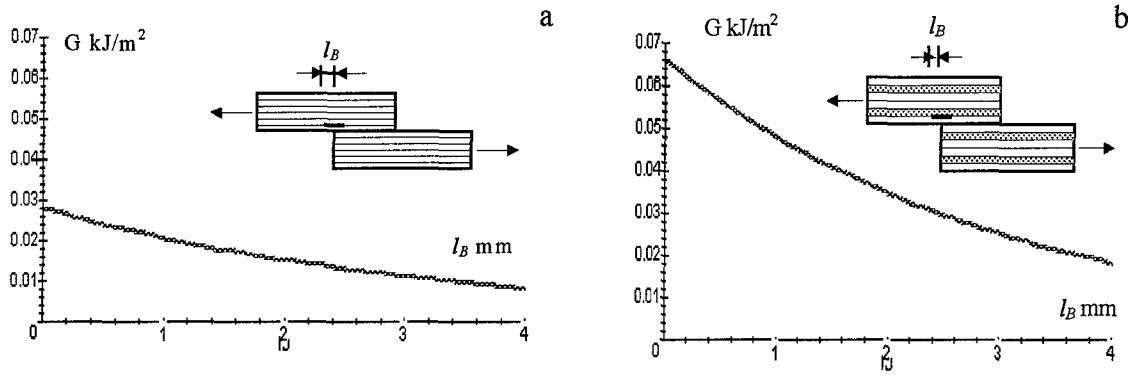

Figure 5: Variation of strain energy release rate at the crack tip B with crack length: joints with UD (a) and CP (b) adherends

For both joints, the strain energy release rate decreased as the delamination length increased.

Figure 6 shows the variation of the total strain energy release rate at tip A of the crack located between the second and third plies in the joints with unidirectional and cross-ply adherends. For both joints, the strain energy release rate was smaller compared to the case with the delamination located between the first and second plies (Figure 4). However, the strain energy release rate in the joint with the unidirectional adherends decreased more rapidly than that in the joint with the cross-ply adherends. As a result, the ratio of the strain energies in the two joints increased as the depth of the crack decreased. The same effects of the crack depth were observed for the strain energy release rate at crack tip B.

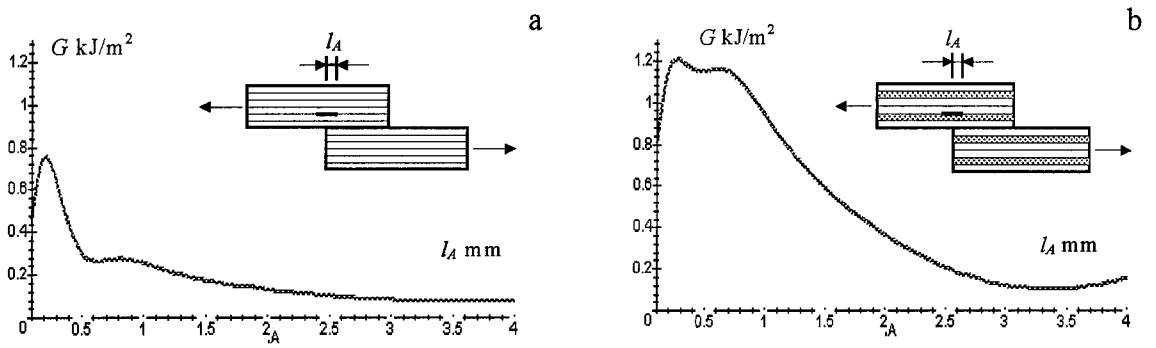

Figure 6: Variation of strain energy release rate at the crack tip A with crack length: crack located between the second and third plies in joints with UD (a) and CP (b) adherends

Figure 7 shows the variation of the maximum strain energy release rate at the crack tip A with delamination depth in the joints with the unidirectional and cross-ply adherends. It is seen that, for both unidirectional and cross-ply adherends, the maximum strain energy release rate decreased as the delamination depth increased. The ratio of the maximum strain energy release rates for the joints with the cross-ply and unidirectional adherends also increased with the delamination depth.

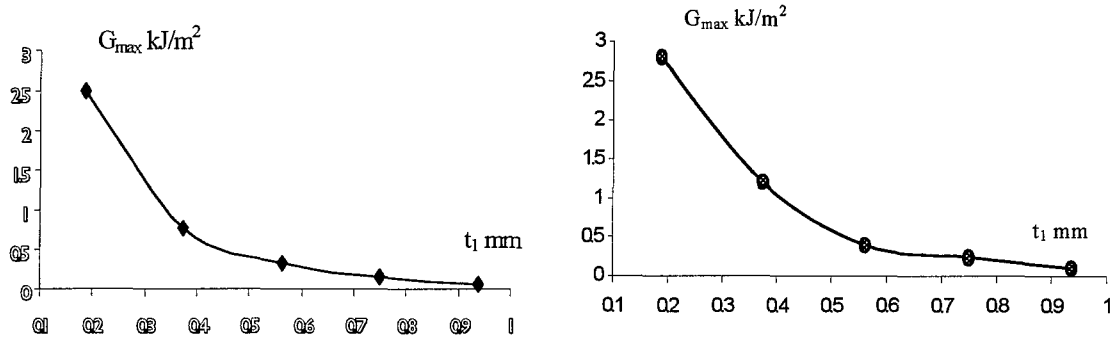

Figure 7: Variation of maximum strain energy release rate at the crack tip A with crack depth: joints with UD (a) and CP (b) adherends

Overall, the analysis showed that both single lap adhesive composite joints were delamination tolerant. In all cases studied, the strain energy release rate decreased as delamination length increased. The strain energy release rate in the joints with the cross-ply adherends was greater than that in the joints with the unidirectional adherends. For both joints, the strain energy release rate decreased as the delamination depth increased.

3.3 FEM Analysis

3.3.1 Model formulation

A two-dimensional 8-nodes quadrilateral plane strain finite element was used to model the behavior of a single lap joint with unidirectional and cross-ply adherends. ANASYS 5.3 code was used to simulate the mechanics characteristics of the single lap joint. The geometry and boundary

conditions of the finite element model are shown in Figure 8. Mesh at the crack tip was refined to less than 0.008 mm (Figure 9).

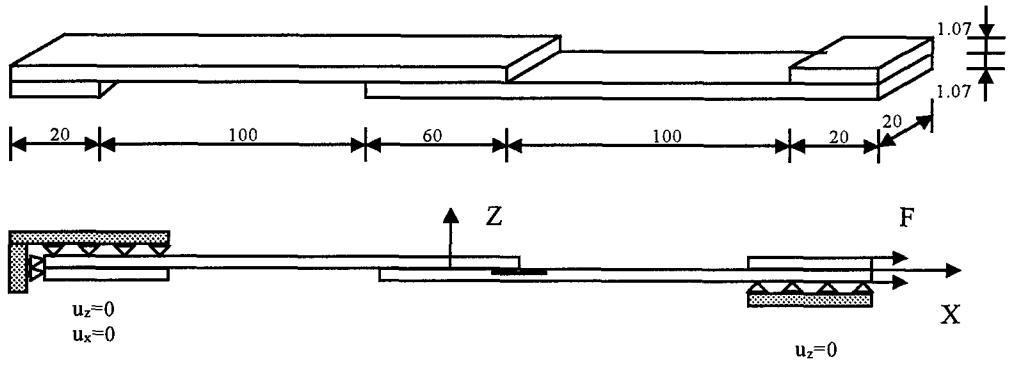

Figure 8: Single lap joint with delaminated adherend and boundary conditions

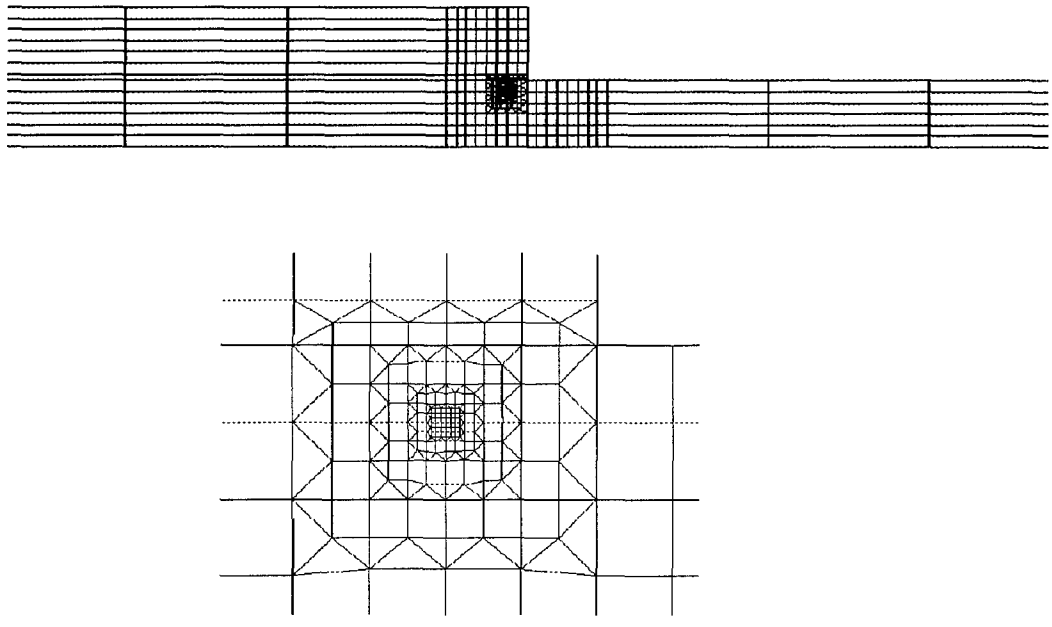

Figure 9: Mesh details

The model was used to calculate strain energy release rates in single lap joints with adherends made of Hexcel T2G_190-12"-F263 graphite-epoxy composite. The strain energy release rate was calculated as follows:

$$G_I = \frac{F_{z1} \cdot \Delta d_{z34} + F_{z2} \cdot \Delta d_{z56}}{2\Delta a} \tag{5}$$

$$G_{II} = \frac{F_{x1} \cdot \Delta d_{x34} + F_{x2} \cdot \Delta d_{x56}}{2\Delta a}$$

$$G_{total} = G_I + G_{II}$$

where F — nodal forces, Δd — relative nodal displacements.

The indices in (5) are as shown in Figure 10.

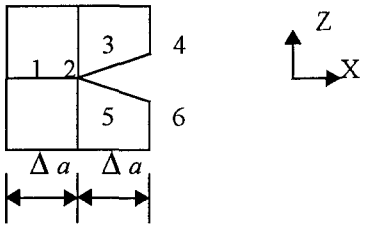

Figure 10: Schematic of the crack tip

Unidirectional $[0]_6$ and cross-ply $[0/90/0]_S$ adherends were analyzed. The mechanical properties of the graphite-epoxy ply were $E_{11} = 132.7$ GPa, $E_{22} = E_{33} = 8.83$ GPa, $\nu_{12} = \nu_{13} = 0.36$, $G_{12} = 4.76$ GPa. The ply thickness was 0.17 mm.

3.3.2 Parametric studies

The strain energy release rates were calculated with geometrical linear and non-linear models. Figure 11 shows the variation of the total stain energy release rate (G_{total}) and the Mode I (G_I) and II (G_{II}) strain energy release rates in the UD joint with delamination crack length under the far field stresses 400 MPa and 250 MPa. Similar results for the CP joint are shown in Figure 12. In these cases, the crack was located between the first and second plies. The analyzed crack tip was located inside the overlap. It is seen that the nonlinear analysis produces considerably lower energies compared to the linear analysis. This corresponds to the analysis of joints in Appendix 2 of this report. As before, joints with the CP adherends produced higher energy release rates compared to the UD joints.

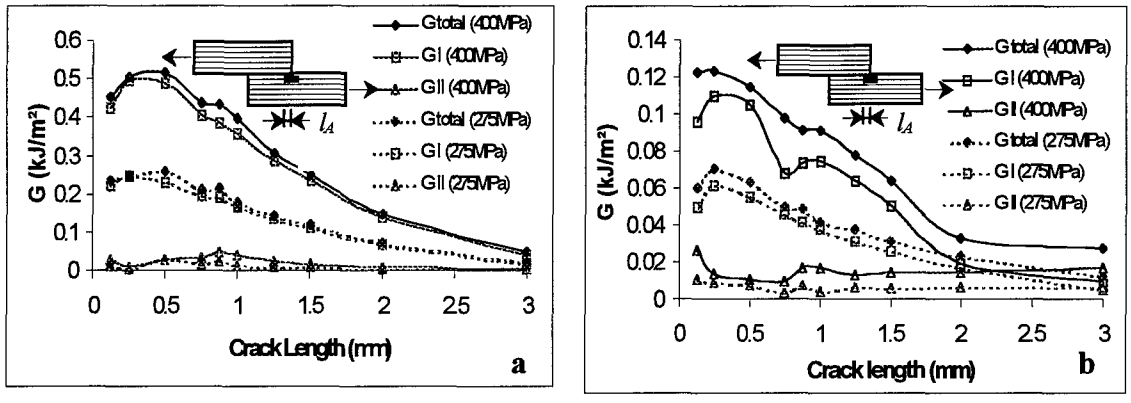

Figure 11: Variation of energy release rate in joints with UD adherends: Geometrically linear (a) and non-linear (b) analysis

Variations of the energy release rates in the joints with UD and CP adherends for the crack located between the second and third plies are shown in Figure 13 for the far field stress 400 MPa.

Again, the geometrically non-linear analysis resulted in lower energy release rates and the energy release rates for the UD joints were lower than those for the CP joints.

Comparisons of the FEM results with the beam theory data shows that both methods yielded qualitatively similar energy variations with crack length and depth. However, the FEM calculations produced substantially lower values of strain energies. The nonlinear FEM model was shown to adequately describe joint deformation (see Appendix 2). Therefore, the results of present analysis show that the beam theory approach can severely overestimate the elastic strain energies in the single lap joints with both composite adherends studied.

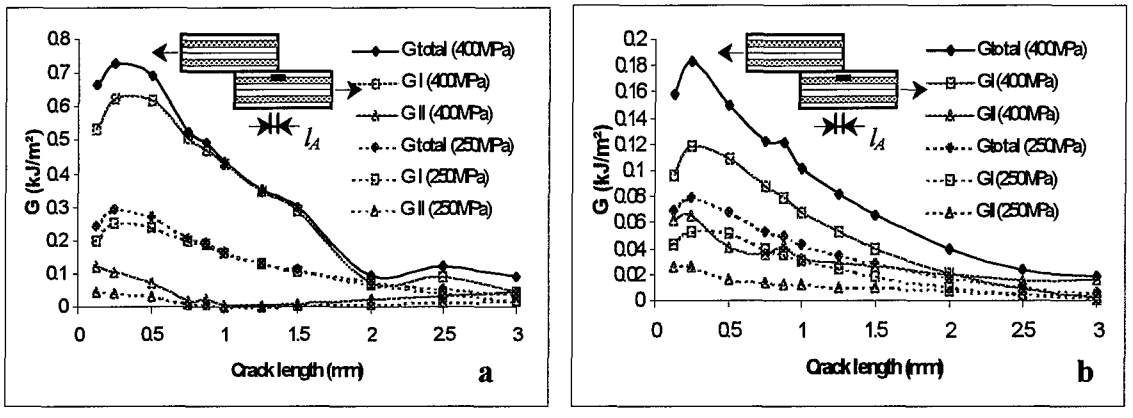

Figure 12: Variation of energy release rate in joints with CP adherends: Geometrically linear (a) and non-linear (b) analysis

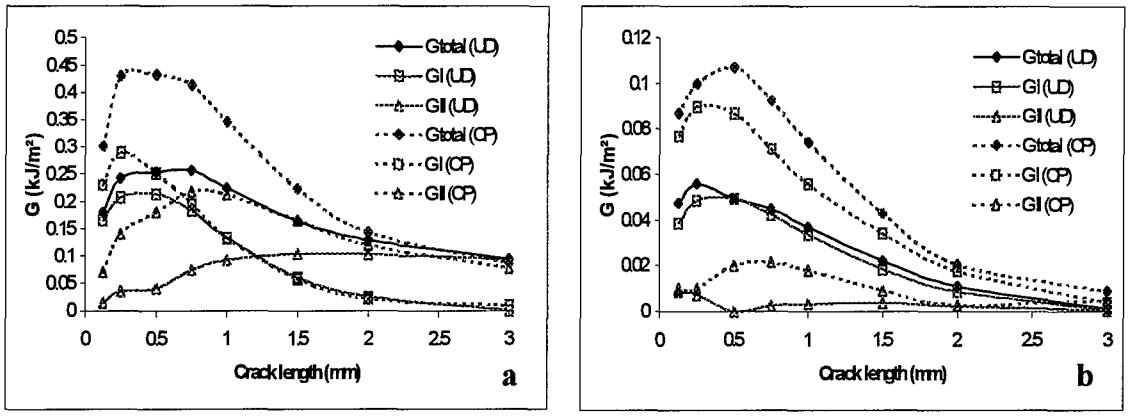

Figure 13: Variation of energy release rate in joint with UD & CP adherends: Geometrically linear (a) and non-linear (b) analysis. Crack is located between the second and third ply.

3.4 Experimental Analysis

3.4.1 Specimens and testing

Experiments were performed on adhesive composite joints with deliberately introduced delaminations. Several single lap adhesive composite joints were manufactured from Hexcel T2G190-12-F263 graphite/epoxy prepreg and Cytec 300-2M adhesive film. Unidirectional and cross-ply lay-ups were utilized. The joint panels were prepared by secondary curing using manufacturer recommended curing cycles. The panels were cut into specimens by a high speed diamond saw. The specimen geometry is shown in Figure 14. The overlap length was 60 mm. Initial delaminations were introduced into the adherends by a thin Teflon film inserted during manufacturing. The location of the delamination tip in the overlap section and the depth of delamination were varied.

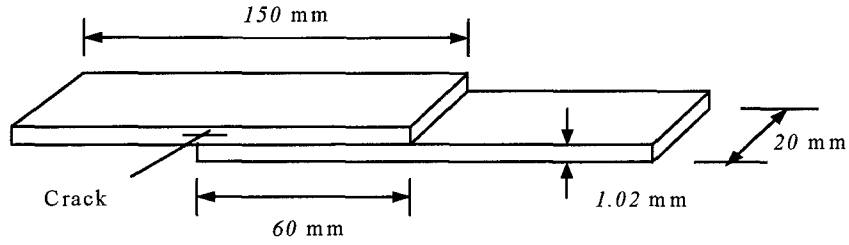

Figure 14: Specimen geometry

Mechanical testing was performed on a servohydraulic MTS testing machine retrofitted by an Instron digital test control and data acquisition system. An on-line video microscopy system (Figure 15) was used to characterize delamination growth.

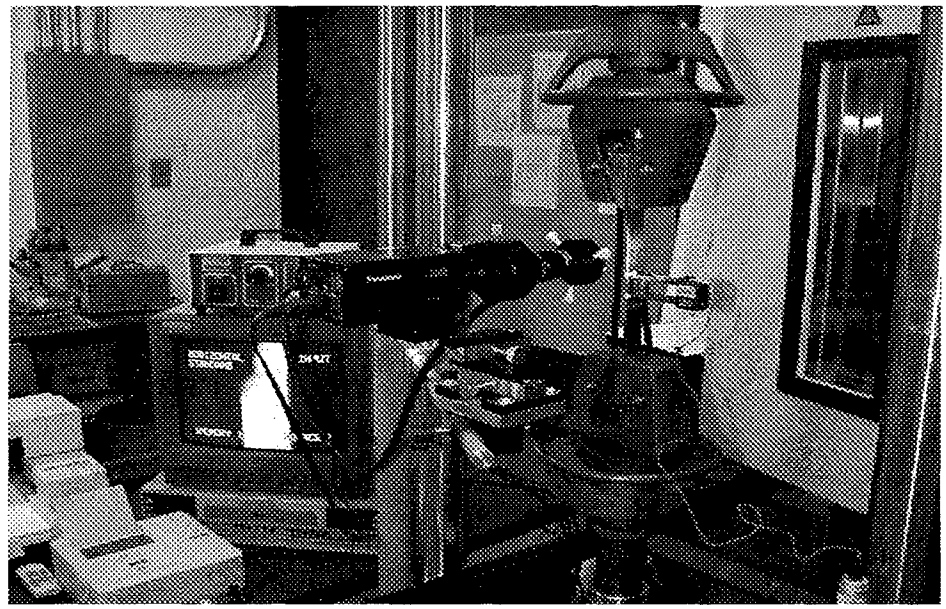

Figure 15: Experimental setup

3.4.2 Experimental observations of delamination propagation

Figure 16 shows delamination growth with load between the first and second plies of the unidirectional adherend. The positions of the delamination crack tips at different loads are indi cated in the microphotographs by arrows. As the far field stress increases, the delamination crack tip position measured from the overlap edge propagates from the initial position at about 0.1 mm to approximately 0.4 mm at 275 MPa and further to 1.45 mm at 400 MPa.

Figure 17 compares the growth of delamination between the first and second plies in the two unidirectional joints with different initial crack length (tip position inside the overlap). Both joints were loaded to the far-field tensile stress 400 MPa. The delamination crack length appeared to be independent of the initial crack tip position and depended only on the external load. The crack length at 400 MPa was about 1.45 mm in both cases studied.

Figure 18 compares the delamination growth between the first and second plies and the second and third plies in the two specimens with unidirectional adherends. The initial crack tip position was the same in both joints. The joints were loaded to 400 MPa and 450 MPa, respectively. The crack tip positions at these loads are indicated in the microphotographs by arrows. It is seen that the length of the crack located between the second and third plies was smaller than that of the crack located between the first and second plies, even though the external load in the former case was higher.

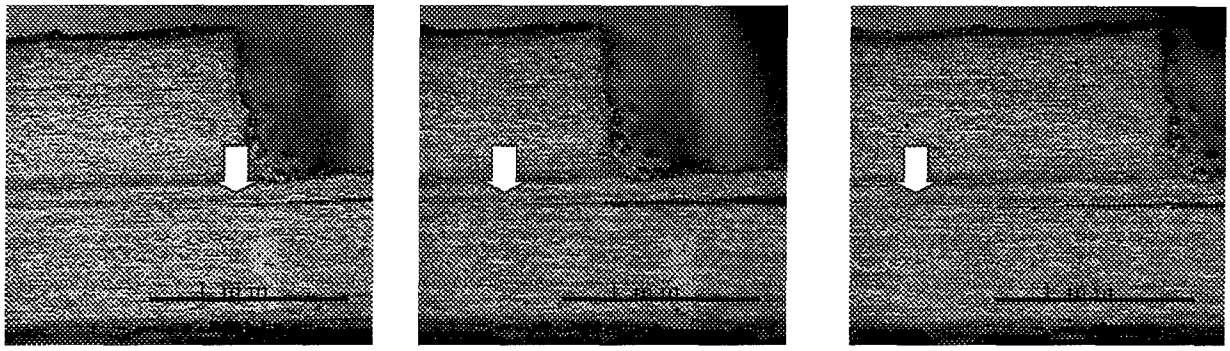

Initial tip position 0.1 mm (0 MPa) Tip position 0.4 mm (275 MPa) Tip position 1.45 mm (400 Mpa)

Figure 16: Delamination growth in unidirectional adherend (far-field stress is given in parentheses)

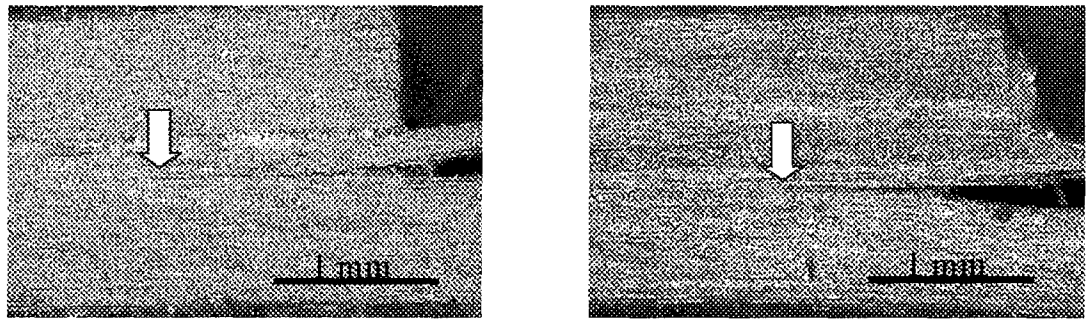

Initial tip position = 0.05 mm Initial tip position = 0.5 mm

Figure 17: Delamination growth in unidirectional adherends with various initial crack length (far-field stress 400 MPa)

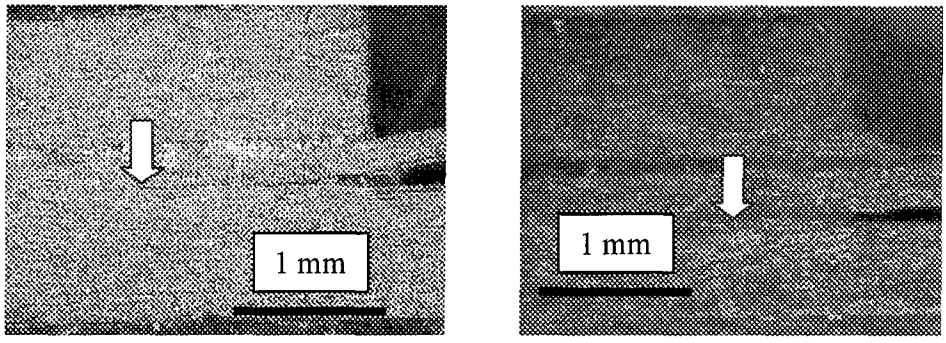

Crack between 1st & 2nd plies (400 Mpa) Crack between 2nd & 3rd plies (400 Mpa)

Figure 18: Delamination growth in unidirectional adherends with various initial crack depth (far-field stress is given in parentheses)

Figure 19 shows growth of delamination initially located between the first and second plies of the cross-ply adherend. The initial crack tip position was 0.35 mm from the overlap edge. The positions of the crack tip at different loads are indicated in the microphotographs by arrows. It is seen that when the load reached 250 MPa, the crack in the cross-ply adherend has kinked and migrated to the next ply interface. This could be due to the mixed mode stress state at the crack tip. The direction of the maximum strain energy release rate under the mixed mode loading condition is at an angle to the initial crack direction. The crack in the cross-ply adherend then propagated along the interface between the second and third plies. As the far field stress increased, the position of the delamination crack after the kink changed from approximately 0.5 mm at 250 MPa to 1.15 mm at 400 MPa. As was noted earlier, the propagation of the cracks located at interfaces further away from the bondline is more difficult (see Figure 18). Similar results were observed on another CP specimen with different initial crack tip position 0.1 mm (Figure 20). Again, the crack propagated along the initial interface until about 250 MPa at which load the crack has kinked

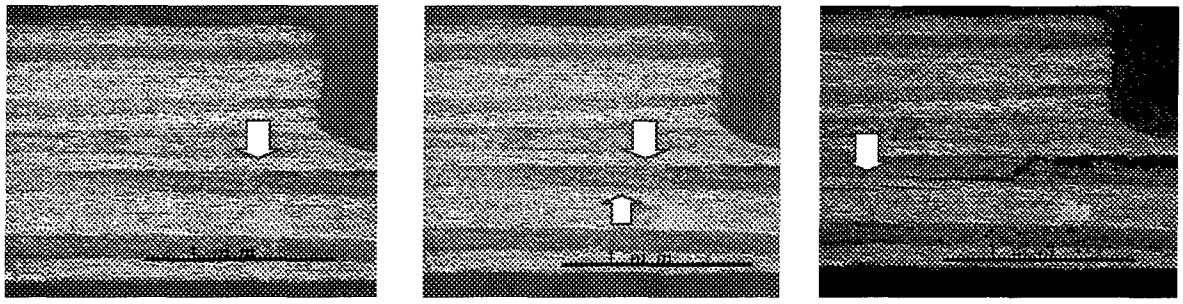

Initial tip position 0.35 mm (0 MPa) Tip position 0.5 mm (250 MPa) Tip position 1.15 mm (400 Mpa)

Figure 19: Delamination growth in cross-ply adherend (far-field stress is given in parentheses)

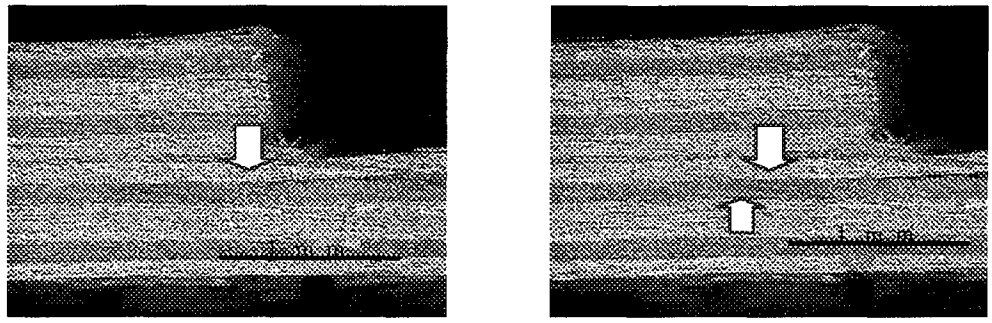

Initial tip position 0.1 mm (0 MPa) Tip position 0.5 mm (250 MPa)

Figure 20: Delamination growth in cross-ply adherend (far-field stress is given in parentheses)

through the 90-degree ply to the next ply interface.

Comparison of delamination growth in the joints with unidirectional adherends (Figures 16-18) and cross-ply adherends (Figures 19 and 20) showed that the latter exhibit larger cracks at similar loads and depths.

The observations made during the experiments are summarized as follows.

- Crack tips outside the overlap did not propagate
- Crack tips inside the overlap propagated through finite length depending on loading
- Shallower cracks located nearer to the bondline propagated through larger length than deeper cracks
- Cracks in the joints with the cross-ply adherends started to propagate earlier and propagated through larger length than cracks in the joints with the unidirectional adherends

These experimental observations corroborate well the theoretical predictions. Note that when tested to failure, most joints with delaminated adherends failed through the bondline, similar to the undamaged joints (Appendix 1). However, the delaminations in most cases propagated in parallel to the bond crack. The observed phenomenon of parallel crack propagation may be important for overall fracture toughness of bonds (e.g. energy consumption under impact failure) and seems to warrant additional investigations. The phenomenon of crack kinking and branching into the adherends is also interesting and can be studied separately.

3.4.3 Evaluation of critical energy release rate

According to the experimental observations, in the unidirectional joints, when the far field stress is 275 MPa the crack length is 0.4 mm and when the far field stress is 400 MPa the crack length is 1.45 mm. The critical total strain energy release rates can be then evaluated for this cases based on the energy calculations performed by the geometrical nonlinear FEM model. The analysis in Figure 21 yields the value of critical total energy 0.067 kJ/m^2.

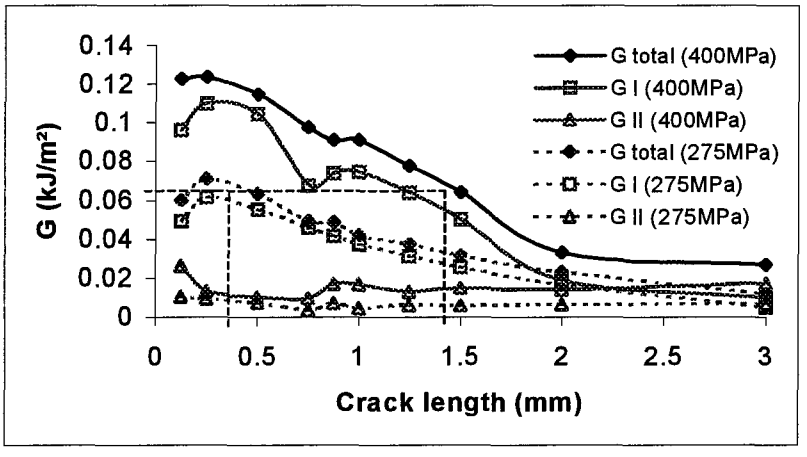

Figure 21: Critical G for UD adherends based on the geometrically non-linear FEM analysis

For the joints with the cross-ply adherends, when the far field stress is 250 MPa the crack length is 0.5 mm and when the far field stress is 400 MPa the crack length at another interface (between the second and third plies) is 1.15 mm. The critical total strain energy release rate computed based on the nonlinear FEM data (Figure 22) is again 0.067 kJ/m ^{2}.

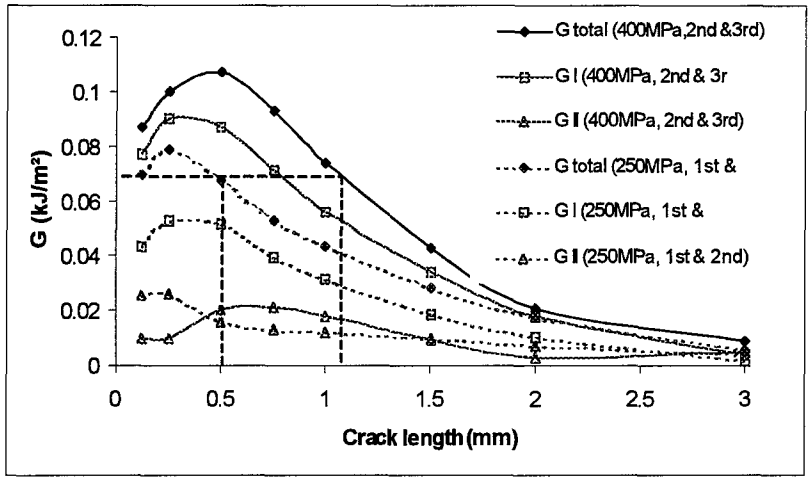

Figure 22: Critical G for CP adherends based on the geometrically non-linear FEM analysis

Good correlation between the critical energy values for the two adherend lay-ups may indicate that the delamination fracture resistance is matrix related material property.

The critical values of the strain energy release rates for Mode I and Mode II in both cases are around 0.051 kJ/ ^{2} and 0.016kJ/m^2 respectively. Apparently, the delamination growth is caused primarily by peel stresses at the crack tip.

3.5 Summary

Beam theory qualitatively corresponds to FEM and experimental data but quantitatively overestimates strain energy release rates for both lap composite joints studied. Geometrically lin ear analysis also overestimates the energies compared to the geometrically nonlinear calculations.

Analysis of the strain energy release rates showed that the single lap joints were delamination tol erant. In all cases studied, the strain energy release rate decreased as the crack length increased. The strain energy release rate in the joints with the cross-ply adherends was greater than the strain energy release rate in the joints with the unidirectional adherends. For both joints, the strain energy release rate decreased as the depth of crack increased. The critical energy release rate was obtained by comparison of experimental and FEM analysis results. Good correlation between the critical energy values for the two adherend lay-ups indicates that the delamination fracture resi tance may be matrix related material property. The observed phenomena of parallel crack propagation prior to failure and delamination crack kinking and branching into the adherends require additional investigations.

3.6 References

[1] Goland, M., and Reissner, E., "The Stress in Cemented Joints", *Journal of Applied Mechanics*, Vol. 66, 1944, pp. A17-27

[2] Williams, J.G., "On The Calculation of Energy Release Rates for Cracked Laminates", *International Journal of Fracture*, Vol. 36, 1988, pp. 101-119

[3] Tong, L., Zhu, X.C and Steven, G. P., "Damage Tolerance of Adhesively Bonded Composite Single Lap Joints", *Key Engineering Materials*, Vol. 145-149, 1998, pp. 537-542

[4] Sun, C.T. and Pandey, R.K., "Improved Method for Calculating Strain Energy Release Rate Based on Beam Theory", *AIAA Journal*, Vol. 32, No. 1, 1994, pp. 184 -189

APPENDIX 4: ACOUSTIC EMISSION ANALYSIS OF DAMAGE AND FRACTURE MICROMECHANISMS

Contributors: J. Qian, I. Saunders, D. Wu

4.1 Introduction 114
4.1.1 Damage in composites 114
4.1.2 Acoustic emission analysis of damage mechanisms 117

4.2 Experimental 122
4.2.1 Materials and manufacturing 122
4.2.2 Mechanical testing 123
4.2.3 Acoustic Emission Testing 125

4.3 Static Analysis of UD and CP Composites Composites 128
4.3.1 Mechanical response 128
4.3.2 Conventional parametric AE analysis 131
4.3.2.1 Overall AE histories 131
4.3.2.2 Parametric Distributions and Correlations 135
4.3.3 Transient AE analysis 139
4.3.4 Development of hybrid transient-parametric method 141
4.3.4.1 Multiparametric regions for characteristic waveforms 141
4.3.4.2 Classified AE histories for unidirectional composites 142
4.3.4.3 Correlation of waveforms and damage mechanisms 144
4.3.5 Microdamage evolution histories in cross-ply laminates 147
4.3.5.1 Classified AE histories for cross-ply laminates 147
4.3.5.2 Evaluation of quality of parametric filtering 151

4.4 Static Analysis of Quasi-Isotropic Laminates 153
4.4.1 Mechanical response 153
4.4.2 Overall AE histories 153
4.4.3 AE histories for different waveforms 157

4.5 Fatigue Analysis of Quasi-Isotropic Composites 160
4.5.1 Mechanical response 160
4.5.2 Overall AE histories 162
4.5.3 Elimination of the AE from internal friction 164
4.5.4 AE histories for different waveforms 171

4.6 AE Analysis of Joints 174
4.6.1 Experimental 174
4.6.2 Static behavior 176

4.6.3 Fatigue behavior 181
4.6.3.1 Filtering out internal frictional noise 181
4.6.3.2 Overall AE histories 182
4.6.3.3 Crack tip location monitoring 184
4.7 Summary 185
4.8 References 187

Appendix 4 reports analysis of evolution of microdamage and fracture in advanced composites and joints. A new method of acoustic emission (AE) analysis of histories of different damage mechanisms was formulated based on a combination of transient AE classification and multiparameter filtering. The capabilities of the method were illustrated on examples of damage evolution in several graphite/epoxy composites. Three characteristic AE waveforms with different frequency spectra were identified based on the transient analysis. Regions occupied by these waveforms in the amplitude-risetime parametric space were identified for the $[0]_8$ and $[90]_{16}$ unidirectional composites. Multiparameter filtering was applied to extract evolution histories for the characteristic waveforms. The results were compared with actual damage in the specimens and the three characteristic AE waveforms were associated with matrix cracks, fiber breaks, and 'macrodamage', such as delaminations or longitudinal splitting in unidirectional plies. The multiparameter filters based on the analysis of the unidirectional composites were used to extract the damage evolution histories for the cross-ply $[0/90]_{3S}$ and angle-ply $[+-45]_{4S}$ composites. The results compared favorably with the observed damage in these materials. An inverse analysis of the quality of the multiparameter filtering for the laminated composites indicated that the filters developed for unidirectional composites can be applied to the analysis of laminated composites with reasonable reliability. The new method of acoustic emission analysis of damage micromechanisms is expected to be especially advantageous for fatigue damage evolution studies in composites and structures. The method was further applied to two quasi-isotropic laminates subjected to static and fatigue loads. AE analysis of joints is also reported

4.1 Introduction

4.1.1 Damage in composites

Homogeneous engineering materials subjected to loads usually fail as a result of critical crack propagation. Advanced composite materials, in contrast, exhibit gradual damage accumulation to failure (Masters and Reifsnider, 1980). Damage development in composites starts early in the loading process due to the inherent inhomogeneity of these materials. Advanced composite materials consist of reinforcing elements, such as fibers, embedded in a matrix. The reinforcing elements are stiff and strong, and often exhibit substantial anisotropy of mechanical properties. The matrix material, on the other hand, is usually soft and isotropic. An external load applied to such a composite results in severely inhomogeneous stress and strain fields (see, for example, Tsai and Hahn, 1980). Early damage starts to develop in the microvolumes of the composite in which the localized stress has reached the strength or fracture limit of a particular constituent or an interface between the constituents. The resulting crack sizes correlate with the sizes of material inhomogeneities responsible for the stress inhomogeneity. The microcracks that develop are usually too small to cause final failure of the composite. A substantial number of these microcracks accumulate in the composite before failure.

If not for the inherent randomness of composite microstructure and properties, the microcracks of a particular type would all occur in the repeating volumes of the material at the same load. However, the microstructure of composites is random at the microscale (Gunyaev, 1985). Parameters, such as volume fraction and orientation of fibers, ply thickness, and localized fiber spacing and packing often exhibit wide statistical variations, when evaluated at the microscale.

Therefore, some localized microvolumes in composite are always stressed more than others. The stress inhomogeneity is further enhanced by the inhomogeneity of the elastic properties of the composite constituents. The inhomogeneity of the stress field, coupled with the inhomogeneity of the strength and fracture properties of the reinforcing elements, the matrix, and the interface, lead to the gradual damage development in composites. As a result, the overall failure process in composites is often viewed as a process of formation, accumulation, and coalescence of damages of different types.

Many damage micromechanisms are observed in composites. For advanced fiber-reinforced composite laminates, most typical damage mechanisms are matrix cracks, fiber breaks, and delaminations. The characteristic size of matrix cracks and fiber breaks is small. The characteristic size of delaminations is larger than that of the matrix cracks and the fiber breaks. As a result, the delamination damage is sometimes referred to as 'macrodamage'. However, even the delamination 'macrocracks' are typically small in size compared to the structural level damage. In this work, the word 'macrodamage' will be used in a relative sense, in order to distinguish damage mechanisms that have characteristic sizes larger than those for typical matrix and fiber damage.

Studies of mechanisms and histories of damage in composites are necessary for better understanding of their ultimate failure and life. Theoretical analysis of damage evolution in composites has been performed by many authors. A continuum damage mechanics approach was applied, for example, by Allen *et al.* (1987); Ladeveze *et al.* (1993); and Reifsnider *et al.* (1995). Elaborate analyses were conducted to evaluate the effects of damage on stiffness characteristics. The stochastic nature of gradual damage accumulation in composites was explicitly taken into account in statistical models of damage accumulation in composites developed, for example, by

Rosen (1964), Zweben (1968), Tamuzh (1979), Harlow and Phoenix (1979), Batdorf (1982), Ovchinskii (1988), Phoenix (1993), Curtin (1993), Dzenis *et al.* (1993, 1994), and Dzenis and Joshi (1997). The models predicted gradual damage accumulation of different types under various loads. Development and verification of theoretical models of damage evolution in composites require experimental studies of damage development in these materials.

Experimental analysis of damage evolution in composites is not easy, however. A number of nondestructive evaluation (NDE) techniques were applied for this purpose. These included thermography, eddy current, optical holography, radiography, X-ray tomography, and ultrasonic resonance, pulse-echo, and through-transmission techniques (see, for example, Pipes, 1979; Summerscales, 1987; and Masters, 1992). The majority of these methods were capable of detecting larger individual flaws and delaminations in composites. However, the characteristic sizes of the matrix cracks, fiber breaks, fiber-matrix disbonds, and ply-damage induced delaminations were usually too small for these defects to be detected by the conventional NDE techniques. High resolution, multiparametric ultrasonic scanning was applied to detect cumulative microscopic damage and fiber-matrix disbonds in composites (Knollman, 1980; Knollman and Yee, 1988; Hu, 1996). This method has a potential for morphological analysis of spatial distributions of damage in laminates. However, the real-time analysis of damage evolution cannot be performed by this method, at present. High resolution imaging requires research quality ultrasonic instruments (such as acoustic microscopes) performing high frequency scanning under well controlled conditions. A specimen has to be unloaded, removed from the testing machine, and scanned in a water tank. The scan time varies from tens of seconds to minutes. Because of the large scan time, even the on-line versions of this technique that allow direct scanning of a loaded specimen utilizing water squirters or laser-generated ultrasound, cannot be used for the real-time damage monitoring under loading.

An acousto-ultrasonic (AU) analysis was shown capable of detecting diffuse microcrack populations in composites (Vary, 1982 and 1993; Duke, 1988; Lorenzo and Hahn, 1988). Unlike ultrasonic scanning where a focused high frequency ultrasonic wave propagates through the thickness of a specimen, in the AU method, a wave of lower frequency (usually, hundreds of kHz) propagates in the specimen plane. Changes in the waveshape due to the wave interaction with accumulated damage are analyzed. A number of parameters describing the waveshape can be extracted and serve as measures of cumulative damage. It was shown that a parameter, called the stress wave factor (SWF), can be correlated to the residual strength of composites. A possibility of continuous evaluation of damage by AU was demonstrated by Tiwari and Henneke (1993) and Tiwari *et al.* (1995). As the ultrasonic wave velocity in solids is high, the time of a single AU measurement is small (usually, in the millisecond range). Therefore, in general, the behavior of composites under loading can be studied in real time. However, small damage increments will hardly be discernible by this method. Also, the interpretation of AU data and extraction of information on the type and relative content of damage by this method is difficult.

4.1.2 Acoustic emission analysis of damage mechanisms

A method that was shown capable of real time damage monitoring in composites is acoustic emission (AE) analysis (see, for example, Yamaguchi, 1991). In this method, ultrasonic waves generated by the rapid release of elastic strain energy during damage events are detected and analyzed.

Two approaches to acoustic emission analysis were developed: parametric AE analysis and transient AE analysis. The bulk of the research on damage development in materials to date

was performed by the parametric method. This method is based on the extraction of a number of parameters from individual AE signals. A typical AE signal is shown in Figure 1. Some of the AE parameters are defined in this Figure, including signal amplitude, duration, rise time, decay time, and AE counts. Other parameters can be defined, for example average frequency, energy, etc. Flags related to the signal shape, such as a multipeak flag, can also be defined.

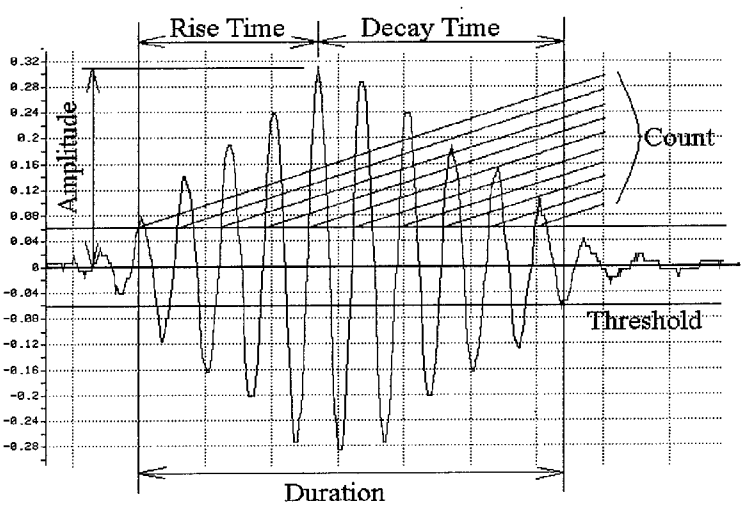

Figure 1: Typical acoustic emission signal

Most acoustic emission systems operate in the parametric mode as follows. An ultrasonic wave caused by the damage event is detected by a piezoelectric AE sensor. The sensor converts the mechanical vibration into an analog signal. The signal is amplified by a preamplifier and digitized by the AE system. The system electronically extracts a number of parameters for each acoustic emission event. These AE parameters along with some additional information, such as time of arrival, and some external parameters, such as current load, are recorded into a parametric AE file. The AE signal itself is discarded in the parametric AE analysis. An advantage of the para-

metric analysis method is its simplicity. Modern AE systems provide powerful analysis and filtering capabilities for the AE parameters. AE histories, statistical distributions, and correlations can be generated and studied. Cluster analysis can be performed. AE location information can be extracted from the data from two or more sensors.

Parametric AE analysis was used to evaluate overall damage accumulation in composites by Williams and Reifsnider (1974), Awerbuch and Ghaffari (1988), Bakuckas *et al.* (1994), Ely and Hill (1995), Luo *et al.* (1995) and Shiwa *et al.* (1996). Williams and Reifsnider (1974) showed that the AE rate generally correlated with the rate of stiffness reduction due to damage. Numerous attempts to identify sources of the AE signals in composites were made. Different damage mechanisms were expected to produce AE signals with different AE parameters. Energy discrimination was used, for example, by Wevers *et al.* (1991). However, the attempts to apply single parameter filtering (single AE parameter threshold) to separate the damage mechanisms were largely unsuccessful due to overlap of the parametric ranges for different damage mechanisms (Kouvarakos and Hill, 1996). This parametric overlap is caused by the complexity and randomness of the damage process in composites. As mentioned above, similar microcracks do not occur simultaneously in all the similar microvolumes of the composite because the local microstructure and stress exhibit considerable variations. Similarly, the waves created by the microcracks of the same type are not necessarily the same. Variations in the crack location and orientation and complexity of the wave propagation process in composites (Chang and Sun, 1988; Gorman, 1992) further increase AE signal variability. Multiple reflections from internal and external boundaries and the associated mode conversions interfere with the source wave and change the AE parameters detected. All of the above results in statistical distributions of the AE parameters, even for the signals produced by similar microcracks. Depending on the type of damage and the width of these distributions, the AE

from composites can sometimes result in AE parameter distributions exhibiting multiple peaks. Similarly, multiple clusters of signals (dense areas) can sometimes be observed on the AE parameter correlation plots. However, in practice, these multipeak distributions and clusters are observed rarely. Overall, the parametric AE analysis is capable of providing useful information on damage development in composites. However, the discrimination of damage mechanisms by this method is difficult due to the overlap of AE parameters caused by the complex damage and wave propagation processes in composites.

An alternative to parametric analysis is transient AE analysis. In transient analysis, full digitized waveforms of the AE signals are recorded and analyzed. Transient analysis requires additional hardware compared to parametric analysis, i.e. a transient recorder. The type of AE sensors used in the analysis is also important for the transient analysis. Wideband sensors are usually preferred to resonant sensors. These sensors produce less distortion of the shape of the acquired signal. The results of the transient acquisition are recorded by the AE system into a transient AE file. This file typically contains a list of digitized AE signals (wave signatures) in the order they have been received by the system. Modern AE systems provide powerful advanced signal analysis capabilities. Wave frequency spectra can be calculated and analyzed. Additional AE parameters can be extracted, for example peak frequency, spectral moments, etc. Custom defined parameters can be calculated.

Transient analysis is a relatively new approach for damage analysis in composites. Recently, Ono and Huang (1996), Prosser *et al.* (1995), Kloua *et al.* (1995), and Groot *et al.* (1995) applied the transient waveform analysis for AE source recognition. Methods of pattern recognition analysis and neural networks were used for the AE signal classifications. It was

shown that the characteristic signal shapes can be present in the overall AE from composites. These waveshapes can be associated with particular damage mechanisms. These recent results showed that the transient AE analysis method may provide more powerful and robust capability to discriminate between the damage mechanisms based on the full waveform analysis. A disadvantage of this method for the damage analysis in composites is the large amount of data that has to be acquired and analyzed. Composite materials typically accumulate a large number of microcracks of different types. This is especially true for the long-term loads such as fatigue. The acquisition, storage, and analysis of full waveforms for all these signals is either impossible or impractical. In addition, the automated signal classification is not an easy task. It requires thorough understanding of classification algorithms used and should generally be performed by experienced personnel.

Thus, the parametric and transient methods of AE analysis have advantages and disadvantages in regard to damage evolution studies in composites. Modern AE systems can provide both transient and parametric analysis capabilities. Such systems perform transient and parametric data acquisition simultaneously. The results are recorded in two data files, the parametric AE file and the transient AE file. Some systems have a capability to relate the transient records to the parametric records, thus providing means for simultaneous transient-parametric analysis. Such an analysis could theoretically combine the power of transient classification and the simplicity of parametric filtering. It would seem especially advantageous for composite damage evolution studies.

Such a hybrid transient-parametric method to separate overall AE histories into the histories for different damage micromechanisms was developed in this research. The method is based

on the combination of the transient AE waveform analysis and multiparameter filtering. The method is applied for static damage evolution analysis in six progressively more complicated composites, i.e. unidirectional composites, $[0]_8$ and $[90]_{16}$, cross-ply composite $[0/90]_{3S}$, angle-ply composite $[+-45]_{4S}$ and two quasi-isotropic laminates, $[90/+-30]_{3S}$ and $[0/+-45/90]_{2S}$.

Fatigue damage evolution analysis was performed on two quasi-isotropic composites. A new method to eliminate frictional signals from the crack face fretting under fatigue was developed and applied. The hybrid transient-paametric method of mechanism extraction was applied afterwards. The method of frictional signal elimination was also used on composite joints. It allowed to substantially improve the accuracy of the crack tip location evaluation.

4.2 Experimental

4.2.1 Materials and manufacturing

Composite materials were manufactured from Hexcel T2G-190-12-F263 graphite-epoxy unidirectional prepreg tape. Laminated panels were assembled following hand lay-up procedure and cured in a two-chamber press-clave under controlled temperature, pressure, and vacuum environments. The manufacturer recommended curing cycle was applied. Six composite lay-ups were used in this study: two unidirectional composites, $[0]_8$ and $[90]_{16}$, a cross-ply composite $[0/90]_{3S}$, an angle-ply composite $[+-45]_{4S}$, and two quasi-isotropic laminates, $[90/+-30]_{3S}$ and $[0/+-45/90]_{2S}$. The cured panels were tabbed using strips of a commercial glass fiber woven composite. The tabbing prevented premature failure of composites and reduced acoustic noise from grips.

Rectangular composite specimens were then machined from the tabbed panels by a high-speed diamond saw. The specimen length was in the range from 200 to 250 mm. The specimen width was 25 mm for the $[90]_{16}$ composite, 20 mm for the $[+-45]_{4S}$ composite, and 15 mm for the $[0]_8$ and $[0/90]_{3S}$ composites. The specimen thickness was determined by the lay-up and varied from 1.48 mm for the unidirectional $[0]_8$ composite to 2.86 mm for the angle-ply composite.

4.2.2 Mechanical testing

Tensile mechanical testing was performed by a servohydraulic MTS testing machine digitally controlled with an Instron test control and data acquisition system (Figure 2). All quasi-static tests were performed under stroke control with Instron 8500 software. The displacement rates used were 0.5 mm/min for the $[0]_8$ composite, 0.1 mm/min for the $[90]_{16}$ composite, and 0.3 mm/min for the laminated composites. A uniaxial MTS 632 extensometer and a biaxial Instron 2620 extensometer were used for strain measurement (Figure 3). The axial gauge length was 25 mm. The specimens were clamped with serrated wedge action grips. Special care was taken of specimen installation in grips to ensure alignment. Additional alignment was provided by a Satec spherical alignment coupling.

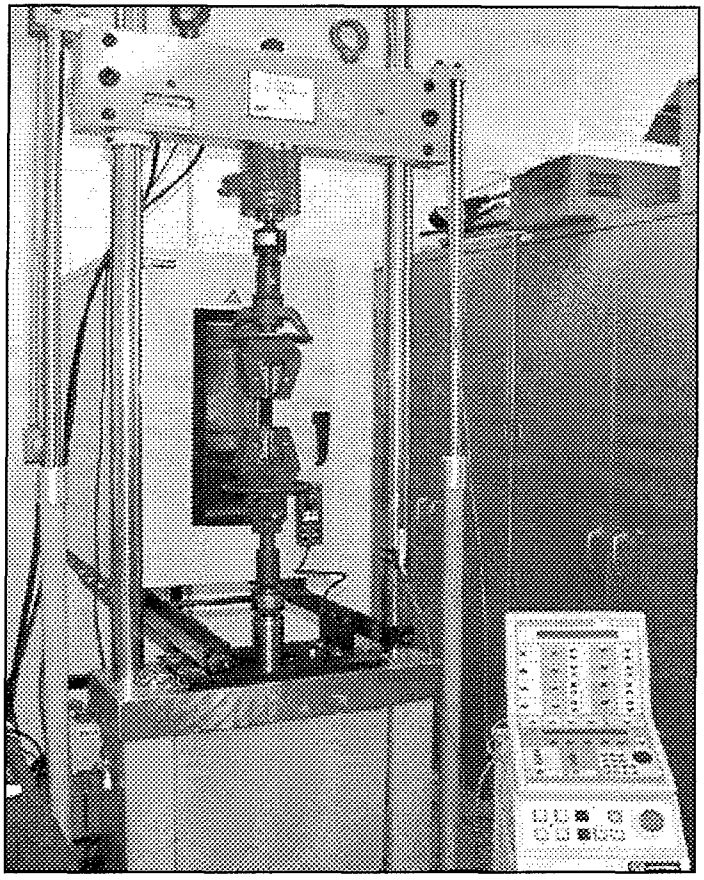

Figure 2: Mechanical testing setup

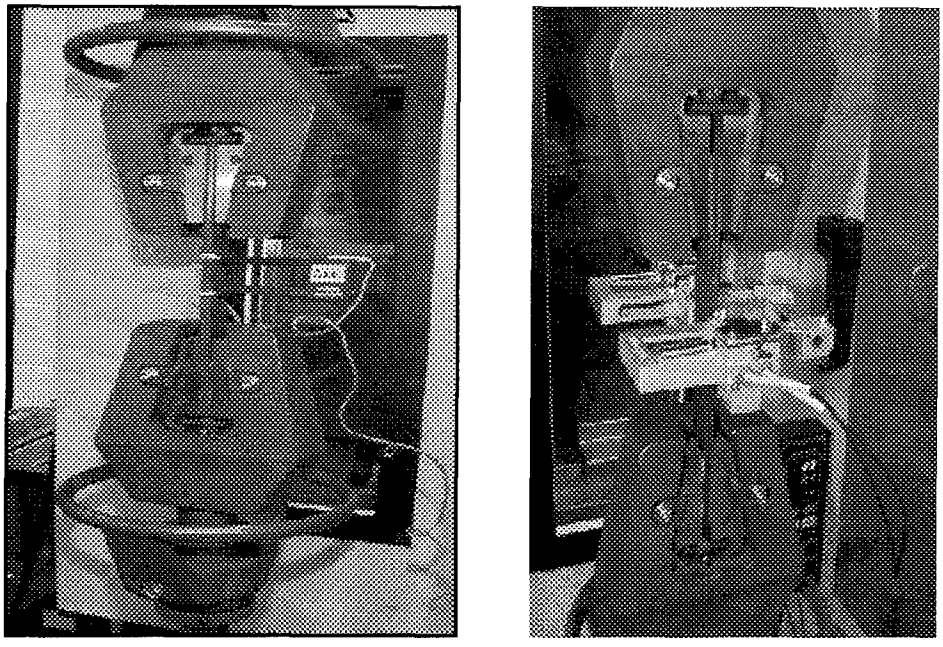

Figure 3: Axial and biaxial extensometer assemblies

4.2.3 Acoustic Emission Testing

A two-channel AMS3 acoustic emission system by Vallen Systeme, GmbH was used for acoustic emission analysis (Figure 4). Each AE channel was connected to a preamplifier attached to an AE sensor. AE events were acquired by the sensor as analog signals. They were preamplified and converted into digital signals by an A/D converter. The AE signal parameters were then extracted by the system, augmented with time of arrival and external parameters (load and strain), and recorded in a parametric AE file. The system was equipped with a transient recorder. In parallel with the AE parameter acquisition, full digitized waveforms of the AE events were acquired by the transient recorder and recorded in a separate transient AE file. Each AE waveform was assigned a unique transient index. This index was stored as one of the parameters in the paramet-

ric AE record, providing the capability to establish the correspondence between the waveforms and the parametric records in the two files.

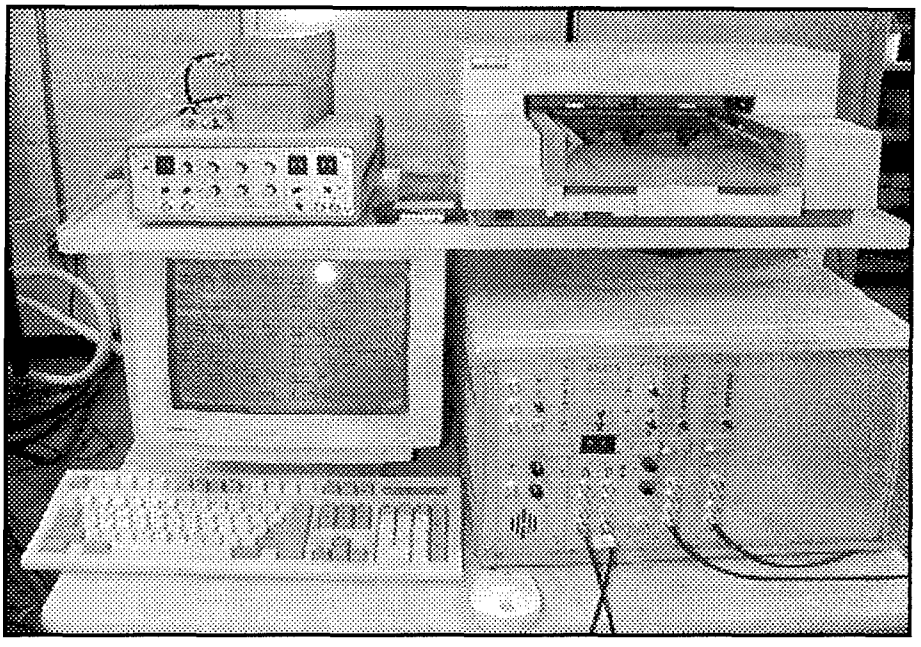

Figure 4: Acoustic emission system

Two wide-band, high fidelity B1025 AE sensors by Digital Wave were used in the analysis (Figure 5). The sensors were mounted on the specimen by means of tape. Vaseline was used as a coupling agent between the sensor and the composite surface. The effect of sensor attachment force was investigated using an ultrasonic pulser. An imitation AE signal was generated by the pulser, transmitted from one sensor to another, and analyzed by the AMS3 system. It was found that the variation of parameters of the transmitted signals saturated at the attachment force about 10N. The 10N force was used in all AE experiments.

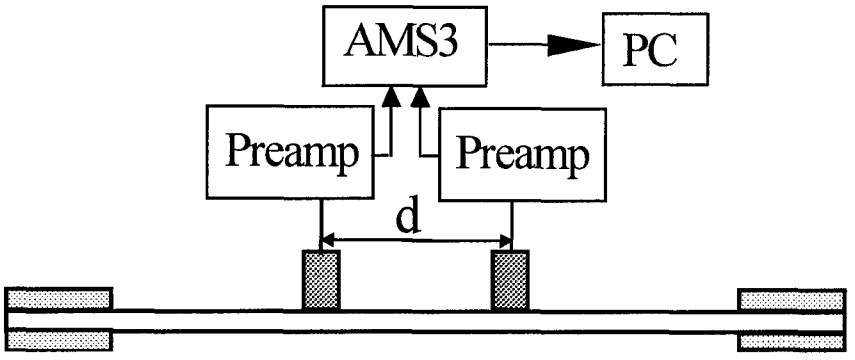

Figure 5: Schematic of AE testing

The acoustic emission gauge zone (the distance between the AE sensors) was 60 mm for the $[90]_{16}$ composite and 80 mm for all other composites. The AE source location analysis was performed on the incoming signals and the signals originating outside the acoustic gage zone were filtered out in order to reduce the acoustic noise generated by the testing machine and grips.

A 34.5 dB system gain and a 40.5 dB threshold were used for the AE acquisition. The AE data acquisition was initiated simultaneously with mechanical loading. The acoustic emission was thus recorded from the beginning of the test to the final failure of the specimen. The information on load and strain was continuously fed from the Instron 8500 system to the AMS3 system. This information was stored in the parametric AE record and allowed to correlate the AE parameters with the load and strain at the time the AE signal was produced.

As a result of each test, two data files were generated for each specimen, the parametric file and the transient file. The former contained a list of parametric data records. The latter contained a list of digitized waveforms. The AMS3 software provided powerful filtering and waveform analysis capabilities that were used for AE data analysis after the tests were completed.

4.3 Static Analysis of Unidirectional and Cross-Ply Composites Composites

4.3.1 Mechanical response

Several specimens of each type were tested in tension. Both biaxial and uniaxial extensometers were used. Quasi-static response of the representative composite specimens are shown in Figures 6 and 7.

Figure 6 shows the stress-strain diagrams of the unidirectional $[0]_8$ and $[90]_{16}$ composites. Both tests were performed with the biaxial extensometer. The positive strain branches of the stress-strain diagrams in Figure 6 correspond to the longitudinal tensile strain. The negative strain branches correspond to the Poisson contraction in the transverse to load direction. The stress-strain diagrams of the unidirectional composites were almost linear. A slight nonlinearity (stiffening) observed in Figure 6a is typical for unidirectional graphite fiber reinforced composites and is due to the nonlinear fiber response. A slight non-linearity (softening) in Figure 6b may be due to damage accumulation. The elastic constants and the ultimate properties of the unidirectional specimens, extracted from the diagrams, are shown in the Figure 6.

Figure 7 presents the stress-strain diagrams for the laminated composite specimens. The angle-ply composite (Figure 7a) exhibited strong nonlinearity. The reverse of the stress-strain diagram at high loads (the decrease of stress with the increase of strain) is typical for these composites tested under displacement control. The branches of the diagram for the $[+-45]_{4S}$ specimen were almost symmetric due to the fact that both the +45 and the -45 plies were loaded in pure

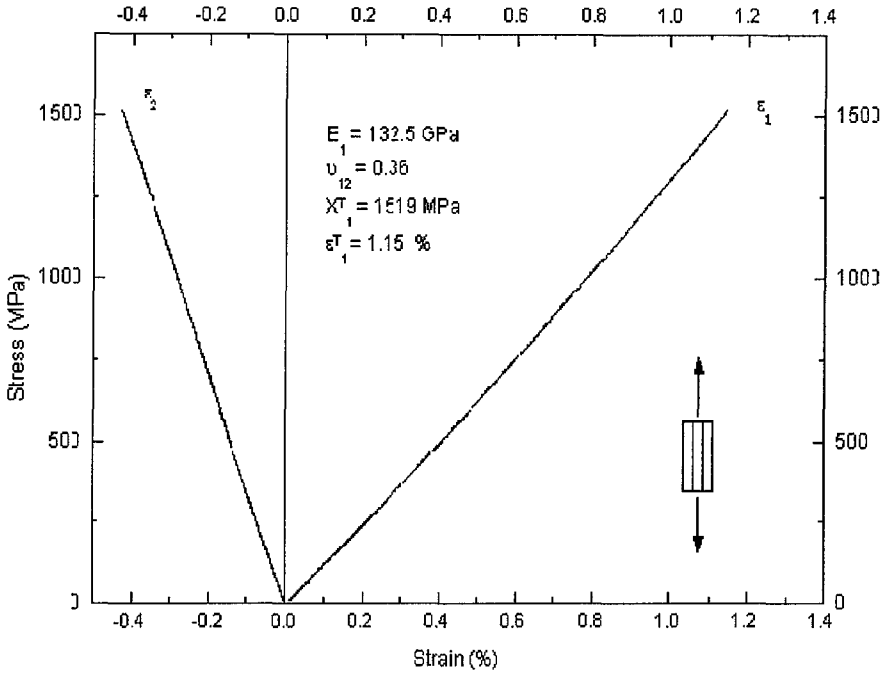

(a)

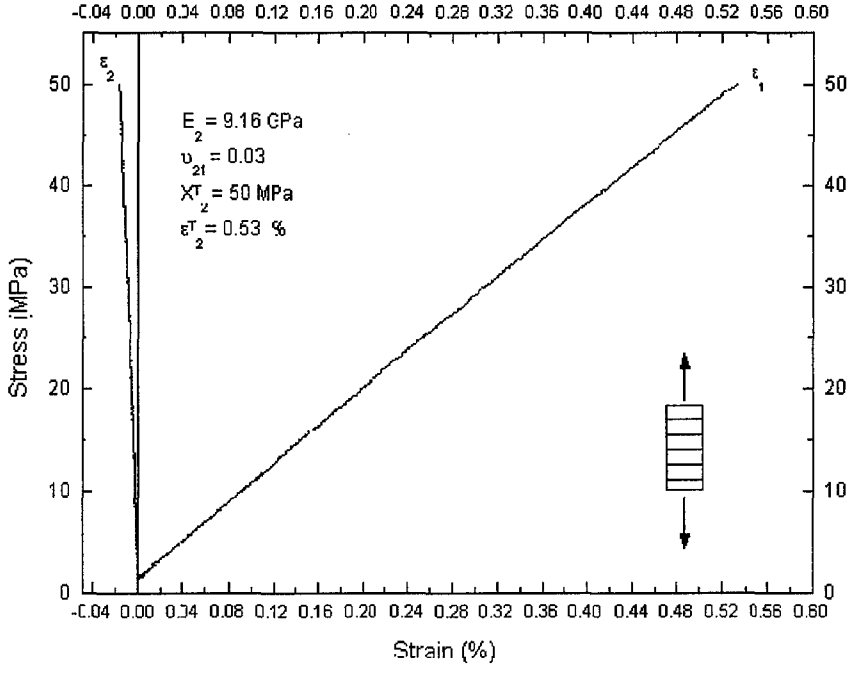

(b)

Figure 6. Quasi-static tensile response of unidirectional composites: $[0]_8$ (a) and $[90]_{16}$ (b)

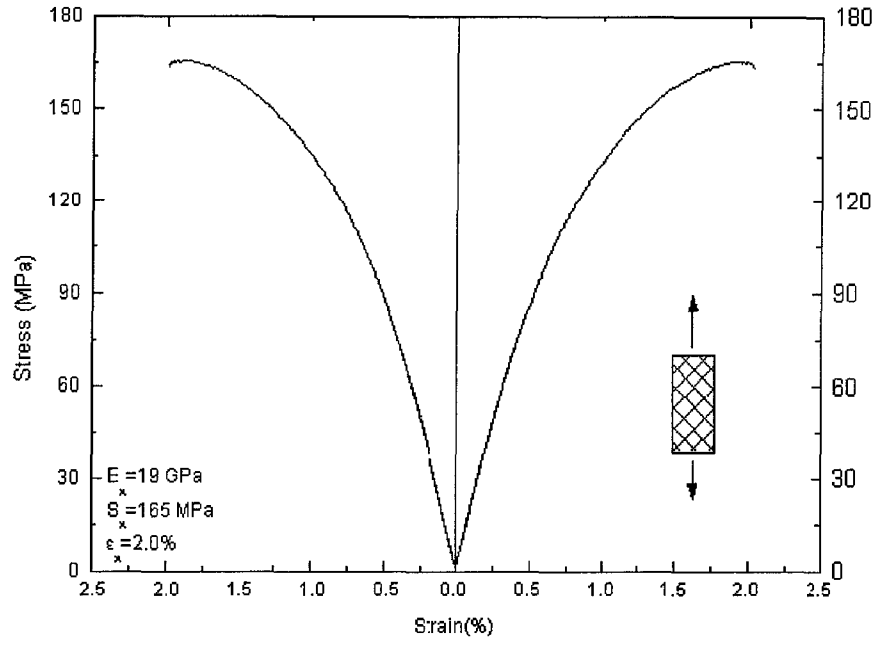

(a)

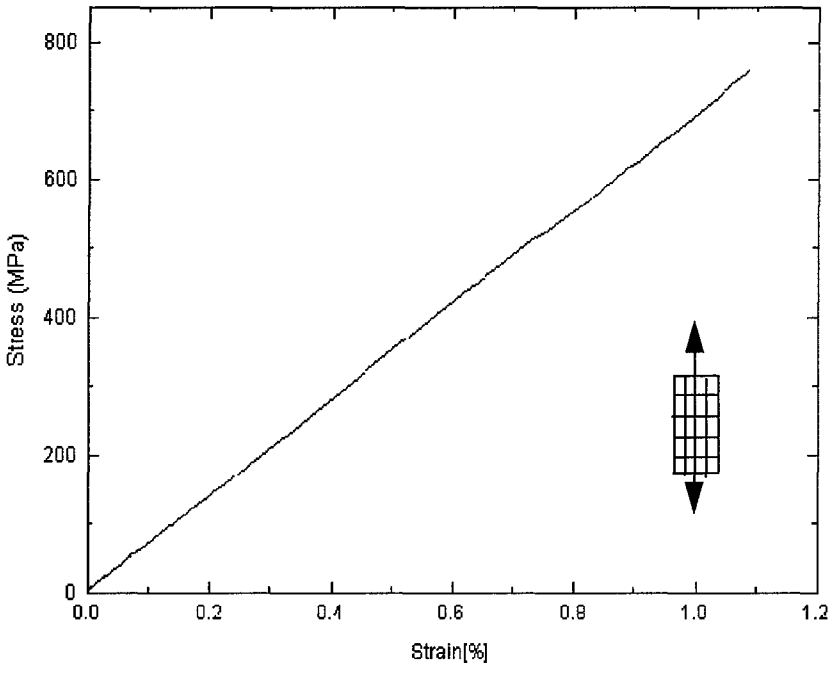

(b)

Figure 7. Quasi-static tensile response of laminated composites: $[+-45]_{4S}$ (a) and $[0/90]_{3S}$ (b)

shear in their respective material axes. Figure 7b presents the axial stress-strain diagram for the cross-ply composite obtained with the uniaxial extensometer. Note that the angle-ply and cross-ply composites represent essentially the same laminated composite material tested in two different directions. Comparisons of Figures 7a and 7b showed strong anisotropy of mechanical properties of this composite. Both strength and stiffness of the cross-ply composite (Figure 7b) were higher than the strength and stiffness of the angle-ply composite. The diagram of the cross-ply composite specimen was almost linear to failure.

Little visible damage was detected in all but the cross-ply composite prior to failure. On-line observations revealed matrix cracking in the 90-degree plies and edge delaminations in the cross-ply composite. Edge delamination in these composites is typical and is caused by the high interlaminar stresses due to the mismatch of the Poisson coefficients of the 0 and 90 plies.

4.3.2 Conventional parametric AE analysis

4.3.2.1 Overall AE histories

Overall stress histories of the AE counts for the two unidirectional composites are shown in Figure 8. In these history plots, the AE counts are presented as a function of tensile stress. The top plots that were marked 1 in Figures 8a and 8b represented the cumulative count histories. The bottom plots that were marked 2 represented the histories of the AE accumulation rates. The AE counts (see Figure 1) provide a convenient measure of the overall AE activity of the specimens.

The acoustic emission in the unidirectional $[0]_8$ specimen (Figure 8a) started at about 40%

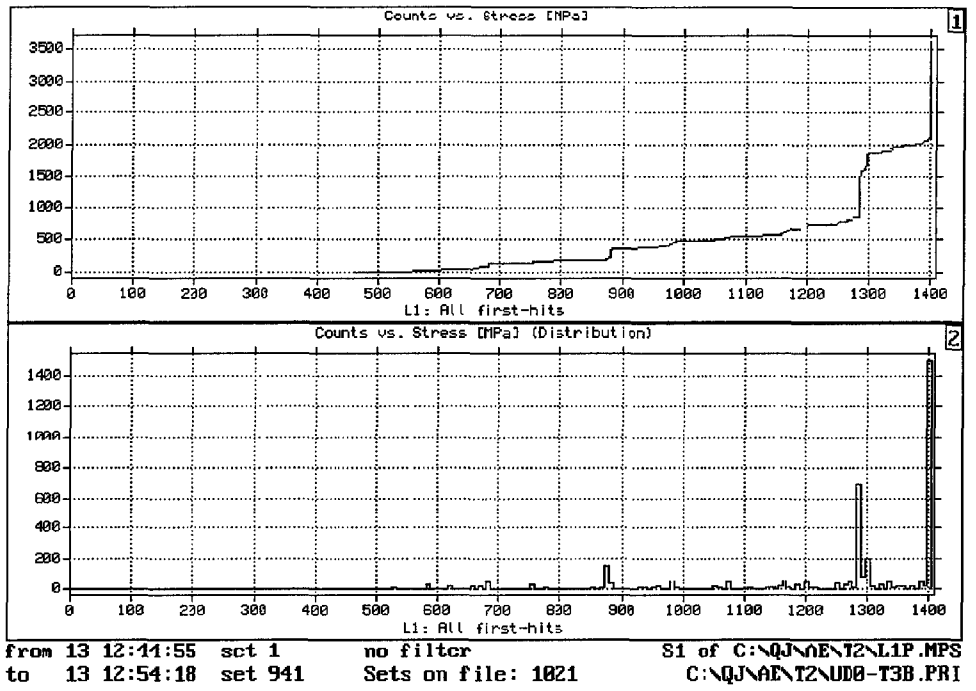

(a)

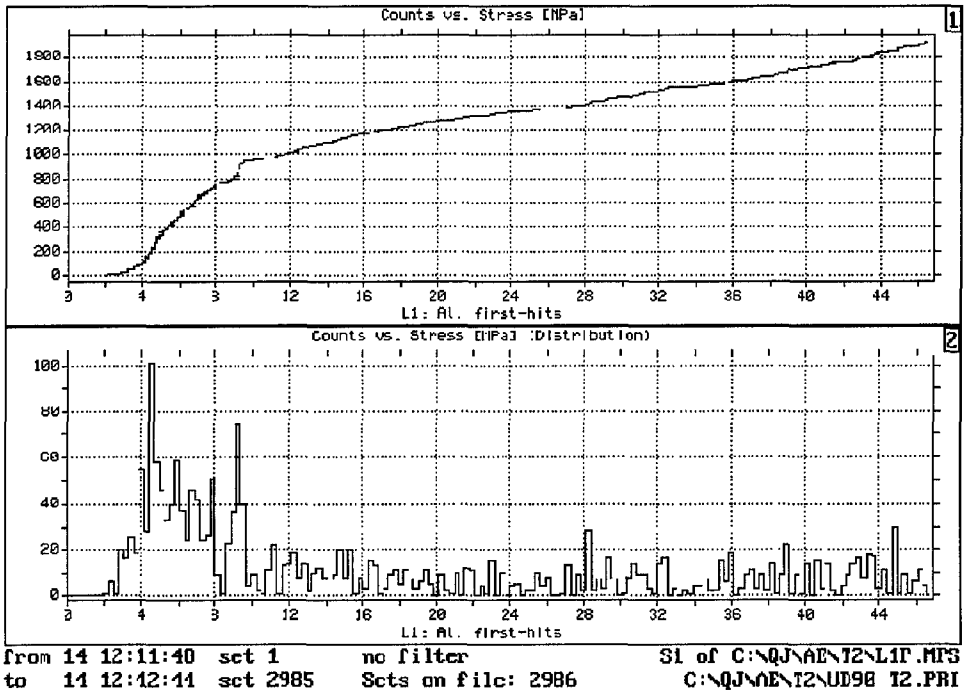

(b)

Figure 8. Overall history of AE in unidirectional composites: $[0]_8$ (a) and $[90]_{16}$ (b)

of the specimen ultimate load and accumulated unevenly to failure with most of the emission generated at higher loads. Two jumps were observed at the stress levels around 900 MPa and 1300 MPa. A final jump was observed near the maximum load. In between these jumps, the AE accumulated with a slowly increasing rate. The unidirectional $[90]_{16}$ specimen (Figure 8b) showed different AE behavior. The AE started to accumulate early in the test, at about 10-15% of the ultimate load. The accumulation rate (plot 2 in Figure 8b) reached the maximum, decreased, and then stayed almost constant to failure.

The laminated composites (Figure 9) produced considerably more acoustic emission indicating more extensive damage development in these materials. In the case of the cross-ply composite (Figure 9a), the emission started at about 50% of the ultimate load. The accumulation rate grew rapidly in the beginning of the damage process and reached the maximum at about 65% of the ultimate load. The damage process then showed signs of saturation with the accumulation rate decreasing monotonically to failure.

Due to the nonlinear stress-strain response of the angle-ply composite, the cumulative history of the AE counts for this material was studied as a function of time (plot 2 in Figure 9b) rather than stress. The stress-time dependence is shown in plot 1 of Figure 9b, for reference. The analysis showed that the AE accumulation in this composite started at about 70% of the maximum load. The accumulation rate increased monotonically to failure. It is interesting that the accumulation rate continued to increase even when the load started to decrease near the failure.

Both laminated composites exhibited more extensive damage due to the more inhomogeneous stress fields in these materials composed of strongly anisotropic plies with different fiber orientations. As a result, smoother cumulative AE histories were observed.

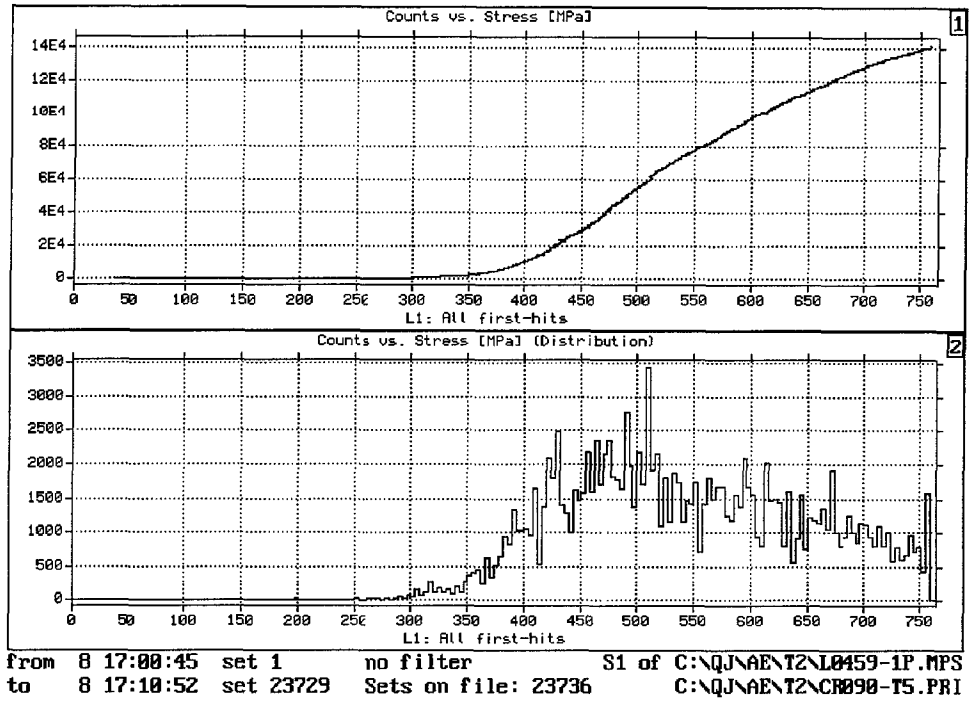

(a)

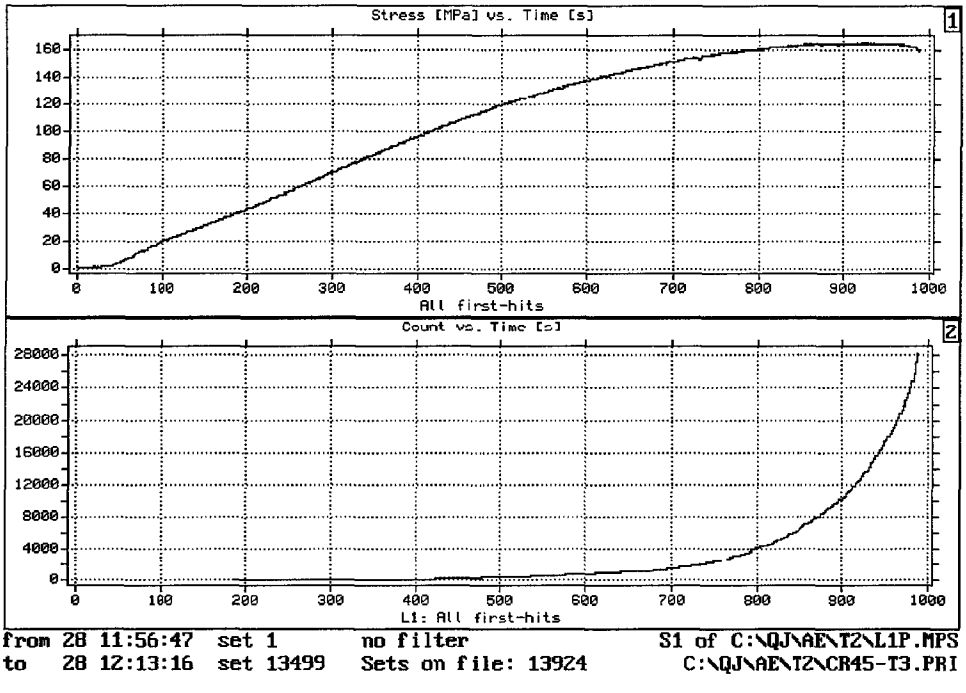

(b)

Figure 9. Overall history of AE in laminated composites: $[0/90]_{3S}$ (a) and $[+-45]_{4S}$ (b)

4.3.2.2 Parametric Distributions and Correlations

Results of the parametric AE analyses are shown in Figures 10 and 11. Each graph contains four plots marked 1 through 4 in their upper right corners. The histogram plots 1-3 represent the statistical distributions of the duration (1), rise time (2), and amplitude (3) of the AE signals acquired during a particular test. The count numbers on the vertical axes in these plots represent the frequency of occurrence of the AE signals with a particular value of the AE parameter shown on the horizontal axis. The correlation plot 4 represents the correlations of the amplitude (vertical axis) and duration (horizontal axis) of the AE signals. In these plots, each dot represents an individual AE event. The parametric scales in all plots in Figures 10 and 11 are kept the same for easier comparisons.

The analysis of the unidirectional specimens (Figure 10) showed that the $[0]_8$ composite (Figure 10a) generally produced signals with higher duration and amplitude, but lower rise time. However, the ranges of variation of the AE parameters were wide for this composite. The analysis of the laminated specimens (Figure 11) was more meaningful because of the larger numbers of signals produced by these composites. The cross-ply specimen (Figure 11a) exhibited duration and amplitude histograms with two peaks. The rise time of the signals from this specimen was widely distributed, however. The correlation plot showed some amplitude-duration correlation for the signals with longer duration. The results of the similar analysis for the angle-ply composite (Figure 11b) showed that this specimen exhibited a weak second peak on the duration histogram but did not exhibit multiple peaks on the amplitude histogram. In addition, the positions of the major peaks in all histograms shifted compared to the corresponding positions of the peaks for the cross-ply composite.

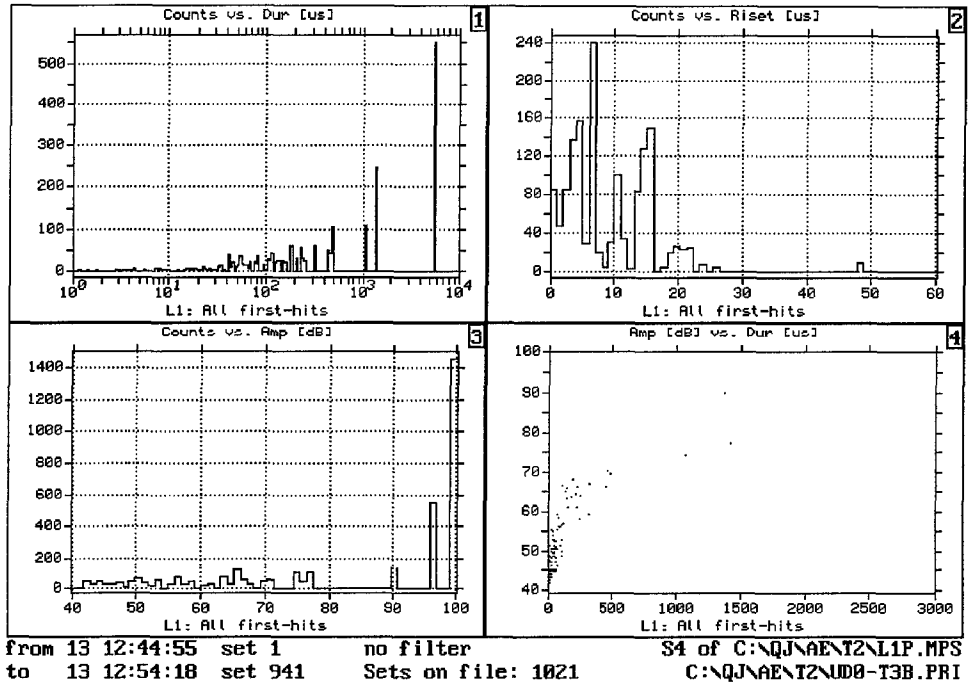

(a)

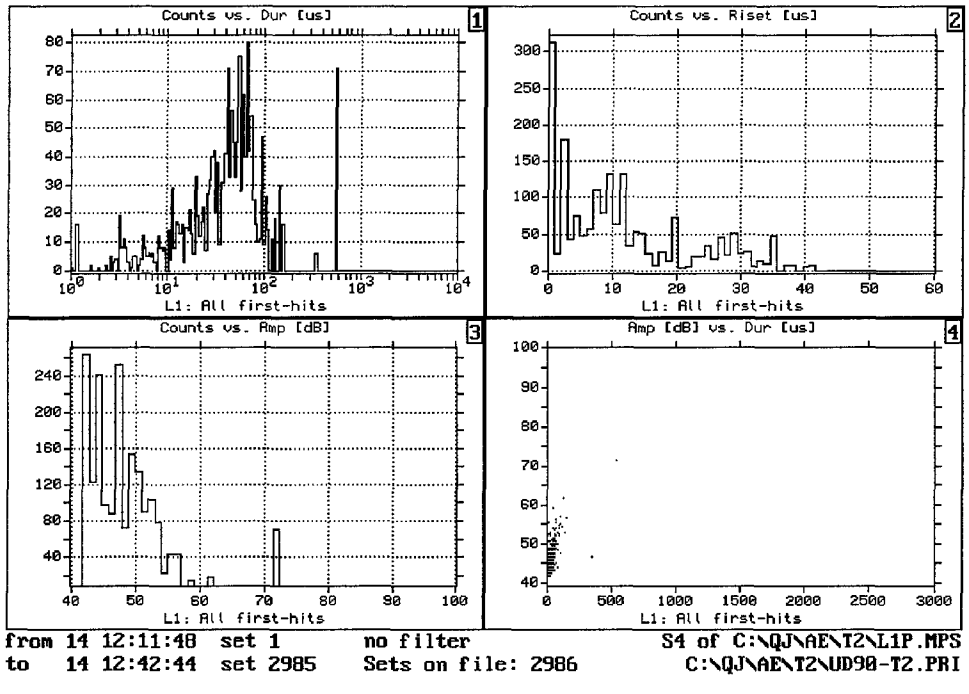

(b)

Figure 10. AE parameter distributions and correlations for unidirectional composites: $[0]_8$ (a) and $[90]_{16}$ (b)

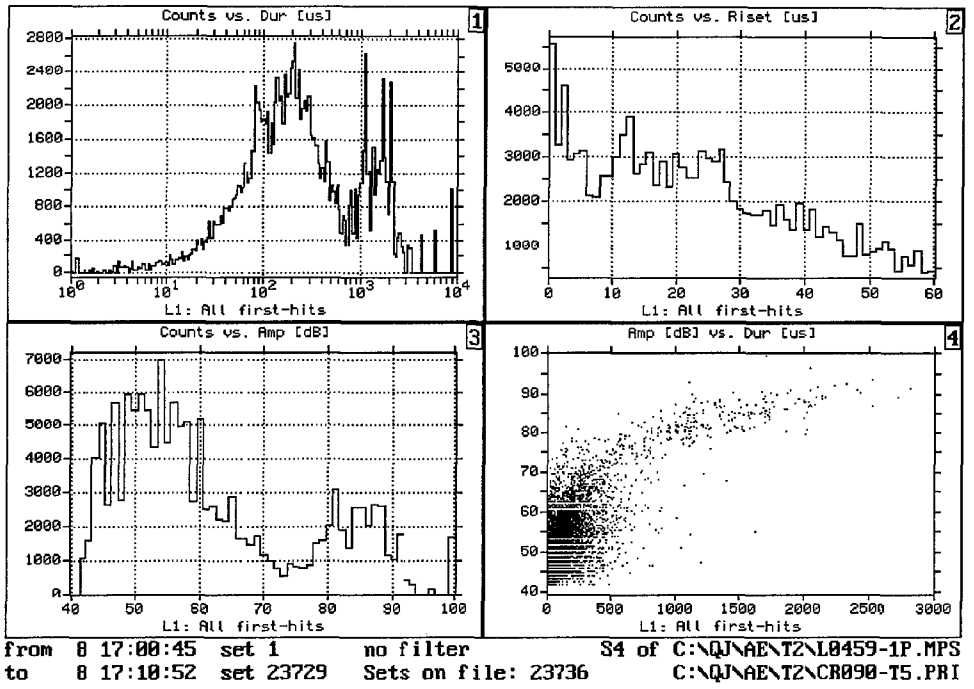

(a)

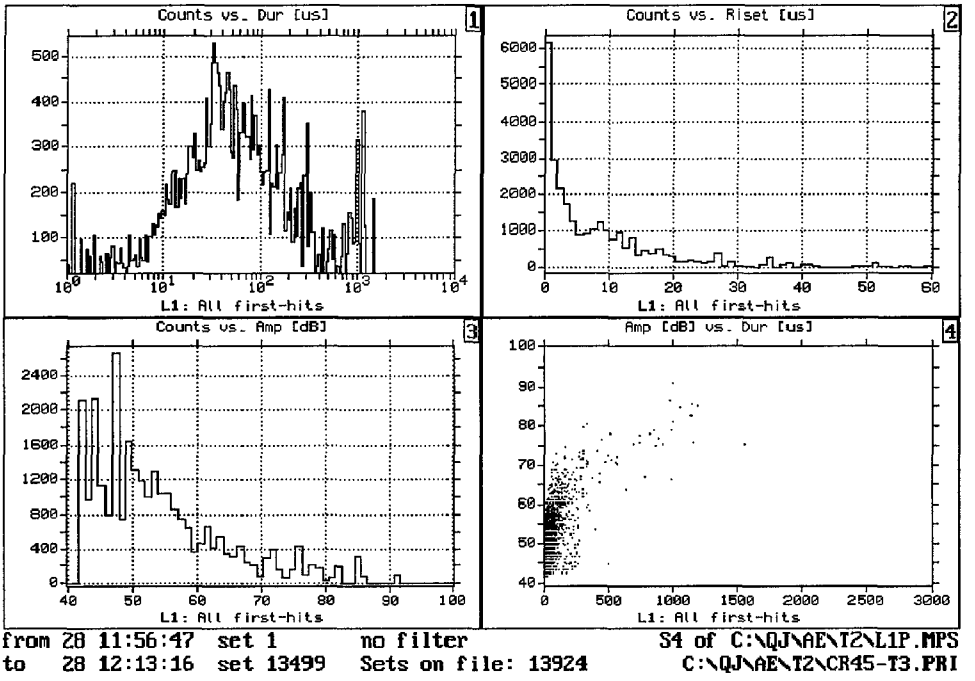

(b)

Figure 11: AE parameter distributions and correlations for laminated composites: $[0/90]_{3S}$ (a) and $[+-45]_{4S}$ (b)

As mentioned above, multiple peaks in the distribution histograms can be caused by signals produced by different damage mechanisms. The two peaks on the duration histogram of the cross-ply composite (Figure 11a) are separated by the threshold duration around 1000 μs. It is interesting that this threshold was used by Qian and Dzenis (1999) to distinguish the characteristic long duration signals in the unidirectional composite. These signals were associated with the 'macroscopic' damage, namely with the longitudinal splitting in the $[0]_8$ composite. To understand the nature of these signals in the cross-ply composite (Figure 7a), a duration filter was applied. The signals with durations above 1000 μs were extracted and the parametric analysis, similar to the analyses in Figures 10 and 11, was performed. The results of this analysis are shown in Figure 12. It is seen that the signals with long duration accounted for the second peaks in both duration and amplitude histograms (compare plots 3 in Figures 11a and 12). However, the rise time of these signals was distributed in a very wide range. The high duration signals were associated with the 'macroscopic' damage in composites by other authors. The fact that 'macroscopic' delaminations were observed in the cross-ply composite corroborated this assumption.

Overall, the parametric AE analysis provided useful information on the damage development in composites. The damage started to develop early in the specimens tested and the accumulation rates increased with loading. One of the composites (the cross-ply composite) exhibited two double-peak parametric histograms. These peaks correlated with each other and could be associated with the 'macroscopic' damage in the form of delaminations. Apart from these two double-peak histograms, all other histograms exhibited wide statistical distributions of the AE parameters with no discernible borders (thresholds) between the signals from different damage modes. The correlation plots did not produce discernible clusters of signals. Other methods are needed to extract the AE from the other damage mechanisms, such as the fiber and matrix cracks.

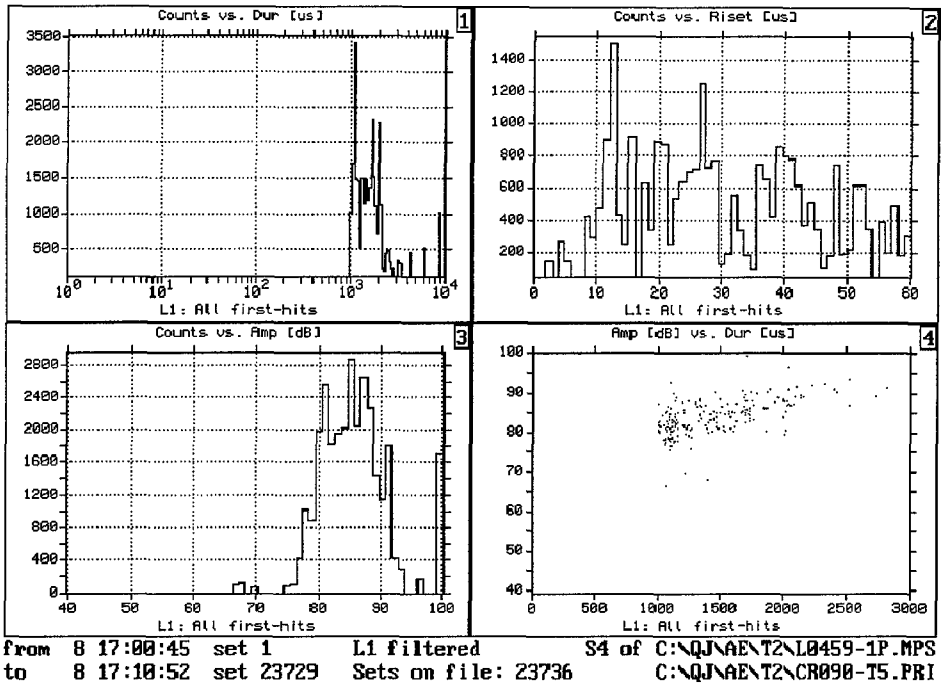

Figure 12. Filtered AE parameter distributions and correlations for $[0/90]_{3S}$ composite

4.3.3 Transient AE analysis

Transient acoustic emission analysis of the signals recorded in the quasi-static tests was performed by the AMS3 system. The frequency spectra of the signals were calculated by the Fast Fourier Transform. The transient AE waveforms along with their FFT spectra were screened in a search for characteristic AE waveforms. The screening revealed that three typical waveforms were produced frequently by composites (Figure 13). Classification was based primarily on the shape of the frequency spectrum. The A type waveforms had low amplitude, medium to long rise time, and the peak frequency between 100 and 220 kHz. The B type waveforms had medium to

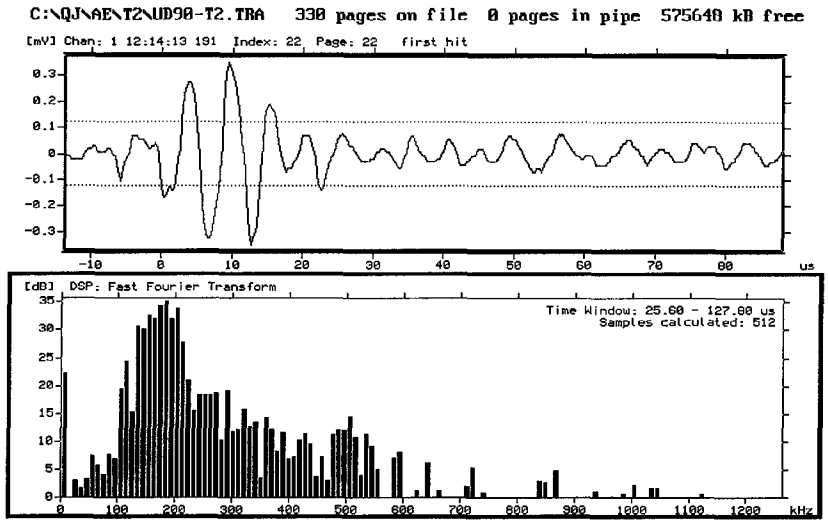

(a)

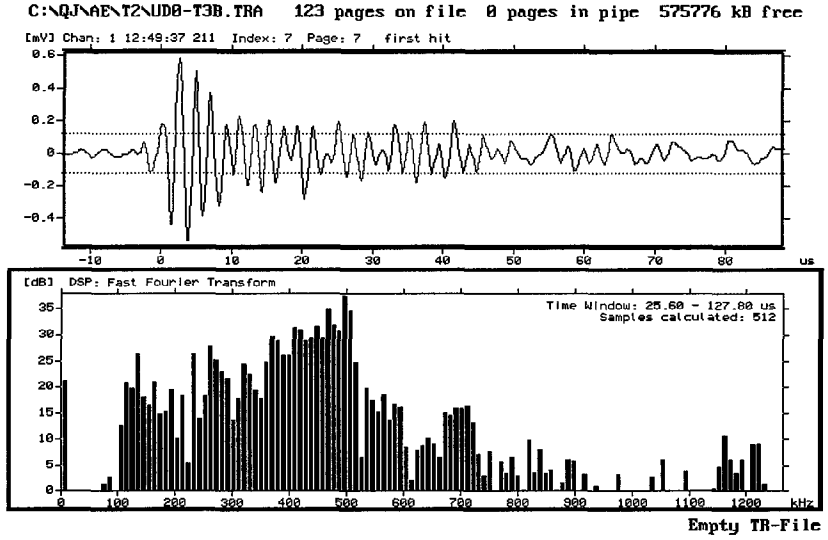

(b)

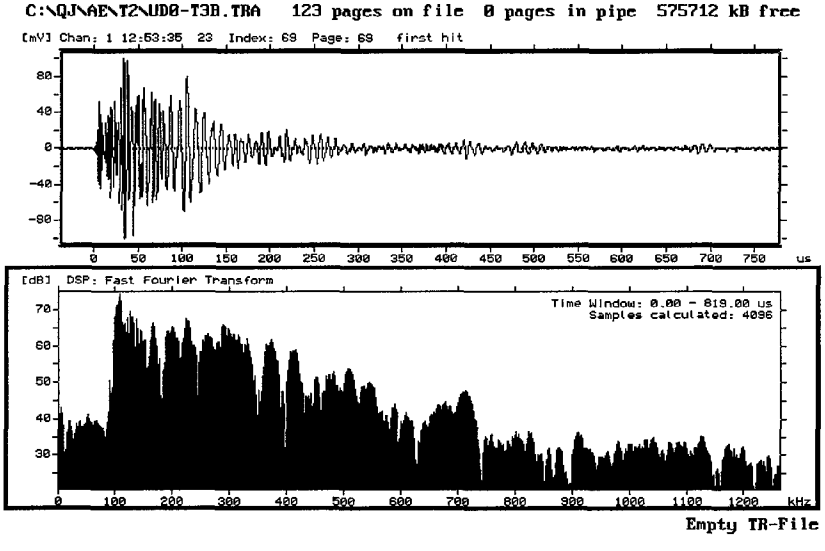

(c)

Figure 13. Characteristic AE waveforms and their frequency spectra: type A (a), B (b), and C (c) signals

high amplitude, shorter rise time, and the peak frequency between 300 and 700 kHz. The C type waveforms had very wide frequency spectrum and very long duration. The shape of the frequency spectrum was more robust and exhibited less variability than the signal parameters. The characteristic waveforms (Figure 13) were first found by the analysis of unidirectional composites (Qian and Dzenis, 1999). The same characteristic waveforms were observed in the laminated composites. The signals of the three types described above accounted for a substantial portion of the overall acoustic emission. However, some signals in the overall AE could not be classified. The latter fact correlated with the diversity and complexity of the damage and wave propagation phenomena in composites.

The histories of the AE with different characteristic waveforms can theoretically be extracted from the transient records. However, the amount of the AE in composites is often too large to make this analysis practical. This is especially true for the damage analysis of composites under fatigue. Application of this methodology to the analysis of unidirectional and laminated composites is described below.

4.3.4 Development of hybrid transient-parametric method to extract microdamage evolution histories in composites (patent pending)

4.3.4.1 Identification of multiparametric regions for characteristic waveforms

The correlation was established between the parametric and transient records by using the transient index as explained above. The analysis of the $[0]_8$ composite showed that the majority of the signals with the duration above 1000 μs belonged to the C type waves. The C type signals

were, therefore, extracted by the duration filtering. However, the signals of the types A and B had overlapping parameters. The analysis showed that no single AE parameter could be used to discriminate these signals.

An attempt was made to find a multiparametric space that would show a separation of the A and B type signals. Several parametric spaces were checked for this purpose. Correlation plots similar to the ones in Figures 10-12 (plots 4) were constructed and analyzed. Using transient index, the locations of the signals with a particular waveform were identified on the correlation plots. The analysis showed that the best separation of the A and B type signals was in the amplitude and rise time space (Figure 14). Figure 14 shows the parametric areas occupied by the signals of these two types on the correlation plots for the unidirectional composites. The horizontal and vertical axes in these plots represent the signal rise time and amplitude, respectively. The same regions were identified for the $[0]_8$ and $[90]_{16}$ composites. For both composites, the marked regions contained the signals of the particular assigned type and some unclassified signals. No signals of the opposite type were observed in these regions. The narrow area between the two marked regions contained the waveforms of both types, as well as other, unclassified signals, and was, therefore excluded. The regions in Figure 14 were used for the parametric analysis of histories of the characteristic AE signals.

4.3.4.2 Classified AE histories for unidirectional composites

The regions in Figure 14 were broken into rectangular boxes and the multiparameter filters. The multiparameter filtering capability of the AMS3 system was then utilized to extract the AE histories for the A and B type waveforms. Note that the C type signals were extracted prior to

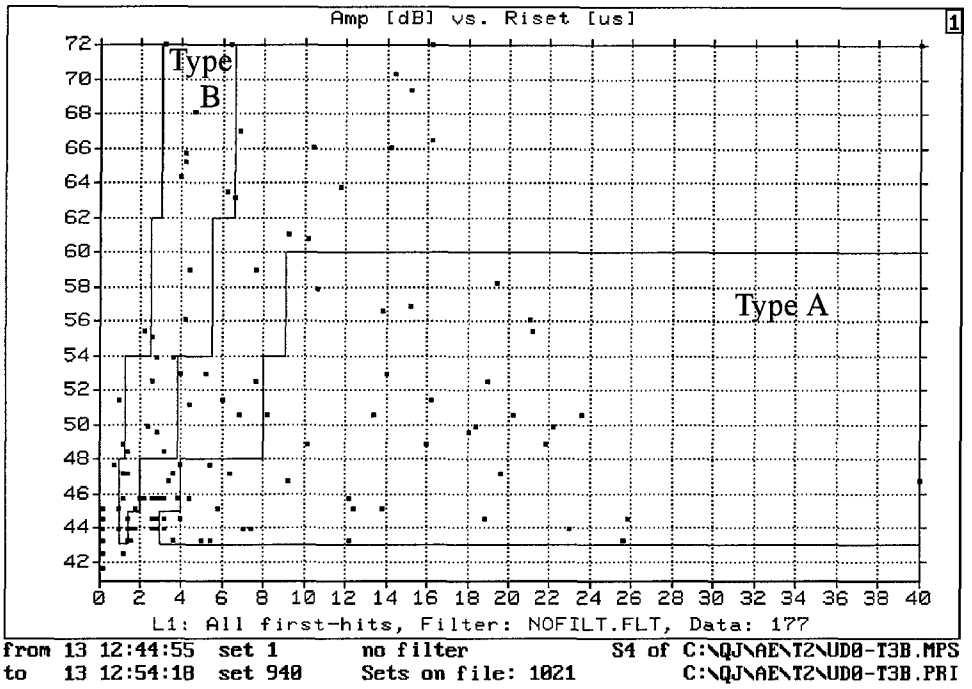

(a)

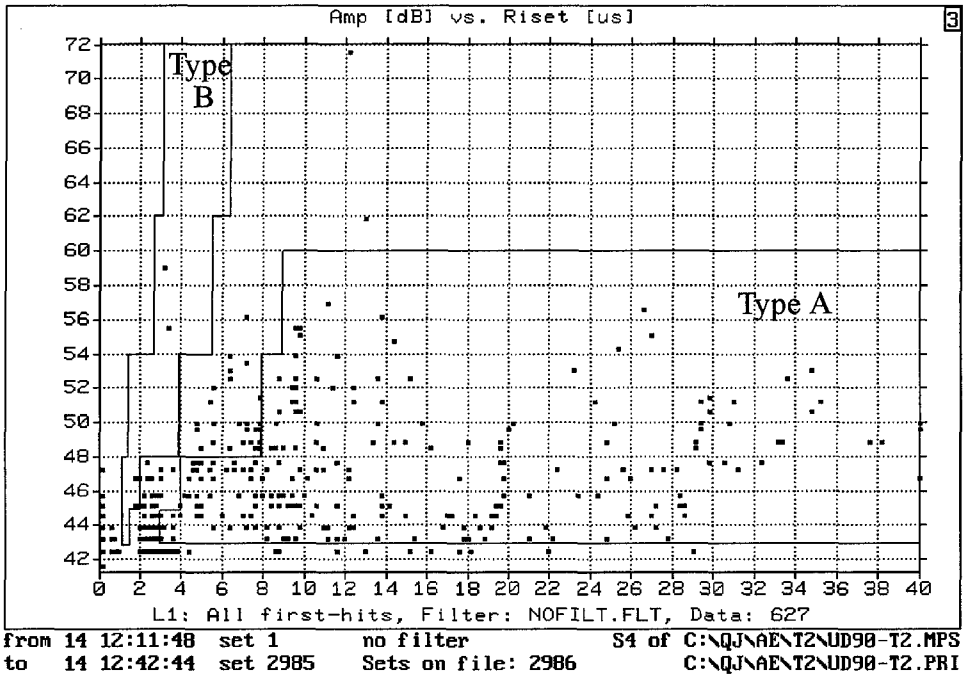

(b)

Figure 14. Amplitude and risetime correlation for unidirectional composites: $[0]_8$ (a) and $[90]_{16}$ (b)

multiparameter filtering by the simple duration filter. The results of this analysis are shown in Figure 15.

Figure 15a presents the classified AE histories for the $[0]_8$ composite. The A type signals initiated first, at a very low stress. The B type signals began to accumulate next, at about 50% of the ultimate stress. The C type signals developed last. They started to accumulate shortly after the beginning of the B type emission. The A and B type signals accumulated relatively uniformly, with several small jumps observed on the B type curve. However, the C type signal accumulation was rather abrupt with several substantial jumps observed at different loads. Comparisons with the overall AE history in Figure 4a showed that the jumps in the overall history were due to the C type signals. Some correlation could be observed between the history plots for the B and C type AE signals.

Figure 15b presents the classified AE histories for the $[90]_{16}$ composite. The A type signals initiated at low stress and dominated throughout this test. A small number of the B type signals were also accumulated. No C type signals were detected in the $[90]_{16}$ specimen.

4.3.4.3 Correlation of characteristic waveforms and damage mechanisms

The ultimate AE content in the unidirectional composites is summarized in Table 1. Note that the sums in the Table are less than 100%. This is because of the fact that signals with parameters falling outside of the marked regions for the A and B type signals in Figure 14 were excluded from the analysis.

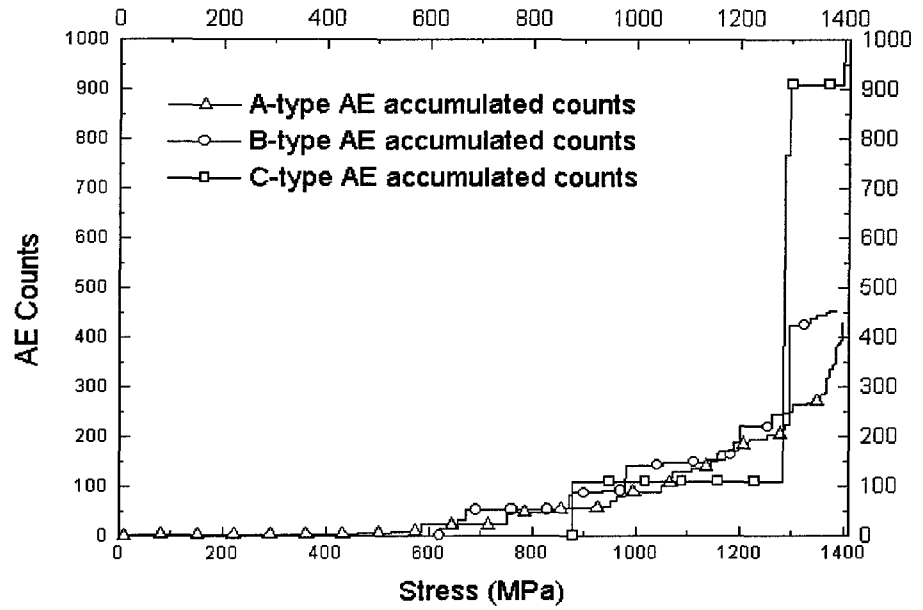

(a)

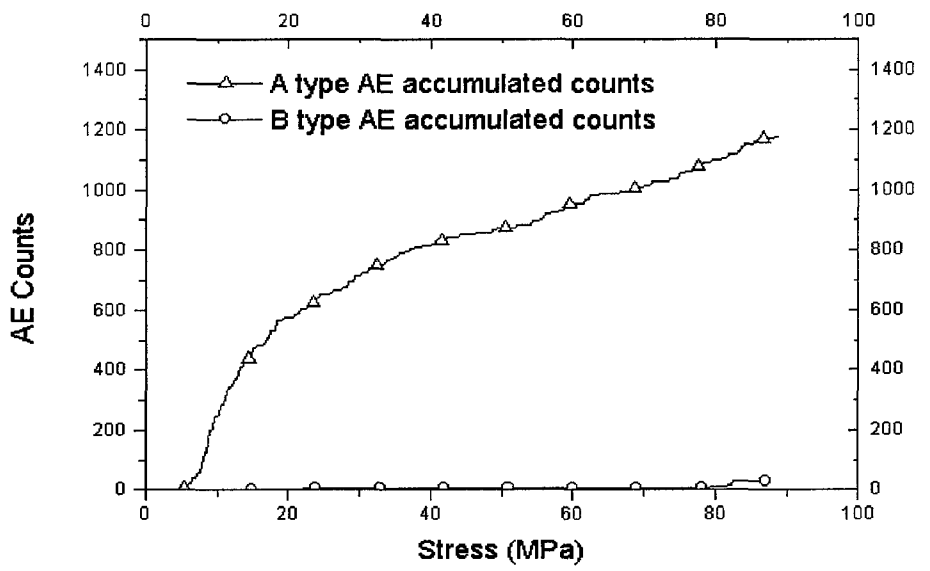

(b)

Figure 15. Classified AE histories for unidirectional composites: $[0]_8$ (a) and $[90]_{16}$ (b)

Table 1: Ultimate AE content for unidirectional composites

Composite	A	B	C
$[0]_8$	20%	22%	48%
$[90]_{16}$	70%	1.4%	None

One expects the failure of the $[90]_{16}$ composite to be dominated by matrix damage with little or no damage of the other types. The $[0]_8$ composite, on the other hand, is expected to develop fiber breaks and matrix cracks. In addition, unidirectional composites loaded in the fiber direction often develop longitudinal splitting cracks along the fiber direction. The photographs of the failed unidirectional specimens analyzed in this work are shown in Figure 16. The photographs corroborate the expected damage modes in these composites described above. Correlations of the observed damage mechanisms in the unidirectional composites with the classified AE histories and the ultimate AE content in these materials (Table 1) showed that the A type AE signals can be attributed to matrix cracking, the B type signals to fiber breaks, and the C type signals to 'macrodamage' in the form of splitting along the fiber direction.

The classified AE histories in Figure 11 show, therefore, that the $[90]_{16}$ composite (Figure 15b) produced mostly matrix damage. Isolated fiber breaks were detected, but their number was very low. No 'macrodamage' was observed in this composite. These results correlate well with the failure mode in Figure 12b.The damage development in the $[0]_8$ composite was more complex. It started with a few isolated matrix cracks developed at a very low load. The fiber breaks started to accumulate at approximately 50% of the ultimate stress and continued to accumulate to

the final failure. Soon after the fiber fracture occurred, 'macrodamage' in the form of splitting began to develop. The macrodamage progressed unevenly with several extensive damage events that were felt on the overall AE history for this composite (Figure 8a). Shortly before the final failure, an extensive splitting event occurred that was followed by a substantial fiber breakage. The final failure of this composite could therefore be associated with the two interacting damage modes: the fiber breaks and the longitudinal splitting. This correlates well with the damage observed in Figure 16.

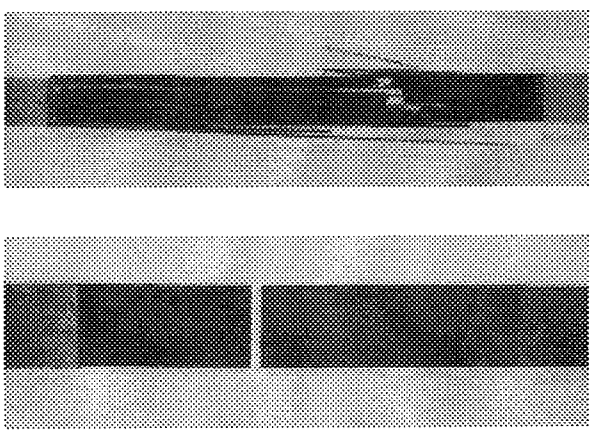

Figure 16. Failed specimens of unidirectional composites: $[0]_8$ (a) and $[90]_{16}$ (b)

4.3.5 Microdamage evolution histories in cross-ply laminates

4.3.5.1 Classified AE histories for cross-ply laminates

The transient analysis of the AE acquired from the laminated composites showed that the characteristic waveforms observed in the unidirectional composites were also observed in both laminated composites. An attempt was therefore made to use the multiparameter filters developed

for the unidirectional composites to extract the classified AE histories for the laminates. The C type signals were separated first by the duration filtering. The A and B type signals were extracted by the multiparameter filters based on the parametric regions shown in Figure 14. The results of this analysis are shown in Figure 17.

It is seen that in the case of the cross-ply composite (Figure 17a), the first damage was in the form of matrix cracks (A type signals). A few isolated matrix cracks occurred very early in the loading process. However, the substantial matrix damage did not begin up to the stress levels of about 50% of the ultimate strength. The increase in the matrix damage at that stress level was followed by some fiber breakage (B type signals) and, almost simultaneously, by the 'macrodamage' development (C type signals). Comparisons with the on-line observations showed that the 'macrodamage' in this composite was in the form of delaminations, rather than the longitudinal splitting observed in the $[0]_8$ composite. The matrix damage accumulation showed a tendency to saturate in the cross-ply composite (A type signals in Figure 17a). A saturation of matrix cracks in the 90-degree plies of a cross-ply composite is, in fact, expected, based on the results of published experimental and theoretical analyses. The fiber damage accumulation in this composite was not substantial (B type signals in Figure 17a). The fiber damage also showed a tendency to saturate. The observed similarities between the fiber and matrix damage accumulation indicated that the fiber breaks in the cross-ply composite might be related to the matrix cracks. For example, isolated fiber breaks in the 0-plies could occur in the vicinity of the matrix cracks in the 90-plies. The delamination in this composite grew steadily to failure. The overall AE activity in the $[0/90]_{3S}$ composite was dominated by the matrix damage and the delaminations. The AE history analysis correlated, in general, with the on-line observations and the observed failure of the composite specimen (Figure 18a).

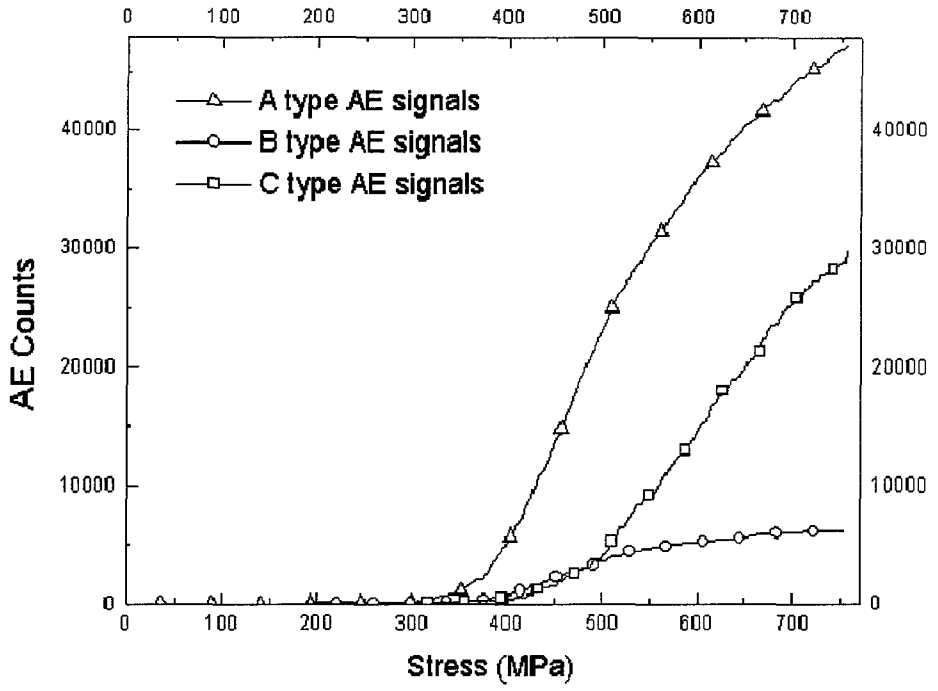

(a)

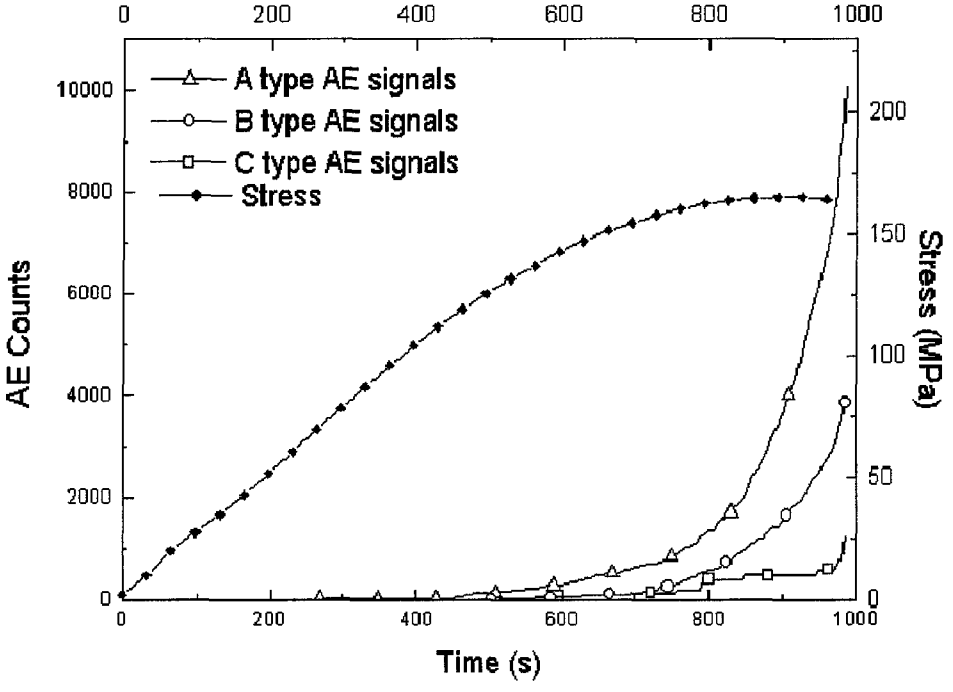

(b)

Figure 17. Classified AE histories for laminated composites: $[0/90]_{3S}$ (a) and $[+-45]_{4S}$ (b)

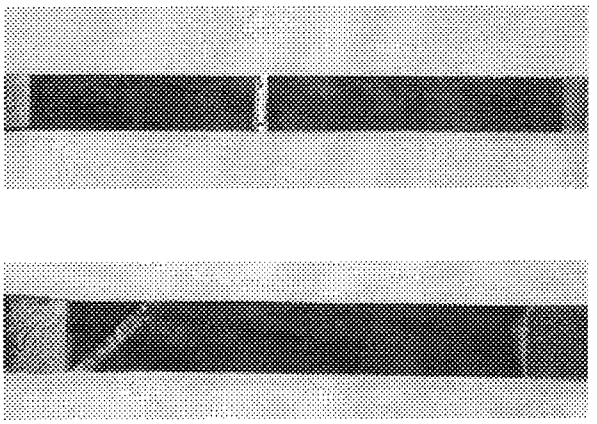

(a)

(b)

Figure 18. Failed specimens of laminated composites: $[0/90]_{3S}$ (a) and $[+-45]_{4S}$ (b)

The classified time histories of the damage evolution in the angle-ply composite are shown in Figure 17b. The stress-time dependence is also shown, for reference. The analysis showed that the substantial damage accumulation in this material started later in the loading process, compared to the cross-ply composite (Figure 17a). The damage sequence was the same as described for the cross-ply composite: the matrix cracks were followed by the fiber breaks and the delaminations. However, no saturation was observed for any of the damage modes in this laminate. In contrast to the cross-ply composite, the rates of accumulation of all three types of damage increased monotonically until failure. This is consistent with the fact that no saturation of any damage mechanism is expected in an angle-ply laminate. The damage process in this composite was dominated by the matrix cracks and the fiber breaks. Little delamination damage was detected. The latter may seem unusual as the delamination damage is practically inevitable in an angle-ply composite, at least before the failure. Analysis of the failed specimen (Figure 18b) showed, however, that the final failure with some delamination occurred outside of the acoustic

gauge zone. The AE signals from this delamination were, therefore, filtered out by the location filtering procedure described above. Thus, the results of the AE analysis of the angle-ply composite corroborate the expected and observed damage in this material.

4.3.5.2 Evaluation of quality of parametric filtering

The multiparameter filters used to obtain the classified AE histories for the laminated composites were developed based on the transient-parametric analysis of the unidirectional composites. The application of these filters to the analysis of the laminated composites was based on the observed similarity of the three characteristic waveforms in the unidirectional and the laminated composites. The results of the classified AE analysis for the laminates seemed to correlate with the observed and expected damage in these composites. A direct check of the applicability of the multiparameter filter definitions across the composite lay-ups was performed by inverse analysis in this section.

The procedure was as follows. The AE signals from a particular parametric region were randomly selected and their parametric records were extracted from the parametric AE file. The waveforms for these signals were found in the transient AE file using the transient index. The frequency spectra were then computed for these waveforms using the Fast Fourier Transform. Finally, the waveforms and their spectra were evaluated for shape and classified. Both the cross-ply and angle-ply laminates were analyzed. Due to the large number of the AE signals in both laminates, a partial check based on the analysis of several hundred signals of each type was performed.

First, the transient records of the signals with long duration were evaluated. The analysis showed that the majority of these signals from both laminates were of the type C. Then, the signals with parameters falling into the parametric regions for the type A and B waves were analyzed. The results of this evaluation are shown in Table 2. The analysis of the cross-ply composite showed that over 60% of all signals in both parametric regions had the correct transient waveform. For the angle-ply composite, the success rate was 57% for the A type signals and 82% for the B type signals. The balance in all cases was composed primarily of the unclassified waveforms. There were few or no waveforms of the opposite type found in the parametric regions of the particular type. The success rates in Table 2 can be considered reasonable, taking into account the complexity of the damage and wave propagation processes in composites and the number of variables involved in the damage accumulation. Overall, the results of this analysis showed that the parametric filters developed for the unidirectional composites could be applied to separate the AE histories in the laminated composites with a reasonable reliability.

Table 2: Characteristic waveform content for laminated composites

Laminate	Parametric Region	Total Checked Waveforms	Correct Waveforms	Success Rate
$[0/90]_{3S}$	A	445	296	67%
	B	216	134	62%
$[+-45]_{4S}$	A	813	465	57%
	B	390	321	82%

4.4 Static Analysis of Quasi-Isotropic Laminates

In the previous section, a method of analysis of the AE histories was formulated based on experimental studies of more complicated and practical quasi-isotropic lay-ups. Quasi-static behavior of the two quasi-isotropic laminates was studied. Characteristic waveshapes and parametric regions similar to the ones obtained for the unidirectional composites were identified. Evolution histories for different waveshapes were extracted. Finally, low-cycle fatigue behavior of these laminates was analyzed.

4.4.1 Mechanical response

Quasi-isotropic $[0/\pm45/90]_{2S}$ and $[90/\pm30]_{3S}$ laminates were manufactured and tested as described above. Figures 19 show the stress/strain curves.

4.4.2 Overall AE histories

Two specimens were tested for each laminate. The AE data acquired from these specimens were consistent. Figures 20 show the overall histories of the acoustic emission from the laminates loaded in quasi-static tension. Total 190,000 counts were acquired in the $[0/\pm45/90]_{2S}$ test. The AE counts had the max accumulation rate at the medium loading level. The similar distribution pattern of AE counts was also observed in the crossply $[0/90]_{3S}$ material described above. We can see that the AE counts substantially increased when the loading reached 55% of the ultimate load. Also, a large peak was observed between 55% and 72% of the ultimate load. After that, the AE

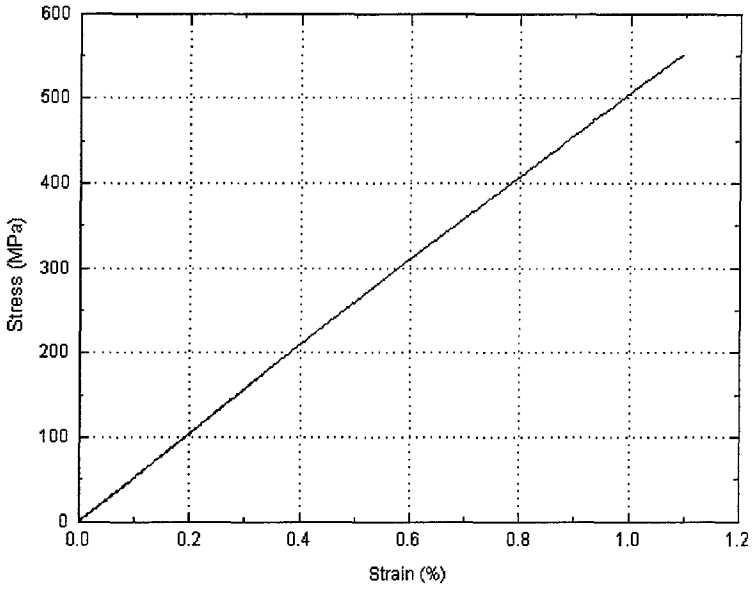

$[0/\pm45/90]_{2S}$

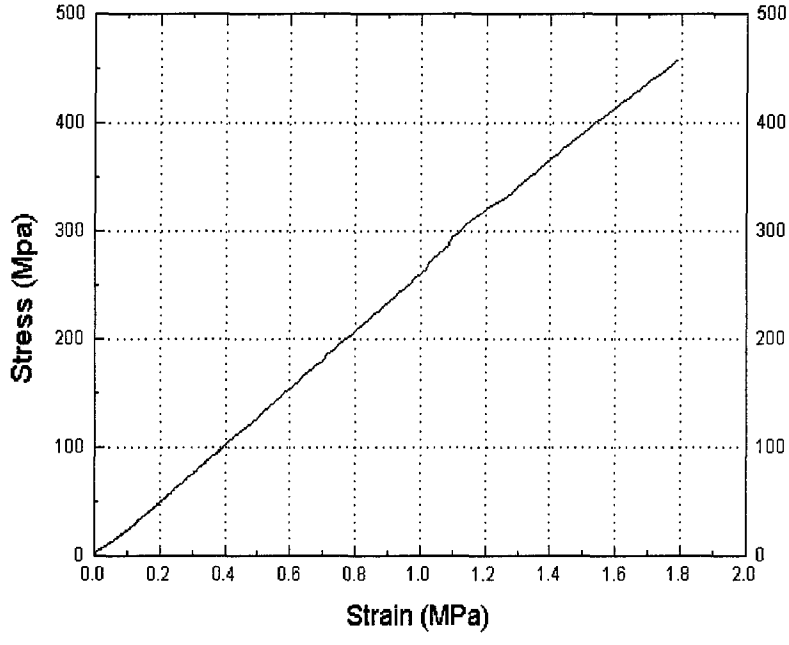

$[90/\pm30]_{3S}$

Figure 19: Stress-strain diagrams of quasi-isotropic composites

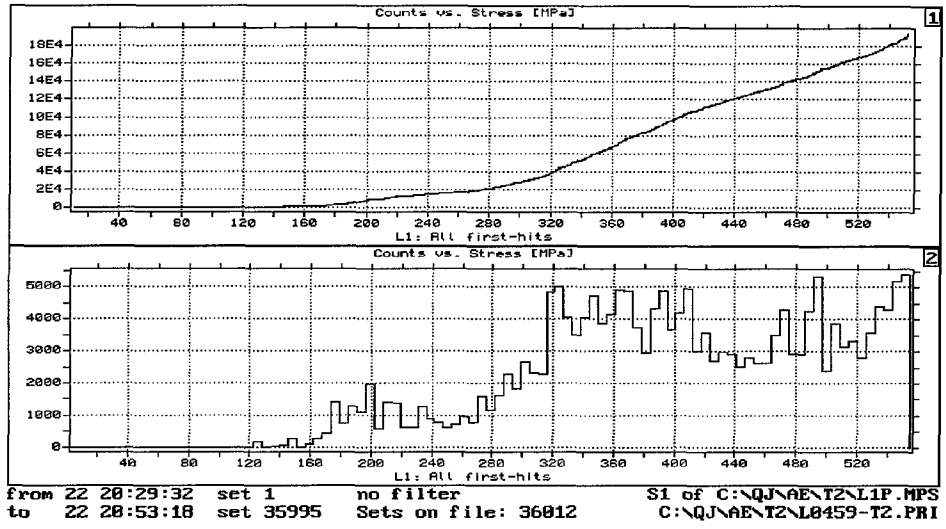

$[0/\pm45/90]_{2S}$

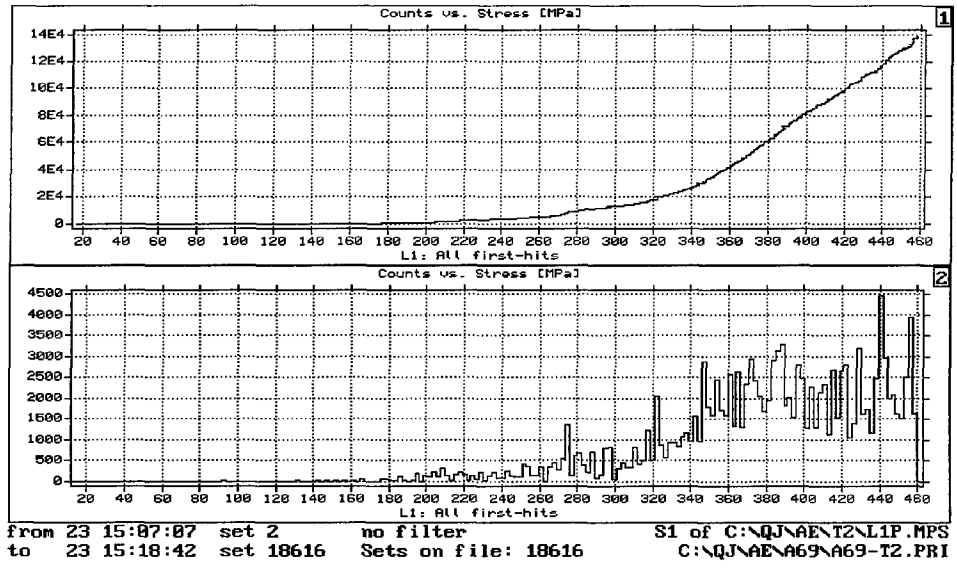

$[90/\pm30]_{3S}$

Figure 20: Overall AE histories of quasi-isotropic composites

counts gradually decreased. The difference from the crossply material was that the quasi-isotropic laminates exhibited additional high AE accumulation peaks. One was near 90% of the ultimate loading and the other one was right before the final failure. The accumulation peaks may relate to some saturation of special damage mechanism, which need to be studied further.

The AE accumulation peaks also can be correlated with mechanical degradation of the specimen. Compared with Figure 19, AE initiation at 180 MPa makes the Young's modulus start to decrease. When AE fast accumulates between 300 MPa and 380 MPa, Young's modulus decreases quickly with almost constant degrading rate.

Analysis of distributions of the AE signals showed only one peak on the duration and amplitude distributions. The peak of high duration and high amplitude could not be clearly identified. The correlation plot of duration and amplitude showed high density of AE events at medium duration and medium to low amplitude. However there are some AE events having relatively high amplitude and duration.

Figure 20 also shows the load history for the $[0/\pm30]_{3S}$ laminate. The AE accumulation history was similar to the history for the $[0/\pm45/90]_{2S}$ laminate. AE initiated at about 260 MPa. The AE accumulation rate increases above 340 MPa. That high accumulation rate remains constant until the final failure happens. This may suggest that the cracks in 90° and ±30° lamina gradually extended until final failure happened. Some small AE peaks between 260 and 330 MPa show in subplot2 of Figure. Refer to Figure 19, these AE peaks may be correlated to modulus jumps. For example, one AE peak at 320 MPa indicates the large damage accumulation, which cause substantial decrease of modulus. When load reached 340 MPa, the Young's modulus gradually decreased with high AE accumulation.

4.4.3 AE histories for different waveforms

The method developed above was applied for data analysis of quasi-isotropic laminate tests. It started with screening AE waveforms and spectra, and identifying typical waveforms. Three typical waveforms, similar to the waveforms extracted from the unidirectional material, were observed. Then analysis was performed in AE parameter space. The objective was to find the parameter range that is occupied by those typical waveforms. Figures 21 show that different waveforms occupied different regions in the correlation plot of amplitude and risetime (1-100 and 1000-1100 data sets). Finally parametric filters similar to ones developed for the unidirectional material were used to classify the AE into different groups.

Figures 22 show loading history for three types of AE signals from the laminates. As can be seen, the "A" type AE signals prevailed for the $[0/\pm45/90]_{2S}$. They had the fastest accumulation rate between 310 MPa and 400MPa. The accumulation rate in this test decreased above 400 MPa and increased only before the final failure of the laminate. The "B" type AE signals started to accumulate early in the test. The accumulation rate of the "B" type AE increased between 320 MPa and 370MPa. This loading range was in the fast accumulating ranges of the "A" type signals. This may be due to fast increasing of the matrix crack leading to stress concentration on the fibers. High stresses caused fiber failures. Following the fiber failure, more matrix cracks were generated and the cracks were likely to propagate. The "C" type AE signals started at about 200 MPa (36% of ultimate loading) and accumulated gradually in whole test. Comparing Figure 22 with mechanical response, the degradation of Young's Modulus started when "C" type AE initiated. Also the fast accumulation of "A" type AE can be correlated to the quick degradation of Young's modulus.

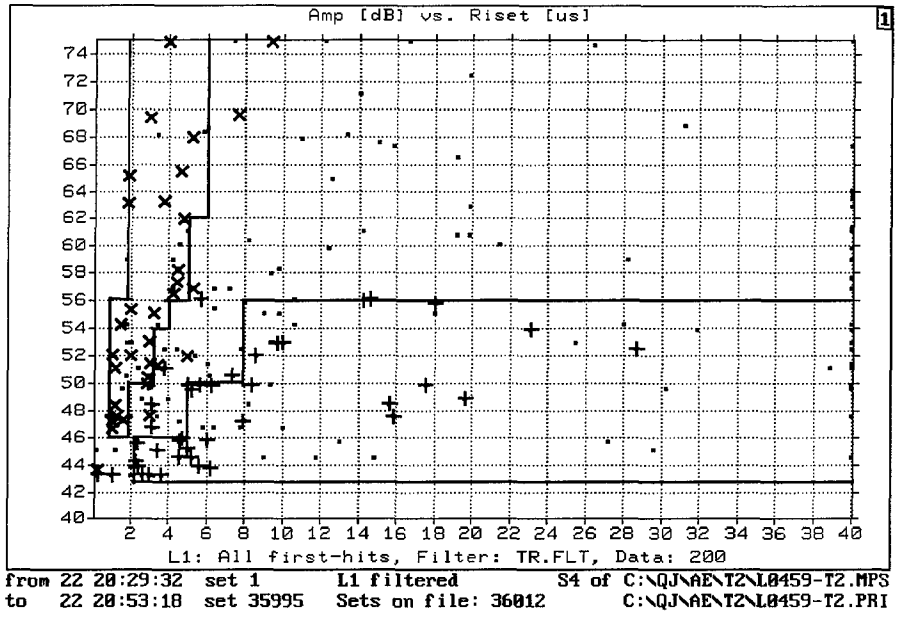

$[0/\pm45/90]_{2S}$

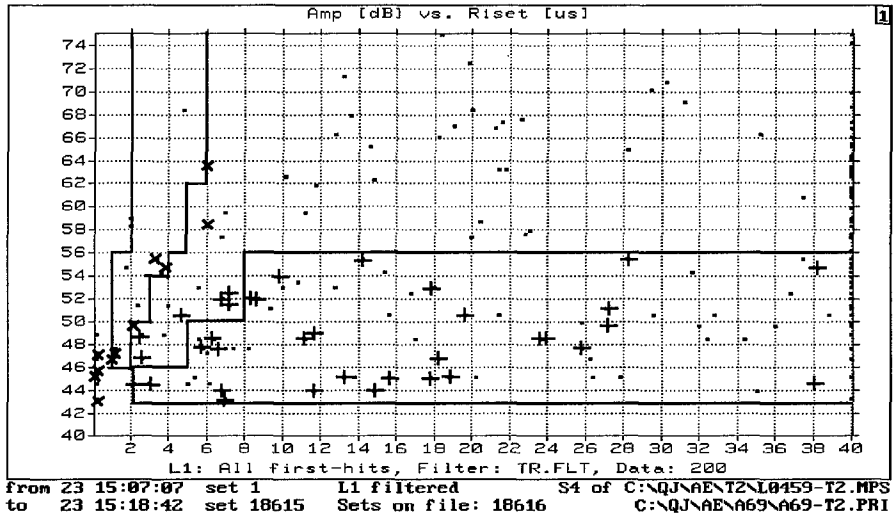

$[90/\pm30]_{3S}$

Figure 21: Parametric regions for quasi-isotropic composites

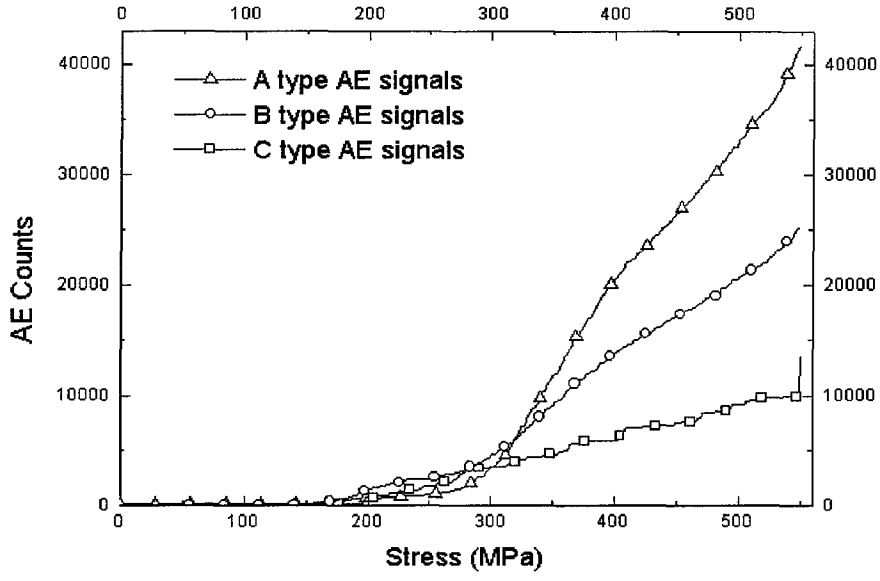

$[0/\pm45/90]_{2S}$

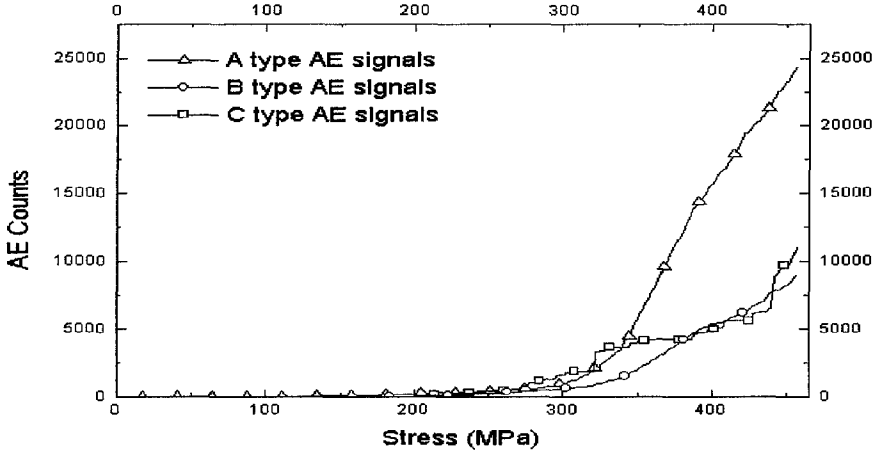

$[90/\pm30]_{3S}$

Figure 22: Classified AE histories of quasi-isotropic composites

Figures 22 also show history of the three types of signals in the $[0/\pm30]_{3S}$ laminate. The content of the "A" type signals was higher than in the $[0/\pm45/90]_{2S}$ laminate. In addition, the "A" type AE signals accumulated faster between 330 MPa and 380 MPa. Above 370 MPa, the accumulation rate slightly decreased and remained constant until the final failure of the laminate. The content of the "B" type AE signals was lower compared with that of the $[0/\pm45/90]_{2S}$ laminate. The fast accumulation range was between 330 MPa and 360 MPa. The "C" type AE signals started at 200 MPa. A jump was observed near 300 MPa, at which the accumulation rate of the "A" type signals started to increase. A jump in the cumulative counts of the "C" type signals occurred before the final fracture of the laminate.

Compared with modulus change, it seems that "C" type damage affects the Young's modulus most substantially. The jumps of "C" type signal are related to the degradation of Young's modulus.

4.5 Fatigue Analysis of Quasi-Isotropic Composites

4.5.1 Mechanical response

Low-cycle tension-tension fatigue was studied. Loading frequency was 0.5 Hz and loading ratio was 0.1. In order to break the specimen in hundreds of cycles, the maximum loading was set to near 90% of the ultimate loading (470 MPa) for the $[0/\pm45/90]_{2S}$ laminate and 80% of the ultimate loading (365 MPa) for the $[90/\pm30]_{3S}$ laminate. More than six specimens were tested in low cycle fatigue. Typical results are presented below. The $[0/\pm45/90]_{2S}$ laminate failed after 480 cycles. The $[90/\pm30]_{3S}$ laminate failed after 425 cycles. Figure 23 shows the Young's modulus

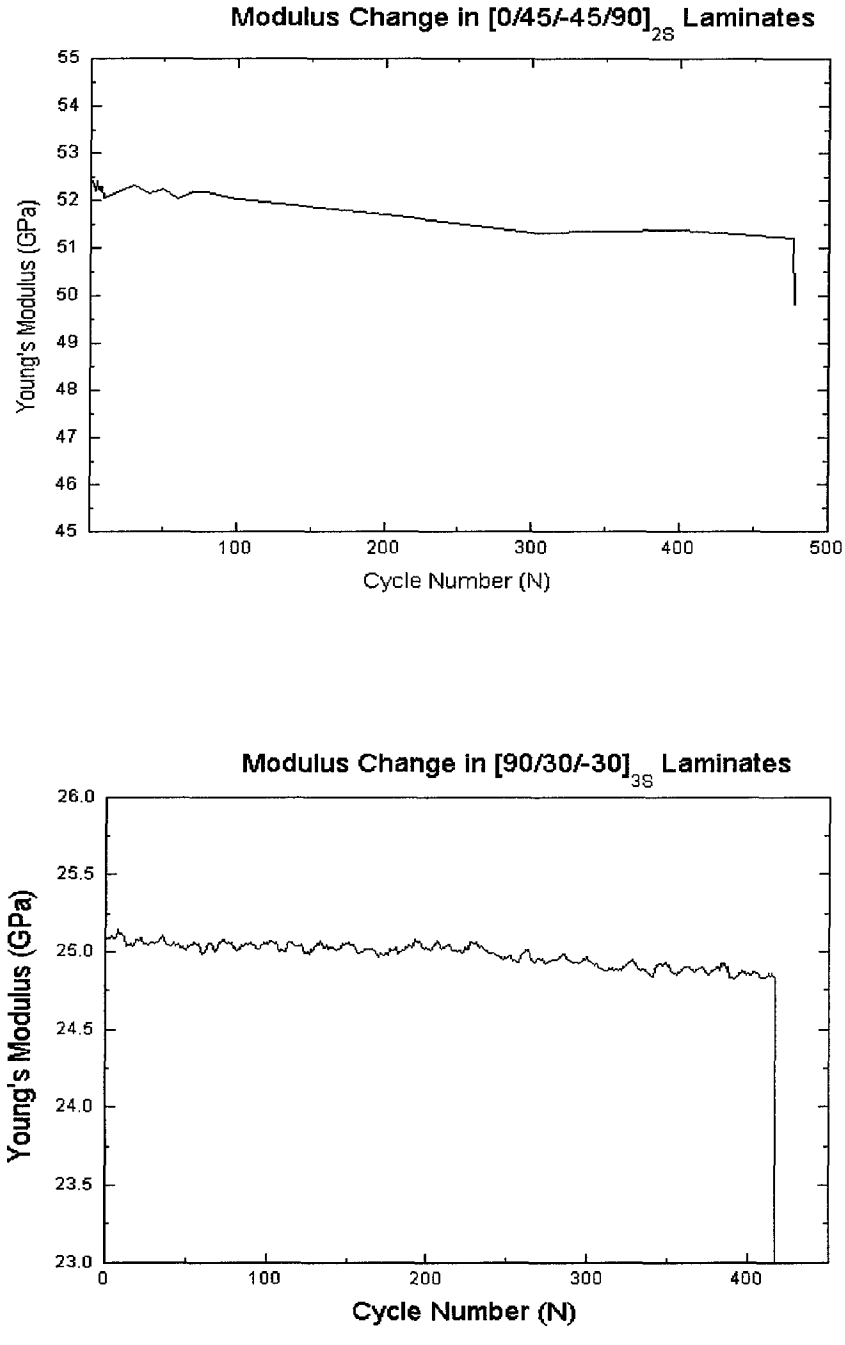

Figure 23: Young's modulus degradation in quasi-isotropic laminates under fatigue

degradation with cycle number. Gradual modulus degradation was observed in both tests. Extensive delamination was observed in the $[90/\pm30]_{3S}$ laminate, but no dramatic delamination was found in the $[0/\pm45/90]_{2S}$ laminate.

4.5.2 Overall AE histories

AE behavior of the $[0/\pm45/90]_{2S}$ and the $[90/\pm30]_{3S}$ laminates under cyclic loading was similar. Therefore, only the $[0/\pm45/90]_{2S}$ laminate is analyzed here in detail. The main result achieved by the similar analysis are also presented for the $[90/\pm30]_{3S}$ laminate below.

Figure 24 shows the overall acoustic emission from the fatigue test of the $[0/\pm45/90/]_{2S}$ laminate. In the subplot 1, the history of the accumulated AE counts is displayed. The distribution of AE accumulated counts are expressed as a function of cycle number. The specimen failed in the 482nd cycle. The subplot 2 is a distribution plot of the AE counts over the loading range. A high peak appears at the very high load level (>80% of the Max loading) and two low peaks appear at the low load levels (between 10% and 60% of the max loading). It is interesting that few AE counts are observed between the high peak and the low peaks. At high loading level, the damage is more likely to generate than at low level. In our experiment, the peak at the high loading level was much higher than the peaks at the low loading levels. However, almost no AE was generated at medium loads. This indicates that the peaks at the low loading levels may not be related to the new damage development.

The location history is shown in the subplot 3. The short lines on this plot represent AE events originated at specific location in the specimen over the number of cycles. These AE events may be due to gradual crack extension or friction between the crack surface. In the correlation

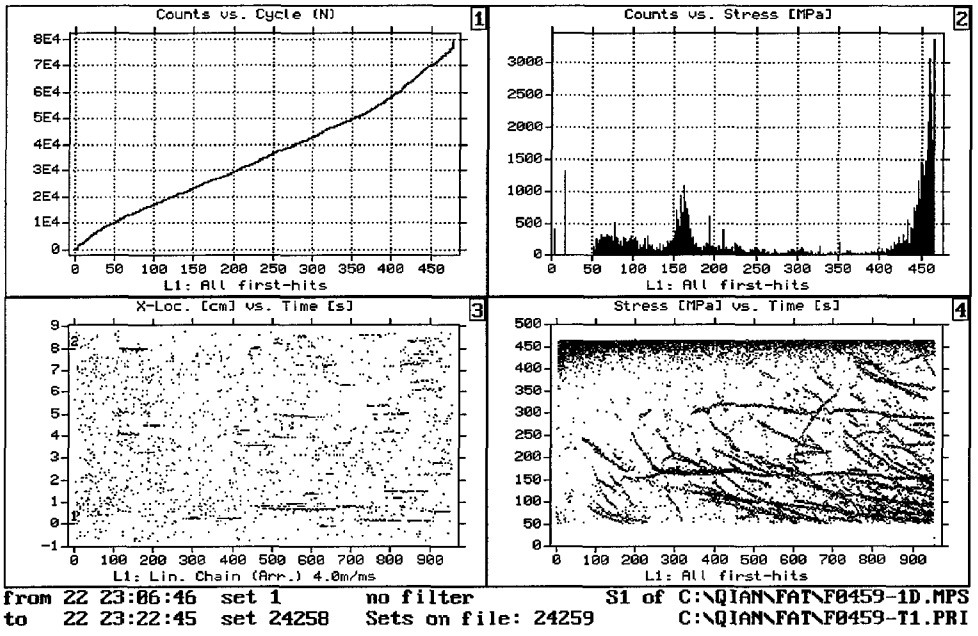

Figure 24: Overall AE history in $[0/\pm45/90]_{2S}$ laminate under fatigue

plot of loading and time (subplot 4), the line pattern is also observed at low loading. They represent emission at same load over the number of cycles. These AE events may be due to gradual extension or frictions. The lines in location and load histories need further explanation. Possible frictional noise has to be eliminated before mechanics separation.

4.5.3 Elimination of the AE from internal friction

Acoustic emission due to friction may have substantial effect on the total acoustic emission during fatigue loading. In order to analyze acoustic emission related to new damage evolution, a separation of the AE from friction is needed.

It is expected that the damage in the material is more likely to develop under the loading state than under the unloading state. For example, the crack in the material opens when the load increases and closes when the load decreases. AE signal from the loading and unloading processes can be separated using unique filter feature in the AMS3 system. Cycle flag in AMS3 system are set to "1" for loading and "0" for unloading. The AE from the loading and unloading processes is shown in Figure 25. The history plots in these figures are qualitatively different in the loading process. The accumulation rate of the AE gradually decreases. As can be seen in the Figure , at the first several cycles the AE accumulation rate is maximum. It reveals that damage accumulates fast under loading at the beginning of the fatigue process. However, the AE counts accumulate in a different style in the unloading process. The accumulation rate gradually increases until the final failure.

In the load distribution subplot 2 of Figure 25a, the high peak at the high load level is

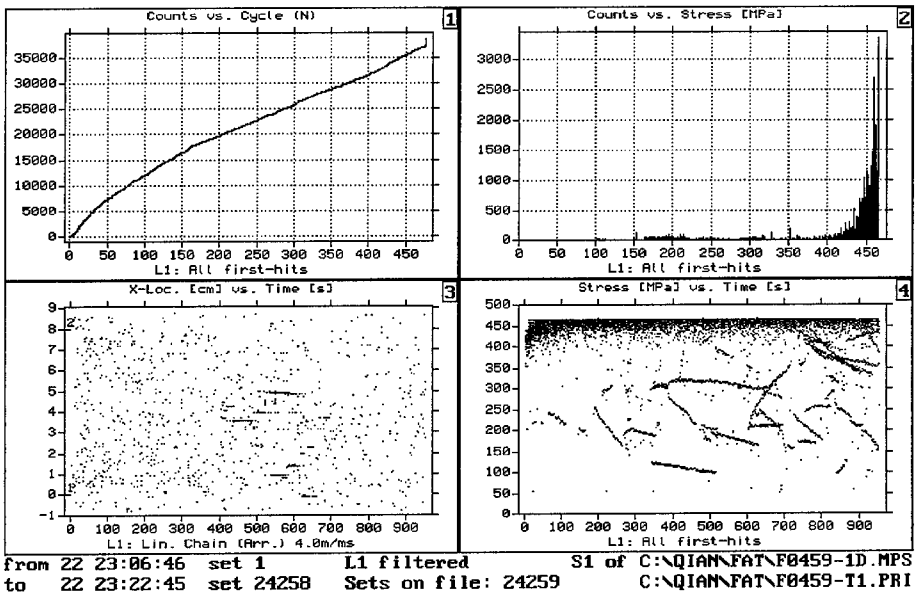

a

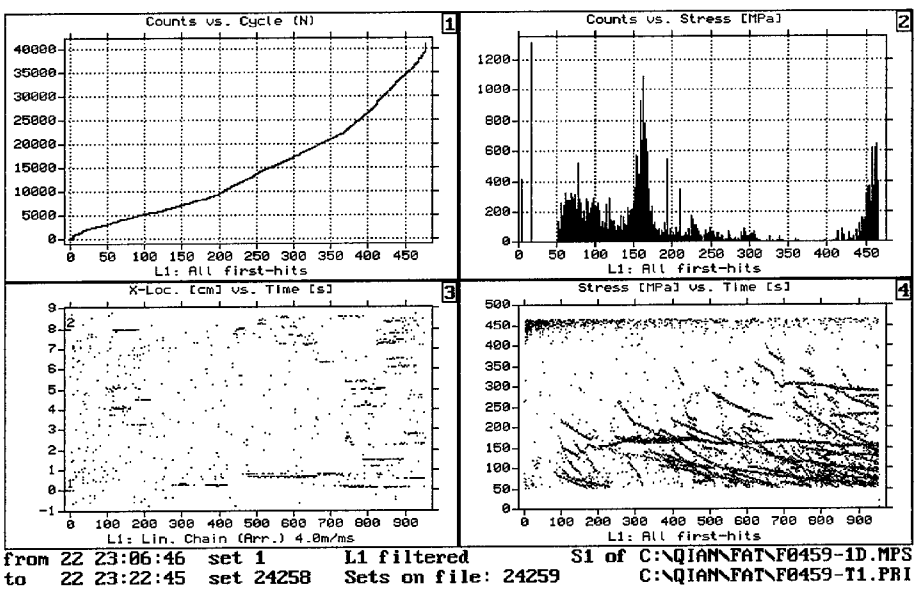

b

Figure 25: AE from loading (a) and unloading (b)

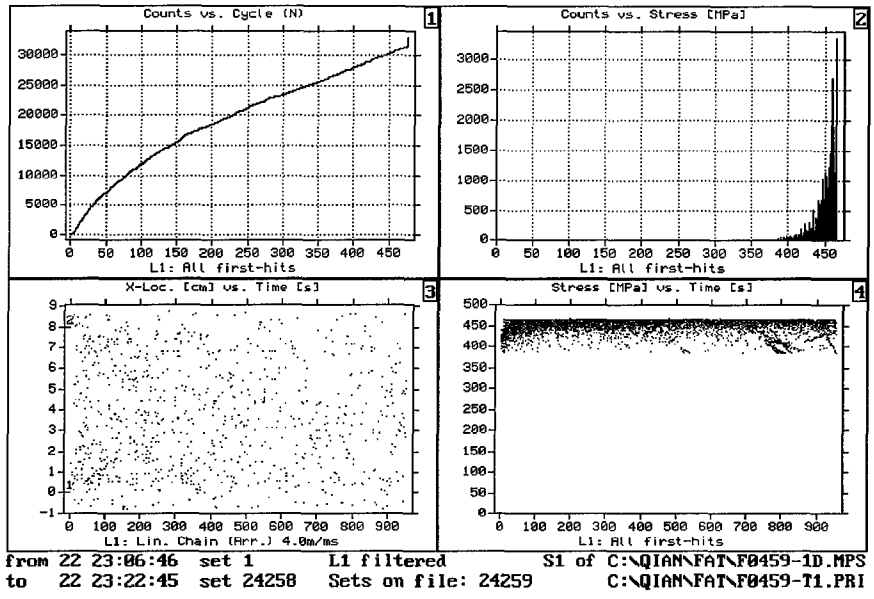

a

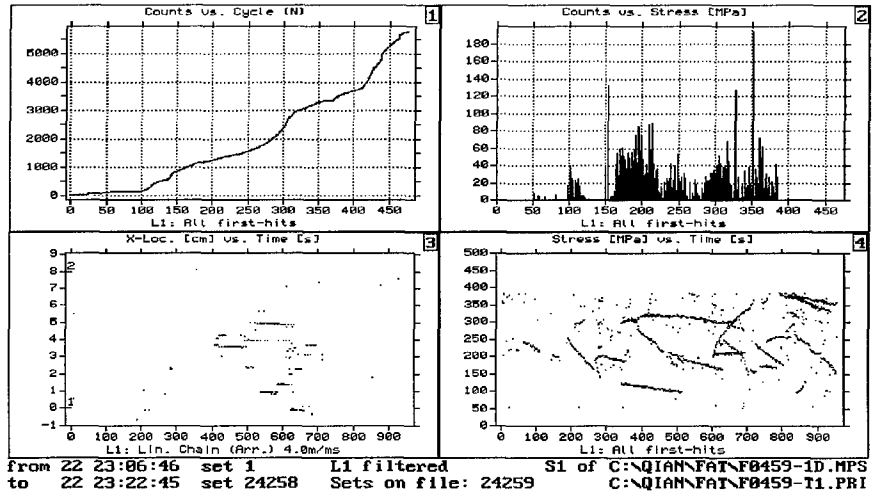

b

Figure 26: AE from high (a) and low (b) loads under loading

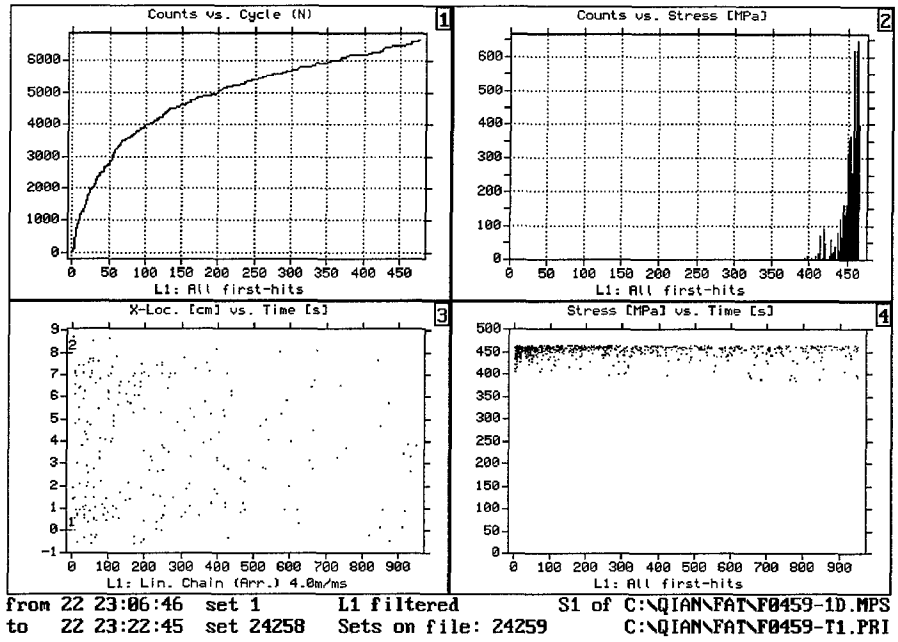

a

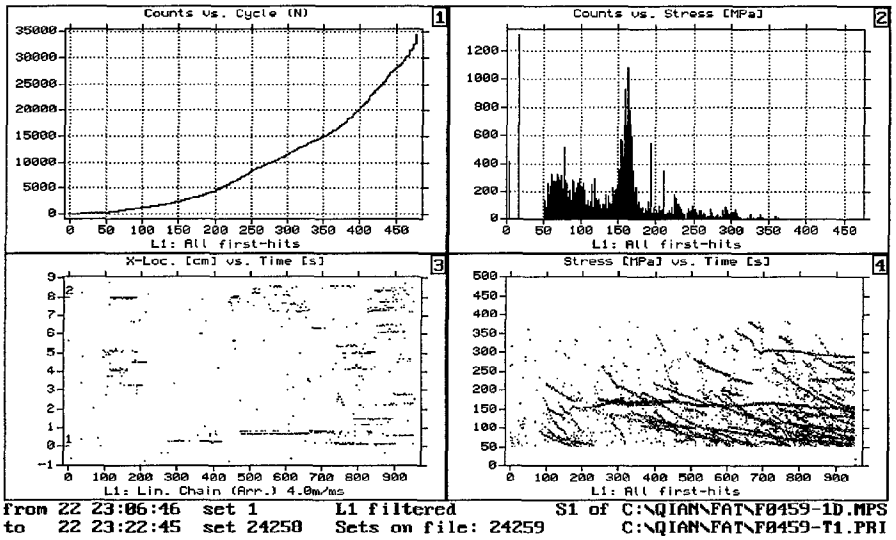

b

Figure 27: AE from high (a) and low (b) loads under unloading

observed, but the peaks at the low load levels disappear. At the same time, the load distribution plot of Figure 25b shows three peaks. The peak at the high load is greatly reduced and the three peaks have similar intensity. This indicates that the AE counts related to the new damage are generated primarily at the high load levels near the accumulation in the specimen. These peaks can be due to friction between the crack surfaces. This is supported by the fact that more short lines are observed in the unloading process than the loading process in the location and time correlation plots (subplot 3). Some of these lines may also be attributed to friction. The correlation plots of stress vs. time provide additional useful information. In the subplot 4 of Figure 25a, the AE events appear primarily at high loading levels. At low loading levels, few AE events exhibit line pattern. In contrast in the subplot 4 of Figure 25b, few AE events occur at high loading levels. However, multiple AE events generated at low loading levels exhibit the characteristic line pattern. It is interesting that only a few AE events were generated at low loading levels in the beginning of the fatigue test. As the cycle number increases, the AE from low loading levels dramatically increases. These again indicated that the source of this AE is friction instead of new damage accumulation. The more damage is accumulated, the more frictional noise is generated in the test.

To further verify our suggestions, the AE events from the loading process were analyzed. Figure 26a shows the AE generated at loading levels is higher than 380MPa (80% of Max loading) under loading state. Figure 26b shows the AE generated at loading levels is lower than 380 MPa. They exhibit different accumulation histories. The accumulation rate at high loading gradually decreases, while at low loading it randomly increases and decreases. As can be seen from the comparison of the subplots 3 of both figures, the AE at high loading is quite scattered, while the AE at low loading is line pattern. Line pattern is also observed in the loading correlation subplots of both figures. We know that it is unlikely for a new damage to consistently develop at the same

location in the specimen. Even in the case of a single crack propagation, as crack length increases, the AE source location changes. Therefore these line pattern AE events in the correlation subplots (subplot 3) must be related to friction between the crack surfaces. It suggests that for the laminate studied, the AE from new damage and friction can be separated by a loading filter. Figures 27 demonstrate the high loading level and low loading level AE in unloading process. It is interesting that the AE at different loading levels are different. However, they are similar to the features at the corresponding loading levels in the loading process. At the high loading level, the AE events are scattered (subplots 3 and 4). In contrast, at the low loading level, the AE events are line pattern in the correlation plots. It implies that the signals from the high loading level (>80% of max load) under unloading are related to damage development in composite material. Comparison between subplots 1 of Figures show that during the first 75 cycles of the fatigue testing, the AE counts generated by damage evolution at high load in the unloading process are equal to one third of the AE counts generated by damage in the loading process. Therefore, it may be inaccurate to eliminate the effect of unloading process on damage evolution study, in laminates, especially at the beginning of the fatigue test.

AE counts acquired at low loading level in the unloading process show gradually increasing rate in Figure 27b. As discussed above, this AE can be related to friction between the crack surfaces. Accumulated total of 35000 counts in the whole test is five times of the accumulative count at the high loading level in the unloading process. Therefore, the AE related to the new damage can be easily masked by noise if no filter is used. On the other hand, since these AE counts from friction increase with the crack density and damage accumulating, it may be possible to evaluate the damage state by the analysis of the frictional noise.

Based on the analysis above, we can conclude that the AE related to new damage evolution in the low cycle fatigue occurs at high loading levels (>80% of max loading). The AE at low and middle load levels can be related to friction between the crack surfaces.

The load filter then was used to eliminate the AE events at low load levels (<80% of max loading). Figure 28 shows the data after filtering. These AE events are believed to be related to the new damage evolution in the material.

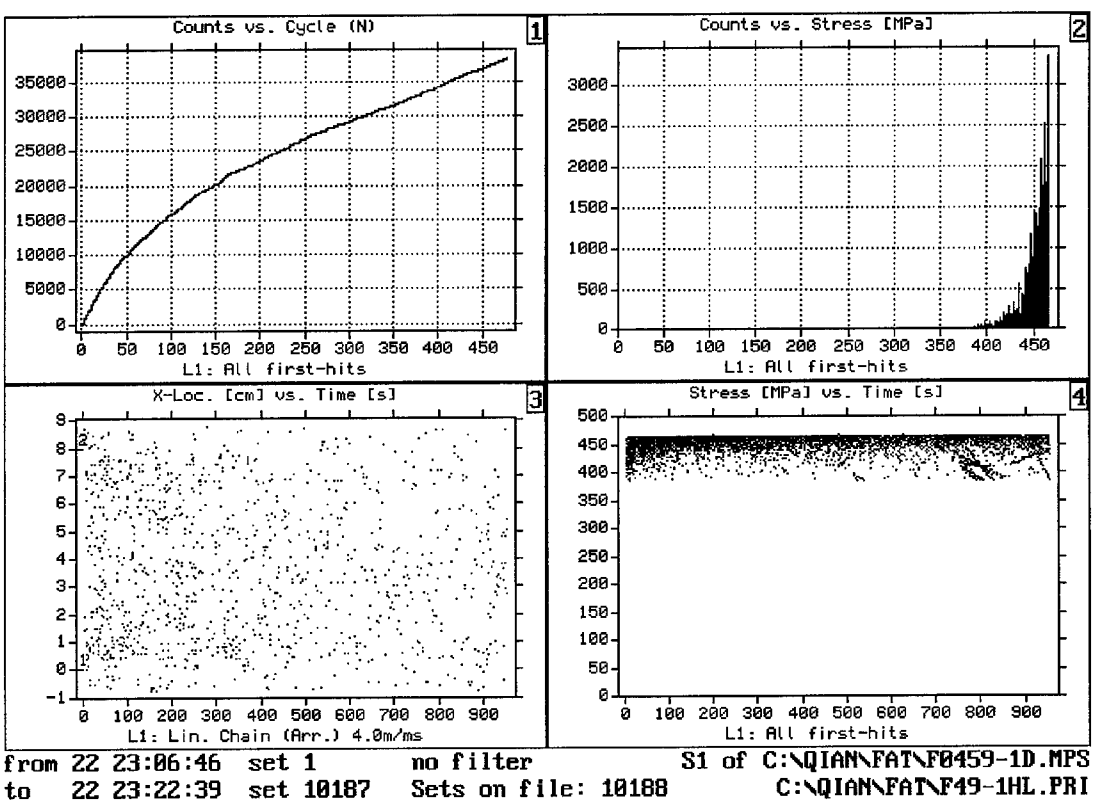

Figure 28: Filtered AE data for $[0/\pm45/90]_{2S}$ laminate

4.5.4 AE histories for different waveforms

Signal classification filters developed for the laminates under quasi-static loading were used to classify the AE events in the fatigue tests. Two different types of the AE events were separated using the amplitude and risetime filters. The "A" type AE events were attributed to matrix cracks, and the "B" type AE events were attributed to fiber breaks. Figure 29 shows the classified AE count histories for the $[0/\pm45/90]_{2S}$ laminate. The plots indicate that the "A" type AE events are dominating in fatigue testing. The "B" type events also play an important role. There was no "C" type AE signals in this fatigue test. It indicated that few longitudinal splitting and delamination happens. It was further proven by the observation of failed specimen. Figure 29 shows that the "B" type AE signals have higher contribution at the beginning of the fatigue test. This contribution gradually decreases with the cycle number increasing. Two stages of the AE accumulation are discernible in both plots. AE signals related to matrix cracking (the "A" type) have slightly higher accumulated rate at the beginning of the test and near the failure of the specimen. These observations reveal that during the first tens of cycles of the fatigue test, a number of fiber breaks and matrix cracks generated in the specimen. This can be characterized as the first stage of damage evolution in the material. After most weak fibers were broken, the rate of fiber breaks gradually decreased but the matrix cracks gradually accumulated. This is the second stage of damage evolution. When the specimen reached its life limit, many fatal cracks were formed inside the specimen. With several critical fibers breaks, the specimen came into an unstable state and the final fraction of the specimen occurred.

Similar low cycle fatigue analysis was performed on the $[90/\pm30]_{3S}$ quasi-isotropic laminate. The classified AE signal histories are shown in Figure 30. It can be seen the "A" type AE

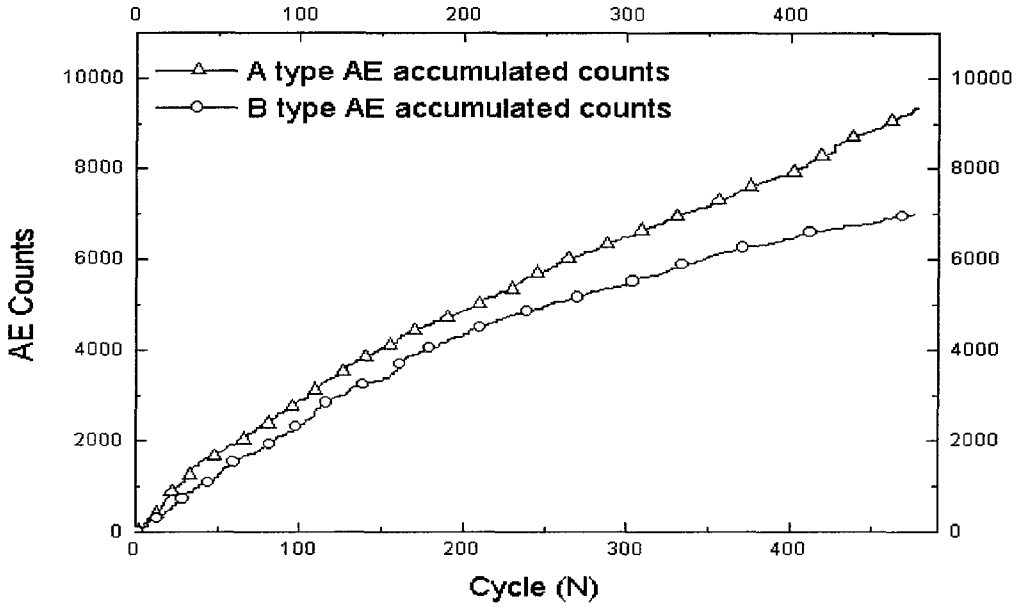

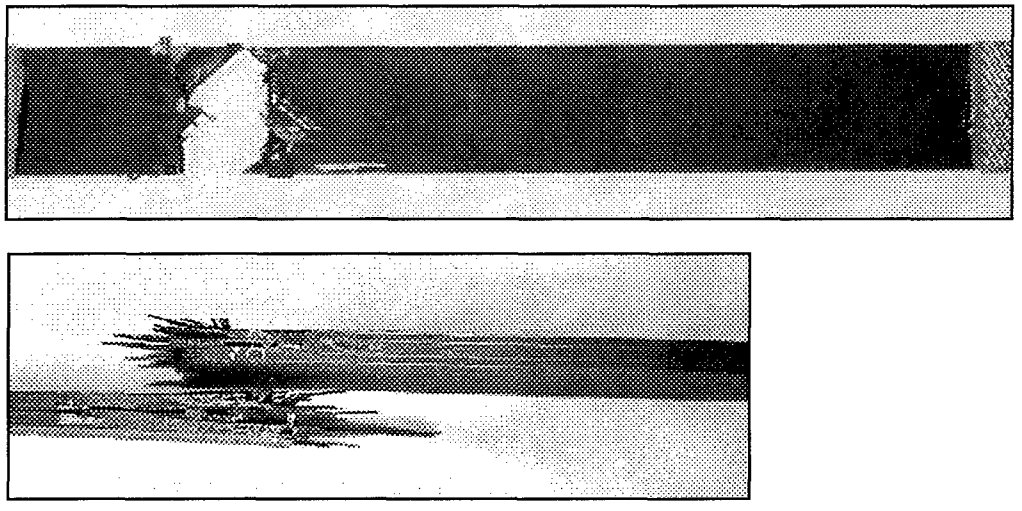

Figure 29: Classified AE histories and failure mode of $[0/\pm45/90]_{2S}$ laminate

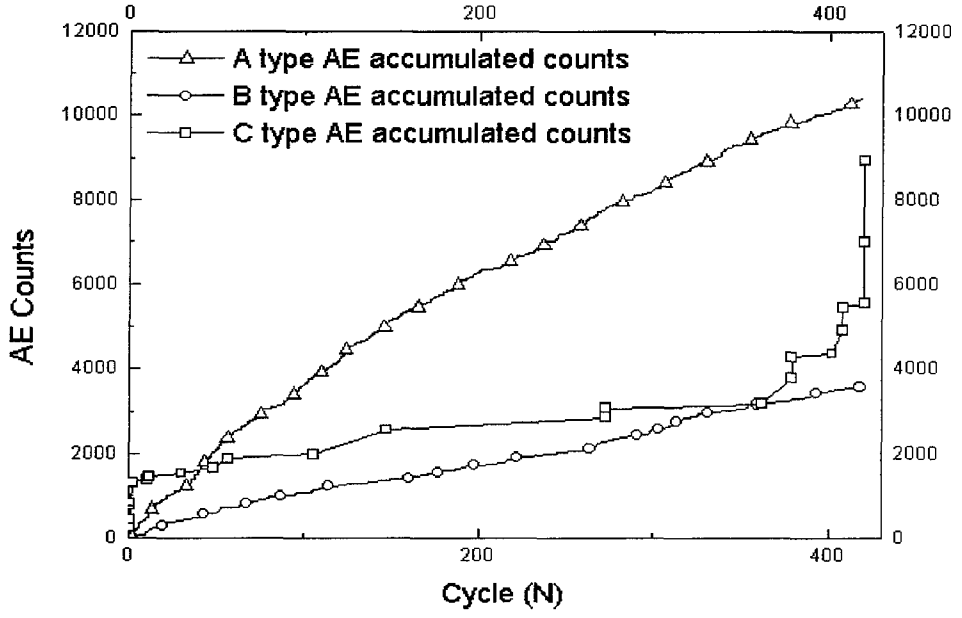

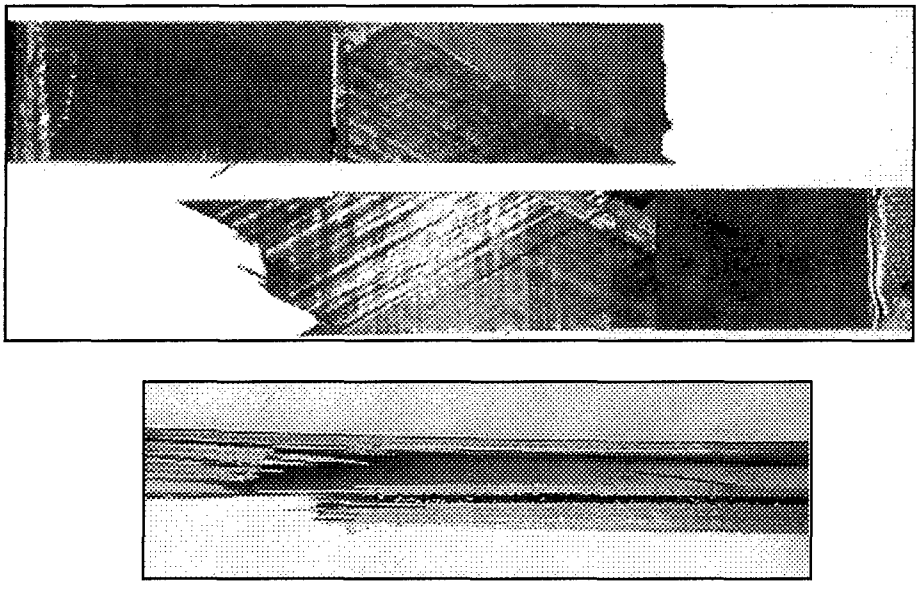

Figure 30: Classified AE histories and failure mode of $[90/\pm30]_{3S}$ laminate

events dominate in this test. Compared with the test of the $[0/\pm45/90]_{2S}$ laminate, the "A" type signals account for the larger portion of the total AE. Their accumulation rate gradually decreases with the cycle number increase. The "B" type signals have a very stable accumulation rate during the whole test. They seem to play a lesser role than in the $[0/\pm45/90]_{2S}$ laminate. The "C" type signals have an interesting accumulation history with several jumps. The jump during the first several loading cycles indicates that some delaminations developed in the very beginning of the fatigue process. These delaminations may be due to the high maximum loading (80% of ultimate quasi-static loading) in this test. Other jumps of the "C" type AE occur near the final failure. These jumps are believed to be the sign of the final failure. We suggest to correlate these jumps of "C" type AE counts with the third stage of damage evolution (final failure), which was not observed in the AE overall history analysis. Overall, this new method appears especially advantageous for damage evolution studies under fatigue loading.

4.6 AE Analysis of Joints

4.6.1 Experimental

The same two-channel AMS3 acoustic emission system by Vallen Systeme was used to analyze the AE emitted from the single lap joint specimens. The specimen with acoustic emission sensors attached in position was shown in Appendix 1 of this report. Two sensors were placed 80 mm apart, each 40 mm from the center of the specimen. Sensor 1 was at the 0 mm position at the top, and sensor 2 was at the 80 mm position below it. The sensors used were wideband B1025 AE sensors by Digital Wave. The sensors were attached to the specimen by means of tape. Vaseline

was used as a coupling agent between the sensor and the adherend surface.

The AE system was calibrated for the specimens tested. This required determination of wave velocities for different specimens. These axial wave velocities were determined as follows. The midpoint of the joint specimen and two positions 20 mm from the midpoint were marked (Figure 31). This corresponded to the positions 20, 40 and 60 mm between the sensors. A lead pencil was held with its tip at the marks on the specimen and then broken by applying pressure. This was repeated several times for every marking with an interval of a few seconds. The AE wave speed was then calculated to obtain the best spread of the experimental points on the location history graph obtained by the AMS3 (Figure 31).

The unidirectional specimens were found to have calibration speeds around 8500 m/s. The cross-ply specimens had calibration wave speeds around 6000 m/s. It is important to note that these are not necessarily the true material wave speeds (an AE wave is a mixture of a flexural and a pressure wave that do not separate while propagating through short distances found in experimental coupons), but rather the calibration speeds that, in conjunction with the AMS3 software, ensured that the calculated location of the acoustic events was accurate.

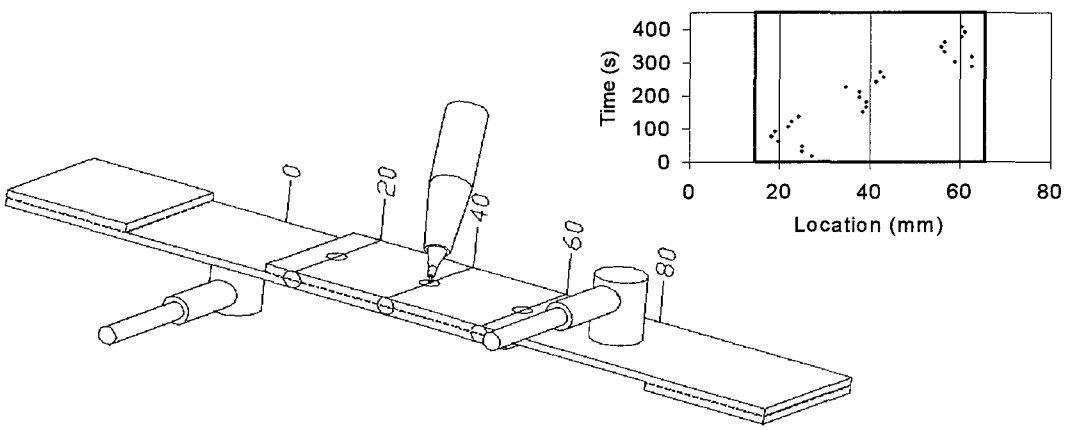

Figure 31: AE location calibration

4.6.2 Static behavior

Results of AE analysis applied to the signals produced during quasi-static tests are shown in Figures 32. Cumulative time histories of the AE from the UD specimens loaded at different loading rates are compared in Figure 32a. Cumulative load histories of the AE from the UD and CP specimens are compared in Figure 32b.

Analysis of the effect of the loading rate showed that although there was a difference as to the rate at which signals were picked up in time (Figure 32a), there was little difference in the amount of signals generated at different load levels (Figure 32b).

Differences in the AE accumulation were observed for the CP and UD specimens (Figure 32b). Both types of joints exhibited an early start of the AE accumulation and almost uniform accumulation rates at lower loads. At certain load levels, however, the accumulation rates

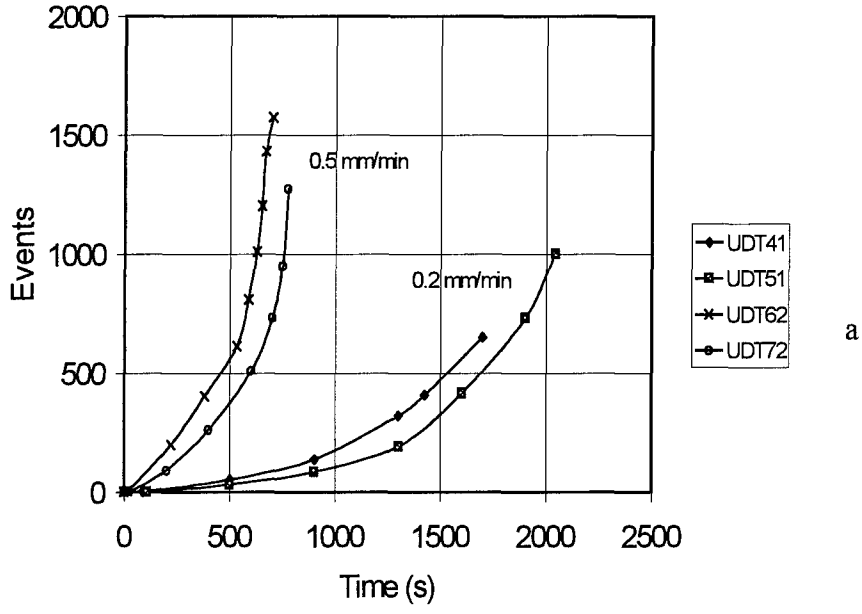

a

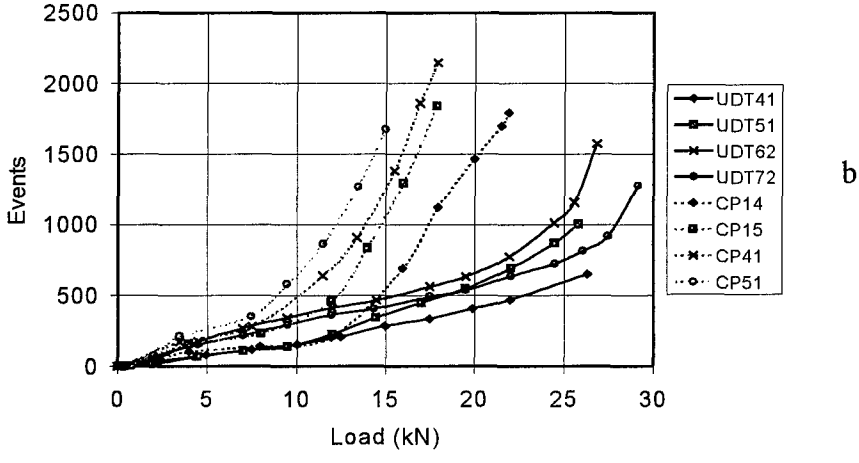

b

Figure 32: Overall static AE histories in joints with UD and CP adherends

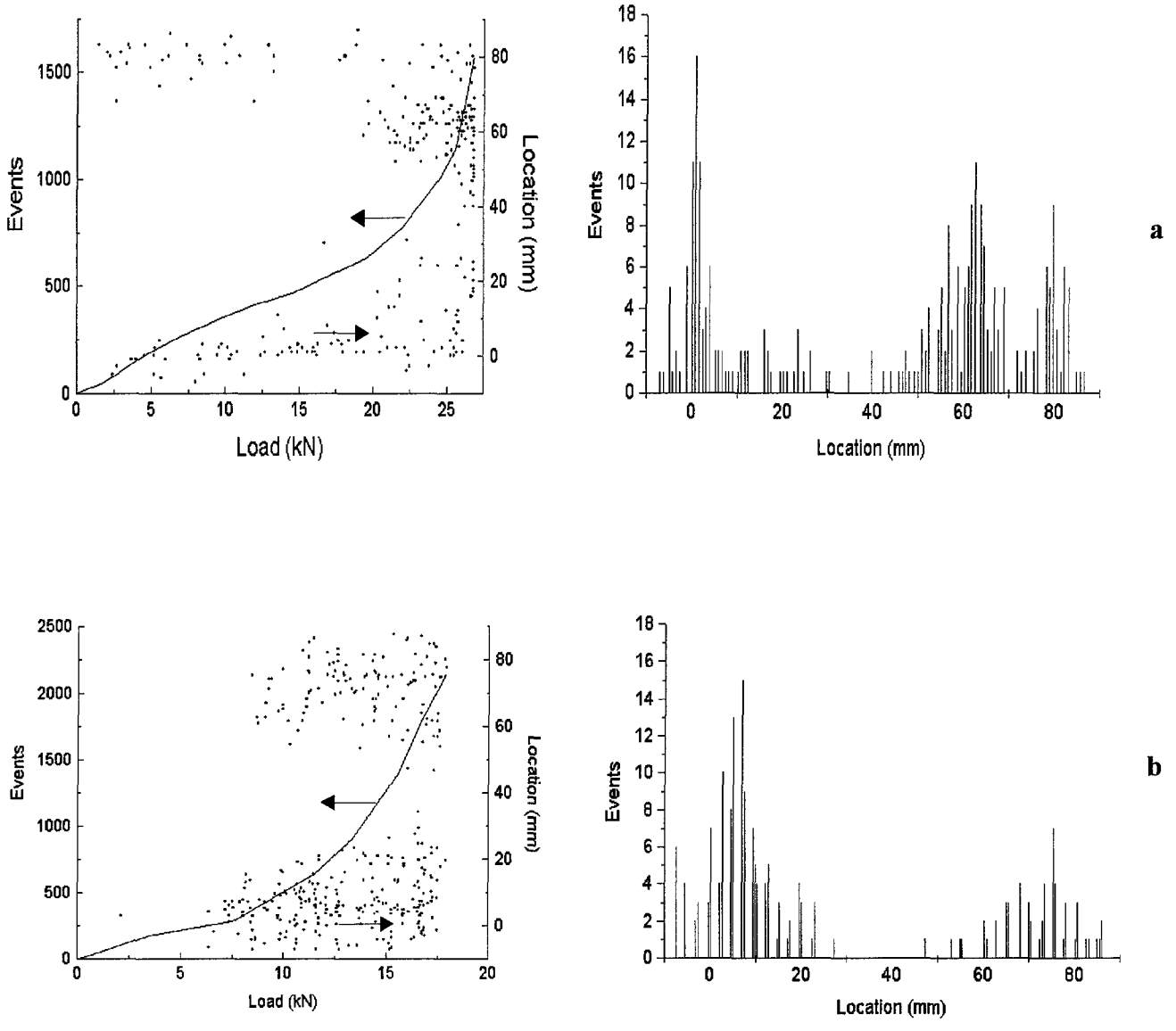

Figure 33: Static AE location analysis of UD (a) and CP (b) specimens

increased. In the case of CP specimens, this rather sudden increase occurred at loads around 10 kN. In the case of UD specimens, the increase was more gradual and occurred at higher loads. As the on-line video microscopy did not show visible fracture up to the maximum loads, the observed AE should be attributed to internal damage. Early development of such damage is typical for composites. The ultimate cumulative AE content was higher for the CP specimens that might be caused by more extensive damage in the cross-ply adherends.

Comparisons between the mechanical response and the cumulative AE load histories (Figure 32) showed that the second non-linearity (softening) in the load-displacement diagrams may be related to damage development in the joints. However, more studies are needed to verify this relationship.

The location of damage in the joints was studied by the linear AE source location analysis. Both the load histories and the total location histograms were computed and analyzed. The results are presented in Figures 33 for the UD and CP specimens, respectively.

The analysis showed that the increase in the AE accumulation rate observed in Figure 32 was caused primarily by damage development near the ends of the overlap. This may be seen from the top graphs in Figures 33. The lines in these graphs represent cumulative AE histories, similar to the ones shown in Figure 32. The dots represent individual AE events with their respective locations shown on the right vertical axis. Further, the analysis of the total AE location histograms (the bottom graphs in Figures 33) revealed that most signals for both the UD and CP specimens were produced near the ends of the overlap. The overlap ends were located at 14.6 mm and 65.4 mm, respectively.

Overall, the AE analysis indicated damage development in the joints prior to bond crack initiation and failure. The damage started to develop early and the damage accumulation rates increased with loading. Correlations with fractographic data showed, however, that the damage seemed to have little effect on the final crack path that was mainly through the bondline with little or no fracture of the adherends.

4.6.3 Fatigue behavior

4.6.3.1 Filtering out internal frictional noise

Two-channel Vallen AMS3 acoustic emission (AE) system was used for acoustic emission analysis of joints under fatigue. Two AE sensors were attached on both sides of the joint. The sensor 1 was at the 0 mm position at the top, and the sensor 2 was at the 80 mm position below it. The acoustic gauge length was 80 mm. The sensors were attached to the specimen by means of tape with Vaseline as a coupling agent. The AE system was calibrated for the single lap specimens tested. The calibration procedure was described in detail above.

It is well-known that composite materials loaded in fatigue produce substantial acoustic emission by internal friction between the faces of accumulating cracks. The fatigue tests, therefore, required additional AE filtering as compared to the quasi-static tests. Two filters were applied to the data acquired during the fatigue tests in this work. The first filter was a loading phase filter. This filter only passed signals detected during the positive loading phase. The load phase filtering procedure was described above. This particular filter ensured that no crack closure noise (noise generated during unloading of the specimen) was included in the analysis. The second filter was a high load filter. This filter only passed signals detected at loads higher than 7 kN. This filter further reduced the frictional signal density, as crack propagation only occurred at higher loading levels. The left graph in Figure 34 shows an example of unfiltered AE location history. The graph on the right in Figure 34 shows the location history after filtering. The positions of the overlap ends were 14.6 mm and 65.4 mm, respectively. These positions are shown in the history plots as vertical lines. The AE analysis, after filtering, seems capable of tracking the bond

crack propagation under fatigue.

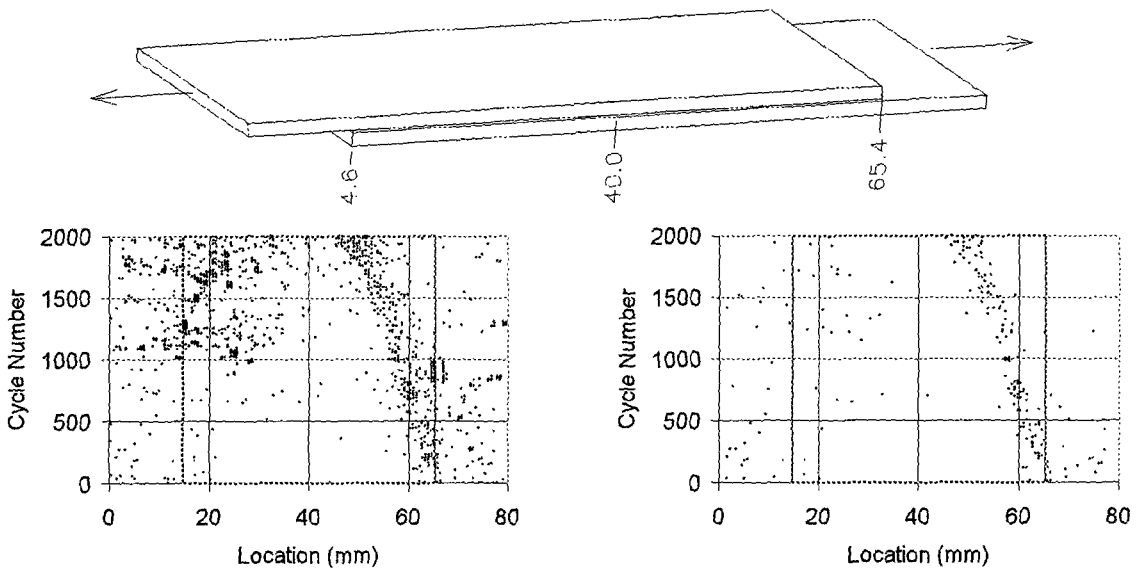

Figure 34: Effect of filtering on AE location history under fatigue

4.6.3.2 Overall AE histories

Figures 35 show cumulative histories of the filtered AE events for the UD and CP specimens, respectively. The signals were filtered according to the procedure described above.

For the UD specimens, the rate of AE accumulation in the crack initiation stage was low. The AE began to increase with the crack initiation. The rate of AE accumulation grew monotonically, for most UD specimens, during the propagation stage. Some specimens produced substantial emission during the final fast fracture (see the experimental curves for specimens UD53 and UD65 in Figure 35).

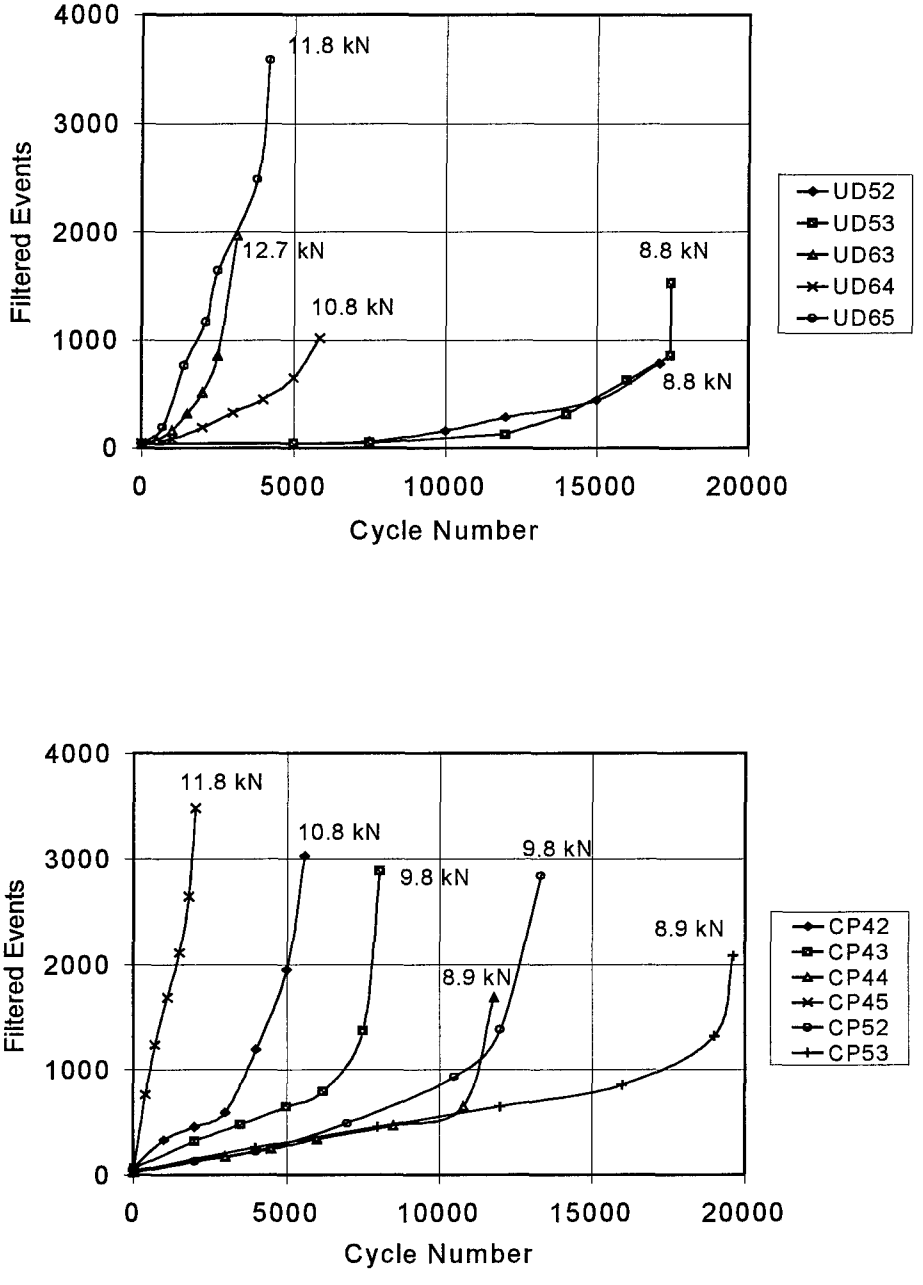

Figure 35: Filtered overall AE histories under fatigue

In the case of CP specimens, the AE accumulation started from the beginning of the fatigue tests. The accumulation continued with an almost constant rate during the crack initiation stage. Some specimens exhibited a decrease in the AE accumulation rate after a few initial cycles of loading (see the experimental curve for specimen CP42 in Figure 35). As in the case of UD specimens, the accumulation rate for the CP specimens began to increase with the crack initiation and grew monotonically during the propagation stage. Overall, more AE signals were picked up from the CP specimens than from the UD specimens. That could be due to more extensive damage in the CP adherends, e.g. matrix cracking within the 90° plies.

4.6.3.3 Crack tip location monitoring

Optical microphotographs of fracture surfaces of the joints broken in fatigue were compared with the results of the linear AE source location analysis (Saunders' M.S. thesis, UNL, 1999). The specimens were roughly classified into three groups: specimens loaded with high loads, intermediate loads, and low loads. The linear AE location analysis was performed by the AMS3 system as described above.

The fractographic analysis of the fatigue specimens revealed that, as in the case of the quasi-static loading, the final fracture was through the bondline, with little or no visible adherend damage. The fracture occurred in both adhesive and cohesive modes. The adhesive type of fracture was accompanied with some fiber breakage and removal from the composite adherends. However, the extent of the fibers fracture was generally low. Some specimens did not exhibit this type of fracture at all.

The slow and fast fracture surface areas created during the second and third stages of the fatigue fracture process could be identified on the specimens by the naked eye. The color of the slow fracture surfaces was generally lighter than the color of the fast fracture surfaces. The analysis showed that, in general, the slow fracture was more adhesive as compared to the fast fracture. The slow cracks propagated through a substantial portion of the total bond area. In all cases, two cracks initiated and propagated from both ends of the overlap. Judging by the final crack fronts in optical micrographs, the propagation of the cracks was not symmetric. Furthermore, the crack fronts were not always perpendicular to the loading direction. However, the geometry of the final crack fronts is not necessarily indicative of the geometry of the crack fronts earlier in fatigue fracture process.

A correlation between fractography and AE location histories revealed that the AE analysis is capable of monitoring the crack front location under fatigue to a certain degree of accuracy. Some of the observed scatter in the AE location data could be due to a complicated crack front geometry mentioned above. The damage in the adherends in the highly stressed areas in the vicinity of the crack tips could also contribute to the location scatter.

4.7 Summary

A new method of acoustic emission analysis of histories of damage micromechanisms was developed in this study. The method was based on a combination of transient and parametric AE analyses. The method was illustrated by the analysis of damage evolution in four graphite-epoxy composites. The characteristic AE waveforms were classified by the transient AE analysis. The

parametric regions occupied by these waveforms in the amplitude-rise time parametric space were identified by the transient-parametric analysis of the unidirectional composites. The multi-parameter filters based on these regions were used to extract the histories of different waveforms for both unidirectional and laminated composites. Physical damage observations were used to correlate the characteristic waveforms with the damage micromechanisms. The quality of the multiparameter filtering for the laminated composites was demonstrated by an inverse parametric-transient analysis.

The hybrid method developed in this work combines the power of the transient AE classification with the relative simplicity of the parametric filtering. The transient waveform classification of the acoustic signals is more robust compared to the parametric classification. The AE parameters of signals from different damage mechanisms often overlap due to the complexity and variability of the damage and wave propagation processes in composites. In many cases, the parametric analysis cannot discriminate between the damage mechanisms. In the examples studied in this work, only one of the four composites, i.e. the cross-ply laminate, exhibited multiple peaks on the distribution histograms. Only one of the two observed peaks could be attributed to a particular damage mechanism. All other composites did not produce multiple peaks in the distribution histograms. None of the composites produced multiple clusters in the multiparameter correlation plots. As a result, even a powerful cluster analysis method could not be applied for parametric signal discrimination. The proposed hybrid transient-parametric analysis, however, allowed the identification of the regions occupied by different AE waveforms in the parametric space. This further allowed the separation of the AE signals from different damage mechanisms by the multiparameter filtering.

It should be noted that the characteristic waveforms and the parametric regions occupied by these waveforms are expected to vary from one material to the other. A separate analysis should be performed for each particular composite system. However, once the transient-parametric analysis is completed and the AE filters are defined, the obtained filters may be applicable for damage evolution studies in other composites within the same material family. The generality of the characteristic waveforms and the parametric regions observed for the four different composite materials in this work corroborates this statement. Since multiparameter filtering procedure requires only the parametric AE data, it is expected that the developed method will be especially advantageous for the study of fatigue damage histories in composites where the full transient waveform analysis may be prohibitive or impractical.

Quasi-static tests of adhesive joints revealed internal damage development in joints prior to bond crack initiation and failure. Most damage was produced at the ends of the overlap region. The damage development might be responsible for the second deformation non-linearity but seemed to have little effect on the final crack path that was through the bondline. Low cycle fatigue tests of joints showed that both deformation histories and filtered acoustic emission histories provided indications of the onset of the bond crack initiation. The AE source location analysis was capable of monitoring the fatigue crack front with a degree of accuracy.

4.8 References

[1] Allen, D.H., Harris, C.E., and Groves, S.E., 1987a. International Journal of Solids and Structures, 23, 1301

[2] Allen, D.H., Harris, C.E., and Groves, S.E., 1987b. International Journal of Solids and Structures, 23, 1319

[3] Awerbuch, J. and Ghaffari, S., 1988. Journal of Reinforced Plastics and Composites, 7, 245

[4] Bakuckas, J.G., Jr., Prosser, W.H., and Johnson, W.S., 1994. Journal of Composite Materials, 28(4): 305-328.

[5] Batdorf, S.B., 1982. Journal of Reinforced Plastics and Composites, 1, p. 153

[6] Chang, C. and Sun, C.T., 1988. Composite Science and Technology, 213-236.

[7] Curtin, W.A., 1993a. Journal of Mechanics and Physics of Solids, 41, p. 217

[8] Curtin, W.A., 1993b. Composites, 23, p. 98

[9] Dzenis, Y.A., Joshi, S.P., and Bogdanovich, A.E., 1994. AIAA Journal, 32, p. 357

[10] Dzenis, Y.A., Joshi, S.P., and Bogdanovich, A.E., 1993. AIAA Journal, 31, p. 2329

[11] Dzenis, Y.A. and Joshi, S.P., 1997. AIAA Journal, 35, p. 1057

[12] Duke, J.C., ed., 1988. Acousto-Ultrasonics: Theory and Application, Plenum Press

[13] Ely, T.M. and Hill, E.v.K., 1995. Materials Evaluations, Feb: 288-294.

[14] Gorman, M.R., 1992. In: Composite materials, 4th Int Symp on AE from Composites, Seattle, 395-400.

[15] Groot, P.J. de, Wijnen, P.A.M., and Janssen, R.B.F., 1995. Composite Science and Technology, 55: 405-412.

[16] Gunyaev, G.M., 1985. In: Handbook of Composites, Vol. 3. - Failure Mechanics of Composites, Elsevier, New York, p. 376

[17] Harlow, D.G. and Phoenix, S.L., 1979. International Journal of Fracture, 15, p. 321

[18] Hu, S., 1996. Composites Science and Technology, 56, 667

[19] Kloua, H., Maslouhi, A., and Roy, C., 1995. Canadian Aeronautics and Space Journal, 41, 21

[20] Kouvarakos, M. and Hill, E.v.K., 1996. Materials Evaluations, Sept: 1025-1031.

[21] Knollman, G.C., Martinson, R.H., and Bellin, J.L., 1980. Journal of Applied Physics, 51, 3164

[22] Knollman, G.C. and Yee, R.C., 1988. Experimental Mechanics, June, 110

[23] Ladeveze, P., Allix, O., Cluzel, C., and d'Evry, I.U.T., 1993. In: Damage in Composite Materials, G.Z. Voyiadjis, Ed., Elsevier, New York, p. 195

[24] Lorenzo, L. and Hahn, H.T., 1988. In: Composite Materials: Testing and Design, ASTM STP 972, American Society for Testing and Materials, Philadelphia, p. 380

[25] Luo, J.-J., Wooh, S.-C., and Daniel, I.M., 1995. Journal of Composite Materials, 29 (15): 1946-1961.

[26] Masters, J.E., ed., 1992. Damage Detection in Composite Materials, ASTM STP 1128, American Society for Testing and Materials, Philadelphia

[27] Masters, J.E. and Reifsnider, K.L., 1980. In: Damage in Composite Materials, ASTM STP 775: 40-65.

[28] Ono, K. and Huang, Q., 1996. Personal communication.

[29] Ovchinskii, A.S., 1988. Fracture Processes in Composite Materials: Computer Simulation of Micro- and MacroMechanisms, Nauka, Moscow (In Russian)

[30] Phoenix, S.L., 1993. Composite Science and Technology, 48, p. 65

[31] Pipes, R.B., ed., 1979. Nondestructive Evaluation and Flaw Criticality for Composite Mate-

rials, ASTM STP 696, American Society for Testing and Materials, Philadelphia.

[32] Prosser, W.H., Jackson, K.E., Kellas, S., Smith, B.T., McKeon, J., and Friedman, A., 1995. Materials Evaluations, Sept: 1052-1058.

[33] Qian, J. and Dzenis, Y.A., 1999. Journal of Acoustic Emission (submitted)

[34] Reifsnider, K.L., Lesco, J., Case, S., 1995. In: COMPOSITES'95: Recent Advances in Japan and the United States, Kyoto, Japan, p. 49

[35] Rosen, B.W., 1964. AIAA Journal, 2, p. 1985

[36] Shiwa, M., Carpenter, S., and Kishi, T., 1996. Journal of Composite Materials, 18, 2019

[37] Summerscales, J., ed, 1987. Non-Destructive Testing of Fibre-Reinforced Plastic Composites, Vol. 1. Elsevier Applied Science

[38] Tamuzh, V.P., 1979. In: Fracture of Composite Materials, G.C. Sih and V.P. Tamuzh, Eds., Sijthoff, Alphen aan den Rijn, The Netherlads, p. 13

[39] Tiwari, A. and Henneke, E.G., 1993. In: Acousto-Ultrasonic Material Characterization (ed A. Vary), ASNT, p. 273

[40] Tiwari, A., Henneke, E.G., and Reifsnider, K.L., 1995. Journal of Composites Technology and Research, 17, p. 221

[41] Tsai, S.W. and Hahn, H.T., 1980. Introduction to Composite Materials, Technomic.

[42] Vary, A., 1982. Materials Evaluation, 40, 650

[43] Vary, A., ed, 1993. Acousto-Ultrasonic Material Characterization, ASNT

[44] Wevers, M., Verpoest, I., De Meester, P., and Aernoudt, E., 1991. In: Acoustic Emission: Current Practice and Future Directions, ASTM STP 1077 (eds W. Sachse, J. Roget, and K. Yamaguchi), American Society for Testing and Materials, Philadelphia, p. 416

[45] Williams, R.S. and Reifsnider, K.L., 1974. Journal of Composite Materials, 8, p. 340

[46] Yamaguchi, K., Oyaizu, H., Johkaji, J., and Kobayashi, Y., 1991. In: Acoustic Emission: Current Practice and Future Directions, ASTM STP 1077 (eds W. Sachse, J. Roget, and K. Yamaguchi), American Society for Testing and Materials, Philadelphia, p. 123

[47] Zweben, C., 1968. AIAA Journal, 6, p. 2325

APPENDIX 5: FRACTURE MECHANICS CHARACTERIZATION OF JOINTS WITH UNIDIRECTIONAL AND CROSS-PLY ADHERENDS

Contributors: I. Saunders, M. Forte (AFRL), S. Donaldson (AFRL)

5.1 Introduction 193

5.2 Experimental 197
5.2.1 Test methods and data reduction 197
5.2.1.1 DCB test method 197
5.2.1.2 ENF test method 199
5.2.1.3 Arcan test method 201
5.2.2 Specimen geometry and manufacturing 204
5.2.3 Specimen nomenclature 207

5.3 Static Mode I Fracture 208
5.3.1 Mechanical response 208
5.3.2 Critical energy release rates 210
5.3.3 Optical fractography and AE source location 210

5.4 Static Mode II Fracture 215
5.4.1 Mechanical response 215
5.4.2 Critical energy release rates 215
5.4.3 Optical fractography and AE source location 217

5.5 Static Mixed Mode Fracture 220
5.5.1 Mechanical response 220
5.5.2 Critical stress intensity factors and energy release rates 220

5.6 Fatigue Fracture (preliminary) 222
5.6.1 Fatigue fracture mechanics 222
5.6.2 Preliminary results 225

5.7 AE Analysis of Fracture Micromechanisms (preliminary) 228
5.7.1 Transient waveshape classification 228
5.7.2 Comparison of parametric filtering and waveshape classification 229
5.7.3 Fracture micromechanisms under Mode I, II, and mixed mode loadings 231

5.8 Summary 233

5.9 References 235

5.10 Enclosure: Large Radius Axisymmetric Damage Model (LRAM) 239

Appendix 5 of this report consolidates data on fracture mechanics characterization of adhesive composite joints. Static mode I, mode II, and mixed mode analysis is performed by DCB, ENF, and Arcan tests. Several data reduction schemes are applied and compared. Fracture mechanisms are studied by fractographic analysis. AE location analysis is applied for crack tip location evaluation. Preliminary fatigue tests and AE analysis of fracture micromechanisms under pure and mixed mode loadings are also reported.

5.1 Introduction

Many isotropic materials fail with the extension of the critical (largest) crack in the material. Fracture mechanics is used to analyze such crack growth. Most composite materials, on the other hand, fail with a gradual accumulation of microcracks of different types that then coalesce. The stress fields that arise at the crack tip of such cracks are also extremely complex. Damage mechanics theories are used to analyze the complicated damage accumulation. In general, the final failure is very complex because of the interaction of the main propagating crack with the distributed damage. Therefore, a combination of damage and fracture mechanics is needed to analyze the failure. This complicated fracture can be expected for joints with composite adherends too. The quantitative measure of the effects of defects in composite structures is a key issue in material selection, manufacturing procedures, maintenance planning, and repair decisions [1-4], and the adhesive fracture problem must be well understood before safe and efficient composite structures can be designed.

In Parts 1 and 4 of this report, it was observed that some damage accumulation occurred in the composite adherends prior to failure under static loading. However, the final failure seemed relatively unaffected by this damage and the crack propagated mostly through the adhesive bondline. Under fatigue loading, the adhesive lap joints failed by progressive crack growth in the bondline. These results indicate that an appropriate failure criterion for joints should be based on fracture mechanics. Fracture of the joint through the bondline resembles interlaminar fracture of composites that is well studied.

Interlaminar cracking or delamination can occur under three basic loading modes, i.e., opening or peel mode (Mode I), forward sliding shear mode (Mode II), or tearing mode (Mode III), or under combinations thereof (mixed mode). The resistance to delamination growth is expressed in terms of the interlaminar fracture toughness, which is measured by the critical strain energy release rates, G_{IC}, G_{IIC}, and G_{IIIC} or critical stress intensity factors, K_{IC}, K_{IIC}, and K_{IIIC}. It was shown in Appendix 2 that the single lap joint under tensile loading is subjected to a mixed mode condition, with contributions from both Mode I and Mode II. In order to analyze mixed mode behavior, simpler pure mode loadings should be carefully studied first.

Since delamination is one of the prevalent life-limiting failure mode in advanced composite structures and is a fundamental issue in their evaluation for both durability and damage tolerance, many test methods have been devised to measure inter-ply fracture toughness of composite lay-ups. These include double cantilever beam (DCB), end notch flexure (ENF), cracked lap shear (CLS), mixed mode bending (MMB), asymmetrically loaded double cantilever beam (ALDCB), mixed mode flexure (MMF) and Arcan test methods.

ASTM standards exist for both DCB [5] and ENF [6] tests. Hinge position for DCB test-

ing is important. ASTM standards show the hinge placed away from the edge of the specimen, but most research is done with the hinge at the edge of the specimen. Round robin test series gave a good understanding of the typical requirements for specimen geometries, apparatus and procedures, and fracture energy calculations.

Round robin DCB test results have been published [7]. This reference points out some difficulties that may be encountered with manufacturing the panels, as well as problems that may be encountered during the conduction of the tests. Interestingly enough, the area method (see Section 4.3) is not recommended due to the fact that neither does it yield an initiation value of G_{IC}, nor a delamination resistance curve.

Pure mode testing has also been found to be a useful tool for screening composites to improve delamination resistance [8]. Significant improvements in delamination resistance can be achieved by tailoring the construction of the laminate. The incorporation of an adhesive in-lay, either by itself or in combination with a Kevlar mat, was found to be effective in increasing delamination resistance [9]. Investigations have also been done on filled and rubber toughened adhesive systems [10], as well as on epoxies filled with glass beads [11]. The results showed the increased crack growth resistance obtained with these methods and therefore an extended fatigue life.

From the discussion it is clear that most of the literature on fracture mechanics of composites centers around the delamination between plies in a composite lay-up. These theories and test procedures can be extended to an adhesive layer between composite adherends. Typical G_C values for a structural adhesive are known to be about 10 times higher than that of a composite 0/0 ply interface [9]. One of the important aspects to address is how accurate are the theories used for

data reduction, and whether they have to be modified to model the adhesive system properly. Computer modeling of the adhesive joint specimen configurations is one way to obtain more accurate theoretical curves.

Once the Mode I and Mode II behavior is known, the mixed mode behavior can be sometimes described utilizing a suitable mixed mode fracture model. A possible form of a mixed mode fracture criterion based on energy release rate is expressed as [13]:

$$\left(\frac{G_I}{G_{IC}}\right)^m + \left(\frac{G_{II}}{G_{IIC}}\right)^n + k\left(\frac{G_I}{G_{IC}}\right)\left(\frac{G_{II}}{G_{IIC}}\right) = 1 \tag{1}$$

where the parameters m, n, and k may be determined by correlating experimental data.

A simpler model for a linear variation has also been used:

$$\left(\frac{G_I}{G_{IC}}\right) + \left(\frac{G_{II}}{G_{IIC}}\right) = 1 \tag{2}$$

Appendix 5 of this report is devoted to static experimental characterization of fracture of the FM300-2M adhesive joints with unidirectional and cross-ply adherends. Preliminary fatigue analysis is also performed and reported.

5.2 Experimental

5.2.1 Test methods and data reduction

5.2.1.1 DCB test method

The double cantilever beam (DCB) specimen for Mode I fracture analysis is shown in Figure 1.

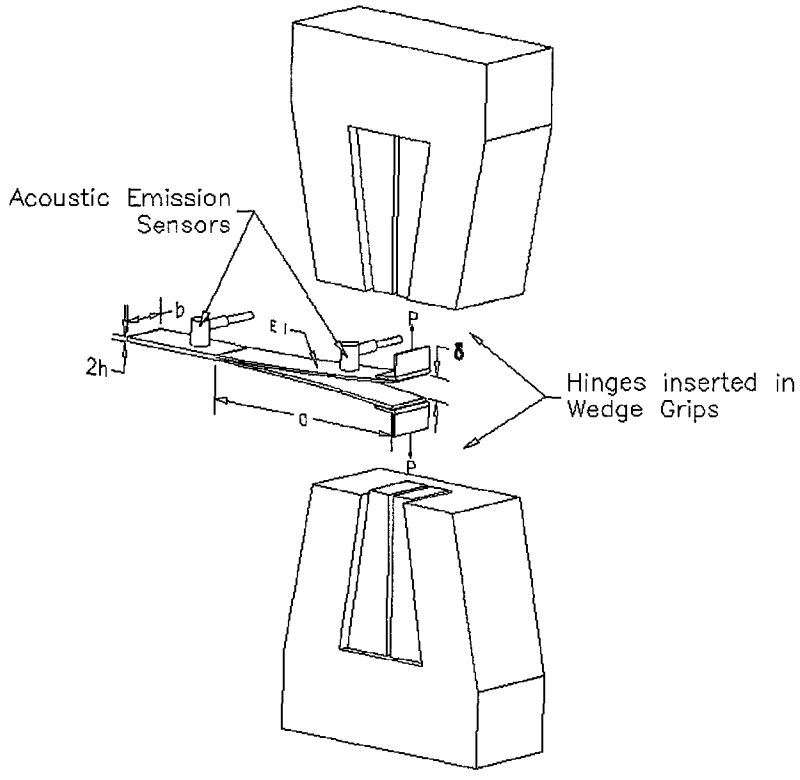

Figure 1: DCB test layout

For linear elastic behavior and the case where the downloading curve returns to the origin, and where the load-displacement curve can be approximated with a straight line, G_{IC} can be determined from the following equation [17]:

$$G_{IC} = \frac{P_A \delta_B - P_B \delta_A}{2b(\Delta a)} \tag{3}$$

where P and δ are the load and displacement at the denoted points, b is the width and Δa is the increment in crack length. This formula equates G_{IC} to the area below the load-displacement curve. An average G_{IC} value is obtained from the total series of loading and unloading. This method is known as the area method, and is only valid for linear load-displacement response.

Beam theory was used to compare results to the area method. In the beam or compliance method, the specimen is assumed to consist of two identical cantilever beams with built-in ends and length equal to the length of the crack. Beam theory for an anisotropic material leads to the following relationship [18]:

$$G_{IC} = \frac{12P^2}{E_1 b^2 h}\left[\left(\frac{a}{h}\right)^2 + \frac{E_1}{10G_{31}}\right] \tag{4}$$

where P is the applied load, a is the crack length, b is the specimen width, and $2h$ is the thickness.

Beam theory, however, does not take into account the thin adhesive layer, which plays a larger role for thin adherends. Dr. Mark Forte applied the Large Radius Axisymmetric Dam Model (LRAM) developed at WPAFB [19] to model the DCB specimen configuration and

obtained a more accurate theoretical prediction for the G_{IC} values (see Appendix). Figure 2 presents the differences between the beam method and the LRAM model in terms of normali energy release rate curves.

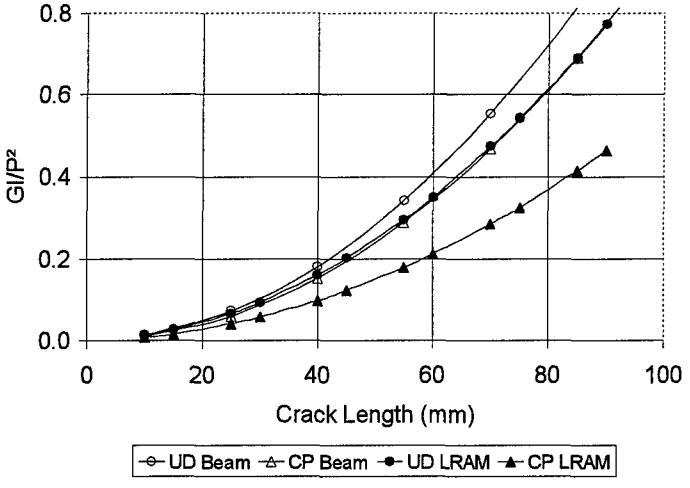

Figure 2: DCB normalized energy release rate curves

5.2.1.2 ENF test method

The end notch flexure (ENF) specimen is shown in Figure 3. The purpose of this test is to determine the critical strain energy release rate in Mode II loading. The configuration produces shear loading at the crack tip without introducing excessive friction between the crack surfaces.

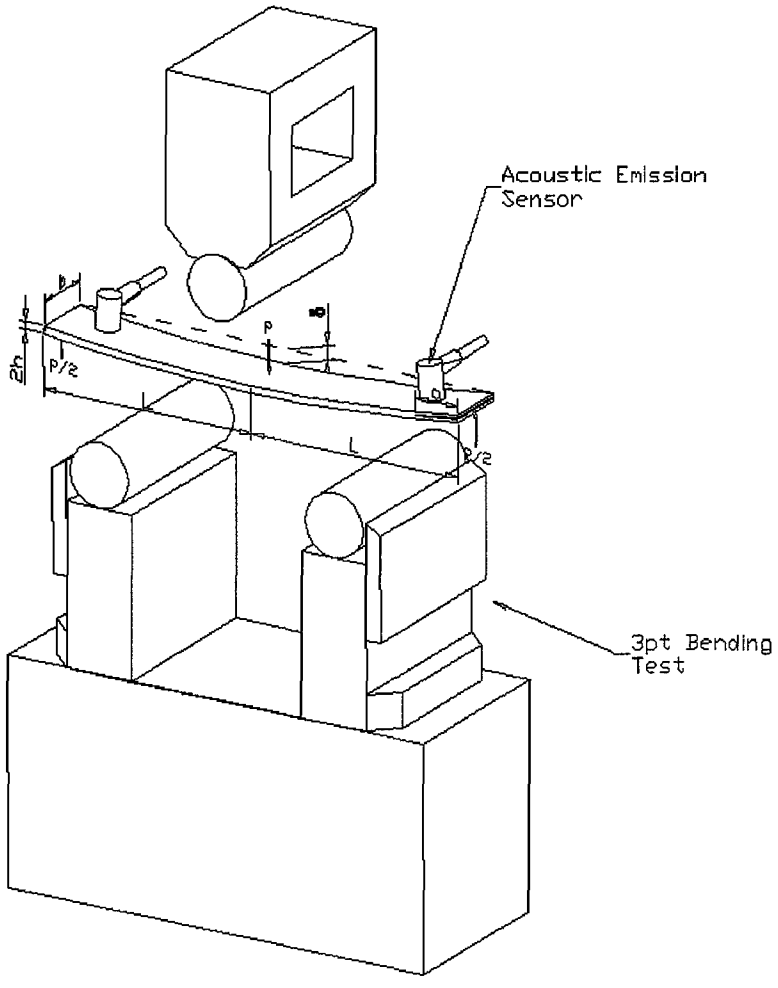

Figure 3: ENF test layout

For the ENF fatigue testing it was necessary to fix clips to the specimen to ensure that it did not move relative to the rollers during the cyclic loading. From elastic beam theory, the following expression for the strain energy release rate can be derived for the anisotropic case [18]:

$$G_{IIC} = \frac{9P^2a^2}{16E_1b^2h^3}\left[1 + 0.2\frac{E_1}{G_{31}}\left(\frac{h}{a}\right)^2\right] \tag{5}$$

where P is the applied load, a is the crack length, b is the specimen width, $2h$ is the thickness, and L is the span between the central loading pin and the outer support pins.

In the derivations of the above equation, the influence of friction between crack surfaces was neglected. As a conservative estimate, the beam theory expression appears satisfactory. For the commonly used $a \approx L/2$ the crack growth is unstable even under fixed grip conditions.

Figure 4 presents normalized energy release rate curves obtained by the beam theory and LRAM modeling (see Appendix), similar to those presented in the DCB case.

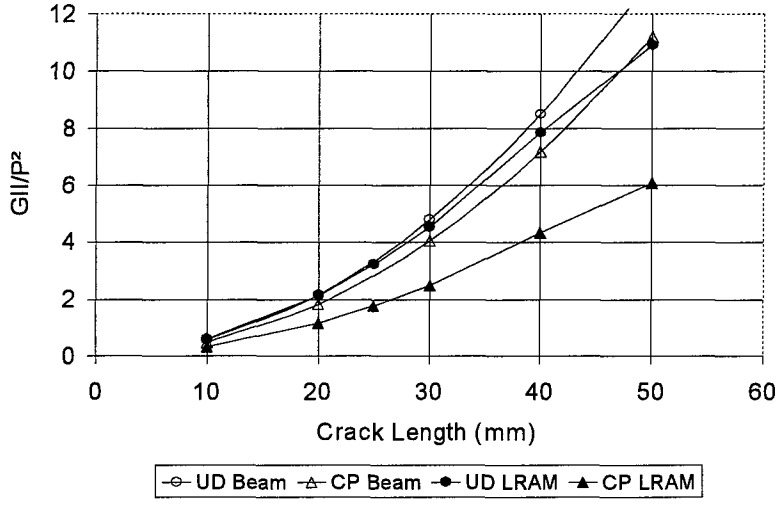

Figure 4: ENF normalized energy release rate curves

5.2.1.3 Arcan test method

The Arcan fixture (shown in Figure 5) and specimen geometry were developed by Arcan et al. in an attempt to produce uniform plane stress in the test section [17]. By varying the angle, α, from 0° to 90°, Mode II, mixed mode, and Mode I data may be obtained.

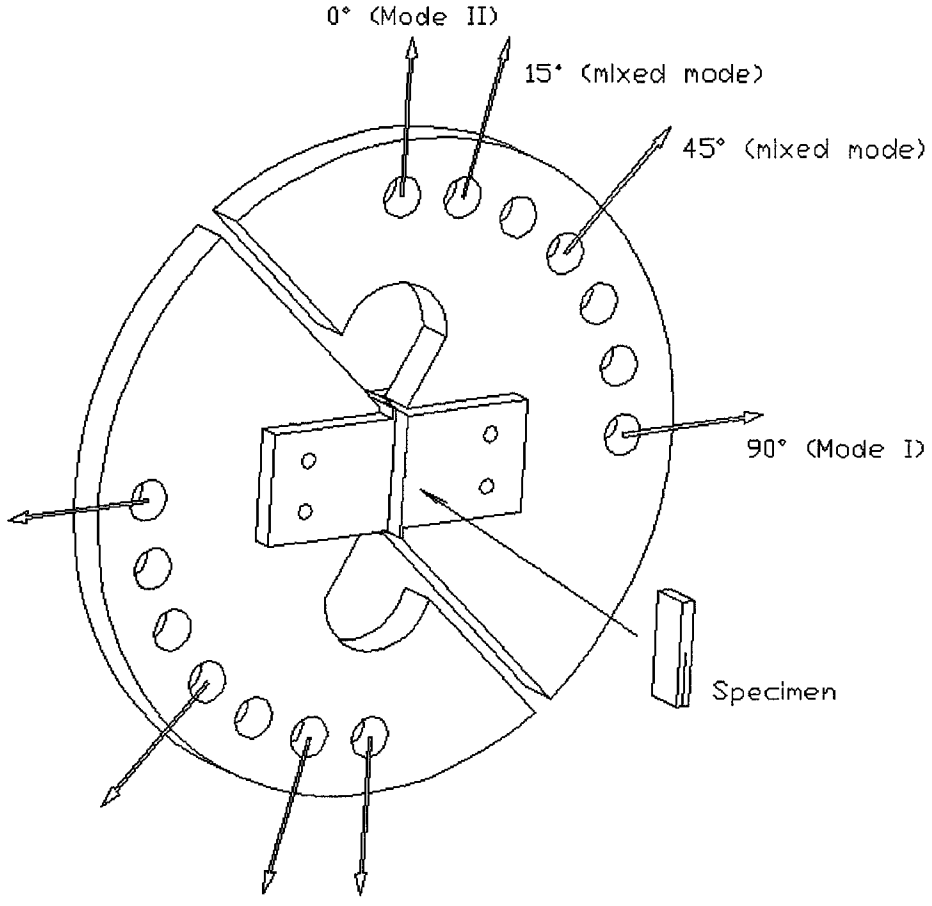

Figure 5: Arcan test layout

For a given angle, α, the 'far field' normal and shear stresses may be determined as:

$$\sigma^{\infty} = \sigma_A \sin\alpha$$
$$\tau^{\infty} = \sigma_A \cos\alpha \qquad (6)$$

Based on the normal and shear stress components, the stress intensity factors K_I and K_{II} associated with the opening and shearing mode may be determined as:

$$K_I = \sigma^{\infty}\sqrt{\pi a} f_I\left(\frac{a}{c}\right)$$
$$K_{II} = \tau^{\infty}\sqrt{\pi a} f_{II}\left(\frac{a}{c}\right) \tag{7}$$

where a is the crack length, c is the dimension of the specimen along the crack, and f_I and f_{II} are correction factors for finite crack length to specimen length ratio, given as:

$$f_I\left(\frac{a}{c}\right) = 1.12 - 0.231\left(\frac{a}{c}\right) + 10.55\left(\frac{a}{c}\right)^2 - 21.27\left(\frac{a}{c}\right)^3 + 30.39\left(\frac{a}{c}\right)^4$$
$$f_{II}\left(\frac{a}{c}\right) = \frac{1.122 - 0.561\left(\frac{a}{c}\right) + 0.085\left(\frac{a}{c}\right)^2 + 0.180\left(\frac{a}{c}\right)^3}{\sqrt{1-\left(\frac{a}{c}\right)}} \tag{8}$$

For a crack in a homogeneous isotropic material, a simple relationship exists between the energy release rates and the stress intensity factors [4]:

(9)

$$G_{IC} = \frac{K_{IC}^{\ 2}}{E'} \qquad G_{IIC} = \frac{K_{IIC}^{\ 2}}{E'}$$
$$E' = E \quad \text{- for plane stress}$$
$$E' = \frac{E}{(1-\nu^2)} \quad \text{- for plane strain}$$

For a crack at the center of an adhesive layer, relatively distant from any interface, it was assumed that the above expression is still valid, and the appropriate values of the elastic properties for the adhesive were substituted [20]. The condition of plane strain was assumed in the case of the Arcan specimen. Alternatively, the strain energy release rate components G_I and G_{II} may be

obtained as follows from the stress intensity factors in the case of composite material adherends [17]:

(10)

$$G_I = K_I^{\,2}\left(\frac{S_{11}S_{22}}{2}\right)^{\frac{1}{2}}\left[\left(\frac{S_{22}}{S_{11}}\right)^{\frac{1}{2}} + \frac{2S_{12}+S_{66}}{2S_{11}}\right]^{\frac{1}{2}}$$

$$G_{II} = K_{II}^{\,2}\frac{S_{11}}{\sqrt{2}}\left[\left(\frac{S_{22}}{S_{11}}\right)^{\frac{1}{2}} + \frac{2S_{12}+S_{66}}{2S_{11}}\right]^{\frac{1}{2}}$$

The S_{ij} are elements of the compliance matrix for orthotropic composite material.

5.2.2 Specimen geometry and manufacturing

Manufacturing of the composite joint specimens for fracture tests was similar as to that of the lap joint specimens described in Appendix 1. Lay-up, curing, and composite adherend and adhesive surface preparation were the same. The geometries of the fracture specimens were different. Also, new surface preparation techniques had to be applied to bond DCB and Arcan composite specimens metal fixtures.

The new geometries are presented first, and after that a detailed description of adequate surface preparation is given.

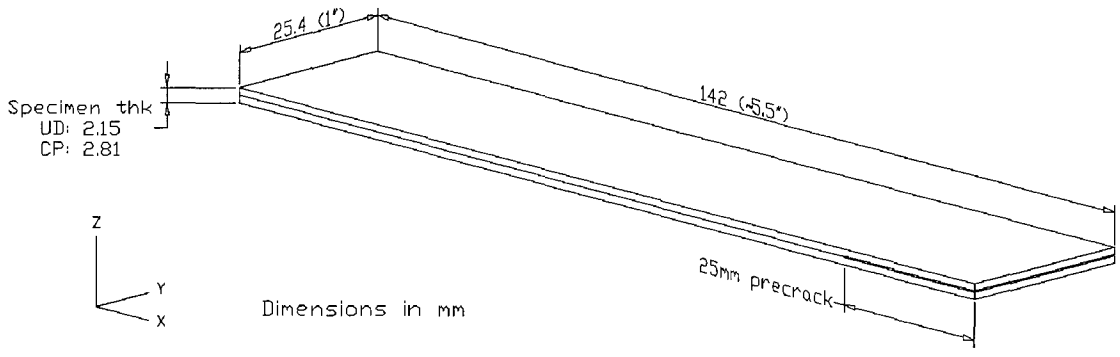

Figure 6: DCB and ENF specimen geometries

The DCB and ENF specimens had similar geometry, as shown in Figure 6. The UD specimens had an average thickness of 2.15 mm and the CP specimens had an average thickness of 2.81 mm. The specimens had a pre-crack of 25 mm created by a thin Teflon film inserted during manufacturing. In the DCB specimens, the crack was advanced 15 mm to obtain a natural crack. The energy release rates were measured from crack lengths of 40 mm onwards. The ENF specimens were placed on the bottom rollers spaced 100 mm apart. The top roller pushed down at the center of the specimen (Figure 3).

The Arcan specimens were all unidirectional and had an average thickness of 4.4 mm. All of the specimens were 35 mm long, and had a Teflon pre-crack of 20 mm (Figure 7).

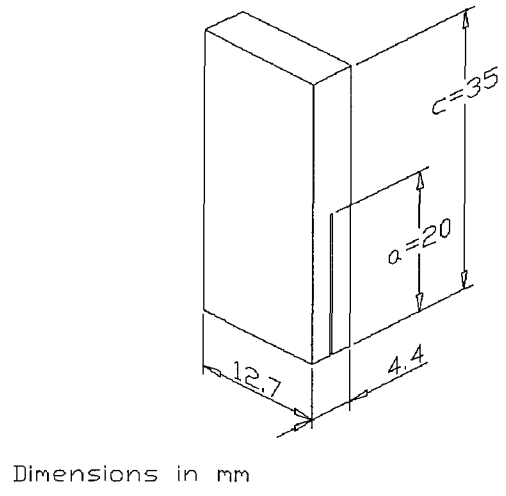

Figure 7: Arcan specimen geometry

Metal hinges had to be attached to DCB specimens, and Arcan specimens had to be bonded to two metal brackets. The surface preparation for the DCB hinges and Arcan brackets required serious attention and therefore a review of adhesion between metals and composites is presented.

Except for a little mechanical keying, one relies on adsorption of the adhesive on clean, reactive, high-energy metal surfaces that may, in some cases, be rough and have an increased surface area. Any contamination will reduce the surface energy and the possibility of any chemical bonds, while increasing the distance over which the van der Waals forces must operate. These forces are close-range attractive forces. They operate over a limited distance, which explains why two rough surfaces do not adhere properly. For this reason, low-viscosity primers, which flow and wet a surface, also provide a good base for an adhesive. The reason for using a liquid adhesive is that it can get into this necessary close-range contact in which the van der Waals forces

operate. The adhesive must also have a lower surface energy than the surfaces to be bonded.

Although many factors affect the performance of metal adhesive bonding, surface preparation is the one factor that will decide the success or failure of metal adhesive bonds, especially under hot and/or wet conditions. Both the type of treatment and the quality to which it is performed will have more effect on durability than any other factor and possibly more effect than all others combined.

The following methods for metal surface preparation were used in the laboratory (in order of application):

- Grit blasting / Abrasion Too
- Ultrasonic cleaning: The part to be cleaned is immersed in a bath of cleaning liquid or solvent that is ultrasonically activated by a high-frequency transducer. High-frequency vibrations then dislodge the contaminants within a matter of seconds.
- Solvent cleaning (Miller Stephenson Safezone cleaning solvent MS-944/CO2)

5.2.3 Specimen nomenclature

The nomenclature of the fracture mechanics specimens was as follows:

- UDCB Unidirectional adherends, DCB test configuration
- CDCB Cross-ply adherends, DCB test configuration
- UENF Unidirectional adherends, ENF test configurati
- CENF Cross-ply adherends, ENF test configuration

Similarly to the lap joint specimens, the first number referred to the number of the plate manufactured, and the last number referred to the number of the specimen cut from that plate. All unidirectional adherends had a $[0]_6$ lay-up, except for the Arcan specimens, which had a $_{12}$ lay-up. All cross-ply adherends had a $[0/90]_{2S}$ lay-up.

For example, UDCB12 has a unidirectional lay-up, and it was cut from the 1st plate, the 2nd specim

5.3 Static Mode I Fracture

5.3.1 Mechanical response

Results of the typical mechanical response from static DCB testing of UD and CP s are shown in Figures 8 and 9, respectively. Marker lines were made on the specimen side at 15 mm intervals. The specimen was then loaded with a crosshead rate of 2 mm/min. Load-crack opening displacement curves were generated. Crack opening displacement was measured directly form the position of the piston. After each 15 mm crack propagation interval, the specimen was unloaded, therefore the triangular loading patterns. The loading curves were approximated afterwards with straight lines to indicate the area method triangles and the points used for the beam method.

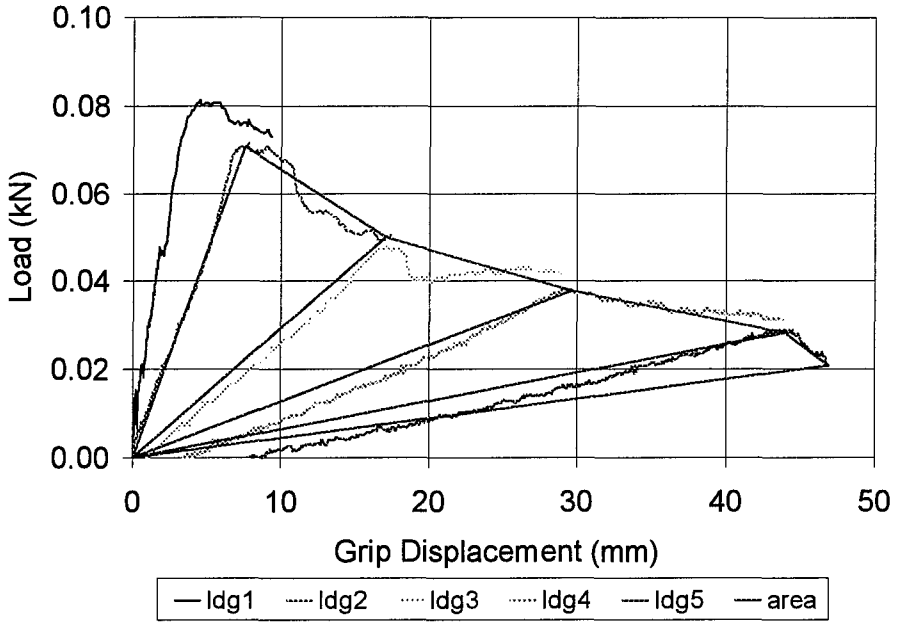

Figure 8: Load-displacement curve of UDCB13 test

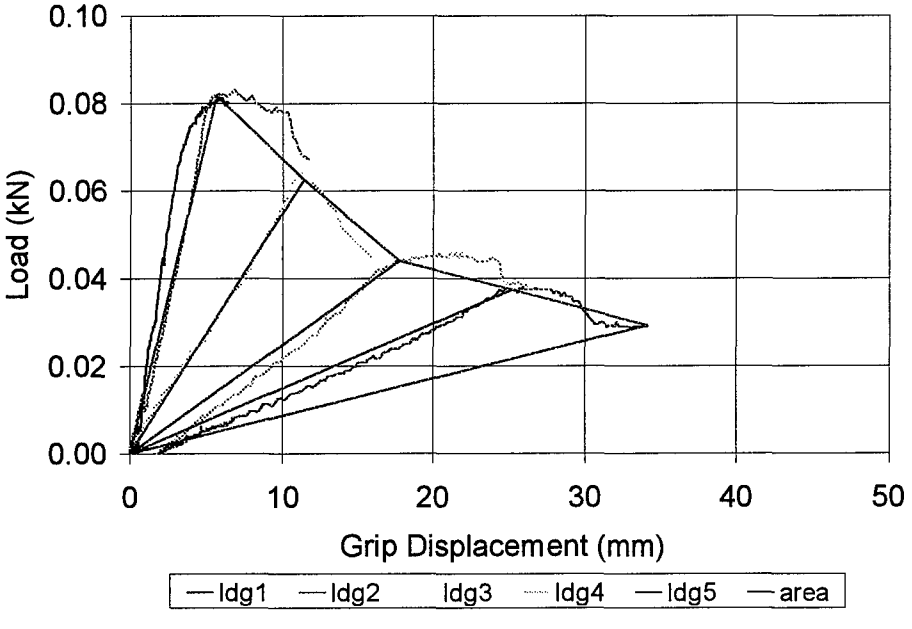

Figure 9: Load-displacement curve of CDCB13 test

5.3.2 Critical energy release rates

Results for energy release rates given by the area, beam, and LRAM methods are shown in Figures 10 and 11. Figure 10 shows the results obtained for UD specimens and Figure 11 shows the results obtained for CP specimens.

In both UD and CP cases, the points measured at larger crack lengths gave smaller energy release rates, especially in the case of UD specimens.

5.3.3 Optical fractography and AE source location

Results of optical fractography and the corresponding AE source location are shown in Figures 12 to 15. The slow and fast fracture areas (Figure 12) are not the same as those described in Appendix 1. The slow fracture was created by the static testing, and the fast fracture was formed when the specimen was torn apart by hand after the test.

Mode I failure of adhesive bonds resulted in a fuzzy surface caused by the polyester fibers being torn from the adhesive. This may be seen clearly from the zoomed pictures in Figure 13.

Below the fractographic pictures are the AE location graphs. The signals were filtered form the original AE data set with a simple amplitude filter ($A > 60$ dB). Refer to Appendix 4 for an explanation on AE parameters.

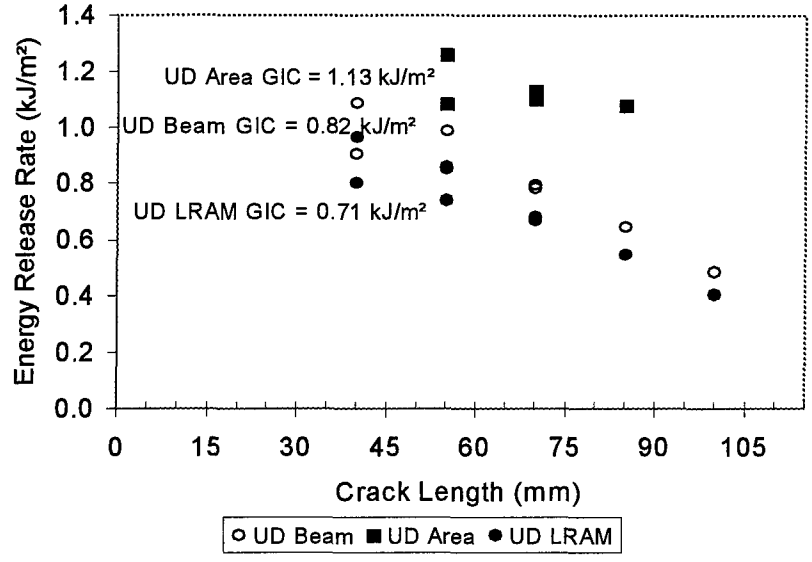

Figure 10: Experimental UD G_{IC} values

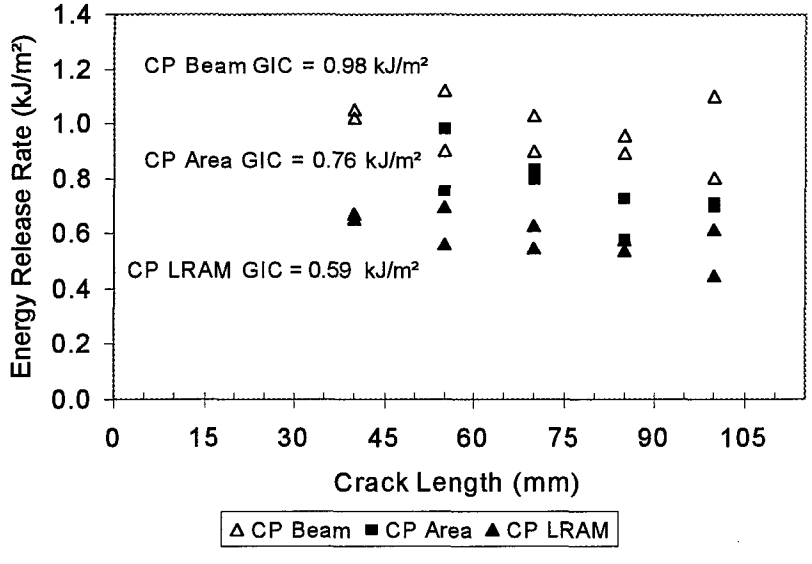

Figure 11: Experimental CP G_{IC} values

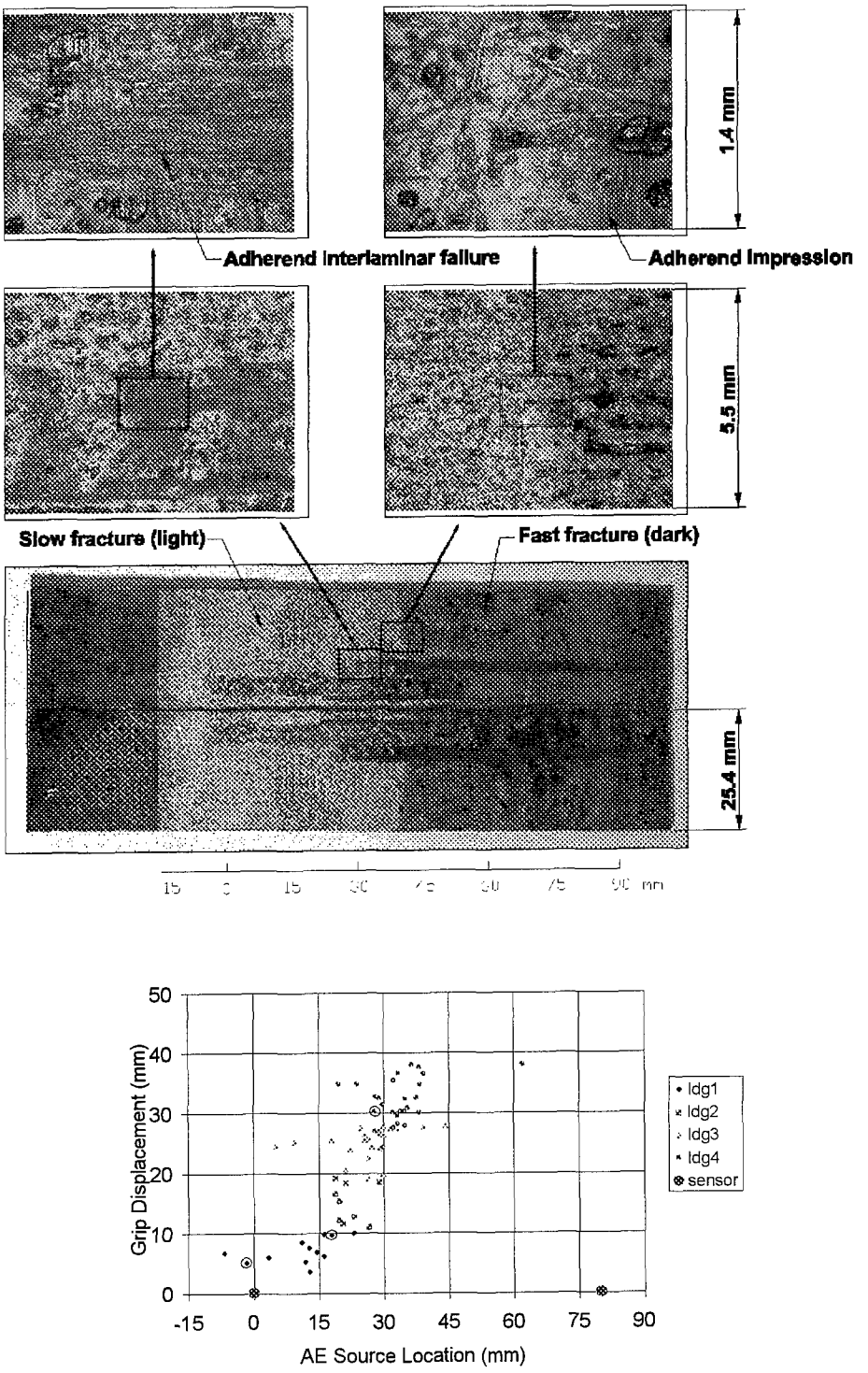

Figure 12: Correlation between fracture surface and AE location for UDCB23

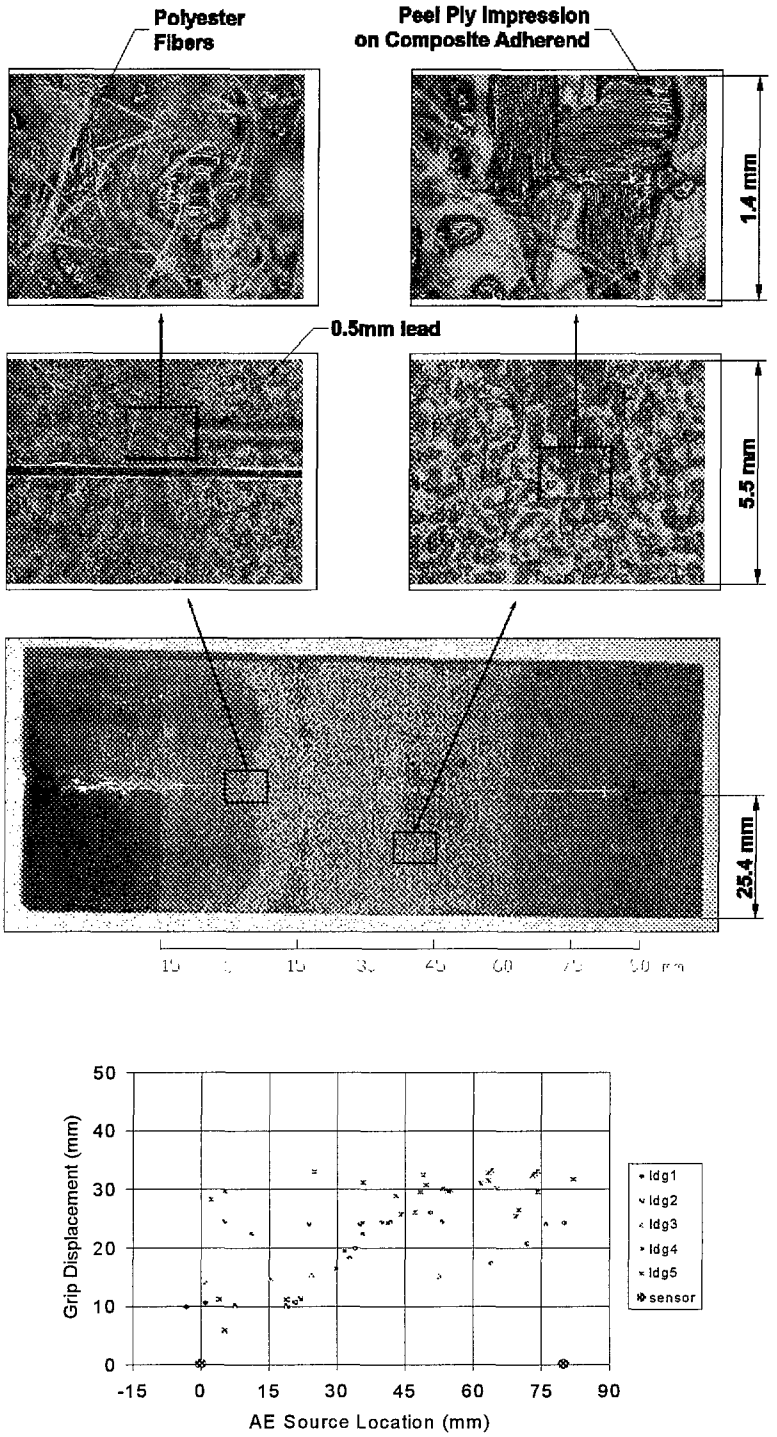

Figure 13: Correlation between fracture surface and AE location for CDCB13

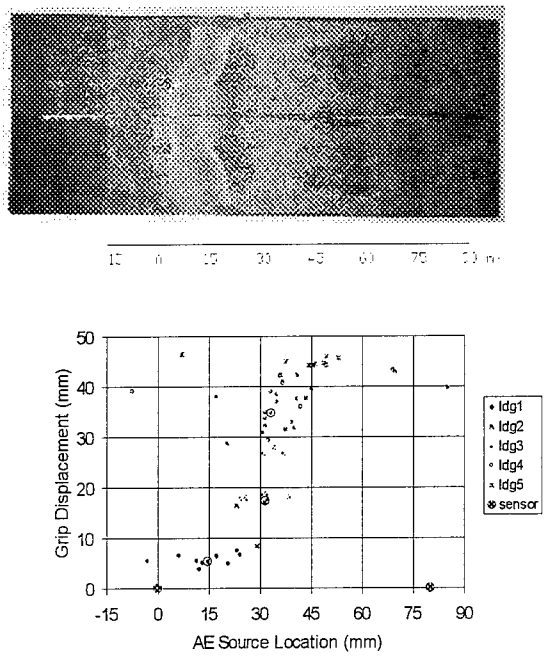

Figure 14: AE location: UDCB13

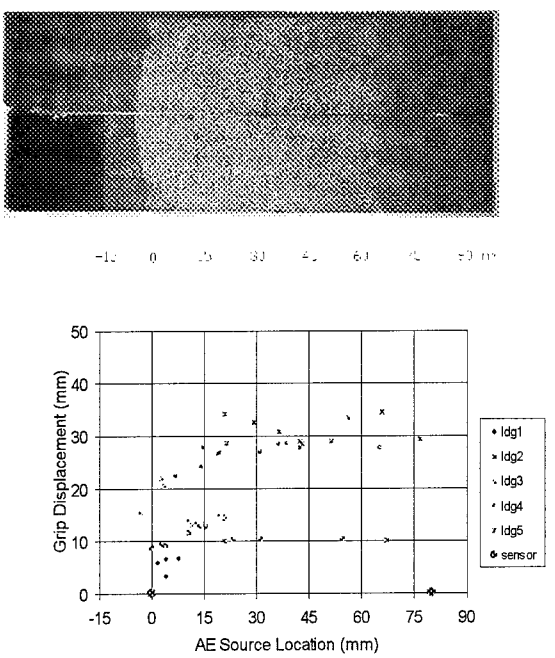

Figure 15: AE location: CDCB23

Note that in AE location graphs the first AE sensor was placed at position that corresponded with a crack length of 40 mm. This means the zero location indicates the position from where the energy release rate measurements started. Also note that crack 1 refers to the initial crack propagation stage from the –15 mm to 0 mm position. Crack 2 lies between 0 mm and 15 mm, crack 3 between 15 mm and 30 mm, etc. The results indicated that the location of the crack could be followed with an accuracy of ±10 mm.

This section therefore shows that AE analysis can be used for Mode I crack monitoring in the adhesive layer.

5.4 Static Mode II Fracture

5.4.1 Mechanical response

Figures 16 and 17 show the mechanical response of the UD and CP specimens in the ENF test, respectively. A crosshead rate of 5 mm/min was used to load the specimens.

Load-displacement curves were generated during the test. Displacement (deflection) was measured from the piston stroke. At some critical load, the crack started propagating in an unstable manner.

5.4.2 Critical energy release rates

Figure 18 shows the critical energy release rates calculated from the four UENF and four CENF specimens that were tested. Note that some of the data points overl

The averages for each data reduction method are shown, as well as their standard deviations. The results are summarized in the Table 1, together with the values obtained from the DCB tests.

Table 1: Experimental critical energy release rates

	Area method	**Beam method**	**LRAM model**
UD G_{IC} (kJ/m^2)	1.13	0.82	0.71
CP G_{IC} (kJ/m^2)	0.76	0.98	0.59
UD G_{IIC} (kJ/m^2)		1.48	1.36
CP G_{IIC} (kJ/m^2)		2.45	1.46

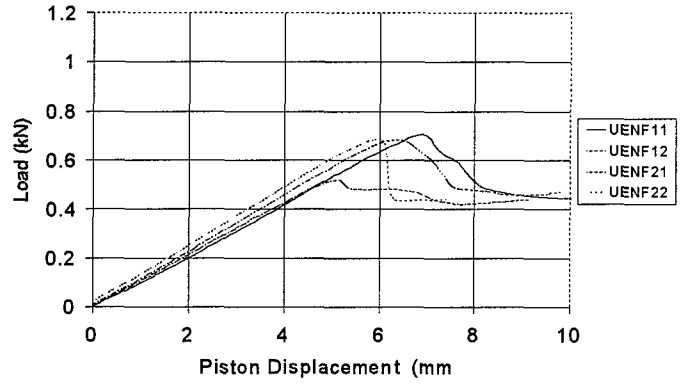

Figure 16: UENF mechanical response

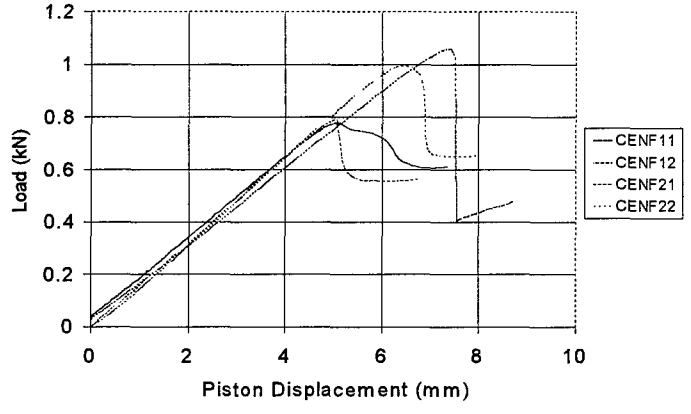

Figure 17: CENF mechanical response

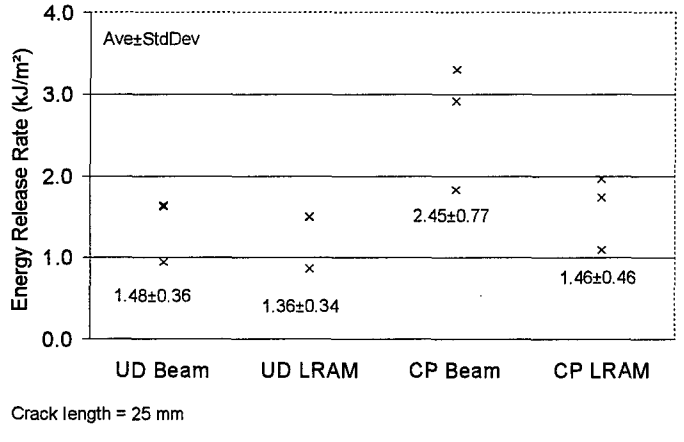

Figure 18: Experimental G_{IIC} Values

Similar to the DCB analysis, it is seen that the beam method overestimates fracture toughness of the adhesive joint.

5.4.3 Optical fractography and AE source location

Figures 19 and 20 show results obtained for fractography and AE source location for the ENF tests.

The pre-crack (manufactured with Teflon film) is the dark region. Unlike the fracture surfaces produced form Mode I failure, which were fuzzy due to the tear-out of the polyester fibers, the fracture surfaces of the Mode II failure show the adhesive to be more clumpy.

The AE location analysis is plotted below the fractographic images. The acoustic sensors were placed 15 mm into the starter crack region, thus the crack started growing from a location of 15 mm as indicated in the AE figures, and grew to a location of 40 mm. The bottom roller was at position −10 mm, and the top roller pushed downward at position 40 mm.

Two filters were used for the ENF AE extraction. The first was a location filter. Due to the inaccuracy of source location, this filter was applied for location 10 mm to 45 mm. The second filter only allowed signals produced during the crack propagation stage, defined by
ing load in a stroke controlled test..

Extraction of AE signals produced during Mode II failure was more difficult than extraction of Mode I signals.

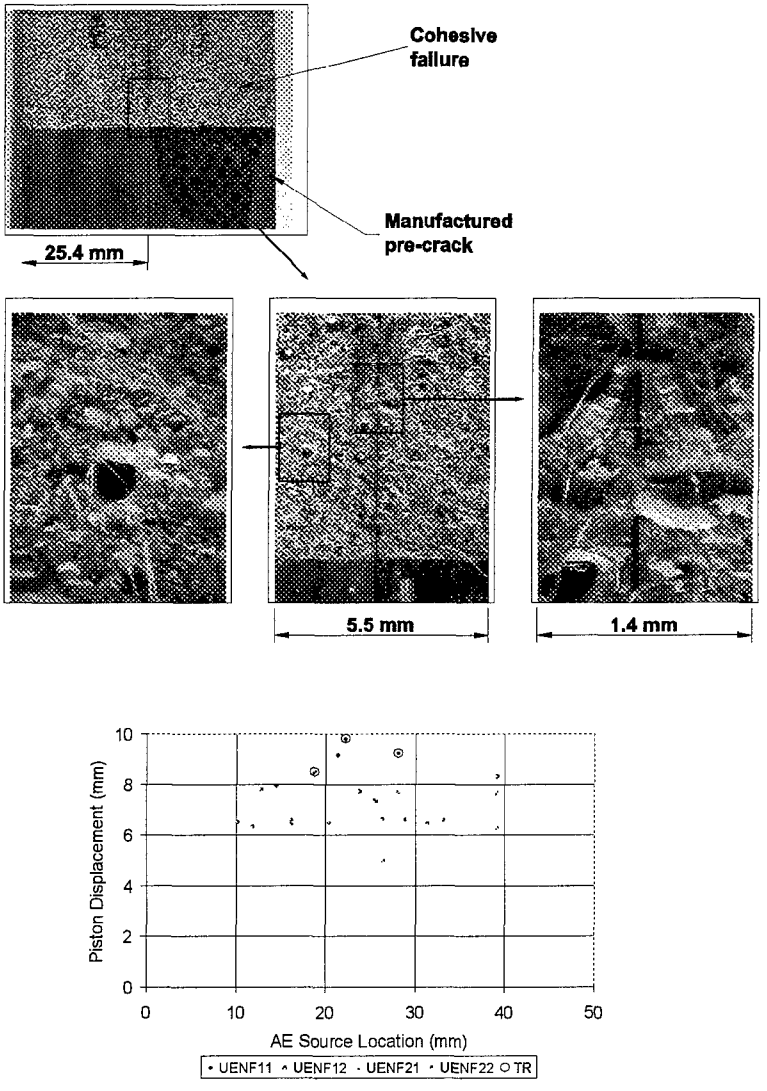

Figure 19: UENF fractography and AE location

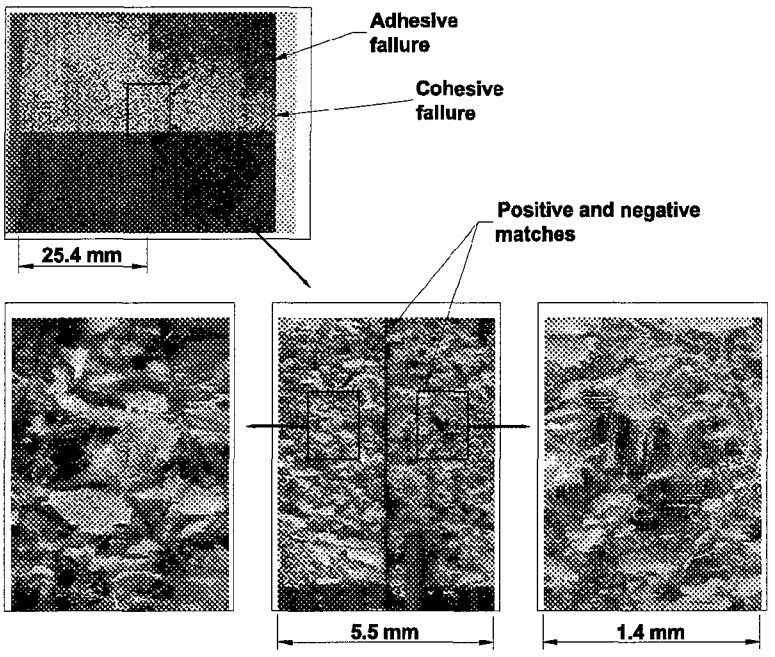

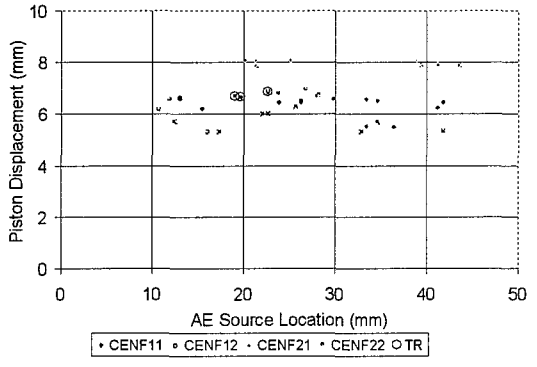

Figure 20: CENF fractography and AE location

5.5 Static Mixed Mode Fracture

5.5.1 Mechanical response

Results for the mechanical response of the Arcan specimens are shown in Figure 21. All specimens had unidirectional adherends. There was some play in the mechanical system at low loads, therefore the load-displacement curves were shifted to 0 mm at 0.5 kN. This made it possible to discern the slopes more clearly. The loading rate for all specimens was 0.5 mm/m

The fracture surfaces were analyzed, and if substantial adhesive failure occurred as compared to the adherend failure, the results were accepted. Fracture toughness was much lower if too much adherend failure occurred. Of the 28 specimens manufactured, 21 were tested successfully. The critical loads were reasonably scattered, as can be seen from Figure 21.

5.5.2 Critical stress intensity factors and energy release rates

Results for Arcan tests are presented in the form of critical stress intensity factors first. Figure 22 present lines fitted to average critical stress intensity values obtained from the tests. The Mode I and Mode II contributions were separated according to the theory explained above.

An accurate relation between K and G for the Arcan specimen is not available. Two models were applied for energy calculations. The one was the relation set for isotropic materials (9), and the other was the relation set for orthotropic materials (10).

The orthotropic model produced energy values far below the ones obtained in the pure

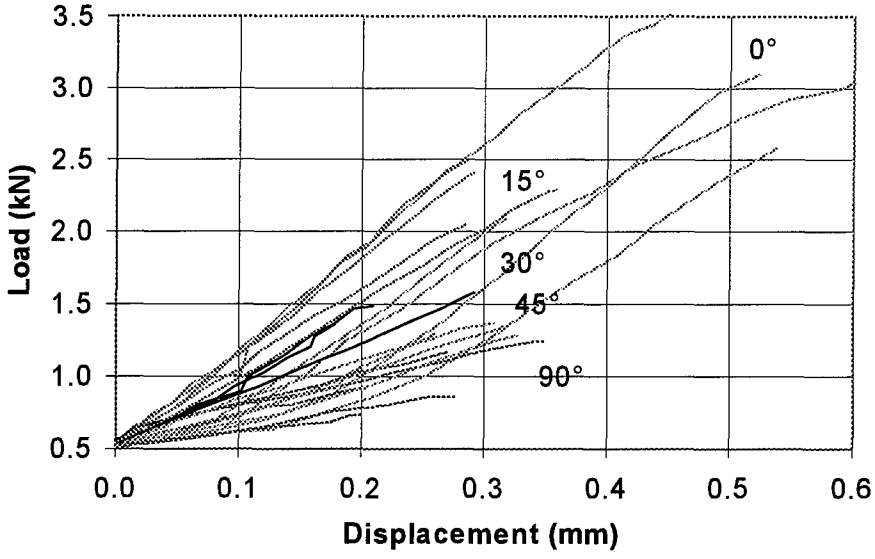

Figure 21: Load-displacement curves for Arcan tests

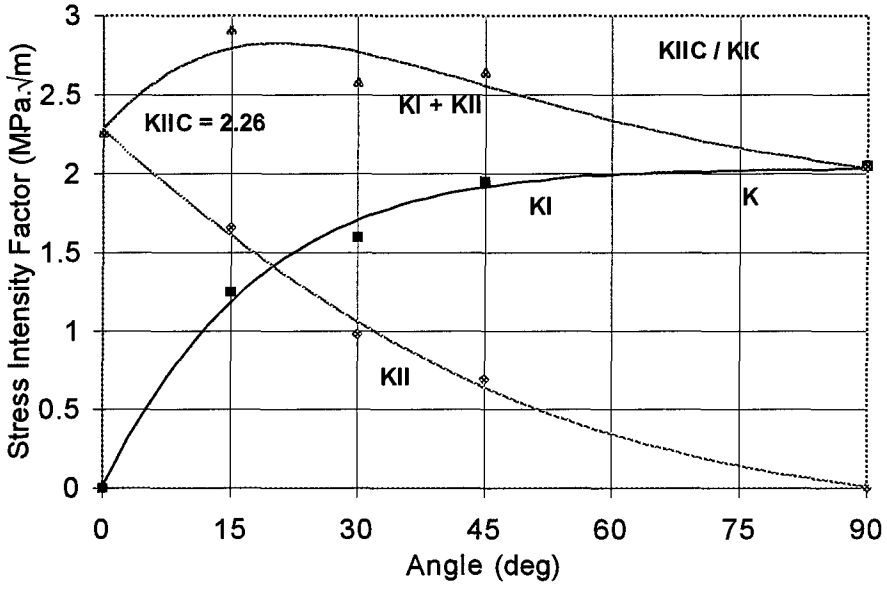

Figure 22: Variation of critical stress intensity factors with load angle

mode tests. Reasonable correspondence to the results for pure mode tests was obtained with the isotropic model. Both results are plotted with the corresponding linear fits (2) in Figure 23. It is apparent that more work is needed for the Arcan test data reduction. Taking into account that this test is also poorly suited for fatigue studies, another test may be better suited for mixed mode studies in the continuation of this research.

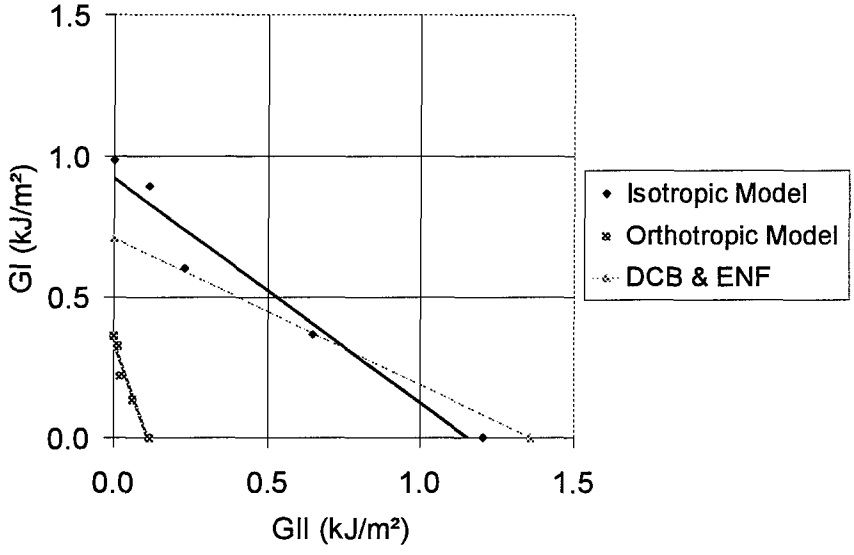

Figure 23: Mixed mode energy release rates computed by different models

5.6 Fatigue Fracture (preliminary)

5.6.1 Fatigue fracture mechanics

Fatigue fracture of isotropic materials has been studied in great detail and the crack

growth principles are reasonably well understood. Fracture mechanisms in composites are more complicated than in the isotropic case and fatigue fracture mechanics of composites is more complicated for the same reason. In Appendix I of this research it was found, however, that the fatigue crack growth in the lap joint specimens was mainly limited to the bond line. This fact makes it possible to attempt to describe fatigue fracture of the adhesive joints by fracture mechanics.

A typical equation used for such analysis is the Paris law (11). Cyclic loading causes a variation of the strain energy release rate from G_{min} to G_{max}. The fatigue loading is therefore described by ΔG, and the crack growth rate by da/dN [21]. It has been shown that stable delamination growth of many materials can be described by the Paris l

$$\frac{da}{dN} = C(\Delta G)^m \tag{11}$$

where $\Delta G = G_{max} - G_{min}$

Most sources present data on delamination growth with ΔG on a logarithmic horizontal axes, plotted against da/dN on a logarithmic vertical axis [22-23]. Results from displacement controlled, constant-amplitude fatigue DCB tests indicated that, if G_{Imax}/G_{IC} is less than 0.5, da/dN was reduced below 25 μm/cycle, approaching a 'no growth state' [12].

Characterization of Mode I (DCB) and mixed mode (CLS) debond growth of adhesively bonded composite joints has been done previously [24]. This study concentrated on two bonded systems: graphite/epoxy adherends bonded with EC 3445 and FM-300 adhesives. This investiga-

tion indicated that the total strain-energy release rate appeared to be the governing parameter for cohesive debond growth under static and fatigue loadings. This investigation also revealed that debond growth rates were measured at G values that were an order of magnitude below the stati toughness, G_C. This means both debond growth threshold values as well as static strength should be considered during design and material development and selecti

It was possible to identify a threshold value of maximum cyclic G_{II} for interlaminar fracture, below which no delamination occurred after one million cycles [25]. This made it possible to determine a total G threshold criterion that appeared to be sufficient for characterizing the fatigue delamination durability of composite materials with a wide range of static toughness.

Characterization of systems with different interlaminar fracture toughness have been done with DCB, CLS, and ENF specimen types [26]. The measured growth rate data from various fatigue tests were correlated with corresponding strain energy release rates. It was found that cyclic delamination growth resistance increases when the fatigue loading mode is changed from Mode I through mixed mode to pure Mode II.

In general, the results for pure mode fracture can be used for lap joint analysis in conjunction with models predicting energy release rates in lap joint specimens.

The previously described methods of DCB and ENF could be modified and used to determine crack growth rates for the adhesive joints. However, the Arcan test could not be modified in such a fashion, because the crack growth in this test is too unstable.

5.6.2 Preliminary results

Mode I fatigue experiments were performed in DCB test configuration. Figure 24 shows a typical crack tip for DCB crack propagation. The crack tip was reasonably easy to follow with the microscopic zoom head described above.

The crack growth rate curves for the DCB specimens are presented in Figure 25. The curve fitting was done according to the Paris law (11).

The beam method underestimated the crack growth rates. The UD specimens had a higher crack propagation rate than the CP specimens.

Mode II fatigue experiments were performed in ENF test configuration. Figure 26 shows a typical crack tip for ENF fatigue crack propagation. In general the crack tip was more difficult to follow than in the DCB case. The difficulty related to some damage that occurred ahead of the main crack tip.

Similarly to the DCB test, crack growth of the ENF tests was reasonably smooth. Som times, the controller took a while to reach the required loading cycle due to the high cyclic load frequency of 5 Hz.

The crack growth rate curves for the ENF specimens are presented in Figure 27. The curve fitting was done according to the Paris law (11).

UENF beam and LRAM methods overlapped almost completely. CENF beam method once again underestimated fatigue crack growth rate. The UD specimens had a higher crack growth rate than the CP specimens.

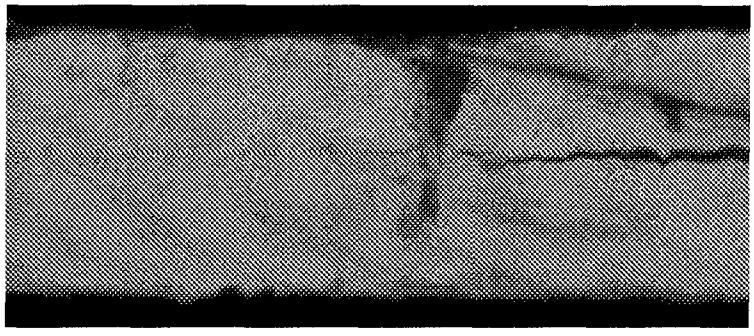

Figure 24: Typical crack tip for crack propagation during DCB test

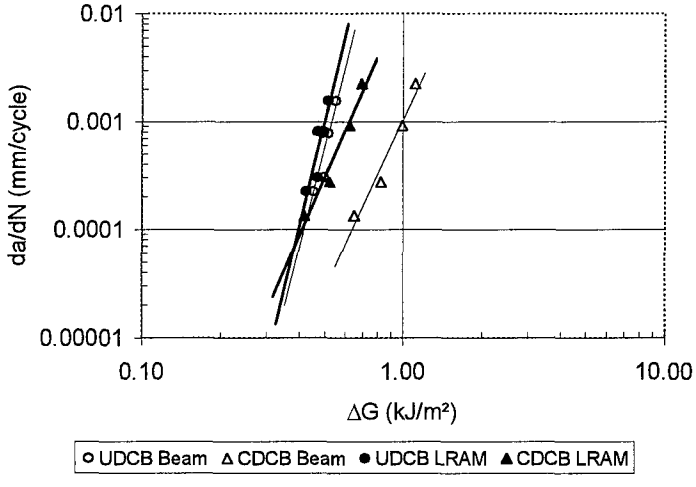

Figure 25: Preliminary data on crack growth for DCB specimens under fatigue

Figure 26: Typical crack tip for crack propagation during ENF test

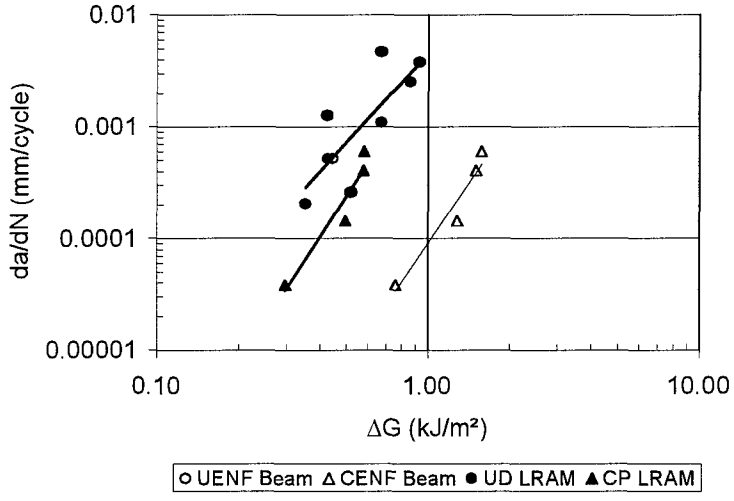

Figure 27: Preliminary data on crack growth for ENF specimens under fatigue

5.7 AE Analysis of Fracture Micromechanisms (preliminary

5.7.1 Transient waveshape classification

Vallen Systeme, GmbH, has developed a classification program called VisualClass that is capable of analyzing transient AE signals and clustering them according to certain features. A further analysis was done to determine if this software would be able to extract the same set of pure mode signals from the overall AE produced during DCB and ENF testing as was extracted by parametric filtering above.

The first step in this analysis was formal classification (clustering) of all unfiltered AE signals (overall AE) from the four pure mode static tests.

The number of time windows and the number of sample points per time window are specified in the feature extraction setup. VisualClass normalizes each waveform over the range of data points to be processed. This range begins with the first data point of the first time window and ends with the last data point in the last time window. For each time window, VisualClass applies a Hamming window function and calculates the FFT. The result of the FFT is a spectrum, formed by "N" spectrum data points. The values of the data points are features. Normalization factors are also used as features.

The features can be interpreted as the dimensions of a multidimensional space. Each waveform is represented by a point in this space. Classes and clusters are "clouds" of points (waveforms) in the feature space. VisualClass helps to find the features of highest discrimination quality and to use them for efficient separation of classes or clusters.

VisualClass uses Fisher ratios to separate classes into groups. The Fisher Ratio is an indicator for the discriminative quality of a feature. The higher the Fisher Ratio of a feature (compared to other features in the same plot) the better that feature is suited for the separation of classes.

Feature-feature projections are scatter (or point) plots of two features where the two axis are user-chosen basic or transformed features. This corresponds to a projection of the feature space to the plane defined by the two features. Different shapes indicate the different cluster types. A classifier file can be generated that describes the clusters (collections of similar signals) that were found.

The results of application of this procedure to four overall AE files are shown in Figures 28 to 31. Four classifier files were then developed from the clustering for each test. (UDCB, CDCB, UENF, and CENF).

5.7.2 Comparison of parametric filtering and waveshape classification

The classifier files from overall waveshape classification above were used to analyze the fracture signals obtained by parametric filtering. Application of this procedure to the signals from UD specimen fracture resulted in their classification into clusters marked 'cluster 1' in Figures 28 and 29.

Application of the procedure to the signals from CP specimen fracture resulted in their classification primarily into clusters marked 'cluster 2' in Figures 30 and 31. The quantity of signals classified into the corresponding clusters is given in Table 2.

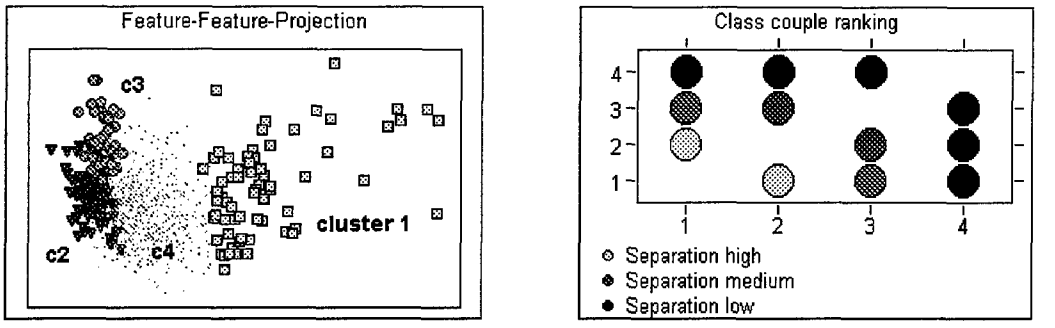

Figure 28: Results of overall AE signal clustering by VisualClass for UDCB

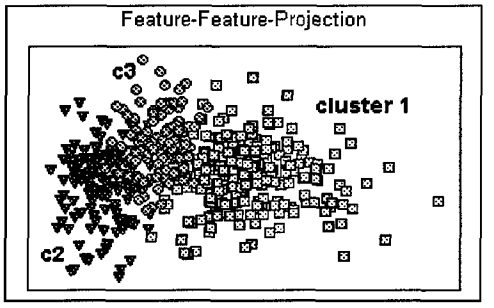

Figure 29: Results of overall AE signal clustering by VisualClass for UENF

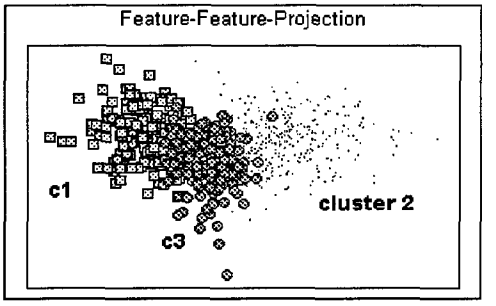

Figure 30: Results of overall AE signal clustering by VisualClass for CDCB

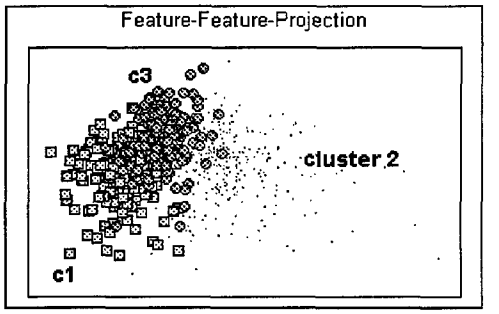

Figure 31: Results of overall AE signal clustering by VisualClass for CENF

Table 2: Success rate of classification of fracture signals into corresponding cluster

	UD adherends	CP adherends
Mode I	100%	96%
Mode II	79%	82%

The results indicate that the VisualClass software has the capability to cluster crack propagation signals together with high degrees of accuracy. The definitions of specific clusters can be used to extract the Mode I and Mode II fracture signals from other tests without using the parametric filtering.

5.7.3 Fracture micromechanisms under Mode I, Mode II, and mixed mode loadings

VisualClass also allows to analyze several AE transient files to find cluster definitions that produce best separation of signals from different files. This analysis was applied to the AE data from three fatigue tests: DCB, ENF, and lap joint. The AE data was collected during approximately 20 minutes of fracture tests in the crack propagation stage.

Pure mode signals were extracted during DCB and ENF fatigue tests described in this Part. Mixed mode signals were extracted during fatigue crack growth lap joint tests described in Appendix 1. Mixed mode extraction was done according to filtering described for fatigue tests described in Appendix 4. Extraction for both UD and CP specimens were made.

Figure 32 shows the three different UD files (Mode I, Mode II, mixed mode) analyzed by VisualClass. The analysis shows that the signals from the lap joint test are closer to the Mode II

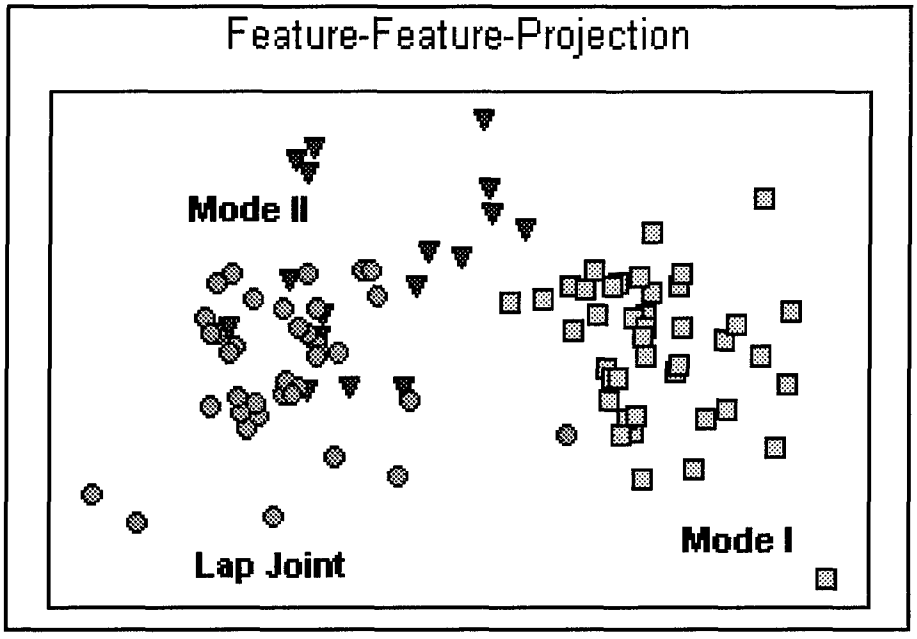

Figure 32: UD pure modes and mixed mode comparison

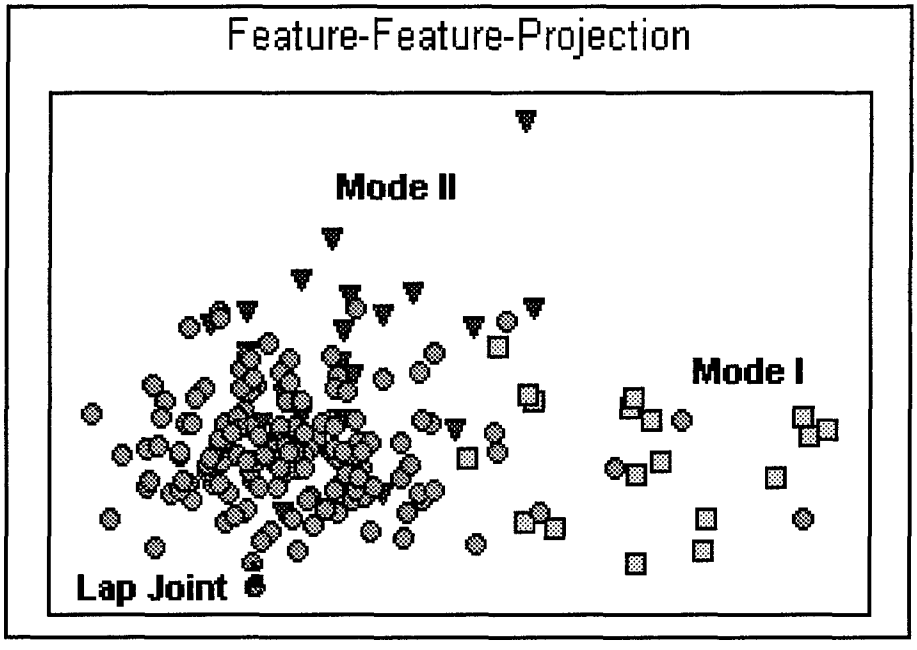

Figure 33: CP pure modes and mixed mode comparison

signals.

Figure 33 shows the same analysis done for CP specimens. Once again, lap joint signals showed a higher correspondence to the Mode II signals.

The results of this section indicate that AE TR signals generated during mixed mode lap joint fracture had a much closer correspondence to signals produced during Mode II failure than signals produced during Mode I failure for both UD and CP specimens.

The method of analysis used here is based on the transient data. The fact that the transient data from fracture can be separated by pattern recognition analysis provides confidence that the new transient-parametric method developed in Appendix 4 will be applicable to separate histories of fracture micromechanisms in joints.

These experiments are currently in progress.

5.8 Summary

- Area method and beam theories overestimate critical energy release rates. The error is more significant for joints with CP adherends.
- Mode I fracture toughness is larger for joints with unidirectional adherends. Mode II fracture toughness is larger for joints with cross-ply adherends.
- The method of data reduction for the Arcan specimen needs improvement. Different method should be tried for the mixed mode fracture analysis.
- Optical fractography revealed that there is a difference between Mode I and Mode II

failure. Mode I tended to cause a 'fuzzy' surface, due to the tear-out of polyester fibers. The surface formed during Mode II failure was 'clumpy'. Fractography of Arcan tests indicated that a greater tendency might exist for the crack to move into the adherend when mixed mode fracture occurs.

- The unidirectional specimens exhibited faster fatigue crack growth rates than the cross-ply specimens.
- The fatigue crack tip for DCB propagation was easy to identify, but in the case of ENF tests some damage ahead of the crack tip made this more difficult.
- Acoustic emission source location made during pure mode tests gave reasonable results for crack tip location for DCB tests, and only required some amplitude filtering. Although the accuracy was sometimes as bad as ±15 mm, the signals could be seen to follow the crack tip. Isolation of crack signals associated with crack growth was more difficult for ENF tests, and crack tip location could not be confirmed.
- TR extraction of crack signals for both Mode I and Mode II fracture was possible. When these extracted signals were fed into the VisualClass classifier, comparative results of between 79% and 100% were obtained, depending on the adherend lay-up and fracture mode. This means that VisualClass has a capability to identify adhesive fracture signals.
- AE TR signals generated during mixed mode lap joint fatigue fracture had a much closer correspondence to signals produced during Mode II fatigue failure than signals produced during Mode I fatigue failure. This correspondence showed for both UD and CP specimen ty

5.9 References

[1] Bathias, C., "Fracture and Fatigue of High Performance Composite Materials: Mechanisms and Prediction", Engineering Fracture Mechanics, Vol. 40, no.4/5, 1991, pp. 757-783

[2] Beuth, J.L., Narayan, S.H., "Separation of Crack Extension Modes in Composite Delamination Problems", Composite Materials: Fatigue and Fracture (Sixth Volume), ASTM STP 1285, E.A. Armanios, Ed., American Society for Testing and Materials, 1997, pp. 162-178

[3] Krüger, R. and König, M., "Prediction of Delamination Growth Under Cyclic Loading", Composite Materials: Fatigue and Fracture (Sixth Volume), ASTM STP 1285, E.A. Armanios, Ed., American Society for Testing and Materials, 1997, pp. 324-342

[4] Anderson, T. L., "Fracture Mechanics, Fundamentals and Applications", 2nd Edition, 1995

[5] "Proposed Manufacturing and Test Procedure for the Double Cantilever Beam Test", ASTM Round Robin

[6] "Test Procedure for the End Notch Flexure (ENF) Test", ASTM D30.02 Round Rob

[7] O'Brien, T. K. and Martin, R. H., "Round Robin Testing for Mode I Interlaminar Fracture Toughness of Composite Materials", Journal of Composites Technology & Research, JCTRER, Vol. 15, No.4, Winter, 1993, pp. 269-281

[8] Browning, C. E., and Schwartz H. S., "Delamination Resistant Composite Concepts", Composite Materials: Testing and Design (Seventh Conference), ASTM STP 893, J. M. Whitney, Ed. American Society for Testing and Materials, Philadelphia, 1986, pp. 256-265.

[9] Wilkens, D. J., Eisenmann, J. R., Camin, R. A., Margolis, W. S., and Benson, R. A., "Characterizing Delamination Growth in Graphite-Epoxy", Damage in Composite Materials, ASTM STP 775, K. L. Reifsnider, Ed., American Society for Testing and Materials, 1982, pp. 168-183.

[10] Xu, X. X., Crocombe, A. D., Smith, P. A., "Mixed-mode Fatigue and Fracture Behavior of Joints Bonded with either Filled or Filled and Toughened Adhesive", International Journal of Fatigue, vol. 17, 1995, pp. 279-286

[11] Naito, K. and Fujii, T., "Fatigue Crack Propagation Properties of Toughened Epoxy Adhesives Under Mode I Loading", Nippon Kikai Gakkai Ronbunshu, A Hen/Transactions of the Japan Society of Mechanical Engineers, Part A, vol. 63, n612, Aug 1997, pp. 1634-1641

[12] Ramkumar, R. L., and Whitcomb, J. D., "Characterization of Mode I and Mixed-Mode Delamination Growth in T300/5208 Graphite/Epoxy", Delamination and Debonding of Materials, ASTM STP 876, W. S. Johnson, Ed., American Society for Testing and Materials, Philadelphia, 1985, pp. 315-335

[13] Gong, X.-J. and Benzeggagh, M., "Mixed Mode Interlaminar Fracture Toughness of Unidirectional Glass/Epoxy Composite", Composite Materials: Fatigue and Fracture – Fifth Volume, ASTM STP 1230, R.H. Martin, Ed., American Society for Testing and Materials, Philadelphia, 1995, pp. 100-123

[14] Johnson, W. S. and Mangalgiri, P. D., "Influence of Resin on Interlaminar Mixed Mode Fracture", Toughened Composites, ASTM STP 937, American Society for Testing and Materials, Philadelphia, 1987, pp. 295-315

[15] Sriram, P., Khourchid, Y, Hooper, S. J., and Martin, R. H., "Experimental Development of a Mixed Mode Fatigue Delamination Criterion", Composite Materials: Fatigue and Fracture, 5th volume, ASTM STP 1230, R. H. Martin, Ed., American Society for Testing and Materials, Philadelphia, 1995, pp. 3-18

[16] Liechti, K. M. and Lin, C., "An Examination of Fracture Parameters Governing Mixed Mode Cyclic Debonding in Structural Adhesively Bonded Joints", University of Texas, Austin, Texas, USA

[17] Carlsson, L. A. and Pipes, R. B., "Experimental Characterization of Advanced Composite Materials", Prentice Hall, New Jersey, 1987

[18] Daniel, I. M. and Ishai, O., "Engineering Mechanics of Composite Materials", Oxford University Press, Inc., 1994

[19] Forte, M., "A Controlled Study of the Effects of Bondline Reinforcement on the Fracture Behavior of a Brittle Epoxy Adhesive", Ph.D. Thesis, Materials Directorate, Air Force Research Laboratory, Wright Patterson AFB, 1999

[20] Pang, H.L.J., "Stress Intensity Factors for Mixed-Mode Fracture in Adhesive-Bonded Joints", International Journal of Fatigue, 1994, vol. 16, August

[21] Carlson, R. L. and Kardomateas, G.A., "An Introduction to Fatigue in Metals and Composites", Chapman and Hall, 1996

[22] Prel, Y. J., Davies, P., Benzeggagh, M. L., and de Charentenay, F., "Mode I and Mode II Delamination of Thermosetting and Thermoplastic Composites", Composite Materials: Fatigue and Fracture 2nd volume, ASTM STP 1012, 1989, pp. 251-269

[23] Mall, S. and Johnson, W. S., "Characterization of Mode I and Mixed Mode Failure of Adhesive Bonds between Composite Adherends", Composite Materials: Testing and Design (Seventh Conference), ASTM STP 893, J.M. Whitney, Ed., American Society for Testing an Materials, Philadelphia, 1986, pp. 322-334

[24] Mall, S. and Kochar, N. K., "Criterion for Mixed Mode Fracture in Composite Bonded Joints", Department of Engineering Mechanics, University of Missourri-Rolla, Rolla, USA

[25] O'Brien, T. K., Murri, G. B., and Salpekar, S. A., "Interlaminar Shear Fracture Toughness and Fatigue Thresholds for Composite Materials", Composite Materials: Fatigue and Fracture 2nd volume, ASTM STP 1012, 1989, pp. 222-250

[26] Mall, S., Yun, K., and Kochar, N. K., "Characterization of Matrix Toughness Effect on Cyclic Delamination Growth in Graphite Fiber Composites", Composite Materials: Fatigue and Fracture, 2nd volume, ASTM STP 1012, 1989, pp. 296-310

[27] Kayupov, M. and Dzenis, Y. A., "Non-linear Analysis of Single Lap Composite Joints:

Effect of Crack Length", AFOSR Technical Report No. 10, 1998

[28] Dvorak, G., Ed., "Inelastic Deformation of Composite Materials", IUTAM Symposium, Troy New York, 1990

[29] Rybicki, E. F. and Kanninen, M. F., "A Finite Element Calculation of Stress Intensity Factors by a Modified Crack Closure Integral", Engineering Fracture Mechanics, vol.9, 1977, pp. 931-938

5.10 Enclosure: Large Radius Axisymmetric Damage Model (LRAM)

The Large Radius Axisymmetric Damage Model (LRAM) was developed at WPAFB as a convenient way to approximate the thermo-elastic stress field and energy release rates of laminated bodies with cracks subjected to various loads. The formulation employs the idea that the stress field in an axisymmetric cylinder approaches that in a long flat coupon as the radius to lam inate thickness ratio approaches infinity, provided the flat coupon stresses are independent of the length coordinate. In the limit as the ratio of radius to laminate thickness approaches infinity, the gradient of the hoop strain through the wall thickness approaches zero, generating a stress-strain field equivalent to a flat composite coupon under uniform axial strain. Using this methodology, an axisymmetric cylinder with radius much larger than thickness is used to represent a flat lami nate.

Table 1: LRAM prediction of normalized energy release rate G_{II}/P^2 of ENF model, supplied by Dr. Forte (AFRL/MLBC)

mm	UD	CP
10	0.597	0.325
20	2.100	1.147
25	3.195	1.746
30	4.519	2.471
40	7.852	4.297
50	10.916	6.045

Table 2: LRAM prediction of normalized energy release rate G_I/P^2 of DCB model, supplied by Dr. Forte (AFRL/MLBC)

mm	UD	CP
10	0.01294	0.00825
15	0.02610	0.01631
25	0.06613	0.04060
30	0.09300	0.05682
40	0.16043	0.09743
45	0.20101	0.12181
55	0.29585	0.17873
60	0.35012	0.21126
70	0.47235	0.28446
75	0.54031	0.32513
85	0.68991	0.41456
90	0.77154	0.46332